THE UNIVERSITY OF READING

Department of Meteorology
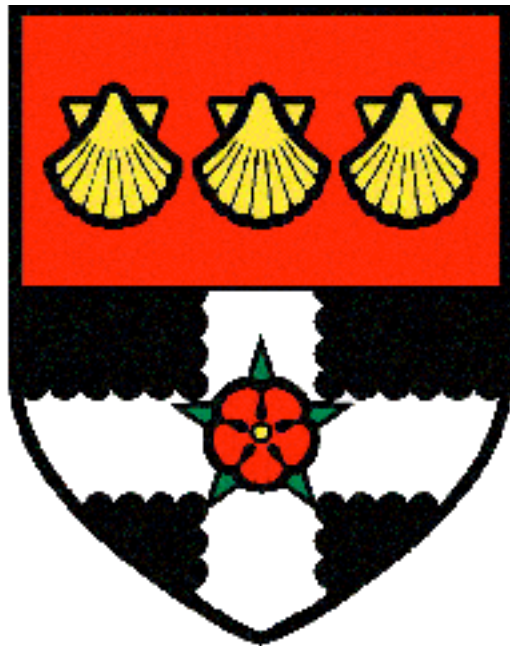
Understanding advances in the simulation of the Madden-Julian Oscillation in a numerical weather prediction model.

Linda Catherine Hirons

A thesis submitted for the degree of Doctor of Philosophy

March 2012

Declaration

I confirm that this is my own work and that the use of all material from other sources has been properly and fully acknowledged.

Linda Catherine Hirons

Abstract

The Madden-Julian Oscillation (MJO) is the dominant mode of intraseasonal variability in the Tropics. It can be characterised as a planetary-scale coupling between the atmospheric circulation and organised deep convection that propagates east through the equatorial Indo-Pacific region. The MJO interacts with weather and climate systems on a near-global scale and is a crucial source of predictability for weather forecasts on medium to seasonal timescales. Despite its global significance, accurately representing the MJO in numerical weather prediction (NWP) and climate models remains a challenge.

This thesis focuses on the representation of the MJO in the Integrated Forecasting System (IFS) at the European Centre for Medium-Range Weather Forecasting (ECMWF), a state-of-the-art NWP model. Recent modifications to the model physics in Cycle 32r3 (Cy32r3) of the IFS led to advances in the simulation of the MJO; for the first time the observed amplitude of the MJO was maintained throughout the integration period. A set of hindcast experiments, which differ only in their formulation of convection, have been performed between May 2008 and April 2009 to asses the sensitivity of MJO simulation in the IFS to the Cy32r3 convective parameterization.

Unique to this thesis is the attribution of the advances in MJO simulation in Cy32r3 to the modified convective parameterization, specifically, the relative-humidity-dependent formulation for organised deep entrainment. Increasing the sensitivity of the deep convection scheme to environmental moisture is shown to modify the relationship between precipitation and moisture in the model. Through dry-air entrainment, convective plumes ascending in low-humidity environments terminate lower in the atmosphere. As a result, there is an increase in the occurrence of cumulus congestus, which acts to moisten the mid-troposphere. Due to the modified precipitation-moisture relationship more moisture is able to build up which effectively preconditions the tropical atmosphere for the transition to deep convection. Results from this thesis suggest that a tropospheric moisture control on convection is key to simulating the interaction between the physics and large-scale circulation associated with the MJO.

Acknowledgments

First, I would like to thank my supervisors, Pete Inness and Frederic Vitart, for their guidance and support throughout this project. Their encouragement, enthusiasm and expertise have helped keep me focused and challenged for the duration of my PhD. I would especially like to thank them for their trust in me when I revealed that I would spend the last 3 months of the project living in Ghana! I would also like to thank Nick Klingaman for the time he has given to discussing and reading this work; I am grateful and have benefited from his input. At ECMWF I am particularly thankful to Peter Bechtold for his willingness to collaborate and share his expertise. I am also grateful for discussions throughout this project with members of the Tropical Research group, which have challenged my understanding and helped me to progress. In addition, Paul Dando at ECMWF provided excellent computing support when I was setting up my experiments. I would also like to thank colleagues at KNUST in Ghana for welcoming and supporting me during the final stages of this project.

I am extremely grateful to my family for their support, particularly my parents for their joint proof-reading effort at the end, and my grandmother for helping me buy my laptop at the beginning. I would especially like to thank Mark who has faithfully and unswervingly supported me throughout. Thank you for listening, reading and always encouraging. Additional thanks has to go to my friends inside and outside the department for all the supportive tea and teacake breaks!

Contents

CHAPTER 1

Introduction

1.1 Tropical Weather and Climate

Understanding the weather and climate of the Earth's tropical regions has proved a long-standing challenge for atmosphere and ocean scientists. Weather systems in the tropics are dominated by convectively-driven circulations, with seasonal variations largely dictated by the position of the Inter-tropical Convergence Zone (ITCZ). The most prominent meridional circulation in the tropics is the thermally direct Hadley circulation, named after the 18th century Englishman George Hadley. With its ascending branch over the ITCZ and descending branch over the subtropics, it is a major mechanism through which heat is transported polewards in the global atmosphere-ocean system. Another Englishman, Gilbert Walker, later recognised that convection in the tropics was far from zonally symmetric: the ascending branch of the zonal circulation migrated depending on variations in land- and sea-surface temperatures. Despite this early theoretical basis, the realistic representation and prediction of tropical convection in state-of-the-art models remains a challenge for both numerical weather prediction (NWP) and global climate models (GCM). For this reason, many modern modelling studies continue to focus on improving our ability to simulate organised tropical convection.

From a modelling perspective, simulating tropical convection provides a rigorous test for a numerical model because it involves interactions across a wide range of temporal and spatial scales. A major mode of intraseasonal variability in the tropics, and the focus of this thesis, is the Madden-Julian Oscillation (MJO; Madden and Julian, 1971). The MJO can be characterised as a planetary-scale convective anomaly, accompanied by an anomalous dynamical circulation, that propagates east through the Indo-Pacifc region. The basic features of the MJO are described in §1.1.1 and discussed in detail in §2.2. Modelling the MJO challenges our understanding of convective processes in the tropical atmosphere because it encompasses multi-scale interactions, ranging from the triggering of individual convective plumes on sub-grid scales, to the organisation and propagation of convection on a planetary-scale. The MJO is highly episodic and has been shown to interact with the major monsoon systems in the tropics, as well as modulate tropical cyclogenesis and affect the strength of the El Niño Southern Oscillation (ENSO; see §1.1.2 for details). Therefore, the MJO

provides an important source of predictability for medium-range forecasts. Reproducing the MJO in numerical simulations is essential to accurately simulate the mean climate and variability of the tropical regions. Despite its significance in the global climate system, the MJO remains poorly represented in numerical simulations, a subject which is addressed in detail in §2.4. This is due, at least in part, to a lack of understanding of the processes involved in the initiation and maintenance of the phenomenon (§2.3).

Furthering our knowledge of the meteorology and climate of the tropics, and consequently improving our ability to produce realistic forecasts, is much more than an academic endeavour. The tropics make up a quarter of the Earth's surface in which almost half of the worlds population live in more than 120 countries. A large proportion of the worlds poorest countries are located in the tropics, where many people's livelihoods depend on rain-fed subsistence agriculture. Therefore, the interaction of tropical phenomena such as cyclones, monsoons, the MJO and ENSO, which can cause severe flooding or drought, affects the lives of millions of vulnerable people in areas where the infrastructure to deal with the impacts is limited. Improving the quality of tropical forecasts can contribute to the development of better early-warning systems, which in turn should help restrict the damage caused to people's livelihoods.

Due to its importance as a source of tropical predictability, its poor representation in current simulations and its wide-reaching socio-economic affects, the motivation for studying the MJO is clear. This thesis focuses on the representation of the MJO in an NWP model and contributes to the understanding of the physical mechanisms a model must capture to accurately reproduce tropical intraseasonal variability.

1.1.1 Basic characteristics of the MJO

The MJO was first documented by Madden and Julian (1971) who, by performing spectrum and cross-spectrum analysis, discovered a pronounced 40-50 day oscillation in upper-tropospheric zonal-wind and surface-pressure data from Canton island in the equatorial Pacific Ocean (3°S, 172°W). A subsequent study (Madden and Julian, 1972) extended the analysis to other tropical stations and confirmed the existence of a planetary-scale, eastward-moving disturbance in wind and pressure which was confined to the tropics. Although considerable detail has been added to this definition during the intervening 40 years of research, this simple description remains accurate.

The 'active' phase of the MJO can be characterised as an equatorial, eastward-propagating, planetary-scale convective and precipitation anomaly. Ahead of and behind the deep convective centre are areas of weak convection known as the 'inactive' or 'suppressed' phase. The active
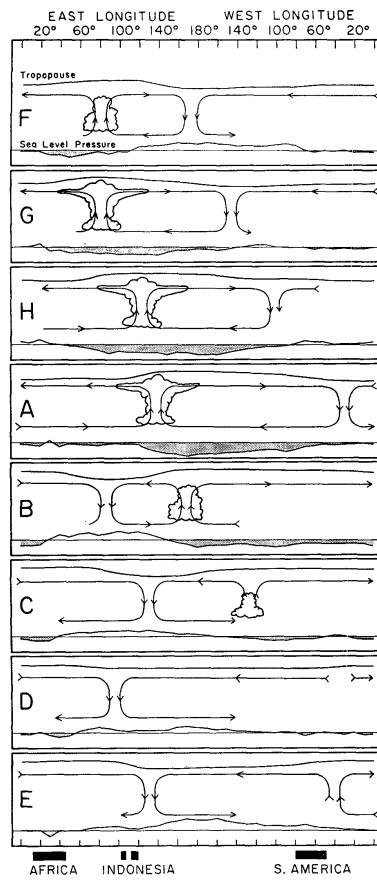
Figure 1.1 *Schematic representation of the different phases of the MJO. Regions of enhanced large-scale convection are indicated by clouds. The mean zonal wind disturbance is indicated by the overturning circulation arrows. The mean equatorial sea level pressure disturbance is plotted at the bottom (with negative anomalies shaded). The relative tropopause height is indicated at the top of each panel. Reproduced from Madden and Julian (1972).*

and suppressed phases are connected by a strong overturning circulation in the zonal wind, with low-level convergence into the convective centre and upper-level divergence out of it. During a 'typical' MJO event, the convective anomaly initiates in the Indian Ocean and propagates east through the Maritime Continent into the West Pacific with an average phase speed of approximately 5 m s^{-1}. Through the Indo-Pacific region, the convection is supported by the warm underlying sea surface temperature (SST). East of the dateline, where the SSTs are cooler, the convective anomaly dissipates and the decoupled large-scale circulation anomaly continues to propagate east with an increased phase speed. As the circulation anomaly re-enters the western Indian Ocean, it can re-excite the convective anomaly and lead to a successive MJO event. The lifecycle of a canonical MJO event is shown schematically in Fig. 1.1. A full description of the structure of the MJO is presented in §2.2.

1.1.2   Impacts of the MJO

While the MJO is an important source of predictability in its own right its interactions with other components of the global atmosphere and ocean system make it a crucial mode of variability for numerical models to capture. If a model is unable to accurately predict the evolution of the MJO, then it will be unable to model the correct teleconnection patterns associated with it. The impacts of the MJO on other aspects of the global circulation are discussed here and summarised in Fig. 1.2. This section is kept reasonably brief because, although important, the teleconnections of the MJO are not the main focus of this study.
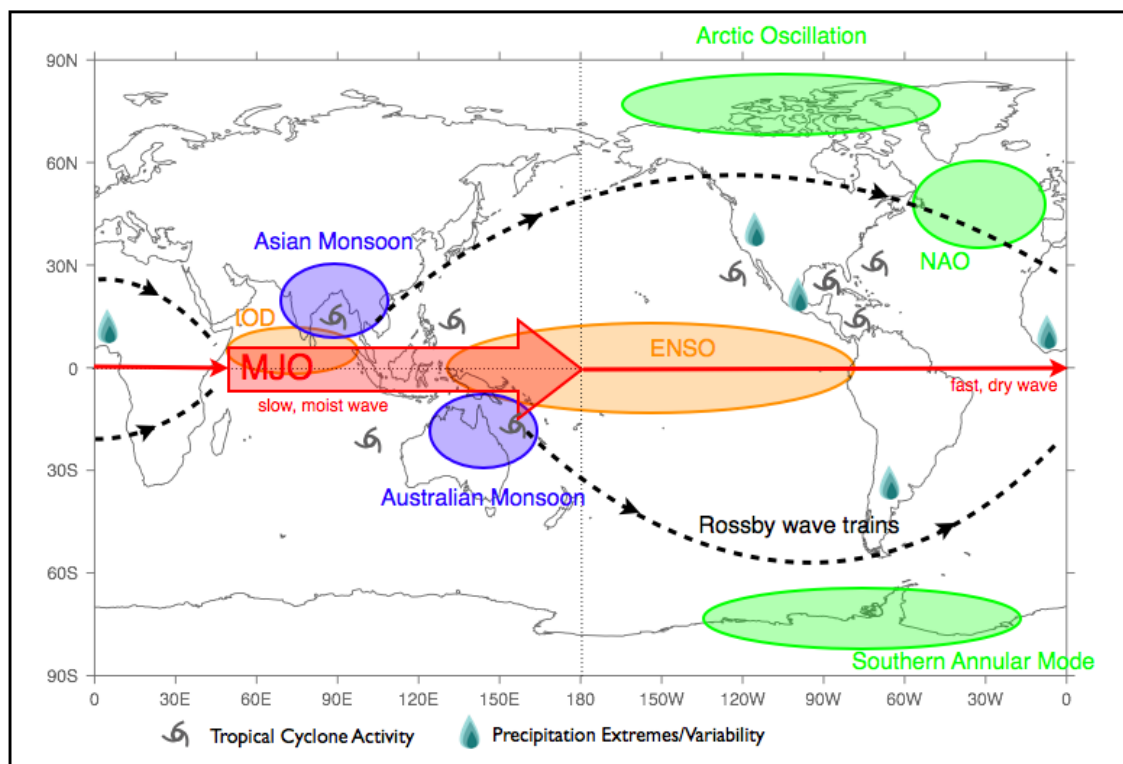
Figure 1.2 *Schematic representation of the global teleconnection patterns associated with the MJO. Adapted and extended from Lin* et al. *(2006).*

The MJO modulates intraseasonal variability in the major monsoon systems. Northward-propagating regions of anomalous convection associated with the eastward-propagating MJO have been shown to influence fluctuations in the characteristic active-break cycle of the Asian summer monsoon (e.g. Yasunari, 1979; Lawrence and Webster, 2002; Goswami, 2005; Vitart and Molteni, 2009a; Klingaman *et al.*, 2011). In the southern Hemisphere, rainfall and outgoing longwave radiation (OLR) anomalies associated with the passage of the MJO through the Maritime Continent modulate the strength of the westerlies associated with the Australian summer monsoon (e.g. Hendon and Liebmann, 1990; Wheeler and McBride, 2005).

Not only does the MJO affect monsoonal rainfall, but it influences rainfall variability and extremes on a near-global scale. For example, the passage of the MJO has been linked with intraseasonal rainfall variability and flooding along the west coast of North America (e.g. Bond and Vecchi, 2003), the occurrence of extreme rainfall events in South America (e.g. Liebmann *et al.*, 2004) and intraseasonal variations in West African rainfall (e.g. Matthews, 2004).

Arguably one of the most significant impacts of the MJO is its interaction with ENSO. The ENSO cycle is a coupled ocean-atmosphere phenomenon that dominates variability in the tropics on interannual timescales, and, through teleconnection patterns, modulates variations in global climate. Forecasting the onset and magnitude of El Niño (La Niña) events, characterised by persistent warm (cold) ocean temperature anomalies in the eastern equatorial Pacific, has received comprehensive study. However, as with the simulation of the MJO, difficulties remain in predicting events at long (> 3 month) lead times. The 1997-98 El Niño event has received particular attention because it developed quickly and had a very large amplitude, but was not accurately forecast. The rapid development of the 1997-98 El Niño conditions in the equatorial Pacific has been attributed to MJO-related westerly wind variability during 1996-97 (McPhaden, 1999), a mechanism that has also been shown to modulate previous ENSO cycles (Kessler and McPhaden, 1995). Prior to the onset of the 1997-98 El Niño a series of westerly wind bursts (WWBs) associated with successive MJO events weakened the trade winds. Each WWB excited a downwelling oceanic Kelvin wave which, as it propagated across the Pacific basin, deepened the thermocline. With each MJO event, the WWB increased in intensity and penetrated further into the central Pacific, which enhanced the deepening of the thermocline. This cut off the coastal upwelling, along the coast of South America, which would normally maintain the cooler SSTs in the eastern Pacific and, therefore contributed to the rapid development and large amplitude of the 1997-98 El Niño event. The termination of Indian Ocean Dipole (IOD) events, a coupled ocean-atmosphere phenomenon in the tropical Indian Ocean, has also been linked to intraseasonal variability associated with the MJO (e.g. Rao and Yamagata, 2004).

The MJO has also been shown to modulate tropical cyclone activity in the major ocean basins. For example, westerly wind anomalies associated with the MJO significantly increase the likelihood of tropical cyclogenesis in the eastern North Pacific, Gulf of Mexico and Caribbean Sea (e.g. Maloney and Hartmann, 2000a,b; Camargo *et al.*, 2008; Vitart, 2009). Similar modulation of tropical cyclone activity by the convectively active phase of the MJO has been shown in the Atlantic (e.g. Mo, 2000; Klotzbach, 2010), Australian region (e.g. Hall *et al.*, 2001; Vitart, 2009) and southern Indian Ocean (e.g. Bessafi and Wheeler, 2006).

The influence of the MJO is not confined to the tropical regions but, through the propagation of Rossby-wavetrains, extends into the extra-tropics (e.g. Hsu *et al.*, 1990; Lin *et al.*, 2009; Vitart and Molteni, 2009b). For example, the MJO has been shown to affect the Arctic Oscillation and Southern Annular Mode (e.g. Miller *et al.*, 2003), as well as act as a predictor for phase changes of the North Atlantic Oscillation (NAO; Cassou, 2008).

1.2   Aims and outline of this thesis

The extent of the effects of the MJO on the global atmosphere-ocean system (§1.1.2) adds further weight to the motivation to study the phenomenon. This thesis examines the representation of the MJO in the Integrated Forecasting System (IFS) at the European Centre for Medium-Range Weather Forecasting (ECMWF). Bechtold *et al.* (2008) showed that recent modifications to the model physics in Cycle 32r3 (Cy32r3) of the IFS, which was implemented in November 2007, improved the simulation of the MJO by better maintaing its amplitude at longer forecast lead times. This thesis aims to (a) investigate which aspects of the Cy32r3 modifications to the physics package were responsible for the advances in the representation of the MJO, and (b) understand the physical mechanisms that led to a better representation of tropical intraseasonal variability in the post-Cy32r3 IFS.

The initial focus of Chapter 2 is to expand upon §1.1.1 by providing a detailed description of the structure and lifecycle of the MJO (§2.2). This is followed by an overview of the current theories for the initiation and evolution of the MJO (§2.3). Finally, a review of the representation of the MJO in numerical models is given, with particular emphasis on the aspects of model configuration to which MJO simulation is most sensitive (§2.4).

Chapter 3 describes the model used in this study, the IFS at ECMWF (§3.2). A full description of the IFS convective parameterization is presented in §3.3. The progression in the representation of the MJO in the IFS over recent years is presented in §3.4. Most notably, the recent modifications to the convective parameterization in Cy32r3 of the IFS, which led to advances in the simulation of tropical intraseasonal variability (Bechtold *et al.*, 2008), are discussed. This discussion provides the motivation for the hindcast experiments conducted in this thesis (§3.5.2). The hindcast experiments are designed to test the sensitivity of MJO simulation to individual components of the modified IFS convective parameterization.

In Chapter 4, a set of recognised MJO diagnostics are applied to assess the representation of the MJO in the control versions of the IFS (§4.3) and the hindcast experiments (§4.4). Through these comparisons and the analysis of MJO case studies (§4.5), conclusions can be drawn about which

components of the modified Cy32r3 convection scheme are responsible for the advances in MJO simulation (§4.7).

Chapter 5 describes how the individual modifications to the convective parameterization affect the mean state of the IFS. The discussion throughout this chapter aims to understand why the observed changes to the mean state occur, and how that consequently leads to an improved representation of the MJO in the IFS. These questions are addressed fully in Chapter 6 through the application of a set of process-based diagnostics. The diagnostics examine the role of moisture in the simulation of the MJO; they are designed to determine the underlying physical mechanisms responsible for the observed improvements in the post-Cy32r3 IFS.

A summary of the key findings of this thesis are presented in Chapter 7. This includes addressing the questions posed in §3.6 (§7.1), and discussing potential future work (§7.2).

CHAPTER 2

The MJO: observed structure, theories and prediction

2.1 Introduction

The initial focus of this chapter builds on the brief MJO description from Chapter 1 through reference to a number of observational studies. The emphasis will then turn to a review of the main theories proposed to explain the characteristics of the MJO, outlining, where appropriate, the assumptions that have been made and the success in applying those theories in modelling studies. Our current ability to model the observed features of the MJO in state-of-the-art global circulation models (GCMs) is evaluated, with particular consideration given to the aspects of model formulation to which the MJO is known to be sensitive. This chapter concludes with the more recent exploitation of the MJO as an important source of predictability for numerical weather prediction (NWP) models.

2.2 MJO description and structure

Due to its complex and varied nature a thorough characterisation of the MJO is by no means a trivial task. Data collected from field campaigns such as TOGA-COARE[1] and the insight gained from observational and modelling studies create a canonical picture of the structure and lifecycle of the MJO. Many techniques were used to characterise and composite MJO events in early studies of its structure. For example, Madden (1986) selected MJO events using measurements of zonal wind at near-equatorial stations, while Knutson and Weickmann (1987) used Empirical Orthogonal Function (EOF) analysis of upper-tropospheric velocity potential. In their study, Rui and Wang (1990) identified and composited 36 (10 strong and 26 moderate) MJO events using 10 years of satellite OLR measurements and 6 years of ECMWF reanalysis (ERA) wind data, both with their interannual variations removed. In a later study, Hendon and Salby (1994) composited the cross-covariances of 11 years of satellite OLR and temperature measurements, along with 11 years of ERA wind data, all of which were band-pass filtered to isolate variability on intraseasonal timescales. Although individual MJO events can differ considerably in their strength and propagation characteristics, composite studies such as these build up a picture of how the large-scale

---

[1] the Tropical Ocean Global Atmosphere Coupled Ocean-Atmosphere Response Experiment

circulation anomaly is modified by the strength and location of the convective anomaly at different stages of a 'typical' MJO event.

The lifecycle of an MJO event typically starts with the development of a convective anomaly, within a weak positive equatorial temperature anomaly, in the western or central Indian Ocean (Fig. 2.1). The associated flow perturbations can be interpreted as a Kelvin-wave-like structure to the east of the convective region, with the zonal maximum on the equator and a Rossby-wave response to the west of the convection. Anomalous ascent occurs in the region of enhanced convection with anomalous descent occurring to the east in the region of suppressed convection. During the amplification of the convective anomaly in the western Indian Ocean, the maximum convective signal is co-located with the maximum low-level convergence. This initiation stage in the development of an MJO is represented schematically in Fig. 2.1.
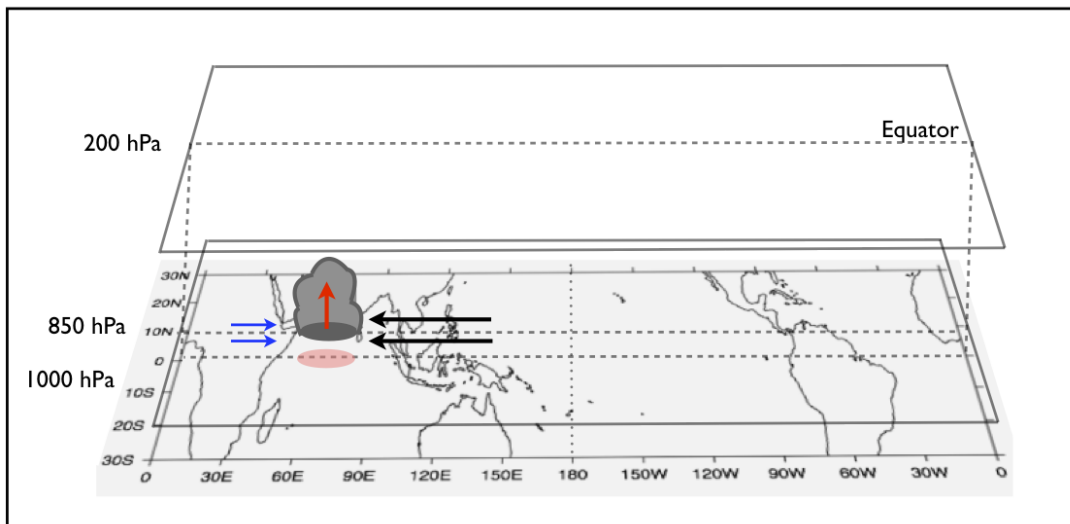
Figure 2.1   *Schematic representation of the MJO as it develops in the Indian Ocean. Red arrows indicate convective ascent, blue arrows indicate wind perturbations associated with the Rossby wave structure, black arrows indicate wind perturbations associated with the Kelvin wave structure. The red shaded region indicates a warm surface temperature anomaly.*

The source of the energy required to initiate an MJO event remains contentious. Broadly speaking the proposed mechanisms fall into two categories: (1) an event that has no convective precursors but produces its own energy through local atmospheric instability, the planetary scale being achieved through convective coupling to the large-scale circulation; (2) the MJO is the response of the atmospheric circulation to an existing forcing in the system, the eastward propagation and coupling being consequences of that response. Relatively few observational studies have focused on collecting detailed meteorological measurements from the initiation region in the equatorial Indian Ocean. Dynamics of the MJO (DYNAMO) is a collaborative observational campaign based in the

Indian Ocean that was due to start in October 2011, with the aim of improving our understanding of the physical processes involved in MJO initiation. The theories proposed to explain the initiation and maintenance of the MJO will be discussed further in §2.3.
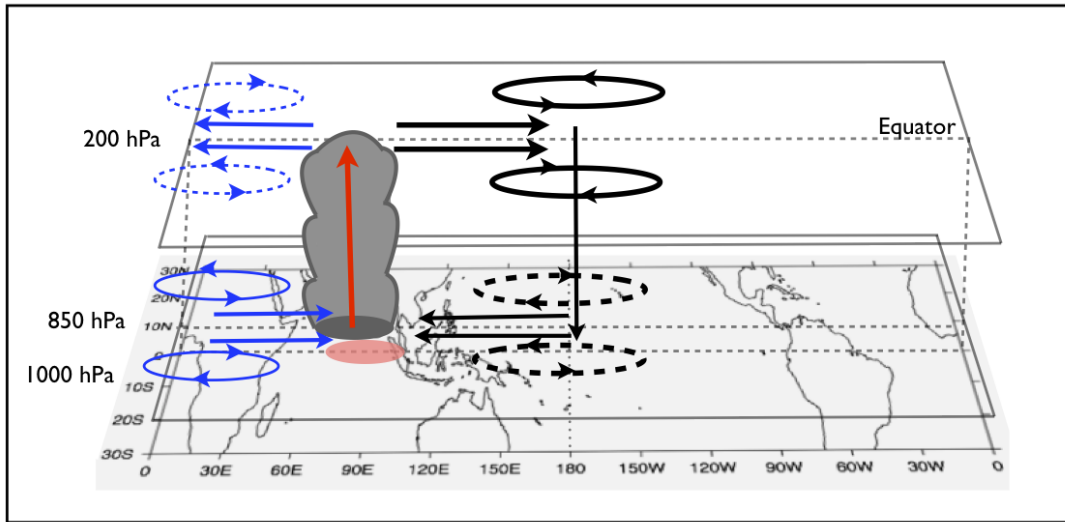
Figure 2.2 *Schematic representation of the MJO in its mature stage in the eastern Indian Ocean. Blue and black ovals represent gyre circulations; solid (dashed) lines represent cyclonic (anticyclonic) gyres.*

Low-level convergence into the convective region, which is now within a stronger equatorial surface temperature anomaly, strengthens the convective anomaly considerably forming a planetary-scale convective envelope (Fig. 2.2). Weak anticyclonic Rossby gyres form at upper levels slightly to the west of the convection with corresponding cyclonic gyres at 850 hPa. This is indicative of the first baroclinic mode vertical structure of the MJO in the Indian Ocean. Upper-level cyclonic gyres form in the West Pacific associated with the region of suppressed convection. According to Hendon and Salby (1994), the maximum convergence and divergence at 850 and 200 hPa respectively are co-located with convection, whereas the maximum surface convergence is approximately 50° ahead of the convective maximum. In contrast, Rui and Wang (1990) suggest that when the convective signal is at its strongest, the convergence maxima at the surface and just above the boundary layer (850 hPa) are located to the east of the convective maximum. Despite the subtle difference, both studies emphasise an offset between low-level or surface convergence and the triggering of deep convection in the Indian Ocean. The time lag suggests boundary layer convergence may play a key role in amplifying the MJO: the free troposphere can only respond once enough moist static energy has built up to trigger deep convection. The convective centre, known as the active phase, strengthens and starts to propagate slowly to the east with an average phase speed of 5 m s^{-1} (e.g. Weickmann *et al.*, 1985), leaving suppressed convective conditions behind it. The convective

anomaly reaches maximum strength in the eastern Indian Ocean. The rapid amplification of these large-scale eastward-propagating disturbances suggests that they are unstable modes. This stage in the lifecycle of a 'typical' MJO is represented schematically in Fig. 2.2.

The amplitude of the convective signal decreases as it propagates into the Maritime Continent (Fig. 2.3; Weickmann and Khalsa, 1990), however, according to Rui and Wang (1990), the area that it now covers increases. The associated upper-level anticyclonic Rossby gyres strengthen in this region. There is still some speculation as to why the reduction in amplitude over the Maritime Continent occurs. Wang and Xie (1998) propose the dissipation of energy over complex orography of the Indonesian islands and continual release of moist static energy by the local diurnal cycle of precipitation as possible mechanisms. The amplitude of the suppressed convective signal east of the dateline weakens, as do the associated upper-level cyclonic gyres. The Kelvin-like structure extends ahead of the convection reaching as far as the dateline. The maximum convective signal has shifted further westward relative to the maximum surface convergence and temperature anomaly. This stage in the lifecycle of a 'typical' MJO is represented schematically in Fig. 2.3.
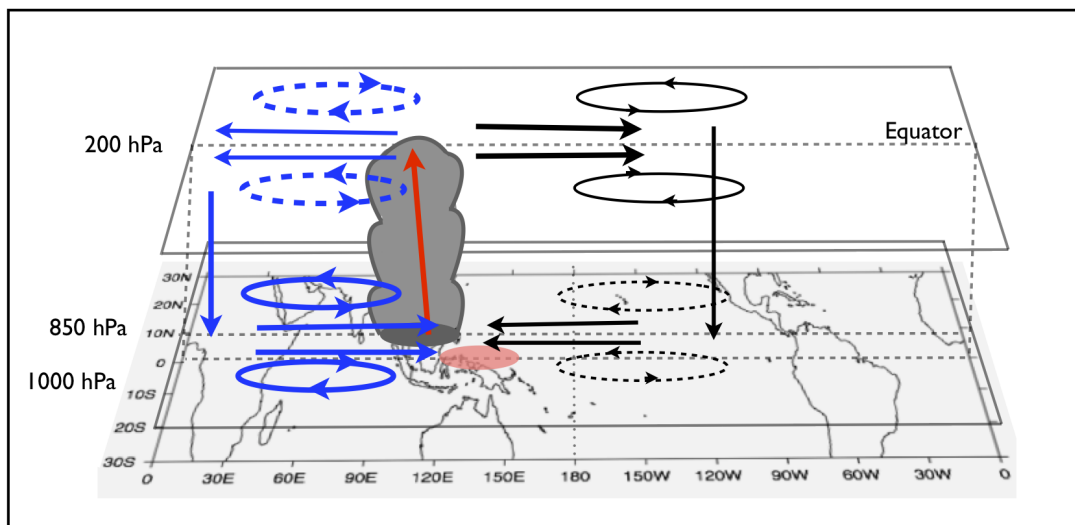
Figure 2.3   *Schematic representation of the MJO as it propagates through the Maritime Continent.*

As the eastward-propagating disturbance enters the West Pacific the convective anomaly, now even further westward relative to the surface convergence and sitting within a cold surface temperature anomaly, continues to decay (Fig. 2.4). However, the associated upper-level anticyclonic gyres maintain their strength. The circulation anomaly, now uncoupled from the decaying convective anomaly, continues to propagate eastward with an increased phase speed of approximately 10 m s^{-1} (Hendon and Salby, 1994). The dominant suppressed convective anomaly is now trailing convection in the Indian Ocean, the amplitude of the anomaly increases and associated upper-level

cyclonic gyres form. As the disturbance propagates into the eastern Pacific the vertical structure of the circulation anomaly, now fully decoupled from convection, becomes less baroclinic but rather tilts westward with height (Sperber, 2003). These features are represented schematically in Fig. 2.4.
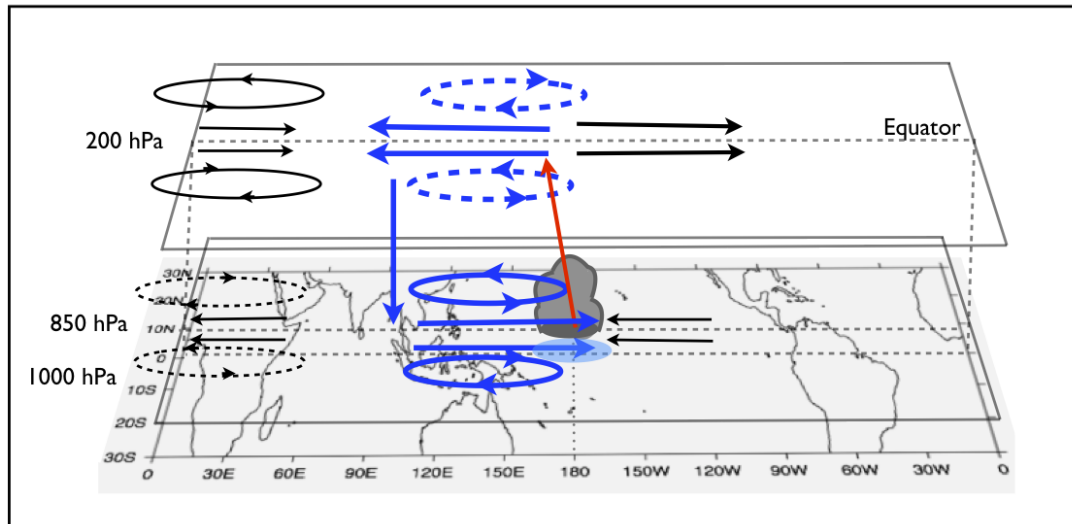
Figure 2.4 *Schematic representation of the MJO in its decaying stage at the dateline. The light blue shaded region indicates cold sea surface temperature anomaly.*

The phase speed of the MJO can vary considerably between different MJO events as well as at different stages of its lifecycle. By considering nine Northern Hemisphere summers (May - October) which covered approximately 30 MJO events, Knutson *et al.* (1986) found that the OLR anomalies in the equatorial Indian Ocean and West Pacific propagated eastward at approximately 3-6 m s^{-1}. The upper-level circulation anomalies propagated through the same region at approximately 6 m s^{-1}. Once the zonal-wind anomaly reached roughly 160°E it accelerated considerably and continued to propagate at approximately 15 m s^{-1}. They suggested that the observed increase in the propagation speed of the wind anomalies in the Western Hemisphere could be a result of changes in the zonal-wind basic state through which the atmospheric wave is propagating. Even though this analysis was carried out during northern summer, the season in which the canonical MJO described above is thought to be less active (e.g. Hendon and Salby, 1994; Zhang and Dong, 2004), other observational studies have also documented this increase in the speed of the circulation anomaly (e.g. Matthews, 2000).

Wang and Xie (1998) proposed that the mechanism which sets the slow propagation speed in the Indo-Pacific warm pool is the coupling of the convective anomaly with the underlying sea surface. The convective signal of the MJO dissipates as it encounters cooler SSTs in the eastern Pacific, whereas the large-scale upper-level divergent signal in the wind completes an entire circuit of the

globe (Knutson and Weickmann, 1987). East of the dateline the wind and pressure anomalies are able to propagate as free equatorial Kelvin waves, which are uncoupled from convection and can travel at speeds of up to 35 m s^{-1} (Milliff and Madden, 1996; Matthews, 2000). As the upper-level signal re-enters the Indian Ocean it coincides with the initiation of a new enhanced convective signal associated with the succeeding cycle of the MJO (Matthews, 2000). This slow eastward propagation is the fundamental characteristic which distinguishes the MJO from other eastward-propagating superclusters. Understanding the mechanisms responsible for the slow propagation of the MJO has formed the basis of, and motivation behind, theoretical study of the phenomenon.

During its active phase the MJO has a horizontal scale of approximately 12,000 to 20,000km and modulates all types of equatorial cloud. More specifically, Mapes and Houze (1993) showed the amount of large, deep convective clusters (up to 100,000 km^2 with cloud-top temperatures of < 208K) increased considerably when the MJO was active, which helps contribute to the rapid growth of the convective anomaly, and its organisation onto planetary scales. Johnson *et al.* (1999) identified a trimodal distribution of cloud in the tropics (Fig. 2.5), the three dominant types being shallow cumulus, cumulus congestus and deep cumulonimbus. Shallow cumulus clouds detrain at the height of the boundary layer inversion; cumulus congestus clouds penetrate into the mid-troposphere detraining at the melting level; deep cumulonimbus clouds penetrate as far as the upper-troposphere, detraining near the tropopause. The role of shallow and deep convective clouds in modulating tropical convection has long been established, however Johnson *et al.* (1999) emphasised the unrecognised importance of cumulus congestus.

Johnson *et al.* (1999) used data from the TOGA COARE period to show that during late November 1992 there was an increase in the occurrence of shallow and mid-level clouds ahead of the region of enhanced convection. The occurrence of these clouds moistened the mid-troposphere, which preconditioned the atmosphere, making it more favourable to deep convection and allowing for the propagation of the MJO in December 1992. Many recent studies have focused on congestus preconditioning as a mechanism for transitioning from shallow to deep convection in the tropics (e.g. Kuang and Bretherton, 2006; Waite and Khouider, 2010). Furthermore, Redelsperger *et al.* (2002) showed that cloud-top height during TOGA COARE was modulated by the intrusion of dry air. These studies highlight the importance of the availability of free-tropospheric environmental moisture in determining the strength and location of convection.

Despite being referred to as an oscillation, the MJO is highly irregular. Only one fully developed MJO can exist in the tropics at a given time. However, there can be extended periods with one
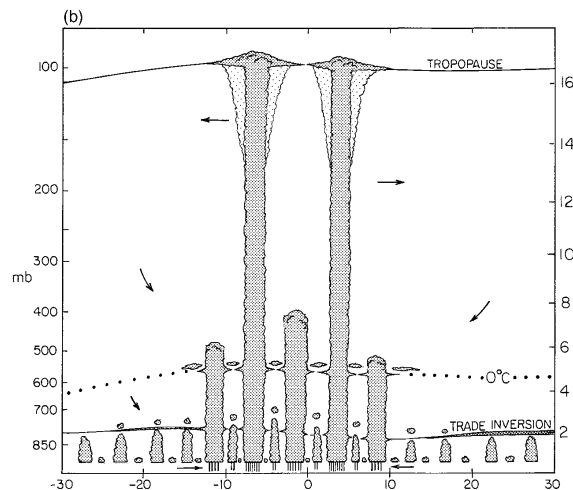
Figure 2.5 *Diagram of the trimodal distribution of tropical clouds. Three stable layers are indicated; shallow convection detrains at the trade inversion, cumulus congestus at the 0° level and deep cumulonimbus forms cirrus anvils at the tropopause. Arrows indicate the meridional circulation. Reproduced from Johnson* et al. *(1999).*

MJO event occurring after another, or extended periods with very little or no MJO activity. As the large-scale circulation anomaly continues to propagate east of the dateline, and once it has been uncoupled from the convective signal in the West Pacific, it can re-excite convection as it enters the Indian Ocean. In his study, Matthews (2008) distinguished between MJO events which had no preceding MJO as primary events, and those which followed an existing event as successive events. He showed that 40% of the MJO events between 1974 and 2005 were primary events. Not only is the MJO highly episodic, but it exhibits a strong seasonal cycle with the main peak in activity occurring on the equator in boreal winter (December-March). The secondary peak, sometimes referred to as the northward-propagating intraseasonal oscillation (NPISO), occurs slightly north of the equator in boreal summer (September-June; Zhang and Dong, 2004). The main peak influences the Australian monsoon (Hendon and Liebmann, 1990), while the secondary peak modulates the active break cycle in the Asian monsoon (Lawrence and Webster, 2002).

The MJO exhibits a multi-scale structure, evident in the satellite images in Fig. 2.6. The large-scale eastward-propagating structure of the MJO is a composite of both eastward- and westward-moving cloud clusters on different spatial and temporal scales, each developing slightly to the east of the preceding system (Nakazawa, 1988). Observational studies have revealed the existence of two dominant high-frequency signals. Firstly, synoptic-scale systems with a period of 2-15 days and propagating eastwards at approximately 13 m s^{-1} (Dunkerton and Crum, 1995), the speed of convectively coupled Kelvin waves. Secondly, mesoscale systems with a period of 2 days which propagate westward (Hendon and Liebmann, 1994). Although the probability of these high-frequency

(a) May 2nd 2002   (b) May 9th 2002
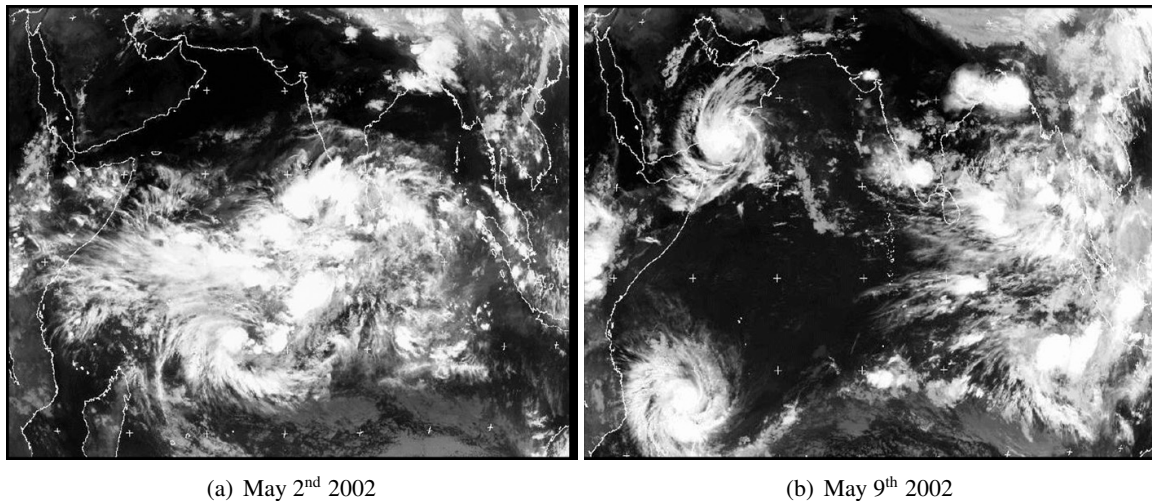
Figure 2.6 *EUMETSAT Infrared (IR) images of the multiscale organisation of tropical convection associated with an MJO over (a) the Indian Ocean on 2nd May 2002 and (b) the Maritime Continent on 9th May 2002 with twin trailing tropical cyclones.*

events occurring is increased during the active phase of the MJO, Clayson *et al.* (2002) showed that they can exist independent of any large-scale convective forcing.

2.3 MJO Theories

A successful meteorological theory is able to describe the structure, and predict the evolution of an observed phenomenon. It is therefore crucial that developments made in simulating the MJO do not occur independently of the ongoing aim to improve our understanding of the physical mechanisms responsible for its structure. Although many theories are complementary and supported by findings from observational and modelling studies, some deficiencies remain; this makes the MJO the "'holy grail" in the quest to understand tropical atmospheric dynamics' (Raymond, 2001).

2.3.1 Equatorial wave dynamics

An appropriate point of reference for the introduction of MJO theories is to review equatorial large-scale dynamics. For a detailed review of the current understanding of convectively coupled equatorial waves see Kiladis *et al.* (2009). The development of equatorially trapped wave theory was documented in the 1960s by Matsuno (1966), who used a divergent barotropic model to carry out his study. By considering the primitive equations on an equatorial β-plane linearised about a barotropic basic state, (i.e., a state with no vertical shear) and by making some other non-trivial assumptions, the author showed that the equations for tropical flow on pressure coordinates could be separated into two distinct atmospheric layers. In the upper layer, flow is governed by vertical motions. The flow in the lower layer is vertically independent and governed by the shallow water

equations (SWEs). Equatorially trapped waves are zonally propagating solutions of the SWEs. These can be thought of as long-wave responses to tropical convective heating.
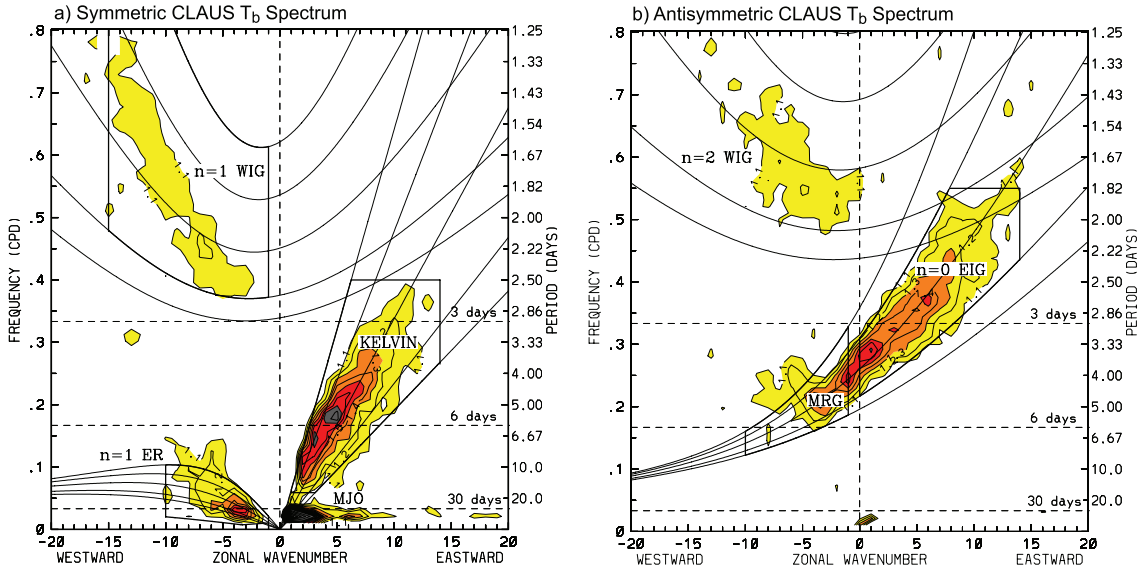
Figure 2.7 *Wavenumber-frequency power spectrum of the (a) symmetric and (b) antisymmetric component of equatorially averaged (15°N to 15°S) brightness temperature (T_b) from the geostationary and polar-orbiting satellite dataset Cloud Archive User Services (CLAUS) for July 1983 to June 2005. A smoothed red noise background spectrum has been removed, leaving the statistically significant spectral peaks (for details see Wheeler and Kiladis (1999)). Contour interval is 0.1; contours and shading begin at 1.1 (where the signal is > the 95% level). Dispersion curves from the shallow water modes in (Matsuno, 1966) are also plotted at equivalent depths of 8, 12, 25, 50 and 90 m. Reproduced from Kiladis* et al. *(2009).*

Solutions found in this way can be divided into two categories: those which are symmetric and those which are antisymmetric about the equator (Fig. 2.7). The dispersion characteristics of the observed convectively coupled equatorial waves, shown by the shading in Fig. 2.7, are in good agreement with the dispersion curves predicted by the linear theory of Matsuno (1966). The most prominent spectral peaks in the symmetric spectrum are the eastward-propagating Kelvin and westward-propagating equatorial Rossby (ER) waves. The antisymmetric spectrum is dominated by mixed Rossby-Gravity (MRG) waves which can propagate east or west. The MJO, despite exhibiting a considerable spectral peak in the observed symmetric spectrum, does not follow a theoretical dispersion curve.

As the only equatorial wave mode which exhibits a planetary-scale zonal wind structure similar to the MJO and propagates to the east, the Kelvin wave was the focus of original attempts to formalise an MJO theory. However, a convectively coupled Kelvin wave propagates east at approximately 15 m s^{-1}, three times the observed MJO propagation speed. It was accounting for the mechanisms by which this reduction in phase speed is accomplished, and hence distinguishing the

MJO from the convectively coupled Kelvin wave, which was the focus of early theoretical studies of the MJO.

To explain the characteristics of the MJO, Chang (1977) took the equatorial-wave theory of Matsuno (1966) and applied a damping represented by Rayleigh friction in the zonal momentum equation and Newtonian cooling in the thermodynamic equation. Yamagata and Hayashi (1984) used the two-dimensional linear response model of Gill (1980) and imposed a localised heat source over the equatorial Asian monsoon region with an intraseasonal period of 40 days. Chao (1987) extended this analysis by applying Gill's model for tropical stationary waves to a mobile frame of reference. This was done by applying a heat source which propagated in the zonal direction at a prescribed constant speed. By emphasising the importance of Rossby waves it was postulated that the observed phase speed of the MJO was a weighted mean of the eastward-propagating Kelvin wave and westward-propagating Rossby wave.

These theories hypothesise that the MJO signal arises as a response to a local heat source which either pulsates on intraseasonal timescales, or moves at a constant speed. However, they could not fully explain the mechanisms which caused the heat source to move, or what selected the oscillation frequency, period and phase speed. A common strand emerging from these (and many other) early studies was the importance of the interaction between local convective heating and the large-scale dynamical circulation. The aim of the next generation of MJO theories was to explain the mechanisms which caused local atmospheric instability and provided the energy for MJO initiation. Theories included the atmospheric instability arising as a result of interaction between (a) convection and large-scale equatorial waves (§2.3.2), (b) surface evaporation and surface winds (§2.3.3) or (c) surface friction and moisture convergence (§2.3.4). Later, recognition was also given to the influence of coupled ocean-atmosphere processes (§2.3.5) and to thermodynamic processes in the atmosphere (§2.3.6).

2.3.2 Wave-CISK

The studies reviewed previously focused on the modification of equatorial-wave theory by convection. Amongst these, the theory which has received the most attention is wave-CISK. Conditional Instability of the Second Kind (CISK) was first documented by Charney and Eliassen (1964) as a mechanism for amplifying tropical cyclones. In conditionally unstable atmospheric conditions, where the lower troposphere is both warm and moist, the CISK theory predicts that the low-level convergence associated with a large-scale tropical disturbance provides sufficient force to lift an air parcel to its level of free convection. The resulting cumulus convection releases latent heat which

acts to strengthen the large-scale system. In terms of tropical-cyclone formation, low-level convergence due to Ekman pumping supplies moisture to trigger convection; the latent heat released from the convection supplies the tropical cyclone with energy to amplify.

The theory was later extended in an attempt to explain the organisation of deep convection onto planetary-scales in the tropics (Yamasaki, 1969; Hayashi, 1970; Lindzen, 1974). In their theories, referred to by Lindzen (1974) as wave-CISK, rather than low-level convergence occurring as a result of Ekman pumping at the surface, convergence results from the low-level wind fields associated with equatorially trapped Kelvin and Rossby waves.

Lau and Peng (1987) investigated the mechanisms responsible for propagating the area of low-level convergence and the associated intraseasonal convective complex to the east. In their study, a 5-level model was used with "positive-only" heating parametrized by a wave-CISK scheme. "Positive-only" heating means the scheme assumes that diabatic heating occurs only in the regions of low-level moisture convergence, with no cooling in the divergent regions. It also makes the assumption that the amount of latent heat released through large-scale ascent is proportional to the amount of moisture converging into the column at low-levels. The model generated both eastward-propagating Kelvin and westward-propagating Rossby waves. The wave-CISK mechanism favours amplification of the divergent Kelvin waves over the rotational Rossby waves, accounting for the eastward propagation of the entire disturbance. However, the disturbance in their model exhibited phase speeds of approximately $19\ \mathrm{m\ s^{-1}}$, much faster than that of the observed MJO, a speed which they suggested was set by the time it took a Kelvin wave to complete a full circuit around the equator. Their simulations showed that the phase speed, growth rate and vertical structure of the oscillation was sensitive to both the static stability of the model basic state and the vertical heating profile.

Numerous studies have been carried out using convective parameterization schemes based on the wave-CISK mechanism in GCMs. Such schemes, where convection is triggered in regions of large-scale moisture convergence, are referred to as Kuo-type schemes (Kuo, 1965, 1974). As one of the first available cumulus parameterizations, the Kuo scheme was a very useful tool. However, it has since been almost entirely replaced by better, more complex schemes. The sensitivity of MJO simulation to the type of convective parameterization used will be discussed in more detail in §2.4.4.

The rationale for applying the wave-CISK mechanism to a cumulus parameterization scheme has since been challenged (Emanuel *et al.*, 1994; Raymond, 1994). It was argued that the direct de-

pendence of convective heating on moisture convergence created an unphysical large-scale control on convection. The fundamental assumption that the convection consumes moisture, rather than potential energy, means that the convection does not alter the stability of the profile and a positive feedback results: more convection leads to more moisture converging into the region which in turn leads to more convection.

The existence and growth rate of unstable wave-CISK type modes in numerical simulations is very sensitive to the type of cumulus parameterization used. Crum and Stevens (1983) showed that wave-CISK growth rates are much weaker with a spectral mass-flux scheme than in a Kuo-type scheme. A hypothesis later confirmed by Brown and Bretherton (1995) who showed that both long and short wavelength wave-CISK modes were damped in their study which also used a mass-flux scheme. Hayashi and Golder (1997) took the opposite approach of suppressing the wave-CISK mechanism in their model to test the effect of its absence on tropical wave activity. This was done by suppressing the convergence feedback in their 9-level spectral model, in which convection was parametrized by a moist convective adjustment scheme. Without the influence of the wave-CISK mechanism, MJO-like signals were weakened, but did not completely disappear. This suggests that other mechanisms must work to sustain the MJO. Although the original wave-CISK mechanism proposed by Lau and Peng (1987) is regarded as being unable to fully explain the structure of the MJO, modified versions of this theory remain relevant today (§2.3.4).

2.3.3 WISHE

The interaction of low-level winds with evaporation from the tropical oceans was proposed as alternative mechanism for destabilising the atmosphere to initiate an MJO (Emanuel, 1987; Neelin *et al.*, 1987). This theory is referred to as wind-evaporation feedback (Neelin *et al.*, 1987) or Wind Induced Surface Heat Exchange (WISHE; Yano and Emanuel, 1991).

In the WISHE theory, rather than convection being a heat source, it is treated as a mechanism that redistributes moisture and heat from the ocean's surface into the troposphere through wind-induced surface latent heat fluxes. It is important to remember that, in the absence of the feedback from wind-induced surface fluxes, the latent heat released due to moisture convergence alone would simply balance adiabatic cooling. The WISHE theory assumes an area of enhanced convection over an equatorial ocean in a mean surface easterly flow. The low-level convergent wind pattern associated with that convective region will enhance (suppress) the surface wind stress to the east (west). These wind stress anomalies will give rise to positive (negative) surface fluxes to the east (west) of the convection, where positive is defined as ocean to atmosphere fluxes. The temperature,

pressure and vertical velocity perturbations associated with the surface fluxes amplify the wave mode and move the trough further to the east, causing the eastward propagation of the entire system.

Neelin *et al.* (1987) and Emanuel (1987) applied their theories to simplified models and were able to produce low-frequency equatorially trapped instabilities which propagated eastward with realistic phase speeds. Many studies have focused on the role of the WISHE mechanism in initiating and sustaining the MJO. Brown and Bretherton (1995) used a hydrostatic, non-rotational model in which the two-dimensional equations of motion were linearised about a basic state in radiative-convective equilibrium. Convection in their model was parametrized using a mass-flux scheme. They showed that all the wave-CISK modes and short-wave WISHE modes were damped by unsaturated downdrafts. The only unstable mode able to amplify was the long wavelength WISHE mode, but it propagated too fast. Lin *et al.* (2000) used a non-linear, intermediate-level atmospheric tropical circulation model to investigate the representation of the MJO. Radiative-convective feedbacks were included in their model; convection was parametrized using a moist convective adjustment scheme. Intraseasonal variability in their simulations was dominated by eastward-propagating, wavenumber-1 signals which resembled the MJO. The conclusion from these studies, and other sensitivity experiments (e.g; Maloney and Sobel 2004), was that the WISHE mechanism increased tropical intraseasonal variability, but alone was insufficient to explain its existence. Additionally, this theory in isolation has difficulty explaining the slow propagation speed of the MJO without relying on arguments from equatorial wave dynamics.

In a similar way to the wave-CISK mechanism, the unstable modes with the largest growth rates in the WISHE theory favour the smallest scales. This problem, which Dunkerton and Crum (1991) refer to as an instability "catastrophe", requires subtle treatment to overcome. In the case of wave-CISK, it is done by assuming positive-only heating. Emanuel (1993) overcame this difficulty in the WISHE theory by introducing a time lag between the surface evaporation and convective heating which had a damping effect at short wavelengths. However, Brown and Bretherton (1995) showed that introducing a time lag in the vertical transport of moisture from the boundary layer into the free troposphere resulted in the oscillation propagating nearly five times faster than the observed phenomenon.

A fundamental assumption in the WISHE theory is that the east-west asymmetrical heating and surface fluxes require a background easterly flow to produce an eastward-propagating disturbance. Although the global mean surface winds in the equatorial regions are easterlies, there are considerable longitudinal variations. Using an 80-year timeseries of monthly mean surface data from comprehensive ocean-atmosphere datasets (COADS), Wang (1988a) showed that in large propor-

tions of the Indian Ocean and West Pacific the mean flow is in fact westerly. This would imply that in those regions, where the observed MJO exhibits the largest amplitudes, the WISHE mechanism is not favoured. Furthermore, many observational studies have shown that the maximum surface evaporation occurs in the westerly phase of the MJO, behind the convective complex (e.g. Lin and Johnson, 1996b; Zhang and McPhaden, 2000), rather than in the easterly phase ahead of it, as the WISHE theory predicts. Comparing Fig. 2.8 (b) in §2.3.8 with the observed schematic representations of the MJO (Figs. 2.1 - 2.4) it is clear that the near-surface structure associated with the WISHE mechanism is not apparent in observations.

2.3.4 Frictional convergence

Positive only, or conditional CISK heating, was used by Lau and Peng (1987) to remedy the instability catastrophe of unrealistic short-wave growth in the wave-CISK theory. Wang (1988b) hypothesised that including the effects of boundary layer, friction-induced, moisture convergence would have a similar suppressing effect on the fast growth of unstable modes at short wavelengths. Using a model with a well-mixed boundary layer and a two-level free atmosphere, Wang (1988b) showed that the frictional convergence coupled with equatorial waves supplies enough moist energy to amplify a slowly eastward-propagating unstable mode, commonly referred to as a moist Kelvin wave. However, the selection and growth rate of that unstable mode were shown to be sensitive to the background vertical distribution of moist static energy. Wang and Rui (1990) included westward-propagating equatorial Rossby waves in their analysis which helped to further suppress the unrealistic fast growth of wave-CISK type modes. The group velocity of the resulting eastward-propagating Rossby-Kelvin wave was slower than the convectively coupled Kelvin wave.

A crucial feature of the frictional convergence theory is that the boundary layer friction occurs in the easterly phase, ahead of the convective centre of the MJO. The friction-induced moisture convergence in the boundary layer increases the moist static energy, destabilising the atmospheric profile east of the convection, therefore favouring the eastward propagation of the amplified convection. Hendon and Salby (1994) showed that the observational relationship between the surface convergence and the amplification and decay of the convective complex of the MJO was consistent with this theory. They referred to this as frictional wave-CISK.

Maloney and Hartmann (1998) studied observational records of 850 hPa zonal winds and surface to 300 hPa column integrated water vapour during different stages of the MJO cycle. They showed that friction-induced moisture convergence occurs in the boundary layer to the east of the convective centre, while regions of divergence were observed to the west. Given that in the West

Pacific and Indian Ocean regions a significant correlation exists between the surface convergence and positive water vapour anomalies, it was suggested that the frictional convergence mechanism was crucial in preconditioning the atmosphere ahead of the convective complex, thus favouring eastward propagation. Kiladis *et al.* (2005) extended this hypothesis in their statistical study. By using dynamical fields from reanalysis products projected onto filtered OLR data, they were able to confirm that low-level convergence occurs ahead of the convective centre of the MJO. The associated boundary layer moistening destabilises the atmospheric profile and triggers shallow convection east of the MJO convection. Over a number of days the moisture gradually penetrates further into the mid-troposphere in the form of congestus clouds, allowing for the rapid development of deep convection, a feature which had been observed during TOGA-COARE (Johnson *et al.*, 1999).

The role of the frictional convergence mechanism in initiating and maintaining the MJO has been examined in many modelling studies. To investigate the interaction between convection and the large-scale circulation, Salby *et al.* (1994) used a system governed by the linearised primitive equations. In their model convection was represented by two components of heating: a climatological component maintained by fixed properties in the large-scale circulation, and a wave-induced component defined using the column-integrated moisture convergence. Their simulations showed that, unlike traditional wave-CISK modes, the frictional wave-CISK mechanism causes modes with the largest zonal dimension to be the most unstable. A further study by Ohuchi and Yamasaki (1997) used an equatorial β-plane model in which convection is assumed to be directly proportional to the vertical velocity at the top of the boundary layer. The unstable frictional Kelvin mode in their simulation exhibited a realistic phase speed of less than 10 ms^{-1}. They were able to show that the maximum boundary layer convergence is located slightly east of the convergence in the free troposphere, which is a key observed characteristic of the MJO (Hendon and Salby, 1994). The existence of friction-induced moisture convergence to the east of the developing region of enhanced convection is thought to be important to the maintenance of the MJO (Lee *et al.*, 2003); it has also been suggested to play an important role in initiating the convective anomaly associated with the MJO in the Indian Ocean (Seo and Kim, 2003).

To test the sensitivity of the frictional moisture convergence mechanism to the formulation of convection, Moskowitz and Bretherton (2000) repeated the analysis of Wang (1988b) using a different convective parameterization but identical Rayleigh friction coefficients. They showed that when a similar surface drag value was used in both configurations the results were very similar, suggesting that the frictional wave-CISK mechanism is not sensitive to the choice of convective parameterization. However, a corollary of that finding is that the feedback of frictional moisture

convergence onto convection is very sensitive to the choice of the Rayleigh friction coefficient.

2.3.5   Air-Sea interaction

The TOGA-COARE in the early 1990s was motivated by the growing endeavour to understand the thermodynamic coupling between the large-scale atmospheric circulation and oceanic mixed layer in the tropics. The campaign provided extensive observational data from the warm pool region in the West Pacific. This formed the basis of studies aimed at understanding the role of air-sea interactions in maintaining the MJO. It was hoped that understanding to what extent the MJO was a coupled phenomenon, and how those interactions worked, would enable advances in modelling the oscillation to be made.

As part of the AMIP (Atmospheric Model Intercomparrison Project), Slingo *et al.* (1996) compared the performance of 15 different atmospheric GCMs at simulating the MJO. All the models in their study underestimated the amplitude of intraseasonal convective activity compared with observations. It was also shown that levels of tropical activity on intraseasonal timescales were not sensitive to the horizontal resolution or the numerics of the model, but were sensitive to the choice of closure in the convective parameterization and the relationship between precipitation and sea surface temperature (SST).

Following the suggestion that the representation of the MJO in numerical models was sensitive to the interaction with the ocean surface, and the availability of new observational data, many studies in the late 1990s investigated the MJO as a coupled phenomenon. Wang and Xie (1998) used a coupled ocean-atmosphere model in which interactions between the atmospheric boundary layer and the ocean surface were simulated by exchanges in momentum and heat. This allowed Wang and Xie (1998) to examine the effect of oceanic feedbacks on the MJO. In the warm pool region of the West Pacific their model favoured an unstable coupled mode which had an intraseasonal timescale and resembled the vertical structure of the MJO. They suggested that it was the thermodynamical coupling with the warm ocean in the West Pacific, which set the slower phase speed through that region.

During the same period, Flatau *et al.* (1997) developed a new conceptual model in which convectively driven SST gradients were allowed to develop. In their theory, which they referred to as air-sea convective intraseasonal interaction (ASCII), the SST ahead of the convective region was shown to increase. Under and west of the convective complex, in the region with strong surface westerlies, the SST was shown to decrease. The zonal gradient in SST results in zonal differences in moist static energy which act as a surface forcing mechanism to modify the MJO. New convective

plumes are triggered in the region of low-level convergence slightly east of the existing convection. Similar to the study by Wang and Xie (1998), they suggested that the feedback mechanism between equatorial convection and SST acted to slow the propagation of the MJO. Based on 15 years of satellite and reanalysis data from the equatorial Indo-Pacific region, Woolnough *et al.* (2000) confirmed that a coherent relationship existed between convection, surface fluxes and SST. They showed that warm (cold) SST anomalies occurred 10 days before (after) the maximum in convection associated with the MJO.

Waliser *et al.* (1999) tested the sensitivity of MJO simulation to the inclusion of SST variations by comparing a GCM run with a specified annual cycle of SST with a run coupled to an idealised slab ocean model. Although the differences in mean SST between the two versions of the model were small, the resulting differences in the representation of the MJO were considerable: the coupled model was able to produce a more realistic MJO. Inness and Slingo (2003) performed a similar GCM experiment with once-a-day coupling to a full dynamical ocean model. The coupled model in their study showed a marked improvement in the eastward propagation of the convection through the equatorial Indian Ocean, although it was unable to propagate the convective anomalies into the West Pacific. However, the inclusion of air-sea interactions in global models does not always lead to an improvement in MJO simulation (e.g Hendon, 2000), and by no means rectifies all the weaknesses highlighted by Slingo *et al.* (1996) in atmosphere-only simulations. In a comparison of 14 coupled GCMs participating in the Intergovernmental Panel on Climate Change (IPCC) Fourth Assessment Report (AR4), Lin *et al.* (2006) showed that only two models exhibited MJO variance comparable with observations.

In a more recent study designed to test the sensitivity of MJO prediction to coupled processes, Woolnough *et al.* (2007) compared forecasts from the ECMWF monthly forecasting system with (a) persisted SST from the initial conditions, (b) coupling to the Hamburg Ocean Primitive Equations (HOPE) model and (c) coupling to a one-dimensional (1D) mixed layer ocean model. Both the coupled experiments extended skilful predictability of the MJO compared with persisted SSTs. The 1D thermodynamic mixed layer model exhibited a greater improvement, extending skilful predictability of the MJO by up to 6 days. The 1D model had a much higher vertical resolution than the full dynamical ocean model and was able to better represent mixing processes in the upper ocean. Despite the substantial improvements in predictability of the MJO in the ECMWF model, Vitart *et al.* (2007) showed that deficiencies remained in accurately capturing the observed amplitude and phase speed of the MJO.

2.3.6 Thermodynamic feedback processes

Early attempts to explain the MJO theoretically focused on the interaction between the large-scale circulation and local convective heating. In such theories the period of the oscillation is often set by the propagation characteristics of the convectively coupled Kelvin wave. However, these theories cannot account for the episodic nature of the MJO. In the early 1990s, it was recognised that the feedback of thermodynamic processes onto the large-scale played an important role in initiating and maintaining the structure of the MJO. Bladé and Hartmann (1993) proposed that water vapour accumulation processes could be the key to setting the oscillatory period of the MJO. In their theory, which they refer to as "discharge-recharge", the 40-day MJO period is set by the time it takes for the atmosphere to destabilise (recharge) after convective stabilisation has occurred (discharge).

A further outcome of their study agreed with the result of Hsu *et al.* (1990) that extratropical forcing could play an important role in initiating the convective anomalies in the Indian Ocean associated with the MJO. They suggest that when processes such as subtropical Rossby wavetrains penetrate into the tropics they can trigger equatorial convection. However, these results must be interpreted in the context in which they were generated. Bladé and Hartmann (1993) used a relatively simple two-level model in which convection was represented using a positive-only CISK parameterization. Therefore, all the deficiencies highlighted in previous sections relating to wave-CISK and positive-only heating would be applicable here.

Many studies have examined the feedback mechanism between water vapour and convection. Analysis of observational data over the equatorial Indo-Pacific region has shown that there is a coherent relationship between convection and surface fluxes of moisture on intraseasonal timescales (Hendon and Glick, 1997; Woolnough *et al.*, 2000). Using a cloud-resolving model (CRM), Tompkins (2001) showed that the positive feedback between water vapour and convection means that future convective plumes are likely to favour regions where convection has already occurred, leading to the organisation or self-aggregation of deep convection onto planetary scales.

Idealised aquaplanet experiments with a cloud-resolving convection parametrisation (CRCP) have shown that suppressing moisture anomalies in the free troposphere prevent MJO-like signals from developing, and significantly weaken any MJO-like signals that already exist (Grabowski, 2003; Grabowski and Moncrieff, 2004). Bretherton *et al.* (2004) proposed that the ability of a model to simulate a realistic relationship between convective rainfall and free-tropospheric moisture was a convenient test of its cumulus parameterization. Derbyshire *et al.* (2004) went on to stress that many

convective parametrizations underestimate the importance of environmental moisture in modulating tropical convective activity.

In addition to the importance of water vapour, studies in the early 1990s recognised that the interaction between radiation and clouds also modulated tropical convective activity. Radiative heating rates differ depending on atmospheric conditions (i.e. cloudy versus clear sky conditions). Radiative cooling is much greater in regions of large-scale subsidence compared with regions of convective ascent. The idea of the cloud-radiation feedback mechanism is that the differential radiative heating rates are allowed to influence the clouds and therefore modulate the local atmospheric stability. The net effect of radiation is to strengthen the existing large-scale convective circulation pattern. Hu and Randall (1994, 1995) proposed that the non-linear feedbacks between cumulus convection, radiation and moisture fluxes at the surface led to a local heat source which oscillated in time, but was stationary in space. They suggested that the stationary oscillation forced the eastward-propagating wave associated with the MJO. Their theory emphasised that it did not rely on the positive feedback between convection and wave propagation, as in the wave-CISK mechanism, but the combination of radiative cooling and surface moisture fluxes to destabilise the atmosphere and trigger convection. However, Zhang and Hendon (1997) statistically analysed a series of almost 8 years of OLR and wind data to show that there was no evidence of a dominant stationary oscillation in large-scale tropical convection on intraseasonal timescales.

Many modelling studies have been designed to test the hypothesis that interactions between radiation and cloud structures are important aspects of simulating the low-frequency disturbance associated with the MJO. Raymond (2001) used a two-dimensional model which had a horizontal resolution of 250 km and included cloud-radiation interactions to study the MJO. The large-scale unstable modes in their simulations were a result of the cloud-radiation interactions and resembled the observed MJO, propagating eastward at approximately 5 m s^{-1}. When the effects of cloud-radiation and water vapour feedbacks were eliminated from their simulations, Fuchs and Raymond (2002) showed that no unstable modes were able to grow.

Lee *et al.* (2001) compared two simplified aquaplanet GCM runs: one with interacting radiation and clouds and the second with prescribed mean radiative cooling rates. Without cloud-radiative interactions an unstable mode resembling the eastward-propagating moist Kelvin wave was simulated. However, when radiation was allowed to be interactive, the simulation of the MJO was significantly weakened, with the unstable growth favouring small-scale westward-propagating disturbances instead. A further study by Fuchs and Raymond (2005) included cloud-radiation effects through moisture perturbations. An increase in available moisture led to an increase in the extent

of cloud. The corresponding effect of those clouds would be to suppress outgoing radiation which would in turn lead to more vigorous ascent. They showed that cloud-radiation feedback played an important role in destabilising the slow moisture modes in their simulations, while the WISHE mechanism was required to propagate the unstable modes eastwards. It is clear that although moist processes play a crucial role in the development of convective anomalies and their organisation onto planetary scales, thermodynamic feedback processes alone cannot sustain the MJO, or account for its slow eastward propagation.

2.3.7 Response to independent forcing

Many of the theories for the MJO discussed so far have focused on 'local' effects. That is, the disturbance produces its own energy through local atmospheric instability and thermodynamic feedbacks. This section considers the 'response' hypothesis for MJO initiation which suggests that the oscillation is the atmospheric response to an existing lateral forcing in the system. This idea is not new: Weickmann (1983) showed that an intraseasonal relationship exists between tropical convective activity and large-scale extratropical jets. Liebmann and Hartmann (1984) showed that tropical convective anomalies lagged extratropical 500 hPa height anomalies, suggesting that on intraseasonal timescales the extra-tropics have a strong influence on the tropical circulation. Other studies have revealed that Rossby wavetrains propagating into the tropics from midlatitudes may play a role in the organisation of tropical convection onto planetary-scales in the Indian Ocean (Hsu *et al.*, 1990), or triggering convection in the central Pacific (Matthews and Kiladis, 1999).

In a more recent study, Lin *et al.* (2007) showed that a dry atmospheric model produced tropical intraseasonal variability exhibiting an MJO-like structure in the winds. They proposed that wave-trains originating in the extratropical Pacific transported kinetic energy equatorwards, forcing the eastward-propagating signal in the tropics. The fact that some features of the MJO were simulated in the absence of moist convective processes supports the argument that extratropical perturbations influence the oscillation. However, the simulated phase speed was three times that of the observed MJO, which reinforces the idea that the coupling of the overturning circulation to deep convection is crucial in explaining the slow propagation speed of the MJO. Ray *et al.* (2009) used a limited-area tropical channel model to simulate the initiation of zonal-wind anomalies in the Indian Ocean during two MJO events. Their tests showed that the existence of the MJO signal was not sensitive to changes in SST, initial conditions or moist processes. However, no MJO signal was produced when the time-varying lateral boundary conditions were replaced with time-invariant ones.

By classifying MJO events into primary (with no preceding MJO event, 40%) or successive

(with a preceding MJO event, 60%), Matthews (2008) showed that with the initiation of successive events there was considerable evidence of influence from the extra-tropics, whereas no such influence was found with the initiation of primary events. While these studies highlight extratropical influences as an efficient mechanism for MJO initiation in some cases, it is clear that they do not apply in all cases. Furthermore, in the absence of moist processes, not all the observed characteristics of the MJO can be explained.

2.3.8   Summary of theories

The MJO is the ultimate challenge of our theoretical understanding of the tropical atmospheric circulation. Despite significant effort, a succinct theory that fully explains all the observed characteristics of the MJO remains elusive. The main instability theories proposed to explain the MJO have been discussed in the previous section; these are summarised in Fig. 2.8.
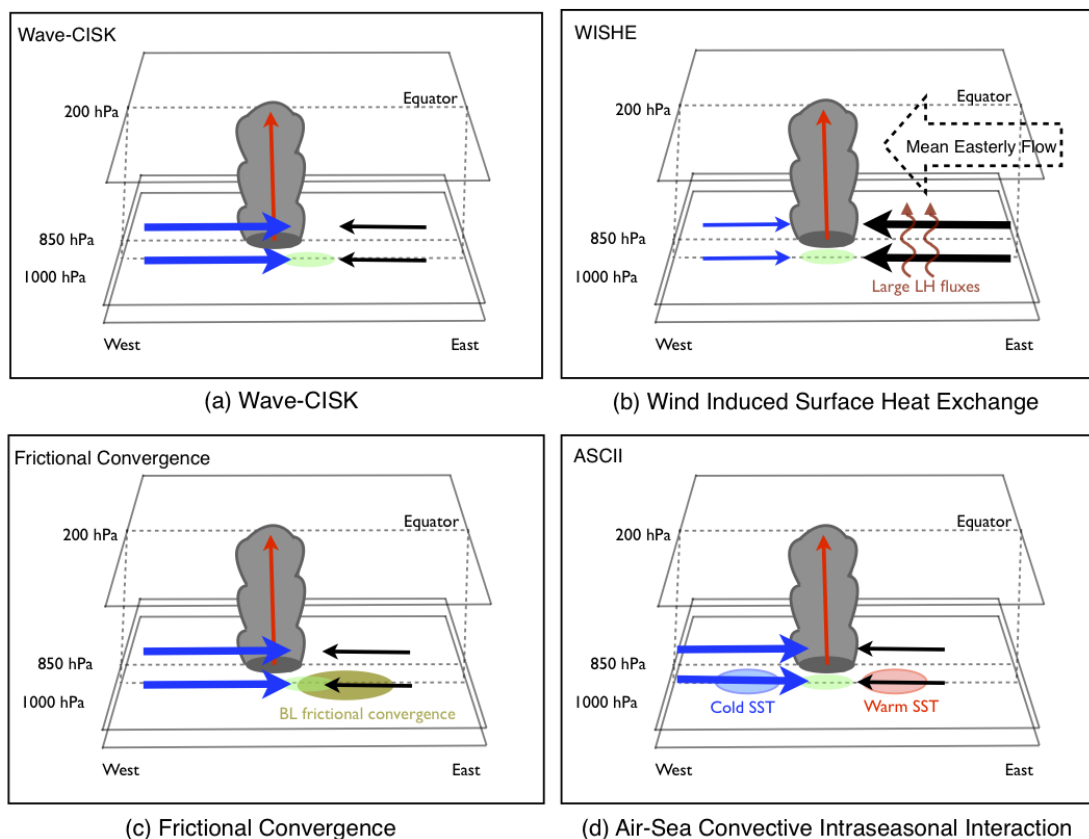
Figure 2.8 *Schematic representation of the theoretical mechanisms described to explain the MJO. Anomalous convective ascent (red arrows) occurs in the convective maximum (grey cloud). Blue (black) arrows indicate flow perturbations behind (ahead of) convection. The green oval represents the region of maximum convergence.*

Crucial to an understanding of the dynamics of the MJO is understanding the multi-scale interactions within it, from the initiation of convection on the smallest spatial scales (O(100m)) to

the organisation of that convection onto planetary-scales ($O(10^4$km)). Theoretical understanding of mid-latitude dynamics has enjoyed significantly faster progress than its tropical counterpart. In the baroclinic instability theory for mid-latitude cyclones, the instability occurs on a comparable scale to the system it produces. In contrast, in the tropics, the instability occurs on the smallest scales but amplifies into much larger systems. This characteristic, referred to as the instability catastrophe, has proved hard to reconcile in theory.

2.4 Numerical modelling and prediction of the MJO

Observational and theoretical study of the MJO has revealed it to be a complex, multi-scale phenomenon. Therefore, the numerical representation of the MJO itself and the teleconnection patterns associated with it act as a rigorous test of all aspects of a global circulation model. Progress in our ability to model the MJO is by no means independent of developments made in our theoretical understanding; rather, results from modelling studies inform theory and vice versa. Although significant progress has been made over the last 40 years, producing a realistic simulation of the MJO, much like having a succinct theory for its existence, remains an ongoing challenge.

Early modelling efforts in the 1980s focused on the ability of models to reproduce the observed large-scale circulation pattern in the upper-level winds (Hayashi and Golder, 1986; Lau and Lau, 1986; Swinbank *et al.*, 1988). These simulations were successful in producing an eastward-propagating disturbance which exhibited coherent intraseasonal signals in zonal wind and precipitation. However, the phase speed and period of the disturbance that was reproduced resembled a convectively coupled Kelvin wave rather than an MJO.

Model inter-comparison studies have been used to assess the progress in the simulation of the MJO. Park *et al.* (1990) compared 3 GCMs of identical resolution with reanalysis data from ECMWF. As part of AMIP Slingo *et al.* (1996) compared 15 then state-of-the-art GCMs to assess the strength and shortfalls in the numerical representation of the MJO. Shortly after this, Sperber *et al.* (1997) performed a comprehensive comparison between the two models which Slingo *et al.* (1996) had found produced the most realistic MJO. Although many of these simulations reproduced eastward-propagating signals, they were often too weak and propagated too fast. Most models had difficulty propagating the convective signal from the Indian Ocean through the Maritime Continent; the convective signal in that region often became completely decoupled from the large-scale overturning circulation. In addition, the spatial distribution of the eastward-propagating signal and its seasonal and interannual cycle were often unrealistic compared with observations. In a more recent study a comparison was made between 14 AR4 coupled GCMs (Lin *et al.*, 2006). It is clear

that in the intervening decade improvements in the numerical representation of the MJO have been made, however many aspects of the MJO signal remain too weak; 12 of the 14 models in their study exhibited only half the observed MJO variance (Fig. 2.9).
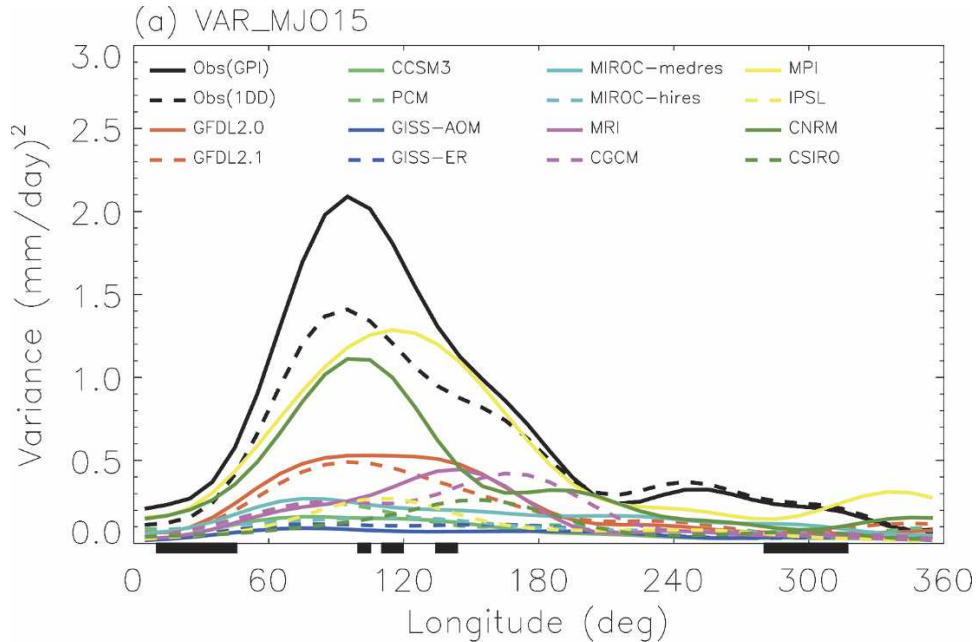
Figure 2.9 *Variance in the MJO mode (eastward wavenumbers 1-6 and periods of 30-70 days) averaged between 15°N and 15°S for 14 different models (coloured lines) compared to observations (black lines). Reproduced from Lin* et al. *(2006).*

More recently the focus has turned to how different modelling efforts can be consistently and objectively evaluated and compared. A collaborative project by the U.S. Climate Variability and Predictability (CLIVAR) MJO Working Group in 2009 aimed to create a standardised, observation-based set of MJO diagnostics (Waliser *et al.*, 2009; Gottschalck *et al.*, 2010) which, when applied to a global model, would form a consistent framework for model assessment. The diagnostics that they proposed vary considerably in complexity, from relatively simple variance calculations to more complex techniques such as EOF analysis. The hope is that having an agreed set of diagnostic will overcome some of the limitations of previous inter-comparison studies, which could not explain why some models performed better than others. This will allow advances in MJO simulation to be put into context with the wider modelling community, and can develop theoretical understanding more effectively.

2.4.1   Predictive skill of the MJO

The MJO is often quoted as being an important source of predictability on intraseasonal timescales, and as such is crucial in bridging the gap between medium-range and seasonal fore-

casting. As a quasi-periodic oscillation one might assume the limit of predictive skill of the MJO to be approximately equal to its period: about 40-50 days. With the aim of quantifying the inherent limit of predictive skill of the MJO, Waliser *et al.* (2003) carried out a twin set of predictability ensembles with the NASA Goddard Laboratory for the Atmospheres (GLA) model, selected because it had a reasonable representation of the MJO. The initial conditions for the simulations were chosen from periods of strong MJO activity to maximise the estimate of potential predictability. Results from their study showed that in the Eastern Hemisphere predictive skill of rainfall and 200 hPa velocity potential signals associated with the MJO were approximately 10-15 and 25-30 days respectively. In a similar study, Reichler and Roads (2005) examined MJO predictability in a set of hindcast ensembles with the NCEP seasonal forecasting model (SFM) run from 'perfect' initial and ocean boundary conditions. Their simulations suggested that the predictability of 200 hPa velocity potential (850 hPa zonal wind and temperature) was approximately 4 weeks (3 weeks).

Despite their somewhat simplified nature, statistical modelling studies have yielded considerable success in skilfully predicting the MJO at lead times comparable with the estimates of inherent predictability studies. In general statistical models use a variable indicator for the MJO, trained on a past validation period to predict the future evolution of the indicator, and hence make an MJO forecast. The indicators used vary in complexity; but a common example is the multivariate MJO index described by Wheeler and Hendon (2004); which uses the first two combined EOFs of zonal wind at 850 and 200 hPa and OLR. Numerous statistical modelling studies have been carried out with varying methods and results, but in general they are able to produce skilful forecasts of the MJO out to lead times of 2-3 weeks (Table 2.1). In this context, a forecast is defined as skilful if its correlation with the observed indicator exceeds 0.6, a stricter threshold than that applied in the study by Reichler and Roads (2005).

Efforts to model the MJO dynamically have fallen short of the target set by the inherent predictability studies described above. Numerical weather prediction (NWP) models vary considerably in their ability to skilfully forecast the evolution of MJO events, from those only showing approximately one week of skilful predictability to those with almost three weeks, (Table 2.1). The current limit in skill in dynamical models is more likely to be linked to errors in initial conditions and model parameterizations and formulations than an inherent limit within all numerical simulations.

In recent years, modifications to numerical models have resulted in significant improvements in the skilful predictability of the MJO. For example, coupling the monthly forecasting system at ECMWF to a higher resolution 1D mixed layer ocean model extended skilful predictability of the MJO by almost a week (Woolnough *et al.*, 2007). Making changes within the model physics of

Table 2.1   *Statistical and dynamical modelling studies of the predictive skill of the MJO.*

	Statistical Modelling		**Skill**[a]
Study	Method	Indicator[b]	(days)
Waliser et al. (1999)	singular value decomposition (SVD)	$\widehat{OLR}'$, $\widehat{u_{200}}'$	5-20, 5-20
Lo and Hendon (2000)	multiple linear regressions	2PCs[OLR'], 3PCs[ψ'_{200}]	10-15
Mo (2001)	singular spectrum analysis (SSA) and maximum entropy	leading SSA modes: 3T-PCs [OLR']	20
Wheeler and Weickmann (2001)	tropical wave theory filtering	OLR'	15-20
Jones *et al.* (2004)	EOF & multiple regression analysis	5PCs[$\widehat{OLR}'$, $\widehat{u_{200}}'$, $\widehat{u_{850}}'$]	20
Love *et al.* (2008)	empirical mode decomposition (EMD)	OLR'	25
Jiang *et al.* (2008)	multivariate lag regression	2PCs[OLR',u_{200}', u_{850}']	7-13
Love and Matthews (2009)	neural network model and EMD	7PCs[OLR']	15-25
Rashid *et al.* (2010)	autoregressive prediction scheme	2PCs[OLR',u_{200}', u_{850}']	8-12
	Dynamical Modelling		**Skill**[a]
Study	Model	Indicator[b]	(days)
Jones *et al.* (2000)	NCEP medium range forecast (MRF) model	u_{200}'	4-7
Wheeler and Weickmann (2001)	NCEP MRF model	$\widehat{OLR}'$	7
Woolnough et al. (2007)	ECMWF monthly forecasting system (MFS) (coupled to 1D mixed layer ocean model)	2PCs [OLR',VP_{200}', u_{850}']	13-14 (14-19)
Vitart *et al.* (2007)	ECMWF MFS with physics changes: DEEP, ICE (coupled to 1D mixed layer ocean model)	2PCs [OLR',VP_{200}', u_{850}']	14-18 (14-21)
Lin *et al.* (2008a)	2 Canadian models GCM3 and Global Environmental Multiscale (GEM) model	2PCs[OLR',u_{200}', u_{850}']	4-11
Rashid et al. (2010)	POAMA, Australia	2PCs[OLR',u_{200}', u_{850}']	12-15

[a]Skill is defined as the forecast lead time at which the correlation between the predicted and observed values of the indicator drop below 0.6.

[b]Symbols ′ and ⌢ indicate where anomalies and band-pass filtering respectively have been used.

the same model extended the upper limit of skilful predictability by a further 2 days (Vitart *et al.*, 2007). This is the experience of one particular model, where changes to the model physics and air-sea coupling have resulted in significant improvements. The remainder of this section will focus on the effects of four aspects of model configuration on the simulation of the MJO: basic state, resolution, convective parameterization and air-sea coupling.

2.4.2   Model basic state

Tropical variability cannot be accurately represented in a global model unless the basic state of the model is accurate. However, the mean state of a model is a composite of variability across all timescales, so without correct representation of the variability it follows that the model basic state will be inaccurate. This impasse makes separating the exact effects of the model basic state on modes of tropical variability such as the MJO very difficult. Slingo *et al.* (1996) suggested that models with a more accurate representation of the seasonal cycle simulated a better MJO. The ECHAM-4 model in both atmosphere-only and coupled mode simulated intraseasonal variability more accurately in boreal winter than summer, which was put down to a more accurate basic state (Kemball-Cook *et al.*, 2002).

Inness *et al.* (2003) used a flux-adjustment method to correct basic state errors of West Pacific SST in the third Hadley Centre Coupled Ocean Atmosphere General Circulation Model (HadCM3) and showed that it improved the eastward propagation of the enhanced convection into that region. However, as is often the case, improvements in one particular region lead to a reduction of skill in another. In this instance, the changes degraded the representation of the oscillation in the Indian Ocean, with many of the events initiating in the western Indian Ocean dissipating as they progressed across the basin. A comparison between two simulations with the same atmospheric component coupled to different ocean models suggested that errors in the mean low-level zonal wind in the West Pacific were more likely to effect the MJO than errors in SST. Inness *et al.* (2003) showed that the MJO favoured regions of mean low-level westerlies, a feature reproduced in the observational study by Zhang and Dong (2004). They examined the observed seasonality of the MJO and its relationship with the mean background flow, finding it to be strongest in the western Pacific.

Zhang *et al.* (2006) showed that the simulated MJO in four pairs of coupled and uncoupled GCMs consistently depended on the mean distributions of precipitation and lower-tropospheric zonal wind, confirming findings from previous studies (Slingo *et al.*, 1996; Inness *et al.*, 2003). Their study went on to suggest that the mean moisture convergence in the boundary layer also played an important role in the simulation of the MJO. Maloney (2009) suggested that in order to

simulate tropical intraseasonal variability accurately a climate model needed to exhibit a realistic meridional humidity gradient. In a recent study, Ray *et al.* (2011) use a tropical channel model to investigate the role of the mean state on the simulation of individual MJO events. They show, for one particular event, that significant errors in the mean basic state of the model actually prevent MJO initiation. The role of, or rather interaction between, the mean state of the model in the simulation of the MJO remains a topic of active research.

2.4.3 Model resolution

With increasing modelling and computing capabilities the resolution of global atmospheric models has increased substantially since the early studies in the 1980s. The spectral model used by Lau and Lau (1986) had 9 vertical levels and resolved up to wavenumber 15. Therefore, the large-scale eastward-propagating signal reproduced in their model was achieved without the influence of unresolved tropical synoptic-scale variability. To put that in context with the current state-of-the-art GCMs, the latest version of the ECMWF Integrated Forecasting System (IFS) has 91 levels in the vertical and a spectral resolution of T_L1279. This leads us to question what the impact of this significant increase in model resolution is on simulation of phenomena such as the MJO.

A number of studies, with inconsistent conclusions, have been carried out to test the sensitivity of MJO simulations to the horizontal and vertical resolution in GCMs. The AMIP study suggested that the simulation of tropical intraseasonal variability was not sensitive to horizontal resolution (Slingo *et al.*, 1996). Inness *et al.* (2001) later showed that using a higher vertical resolution improved the simulated variance associated with the MJO, but did not rectify the lack of eastward propagation of the enhanced convection through the Maritime Continent. Liess and Bengtsson (2004) tested the sensitivity of MJO simulation to vertical and horizontal resolution, showing that a higher vertical resolution produced a slower MJO phase speed. In their simulations, increasing the horizontal resolution produced a noisier, less accurate MJO, although that was partly attributed to the low ratio of vertical to horizontal resolution.

The resolution of global models is inherently limited by available computing power and, in terms of weather prediction, the need for forecasts to be produced in real time. Therefore, the study of the effect of very high resolution on the MJO has motivated the use of high-resolution limited-area models and cloud-resolving models (CRMs). Grabowski (2003) examined the interaction of tropical convection with equatorially trapped waves by embedding a 2D CRM into each column of a 3D non-hydrostatic global model. Within this experimental setup the moisture-convection feedback mechanism is able to successfully produce a coherent eastward-propagating, MJO-like disturbance.

The inconsistent results suggest that the simulation of the MJO is sensitive to changes in model resolution, but that the relationship is not simple; increased resolution does not necessarily lead to improvements in the representation of the MJO. Wang and Schlesinger (1999) suggested that the fact that the effect of changes in resolution on MJO simulation differed between models was to be expected because the effects of resolution are hard to separate from effects of the formulation of convection itself. By construction, many convection schemes are resolution dependent; therefore, changing the model resolution would have an indirect effect on the representation of convection. They agreed with the earlier findings of Slingo *et al.* (1996) that MJO simulation was more sensitive to the type of cumulus parameterization than horizontal resolution.

2.4.4   Convective parameterization

Crucial to our ability to reproduce the MJO in numerical simulations is an understanding of the interactions between local convective heating and the large-scale dynamical circulation. Therefore, in global circulation models the representation of the MJO is intimately linked to the treatment of moist convective processes on sub-grid scales and how those processes feedback onto the large-scale flow. A cumulus parameterization models the bulk effect of convective clouds in a model column, and through changes to the heat and moisture budgets, feeds back onto the large-scale circulation. The variability of tropical convective activity produced in a model is sensitive to the choice of convective parameterization scheme and can significantly effect the amplitude of the MJO (Maloney and Hartmann, 2001). Convective parameterizations vary in formulation, with different closure and convective trigger assumptions resulting in different vertical heating and moisture profiles.

Slingo *et al.* (1996) indicated that models with a stronger relationship between convection and precipitation, and with a convective closure dependent on buoyancy rather than moisture convergence, produced the most accurate tropical variability on intraseasonal timescales. However, the opposite conclusion was reached by Lin *et al.* (2006): coupled models with a convective closure dependent on moisture convergence performed the best. Despite different conclusions these studies reveal a common theme - that the representation of the MJO in GCMs is very sensitive to the choice of cumulus parameterization.

Whereas both Slingo *et al.* (1996) and Lin *et al.* (2006) performed model inter-comparisons, studies where the main focus is the sensitivity of MJO simulation to the choice of convection scheme use a single model and make comparisons between different parameterizations and convective triggers within it. Wang and Schlesinger (1999) compared the effect of changing the strength of the convective trigger on simulations of intraseasonal variability in an 11-layer AGCM with a

Kuo scheme (KUO), an Arakawa-Schubert scheme (AS) and a moist convective adjustment scheme (MCA). For all these schemes, the strength of the relative-humidity criterion for triggering convection was directly related to the strength of intraseasonal variability. Lee *et al.* (2003) agreed with the idea that more strict convective triggers produce better simulations of the MJO. A stronger trigger allows moist static energy to build up without convection being triggered, thus avoiding erroneous growth at small scales but favouring low-frequency phenomenon like the MJO. However, Maloney and Hartmann (2001) showed that increasing the relative humidity trigger in the NCAR Community Climate Model (CCM3) with a relaxed AS scheme did not improve MJO simulation.

Liu *et al.* (2005) compared the NCAR Community Atmosphere Model (CAM2), a model with an MCA scheme closed on CAPE, to versions of it with two mass-flux schemes, each with different closures, to test the impact on MJO simulation. Both mass-flux schemes, one closed on CAPE and one on moisture convergence, produced a more realistic simulation of the MJO than CAM2 with an MCA scheme. Furthermore, their study suggested that a mass-flux scheme closed on moisture convergence was better able to represent the MJO than one closed on CAPE, in agreement with the model inter-comparison study of Lin *et al.* (2006) rather than that of Slingo *et al.* (1996). In AGCM simulations from Seoul National University (SNU), Lin *et al.* (2008b) showed that accurate simulation of convectively coupled waves including the MJO was highly dependent on both the choice of convection parameterization and convective trigger. In contrast to Liu *et al.* (2005), the MCA scheme out-performed both a KUO scheme and a simplified AS scheme at realistically representing the MJO. Increasing the convective trigger improved the eastward propagation of the convective signal in both the KUO and simplified AS schemes but had little effect in the MCA scheme.

The increasing computational capabilities developed over the last decade have given rise to a new multi-scale modelling framework (MMF), in which cloud-resolving models (CRMs) are used as "superparameterizations" in place of convectional cumulus parameterizations to feedback onto the large-scale circulation (e.g. Grabowski, 2001; Khairoutdinov and Randall, 2001; Grabowski, 2003; Khairoutdinov *et al.*, 2005). The extension of this technique from idealised or limited-area models (LAMs) to global model simulations has had significant impacts on the simulation of the MJO. Comparison of the NCAR CAM3 with the "superparameterized" version of the same model (SP-CAM) showed that changing the treatment of convection transformed the absent MJO signal in CAM3 to one displaying strong spectral peaks in low-level zonal wind and precipitation in SP-CAM (Zhu *et al.*, 2009). However, the simulated convective intensity in SP-CAM was shown to be stronger than observations (Benedict and Randall, 2009), with the main bias located in the West Pacific. Thayer-Calder and Randall (2009) suggested that this was due to the tropospheric column

in SP-CAM being too moist compared with a very dry lower- and mid-troposphere in CAM3.

Thayer-Calder and Randall (2009) emphasised that successfully simulating an MJO was crucially dependent on how sensitive the treatment of convection was to environmental humidity, an idea previously highlighted by Derbyshire *et al.* (2004). Bretherton *et al.* (2004) confirmed a strong relationship between environmental moisture and precipitation by analysing satellite observations. Increasing the sensitivity to environmental moisture in cumulus parameterizations has been shown to improve the representation of the MJO in a number of models (e.g. Bechtold *et al.*, 2008; Klingaman, 2011).

2.4.5   Air-Sea coupling

The role of the ocean in the dynamics of the MJO has long been a focus of the theoretical study of the phenomenon (Flatau *et al.*, 1997). In a modelling and prediction context many experiments have been carried out to investigate the sensitivity of MJO simulation to the inclusion of oceanic processes by comparing simulations of the atmospheric component of a model with different atmosphere-ocean configurations. Since a coherent relationship has been observed between tropical convection, surface fluxes and SST (Woolnough *et al.*, 2000), it is reasonable to assume that including the effects of coupled processes would improve the accuracy of MJO simulations. However, in reality that is not always the case. While some models demonstrate a marked improvement with the inclusion of air-sea interaction (Flatau *et al.*, 1997; Waliser *et al.*, 1999), in others the effects are minimal (Sperber, 2004). Hendon (2000) showed that coupling a global GCM to a mixed layer ocean model made no improvement in the simulation of tropical intraseasonal variability. If the atmospheric component of a model is unable to reproduce a realistic MJO, then introducing coupling with the ocean will not rectify that problem.

It is acknowledged that coupled processes are important to the initiation and maintenance of the MJO, but the fact that MJO-like structures exist in atmosphere only integrations suggests that the MJO is primarily an atmospheric phenomenon. Kemball-Cook *et al.* (2002) showed that while coupling does improve the representation of tropical intraseasonal variability, it does not rely on air-sea interaction for its existence. Replacing the existing oceanic component of a coupled GCM with a higher vertical resolution mixed layer ocean has been shown to significantly improve MJO simulation (Woolnough *et al.*, 2007; Klingaman, 2011).

2.4.6   The uniqueness of the NWP approach

Until recently the MJO has been studied in the context of relatively coarse global climate models. As atmospheric models have developed and computational capabilities advanced, the predictive skill of numerical weather prediction (NWP) models has been extended to timescales where the influence of the MJO has become relevant. On such timescales, the MJO provides a crucial source of predictability and simulating it realistically has become an imperative part of any extended-range forecasting system.

Studying the MJO in the NWP context is distinct in many ways from evaluating long climate integrations of the phenomenon. Firstly and perhaps most obviously, NWP models are run for shorter integrations so are able to run at much higher resolution than climate models. The current IFS at ECMWF runs globally at a horizontal resolution of T_L1279 (~16 km), compared with climate models where the typical horizontal grid scale is approximately 100 km. Although parameterizations are still used to represent sub-grid scale processes in NWP models, all synoptic and some mesoscale systems can be fully resolved. Interactions amongst a variety of temporal and spatial scales is a fundamental feature of the MJO; more of these interactions will be able to be resolved within the NWP setup.

NWP models also allow different measures of skill to be applied. When a strong MJO event is observed, with output from an NWP model, forecasts can be directly compared with the observed characteristics of the MJO event in near real time. Within the climate modelling context, MJO statistics are calculated from long integrations and compared with statistics of past observations. A great deal has been learnt of the modelled characteristics of the MJO in this way; however, this approach ignores the heterogeneous nature of individual MJO events. The typical MJO event described in §2.2 - with convection initiating in the Indian Ocean, propagating through the Maritime Continent and dissipating over cooler SSTs in the West Pacific - is not a description which can be applied to every event. For example, some observed events do not propagate through the Maritime Continent at all. By studying the MJO in the NWP context, a model can be tested at its ability to reproduce the observed characteristics of an individual MJO event, rather than the average statistics of MJO activity from climate integrations.

Different sensitivity tests can be applied to NWP output compared with those of climate models. For example the sensitivity of MJO simulation to the initial conditions can be tested effectively in the NWP context. Comparing integrations initialised from different conditions, with the MJO absent or in different stages of its lifecycle, allows a distinction to be made between model error

associated with MJO initiation and model error associated with maintaining an existing MJO event. Considering the changes in MJO simulations as forecast lead time increases adds a dimension to analysing NWP output that is not applicable in climate simulations. This allows us to learn something about how the mean state of the model and structure of the MJO change with increasing forecast lead times, thereby highlighting the physical mechanisms which are important in capturing realistic eastward propagation of the MJO and sustaining the amplitude of the phenomenon.

2.5   Conclusions

The MJO has been the focus of numerous tropical atmospheric studies over recent decades. Considerable progress has been made in understanding the observed structure of the phenomenon, from its multi-scale interactions to its large-scale vertical structure. Observational campaigns have also provided evidence of air-sea interaction during the MJO lifecycle, highlighting the importance of coupled process in maintaining the oscillation. However, there are still aspects of the MJO which would benefit from further observational study. For example, the Dynamics of the MJO (DYNAMO) is a project based in the Indian Ocean which aims to improve understanding of the key physical processes involved in MJO initiation. Another exciting development in understanding the detailed observed structure of the MJO is the use of satellite data. Our understanding of the large-scale vertical structure of the MJO has previously come from global reanalysis products. In addition to the high-resolution satellite measurements of temperature and water vapour, new satellite measurements from CloudSat and CALIPSO[2] add unprecedented detail to the observed vertical structures of cloud during different stages of the MJO. These new satellite datasets will enable the verification of existing global reanalysis products.

As well as observational advances, theoretical understanding of the MJO has progressed enormously (§2.3). Early theories focused on the dynamics of equatorially trapped waves while more recent studies account for thermodynamic feedbacks, air-sea interactions and external influences from the extra-tropics. However, there is still no single theory which is able to quantitatively predict the observed selection of spatial scales and propagation characteristics of the MJO. While theoretical modelling studies of the MJO have enjoyed some success in strongly constrained idealised simulations, more complex global simulations still exhibit considerable deficiencies in their representation of the MJO. This discrepancy suggests that an MJO theory is not made successful by the ability to produce an MJO-like signal in idealised simulations, but by being able to explain and remove the deficiencies in global models which have a more sophisticated representation of

---

[2]CloudSat and Cloud-Aerosol Lidar and Infrared Pathfinder Satellite Observations (CALIPSO) are part of the A-Train satellite mission launched by NASA in 2006

physical processes.

Progress in the numerical simulation of the MJO has varied considerably from one model to another over recent decades (§2.4). Models range from those which have made significant improvements and extended the limit of skilful predictability of the MJO by over a week, to those which are able to produce only a very weak MJO-like signal which dissipates after just a few days. Results from dynamical studies of the MJO should be interpreted in the context of the model which produced them, with the capability of the model to reproduce the observed MJO taken into consideration. MJO simulation is sensitive to many aspects of model configuration (§2.4.2 - §2.4.5). However, the reasons for that sensitivity are less clear and highly model-dependent. Therefore, no generic rules exist for the relationship between physical parameterizations and the ability of a model to reproduce the observed structure of the MJO. Furthermore, the fact that the MJO presents such a tough test for all aspects of a models configuration makes modelling it "simply" difficult to justify.

Observational, theoretical and numerical studies of the MJO should not be independent endeavours. For example, improved observational evidence of the vertical structure of the MJO can help validate numerical simulations and inform theory. The fact that current theories are unable to explain existing model deficiencies suggests a gap in our theoretical knowledge. §2.4.6 highlighted some of the advantages of studying the MJO in an NWP context as well as in long climate integrations. Understanding the relationship between local convective heating and the large-scale dynamical circulation is crucial to our ability to simulate the MJO. Therefore, the simulation of the MJO is intimately linked to the treatment of moist convective processes on sub-grid scales. Many studies have investigated the effect of convective processes on the simulation of the MJO (e.g Deng and Wu, 2010), but few have gone on to analyse the physical processes responsible for resulting improvements in simulation. In the following chapters the simulation of the MJO in an NWP model will be investigated, with particular focus on the developments made by implementing a new convection parameterization scheme.

CHAPTER 3

Model and Methods

3.1 Introduction

The MJO is an important source of predictability for numerical weather prediction models. As the dominant mode of intraseasonal variability in the Tropics, the MJO influences all aspects of the tropical circulation, and the teleconnection patterns associated with it affect weather in the extra-tropics. Despite its immense importance in the global climate system, NWP models have significant deficiencies in predicting the MJO. In recent decades, a combination of higher resolution models and insights from observational campaigns has led to improvements in the representation of the MJO. However, the previous chapter highlighted that the physical mechanisms responsible for the initiation and evolution of the MJO remain poorly understood. This thesis will focus on the representation of the MJO in the ECMWF Integrated Forecasting System (IFS), a state-of-the-art NWP model.

Historically the IFS, like many other NWP models, exhibited a weak representation of the MJO. However, due to a number of model developments over the past decade, substantial progress has been made. The most notable advances in the representation of tropical variability came after modifications to the convection scheme were implemented in Cycle 32r3 in 2007. This chapter starts by describing the IFS, with particular focus on the parameterization of convection (§3.2, §3.3). Advances in the simulation of the MJO over recent cycles of the IFS are discussed in §3.4. A full description of the modifications made to the parameterization of convection in Cycle 32r3 (Cy32r3) and their impact on the representation of tropical atmospheric variability is presented. Finally, the motivation, aims and details of the hindcast experiments carried out on the IFS are described in §3.5.

3.2 Model description

The numerical model used throughout this study is the ECMWF IFS. ECMWF continually develop and implement changes to the IFS, resulting in a non stationary model configuration. For the purpose of this study a single model cycle, Cycle 33r1 (Cy33r1), will be described in detail. Cy33r1 has been chosen for three reasons: it includes the modified convection scheme of Cy32r3, it

has been fully documented (ECMWF IFS documentation, 2007a) and it is the cycle used for many of the experiments described in §3.5.

Cy33r1 became operational on 3rd June 2008. The atmospheric component of the model is run at T$_L$799 resolution (0.225° × 0.225°, ~25 km), a triangular truncation solving up to wavenumber 799 in spectral space. The model uses a linear reduced Gaussian grid in the horizontal with 91 levels in the vertical and a model top at 0.01 hPa (~ 80km). The numerical scheme uses a Semi-Lagrangian two-time-level semi-implicit formulation with a model time step of 12 minutes. Global analysis of wind, temperature, surface pressure, humidity and ozone concentration is carried out using four-dimensional multivariate variational (4D-Var) data assimilation on a 12-hour period on all model levels. The horizontal resolution of the IFS has been increased since Cy33r1; in January 2010, when Cy36r1 was implemented, the horizontal resolution was increased to T$_L$1279 (0.141° × 0.141°, ~16 km), and the model time step reduced to 10 minutes (Miller *et al.*, 2010).

3.2.1 Physical processes

Physical processes which occur on length scales smaller than the horizontal resolution of the model cannot be explicitly resolved. Such sub-grid processes cannot be ignored because they strongly influence the large-scale atmospheric circulation. Parameterization schemes describe the bulk effect of sub-grid scale processes, such as turbulent mixing or convection, in terms of resolved grid-scale variables and hence represent their impact on the large-scale dynamics. The physical processes represented by parameterization schemes in the IFS are schematically represented in Fig. 3.1.
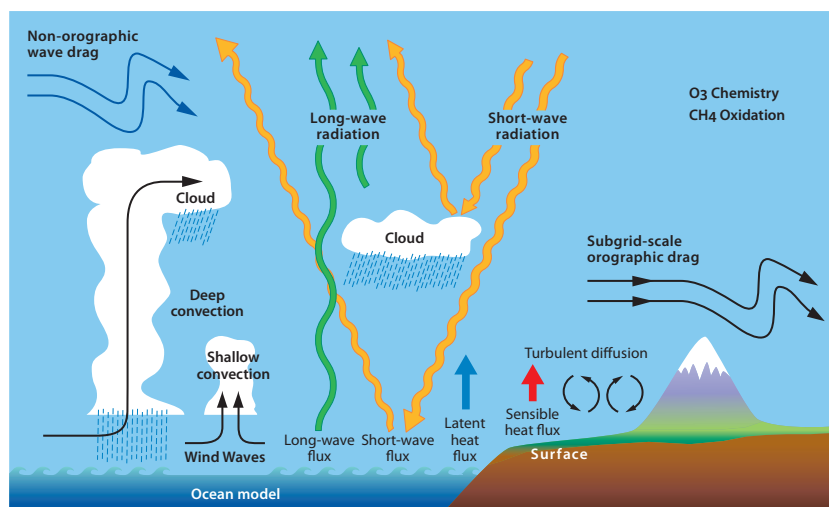
Figure 3.1 *Schematic representation of the parameterized physical processes represented in the IFS model. Reproduced from IFS documentation - Cy36r1, Part IV: Physical Processes, (ECMWF IFS documentation, 2010).*

The entire computational IFS physics package is described schematically in Fig. 3.2. The radiation scheme calculates cloud-radiation interactions using the Monte Carlo Independent Column Approximation (McICA) method. The full radiation scheme (RADINTG), is called every hour and calculates short-wave transmissivities and long-wave radiative fluxes using input of model variables, cloud scheme and aerosol and trace gas climatologies. Short-wave fluxes and all the other parameterization schemes are updated every at time step as part of the main physics package (CALLPAR). A more detailed description of the full physics package in Cy33r1 is given in the ECMWF IFS documentation (2007b). The main focus here will be on the parameterizations which are important to the simulation of tropical convection.
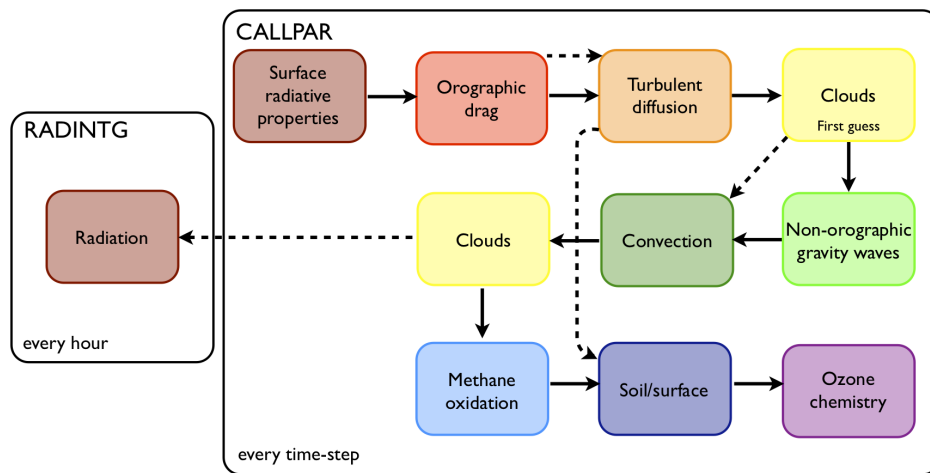
Figure 3.2 *Schematic representation of the IFS physics package. CALLPAR is the main package called every time-step, RADINTG is the full radiation package called every hour. Solid arrows indicate the order of the routines, dashed arrows indicate interactions between different schemes.*

The aim of the integrations performed in this study is to identify and understand the physical mechanisms underlying the ability of the IFS to accurately simulate organised convection in the tropics. The mean climate of the tropics is a composite of interacting convective systems on a wide range of temporal and spatial scales, from individual convective cells to large-scale monsoon systems. Therefore, for an NWP model to simulate tropical variability successfully, it must be capable of accurately representing the interactions between local convective heating and the large-scale dynamical circulation. Cumulus convection plays a key role in the development, maintenance and propagation of an MJO event. Although the horizontal resolution of global NWP models is continually increasing, explicitly resolving individual convective cells remains an unattainable goal with current technology. The horizontal resolution of Cy33r1 of the IFS is approximately 25 km, while the horizontal length scale of a deep convective cell is of the order of 1 km. A cumulus parameter-

ization is required to represent the forcing of individual convective clouds within a grid box on the grid-scale budgets of heat and moisture, and hence their effect on the large-scale dynamical flow.

The need for a convective parameterization was first recognised in the 1960s (Manabe and Stricker, 1964; Kuo, 1965). The aim of such a scheme was to both represent sub-grid convective activity and to avoid the numerical instabilities which had arisen as a result of saturated, grid-scale ascents. Furthermore, it was recognised that accurately simulating the distribution of cloud and precipitation is crucial for correctly determining the radiation budget of the global atmospheric system. A comprehensive review of the past, present and future of cumulus parameterization is given by Arakawa (2004). Broadly speaking, the procedure of a convective parameterization can be divided into two stages: (1) the "trigger", which determines the location and type of convection; a cloud parameterization is usually used at this stage to specify the vertical structure of heating, moistening and changes in momentum; (2) the "closure", which determines the total energy conversion within the column. Convection schemes vary in their "trigger" procedures and "closure" assumptions, but in general they can be classed into three categories, which are discussed below: Kuo-type, adjustment and mass-flux schemes.

A Kuo-type scheme (referred to as KUO in Chapter 2) is based on the assumption that convective activity (or precipitation) is linked to the large-scale convergence of moisture (Kuo, 1965, 1974). In a convective adjustment scheme (referred to as MCA in Chapter 2), if the atmosphere is unstable to a parcel being lifted from the boundary layer, the temperature and moisture fields are adjusted or relaxed back to a reference profile over a convective adjustment timescale, (Betts, 1986; Betts and Miller, 1986). Both schemes are relatively simple and computationally inexpensive to implement. Therefore, in the past, both the Kuo-type and adjustment schemes have been implemented in global climate simulations.

The basic principles of the mass-flux approach to parametrizing convection were established in the 1970s, (Arakawa and Schubert, 1974). Since the method is more complex and computationally expensive to implement, it is only recently that mass-flux schemes have been used in global NWP and climate models. Mass-flux parametrizations can be further categorised into "bulk" and "spectral" schemes. The spectral cloud ensemble approach is more complex as it uses multiple entraining plumes within a grid box to create an ensemble of clouds, each with a different cloud-top height and entrainment rate. The best known spectral mass-flux scheme is the Arakawa-Schubert scheme (referred to as AS in Chapter 2; Arakawa and Schubert, 1974). A bulk cloud model approach significantly reduces computational expense by, for each time step, only considering a single entraining or detraining plume within a grid box. Both the ECMWF forecast model (Tiedtke, 1989), and the

UK Met Office (Gregory and Rowntree, 1990) use a a bulk mass-flux approach to parametrizing convection. Further details of the convection scheme in the IFS are discussed in §3.3.

There are other physical parameterizations, besides the convection scheme, which are important to the simulation of organised tropical convection. For example, the cloud scheme of any global model is intimately linked to its convection scheme. In the IFS, the first call to the cloud scheme provides the 'first guess' profile which is used to determine the vertical structure of heating and moistening for the convection scheme. The IFS cloud scheme solves two prognostic equations, one for liquid (or ice) water content and one for cloud fraction. Solutions represent the formation of boundary-layer, stratiform and cumulus clouds. The scheme includes processes such as precipitation, cloud-top entrainment, evaporation and supersaturation with respect to ice. Clouds and their radiative feedbacks play a key role in modulating global climate. However, the representation of clouds, their effects and how they will respond to global warming remain major sources of uncertainty and bias in climate modelling (Randall *et al.*, 2007; Tompkins and Giuseppe, 2009). With the availability of new satellite products such as CloudSat and CALIPSO from the A-train, there are unprecedented opportunities to analyse the observed vertical structure of clouds within the MJO (Stein, 2011) and to validate the representation of clouds in models.

Since the occurrence and strength of convection is very sensitive to variations of heat and moisture at the surface, the convection scheme strongly interacts with turbulent mixing processes within the boundary layer. The planetary boundary layer is a very active region of the lower troposphere where the flow is strongly influenced by surface dynamical and thermodynamical processes. The turbulent diffusion scheme in the IFS models those effects by representing the turbulent transfers of heat, momentum and moisture between the surface and the first model level. Studies have shown that weather and climate models are sensitive to their formulation of boundary layer processes (Beljaars and Betts, 1992; Hu *et al.*, 2010).

3.2.2   The future of convective parameterization

With the rapid increase in computational capability, the current generation of high-resolution limited-area NWP simulations are reaching horizontal resolutions as high as 1-4 km, which enable deep convective motions to be resolved with reasonable accuracy. Furthermore, an emerging multi-scale modelling approach called "superparameterization" (Randall *et al.*, 2003), which involves nesting a CRM in each grid column of a global model, allows deep convection and cloud-radiation interactions to be explicitly resolved and fed back to the large-scale circulation. The question therefore arises: with ever-increasing resolution and new approaches which explicitly resolve convection,

are "traditional" convective parameterizations becoming obsolete?

There are many reasons why the current and even future computational and modelling capabilities do not negate the need for conventional convective parameterizations. Firstly, even at very high resolution not all convective motions are explicitly resolved. While deep convection occurs on horizontal length scales on the order of 1 km and can be explicitly resolved reasonably accurately, shallow convection occurs on length scales on the order of 100 m. Therefore, even CRMs require some form of parameterization to represent the effect of shallow convective clouds. Secondly, convection-resolving resolution is, and will for some time, remain too computationally expensive for global medium-range NWP forecasts. The resolution required to explicitly resolve deep convection is currently too computationally expensive to produce forecasts beyond 10 days from a full global weather prediction and assimilation system. Finally, higher resolution and explicit treatment of convection does not necessarily lead to more accurate forecasts (Holloway, 2011). As well as introducing more detail to the forecast, higher resolution introduces a lot of "noise" and therefore uncertainty. While the multi-scale modelling approach has an exciting future, more research is required before it can be unequivocally proven that very high resolutions with explicitly resolved convection are worth their computational cost for medium-range NWP forecasts.

3.3   The IFS convection parameterization

The convection parameterization in the IFS is a bulk mass-flux scheme originally developed by Tiedtke (1989). Numerous improvements have since been made to the scheme (Gregory *et al.*, 2000; Jakob and Siebesma, 2003; Bechtold *et al.*, 2004, 2008), and implemented in the IFS. The convection scheme described here is that of Cy33r1 (after the modifications of Bechtold *et al.* (2008)). A detailed description of its numerical implementation can be found in the ECMWF IFS documentation (2007b), and further discussion of the Cy32r3 modifications follow in §3.4.

3.3.1   Trigger and type of convection

For a given convective column, the first stage in the convection algorithm, known as the trigger of convection, determines the type of convection that is activated within it. In the IFS there are three possible, mutually exclusive types of convection (represented schematically in Fig. 3.3): deep, mid-level and shallow.

The occurrence of shallow convection is predominantly associated with undisturbed flow regimes which are not dominated by large-scale convergence. Rather than being controlled by the vertical profile of temperature and moisture in the free troposphere, shallow convection is con-
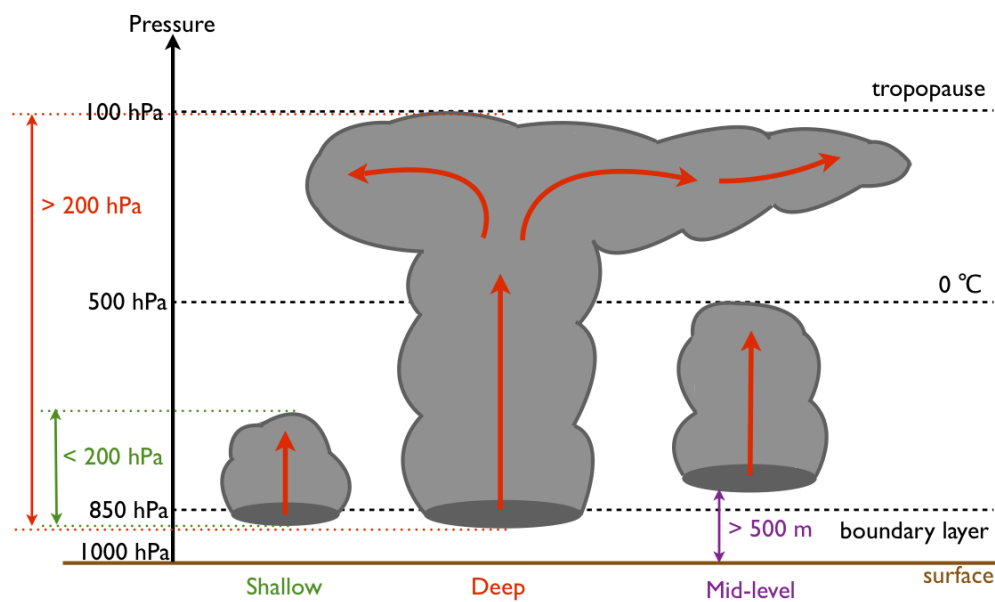
Figure 3.3 *Schematic representation of the types of convection diagnosed by the IFS parameterization.*

trolled by processes such as turbulence in the sub-cloud layer. Examples of shallow convection in the tropics include daytime convection over the islands of the Maritime Continent and cumuli associated with the equatorial trade winds. In contrast to shallow convection, the occurrence of deep convection is associated with large-scale convergence near the surface and strong vertical velocities throughout the lower- and mid-troposphere. Deep convection, such as the active phase of the MJO, exhibits a strong coupling between the surface and upper-troposphere with plumes penetrating to the tropopause. Mid-level convection is characterised as convection which initiates above the boundary layer and usually exhibits cloud-top heights in the mid-troposphere near the melting level (~500 hPa). The moisture source for mid-level convection is often large-scale convergence at the surface. However, typically a low-level temperature inversion exists which inhibits convection from initiating freely from the surface. To overcome the inversion the air needs to be lifted dynamically to its level of free convection.

The procedure used to trigger convection is represented schematically in Fig. 3.4. The first step of the procedure is to determine whether or not convection is active in the grid column; this is the first call to the cloud model. The "first guess" updraught computation from the cloud model determines the cloud-base level, or lifting condensation level (LCL). At this stage a spectral mass-flux scheme (such as that of Arakawa and Schubert (1974)) would define an ensemble of entraining plumes. In contrast, in a bulk mass-flux scheme the type of convection must be determined so that appropriate cloud properties can be applied to the single entraining or detraining plume. The IFS
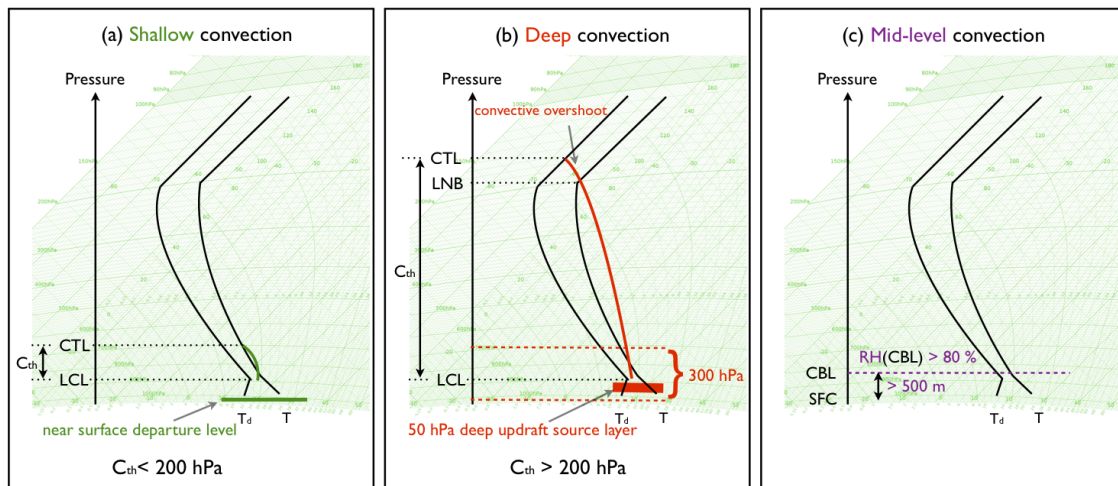
Figure 3.4 *Schematic representation of the procedure used to trigger convection in the IFS parameterization. Black lines indicate environmental profiles of Temperature (T) and dewpoint Temperature (T_d).*

convection scheme first tests for the occurrence of shallow convection (Fig. 3.4 (a)). A temperature (T) and humidity (q) perturbation is calculated based on the latent and sensible heat fluxes at the surface, and then applied to a test parcel at the first model level above the surface. The ascent of the test parcel is performed from that near-surface departure level with a strong entrainment rate ($\sim 3.0 \times 10^{-4}$ m^{-1}). For shallow convection to be activated in the grid column, the test parcel must fulfil three criteria: (1) an LCL must be found for the test parcel; (2) the updraught vertical velocity, w_{up}, calculated from the budget equation for updraught kinetic energy, must be positive at the LCL; (3) the cloud thickness, C_{th}, must be less than 200 hPa. The cloud-top level (CTL), also calculated from the updraught kinetic energy equation, is defined as the level at which w_{up} vanishes.

The next step in the IFS convection parameterization is to test for deep convection originating in the lowest 300 hPa of the atmosphere (Fig. 3.4 (b)). The updraught calculations are repeated, starting from the second model level above the surface. For model levels within 60 hPa of the surface, a depth chosen because it corresponds to the typical mixed layer depth over tropical oceanic regions, a 50 hPa layer average is formed. The average is taken because of the assumption that penetrative convection requires a sufficiently deep source layer to occur. The layer is lifted with an initial T and q perturbation of 0.2 K and 1×10^{-4} kg kg^{-1}, respectively, and a weak entrainment rate of 0.8×10^{-4} m^{-1}. Simplified cloud microphysical processes are accounted for by removing 50% of the condensed water at each model level. As the CTL is defined as the level at which w_{up} vanishes, it may occur above the level of neutral buoyancy (LNB) due to convective overshoot. For deep convection to be activated in the grid column, the following criteria must be met: (1) an LCL must

be found; (2) the corresponding cloud depth must be thicker than 200 hPa. If the required cloud depth is not found at the current departure level, the calculation is repeated from the next model level. Above the first 60 hPa, rather than a 50 hPa thick layer average, each model level is lifted. The process is repeated for the lowest 300 hPa of the atmosphere. If deep convection is identified then the results from the shallow convective test parcel ascent are ignored.

If neither shallow nor deep convection has been identified then a test is done for mid-level convection (Fig. 3.4 (c)). Mid-level convection can occur at any model level above 500 m if the following criteria are met: (1) there is large-scale ascent; (2) environmental air at the cloud-base level (CBL) is sufficiently moist (relative humidity > 80%).

3.3.2 Cloud model equations: updraughts and downdraughts

Once the type of convection is identified, the strength of the updraughts and downdraughts are determined by the cloud model equations. Convective updraughts are thermally direct vertical motions driven by buoyancy. The updraught equations describe the cloud-scale mass continuity, dry static energy, specific humidity, horizontal momentum, cloud water content (divided into total cloud condensate: liquid and ice, and precipitation specie: rain and snow), chemical tracers and kinetic energy. The cloud-scale pressure gradient term in the equations for horizontal momentum is not included in the model, but is represented by additional entrainment and detrainment coefficients. These equations are solved at every model level starting from the LCL.

Convective downdraughts are formed through the interaction of convective precipitation with the environmental air. Some of the precipitation formed in a convective updraught falls out through unsaturated air. As it does so it evaporates, which cools and moistens the environment causing convective-scale downdraughts which form to further cool and moisten the environment. In the IFS, the downdraught plume is treated as an upside down updraught plume. The downdraught equations of the same quantities as the updraught equations are solved at each level starting at the level of free sink (LFS). The LFS is defined as the level at which an equal mixture of cloudy air and environmental air (saturated at the wet bulb temperature) becomes negatively buoyant with respect to the surrounding environmental air. The LFS is typically near the zero-degree isotherm. The equations and details of their implementation are discussed in the ECMWF IFS documentation (2007b).

3.3.3   Entrainment and detrainment

Entrainment ϵ and detrainment δ are the processes through which a convective cloud exchanges mass with its environment. Cumulus entrainment is the dilution of a convective updraught by cool, dry air from the surrounding environment. Cumulus detrainment is the opposite process, the transfer of moist air from an organised convective plume into the surrounding environment. A disadvantage of the mass-flux approach to parameterizing convection is that the entrainment and detrainment rates must be specified. In the IFS convection scheme it is assumed that the entrainment (detrainment) of mass into a convective plume can occur in two ways: (1) turbulent exchange of mass at the cloud edges; (2) organised inflow (outflow at cloud-top). The variation of the convective mass-flux with height can be written in terms of "organised" and "turbulent" contributions of entrainment and detrainment,

$$\frac{1}{M}\frac{\partial M}{\partial z} = \epsilon - \delta = (\epsilon_{turb} + \epsilon_{org}) - (\delta_{turb} + \delta_{org}). \tag{3.1}$$

The updraught entrainment ϵ^{up} and detrainment δ^{up} can be written as,

$$\epsilon^{up} = \underbrace{c_0 F^2}_{\text{turb}} + \underbrace{c_1(1.3 - RH)F^3}_{\text{org, deep, buoy} > 0}; \quad F = \left(\frac{\bar{q}_s}{\bar{q}_{s,base}}\right) \tag{3.2}$$

$$\delta^{up} = \underbrace{0.3c_0}_{\text{turb}} + \underbrace{\propto \frac{\Delta KE^{up}}{\Delta p}}_{\text{org, buoy} < 0} \tag{3.3}$$

$$c_0 = \begin{cases} 3.2 \times 10^{-4} m^{-1} & \text{for deep and mid-level convection} \\ 1.2 \times 10^{-3} m^{-1} & \text{for shallow convection} \end{cases} \tag{3.4}$$

$$c_1 = 0.8 \times 10^{-3} m^{-1} \tag{3.5}$$

The turbulent contributions to entrainment and detrainment in an updraught assume that the fractional entrainment rate is inversely proportional to the radius of the cloud (r_{cld}, equation 3.6). The constant values assigned to c_0 assume the updraught base radius of a deep (shallow) convective cloud to be approximately 625 m (150 m). F is a vertical scaling function, $\bar{q}_s$ and $\bar{q}_{s,base}$ are the environmental saturated specific humidity at the parcel level and the cloud-base respectively and RH is the environmental relative humidity. F decreases rapidly with height and is designed to imitate a cloud ensemble. In the formulation for organised detrainment Δp and ΔKE^{up} represent

the change in pressure and updraught kinetic energy respectively.

$$\epsilon_{turb}^{up} = \frac{0.2}{r_{cld}} \tag{3.6}$$

Organised entrainment is only applied to deep convective clouds that are positively buoyant. The formulation for organised entrainment is dependent on the relative humidity (RH) because observational studies indicate that mid-tropospheric RH strongly modulates cloud-top height (e.g. Redelsperger *et al.* (2002)). The RH dependence was introduced in Cycle 32r3 as part of the modified convection scheme (§3.4). Organised detrainment is active when the parcel is negatively buoyant. It is proportional to the reduction in updraught kinetic energy (KE^{up}) with height.

Defining the entrainment and detrainment rates in downdraughts introduces further uncertainty to the scheme, as the mass exchange within downdraughts is not well constrained by observations. The turbulent contributions of entrainment and detrainment in a downdraught are assumed to be constant:

$$\epsilon_{turb}^{down} = \delta_{turb}^{down} = 2 \times 10^{-4} m^{-1} \tag{3.7}$$

The organised entrainment is based on a buoyancy (b) formulation suggested by Nordeng (1994) in which the downdraught vertical velocity at the LFS is assumed to be $-1\,ms^{-1}$. Organised detrainment is assumed to occur when the downdraught becomes positively buoyant or approaches the surface. The mass-flux M decreases to zero via:

$$\delta_{org}^{down} = \begin{cases} b^{down} < 0 \text{ at surface} & M \downarrow \text{ linearly over lowest } 60\,hPa \\ b^{down} > 0 \text{ above cloud-base} & M \text{ detrained over one model level} \\ b^{down} > 0 \text{ at cloud-base} & \begin{cases} \text{deep convection} & M \downarrow \text{ linearly to 0 at surface} \\ \text{shallow convection} & M \downarrow \text{ quadratically to 0 at surface} \end{cases} \end{cases}$$

3.3.4   Closure

Through entrainment and detrainment processes, the cloud model determines the distribution of heating and moistening through the depth of the troposphere. To determine the overall magnitude

of the heating in the column, an estimate must be made of the mass-flux at the base of the cloud. The convective closure problem refers to the estimation of the cloud-base mass-flux and is the most uncertain part of the convective parameterization process. A different set of closure assumptions are applied to each type of convection defined in §3.3.1. Comprehensive derivations of the cloud-base mass fluxes for each type of convection are given in ECMWF IFS documentation (2007b).

(a) Deep convection

The closure for deep convection in the IFS is based on the method of Fritsch and Chappell (1980), which assumes that convection reduces the convective available potential energy (CAPE), to zero over a specified timescale τ.

$$\left(\frac{\partial CAPE}{\partial t}\right) = -\frac{CAPE}{\tau}; \quad CAPE = \int\limits_{cloud} g(\frac{\theta_v^{cloud} - \bar{\theta}_v}{\bar{\theta}_v})dz. \tag{3.8}$$

This assumption is used to estimate the magnitude of the cloud-base mass-flux (M_{base}^n) for an iteration index n,

$$M_{base}^n = \frac{\dfrac{CAPE}{\tau}}{g \int\limits_{cloud} \dfrac{M_{cloud}^{n-1}}{M_{base}^{n-1}} \dfrac{1}{\rho\bar{\theta}_v} \dfrac{\partial\bar{\theta}_v}{\partial z}dz}, \tag{3.9}$$

where M_{cloud}^{n-1} is the cloud mass-flux from the first full updraught computation initialised with a unit cloud-base mass-flux (M_{base}^{n-1}) given by equation 3.10, and Δt is the model time step.

$$M_{base}^{n-1} = \frac{0.1}{g} \frac{\Delta p_{base}}{\Delta t} \tag{3.10}$$

The convective adjustment timescale τ is proportional to the convective turnover timescale,

$$\tau = \frac{H}{\bar{w}_u^H}\alpha; \qquad \alpha = 1 + \frac{264}{n_T}, \tag{3.11}$$

where $\bar{w}_u^H$ is the updraught vertical velocity averaged over the depth of the cloud H, and α is a proportionality factor depending on the model truncation in spectral space n_T (for example at T_L799 (T_L159), $\alpha = 1.33$ (2.66)). This formulation of τ was introduced with Cycle 32r3 as part of

the modified convection scheme (§3.4).

(b) Shallow convection

Shallow convection is controlled by turbulence in the boundary layer. The closure for shallow convection makes the assumption that the moist static energy (h) in the sub-cloud layer is in equilibrium:

$$\int_{sfc}^{base} \frac{\partial \bar{h}}{\partial t} \bar{\rho} dz = 0. \tag{3.12}$$

That is, the moisture flux at the surface is equal to the moisture flux at the top of the boundary layer, which is equivalent to the cloud-base. Including the effect of all other physical processes (i.e. model tendencies from the other parameterization schemes $_{turb}$, $_{dyn}$ and $_{rad}$), the cloud-base mass-flux for shallow convection is given by

$$M_{base}^{n} = \frac{\int_{sfc}^{base} \left[(\frac{\partial \bar{h}}{\partial t})_{turb} + (\frac{\partial \bar{h}}{\partial t})_{dyn} + (\frac{\partial \bar{h}}{\partial t})_{rad} \right] \bar{\rho} dz}{(h^{u} - \bar{h})_{base}} \tag{3.13}$$

(c) Mid-level convection

Mid-level clouds initiate above the planetary boundary layer; they occur if the flow is dominated by large-scale ascent and the atmosphere is sufficiently moist. The closure for mid-level convection assumes that the cloud-base mass-flux is directly related to the large-scale vertical velocity

$$M_{base}^{n} = \bar{\rho} \bar{w}_{base}. \tag{3.14}$$

3.3.5 Microphysics

The IFS convective parameterization has a simple microphysics scheme which calculates the updraught condensation rate, the conversion from cloud condensate (water or ice) to precipitation (rain or snow), the freezing of cloud condensate in convective updraughts, the fallout of precipitation and the evaporation of rain. Details of the formulation and numerical implementation of the microphysics scheme in Cy33r1 are given in the ECMWF IFS documentation (2007b).

3.4   Advances in simulating tropical variability in Cycle 32r3

The version of the IFS described above is Cy33r1. Significant modifications were made to the model physics in Cy32r3 (implemented before Cy33r1) which led to advances in the simulation of tropical variability on all timescales (Bechtold *et al.*, 2008). This section will start by reviewing the performance of pre-Cy32r3 versions of the IFS in simulating tropical variability and the MJO, then discuss the modifications introduced in Cy32r3 with a particular focus on changes made to the convection scheme and their consequences for the current representation of tropical variability and the MJO.

The IFS has exhibited significant improvements in the simulation of the MJO over the past decade. Previous analysis of the monthly forecasting system at ECMWF, which uses the same atmospheric component as the operational IFS cycle, revealed a distinct loss of MJO amplitude. Averaging over 30 MJO events, Vitart (2003) showed that there was some skill in predicting the eastward propagation of the MJO beyond 20 days lead time, but that the amplitude of the oscillation decreased rapidly over the first 10 days of the forecast. The IFS, like many other NWP models, had difficulty propagating the active MJO signal through the Maritime Continent. Woolnough *et al.* (2007) tested the influence of an interactive ocean on MJO forecasts by comparing integrations of the monthly forecasting system (a) with persisted SSTs, (b) coupled to a full dynamical ocean and (c) coupled to a mixed-layer ocean model with high vertical resolution. Both coupled experiments showed improvements in forecast skill over the experiment with the persisted SSTs. The largest improvements occurred in the experiment with the mixed layer ocean model. When the active convection associated with the MJO was in the Indian Ocean or West Pacific, predictive skill was extended by up to a week. However, the characteristic loss of amplitude after a few days reported by Vitart (2003) remained a problem.

Vitart *et al.* (2007) tested the sensitivity of MJO simulation in the monthly forecasting system to changes in the model physics in both the full dynamical and mixed layer ocean experimental setups used by Woolnough *et al.* (2007). The changes included an increased CAPE threshold in the closure for deep convection (DEEP) and the introduction of a simple parameterization for ice supersaturation (ICE). DEEP improved the propagation of the MJO through the Indian Ocean and Maritime Continent but had little effect on its amplitude. ICE exhibited improved propagation only in the Indian Ocean, but showed a significant increase in the amplitude of the MJO in that region. The largest improvement in skill came from the monthly forecasting system with ICE coupled to the mixed-layer ocean model: when the convection was active in the Indian Ocean or West Pacific,

the model displayed skill in predicting the evolution of the MJO out to 21 days' lead time. Vitart *et al.* (2007) concluded that propagating the convective signal of the MJO through the Maritime Continent remained the hardest phase for the IFS to capture.

In June 2007 a new radiation package, McRad, was implemented in Cy32r2. The modifications in McRad included using the Monte Carlo Independent Column Approximation (McICA) to model radiative transfer in clouds, improved land surface albedo observations from the Moderate Resolution Imaging Spectroradiometer (MODIS) satellite and a new shortwave radiation scheme (Morcrette *et al.*, 2007). McRad improved the representation of cloud-radiation interactions, with the most pronounced impact in the tropical regions. McRad was also reported to reduce systematic errors in the model associated with the location of tropical convection through changes to the vertical structure of diabatic heating (Morcrette *et al.*, 2008).

The Cy32r3 modifications, introduced in November 2007, included revisions to the convection and vertical diffusion schemes. The free-tropospheric diffusion coefficients for heat and momentum were artificially increased, based on Monin-Obukhov functional dependencies, with the aim of reducing the overactive turbulent mixing in the model, avoiding the erosion of cloud-top inversions and generally creating smoother vertical profiles. There were two changes made to the convection scheme in Cy32r3: the introduction of a variable convective adjustment timescale (equation 3.11; Fig. 3.5) and a modified formulation for organised entrainment (equation 3.2). Prior to Cy32r3 the convective adjustment timescale τ over which CAPE is reduced to zero in the closure for deep convection was a resolution-dependent constant close to the model time step ($\tau = 720$ s at T_L799, 1200 s at T_L511 and 3600 s at T_L159). The new formulation for τ is constrained by a lower limit of the model time step and an upper limit of 3 hours ($\Delta t < \tau < 10800s$). The probability density functions (PDFs) of the new variable adjustment timescale at different model resolutions, obtained from equation 3.11, are shown in Fig. 3.5. At T_L799, τ varies between 720 and 3600 s, with a primary peak at approximately 900 s, compared with a constant value of 720 s in previous cycles.

Before Cy32r3 the formulation for updraught organised entrainment, active for deep and mid-level convection, was directly proportional to the large-scale moisture convergence $\bar{\omega}$ (equation 3.15; Tiedtke, 1989):

$$\epsilon_{org}^{MC} \quad = \quad \underbrace{-\frac{1}{\bar{q}}\left(\bar{v}.\nabla\bar{q} + \bar{\omega}\frac{\partial\bar{q}}{\partial p}\right)}_{\text{deep, mid-level}} \qquad (3.15)$$
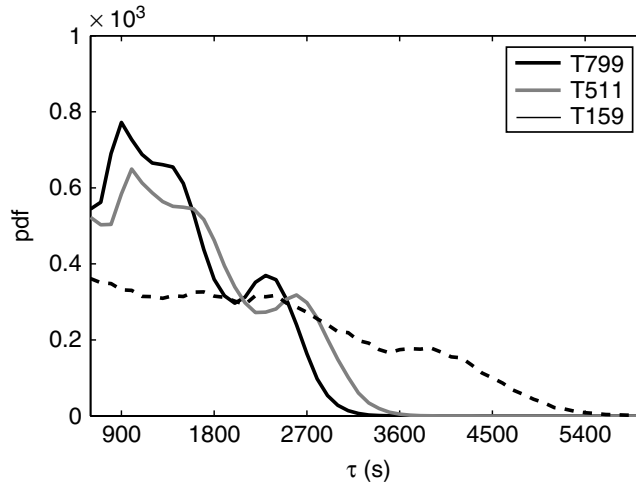
Figure 3.5 *PDFs of variable convective adjustment timescale (τ) for deep convection, sampled at different horizontal resolutions. Reproduced from Bechtold* et al. *(2008).*

It was assumed that large-scale moisture convergence occurred in the lower part of the cloud; therefore contributions from organised entrainment were only considered below the level of maximum vertical velocity. The motivation for this approach came from Lindzen (1988), who showed that linking the cloud-base mass-flux to the large-scale moisture convergence produced profiles of convective heating and mass-flux that compared favourably with GATE observations. However, a moisture convergence-dependent entrainment creates a strong coupling between the convection and large-scale dynamics, which can lead to a nonlinear feedback. Bechtold *et al.* (2008) suggested that feedback was responsible for discrepancies between modelled and observed precipitation and cloud-top height, and presented a new formulation for convective entrainment:

$$\epsilon_{org}^{RH} \;=\; \underbrace{c_1(1.3 - RH)F^3}_{\text{deep, buoy} > 0}; \quad F = \Big(\frac{\bar{q}_s}{\bar{q}_{s,base}}\Big); \quad c_1 = 0.8 \times 10^{-3} m^{-1} \tag{3.16}$$

The new formulation is active for deep convection when the parcel is positively buoyant and depends on the environmental relative humidity (equation 3.16; Bechtold *et al.*, 2008). The modification was motivated by the emerging recognition that environmental moisture plays a key role in modulating tropical convection; the entrainment of dry air into a plume reduces its buoyancy, which allows thermal inversions to control the cloud-top height (Redelsperger *et al.*, 2002). More specifically, environmental moisture has been shown to effect the MJO. Modelling studies have shown that suppressing free-tropospheric moisture anomalies significantly weakens an existing MJO signal and, in extreme cases, prevents MJO-like signals from developing (Grabowski, 2003;

Grabowski and Moncrieff, 2004). It has also been recognised that the correct relationship between free-tropospheric humidity and convective precipitation is crucial for a model to accurately simulate tropical convection (Bretherton *et al.*, 2004). The fact that many convective parameterizations, including that in the IFS, do not exhibit sufficient sensitivity to environmental moisture (Derbyshire *et al.*, 2004), provided further support for the changes introduced in Cy32r3.

It is worth considering the physical interpretation of equation 3.16. Since F^3 and c_1 will always be positive, equation 3.16 reveals that ϵ_{org}^{RH} will be larger and smaller in regions of low and high relative humidity respectively. Therefore, if deep convection is triggered in a dry environment, more dry air will be entrained into the plume, diluting it and preventing it from penetrating as high into the free troposphere. This will result in larger inhibition and, by avoiding spurious deep convective plumes being triggered, will better maintain the moisture anomalies during the suppressed phase of the MJO. Stronger moisture anomalies in the mid-troposphere ahead of the active MJO phase will precondition the tropical atmosphere for the successful eastward propagation of the MJO signal.

The Cy32r3 modifications led to the first realistic representation in the IFS of convectively coupled equatorial Kelvin and Rossby waves (Fig. 3.6). The changes rectified the loss of MJO amplitude reported by Vitart (2003); Cy32r3 was the first IFS cycle to sustain realistic MJO amplitudes for the entire integration period of a monthly forecast (32 days). Previous cycles, such as Cy28r3, lost 50% of the MJO amplitude after 15 days' lead time (Fig. 3.7; Bechtold *et al.*, 2008).

Despite the considerable advances made in the simulation of the MJO in the IFS, deficiencies remain. The Cy32r3 MJO is overactive, exhibiting an amplitude after 10 days lead time which is 20% too strong compared with the ERA-Interim reanalysis. Cy35r3, implemented in October 2009, reduced that bias by a factor of 2. On average the propagation speed of the Cy32r3 MJO is too slow. Cy32r3 MJO events spend too long in each MJO phase; events initiating in the Indian Ocean take approximately 2 weeks to reach the Maritime Continent, compared with only 10 days in observations. This is not true of all MJO events; the model is sometimes able to produce an MJO which exhibits propagation characteristics that agree well with observations. The IFS still has some difficulty propagating the MJO through the Maritime Continent. Although some model events do reach the West Pacific, on average fewer events propagate through the Maritime Continent in the model compared with observations (Vitart and Molteni, 2009b).

3.5 Experiment design

The advances made in MJO simulation in the IFS have been well analysed and documented. However, there has not been sufficient emphasis placed on the mechanisms by which those im-
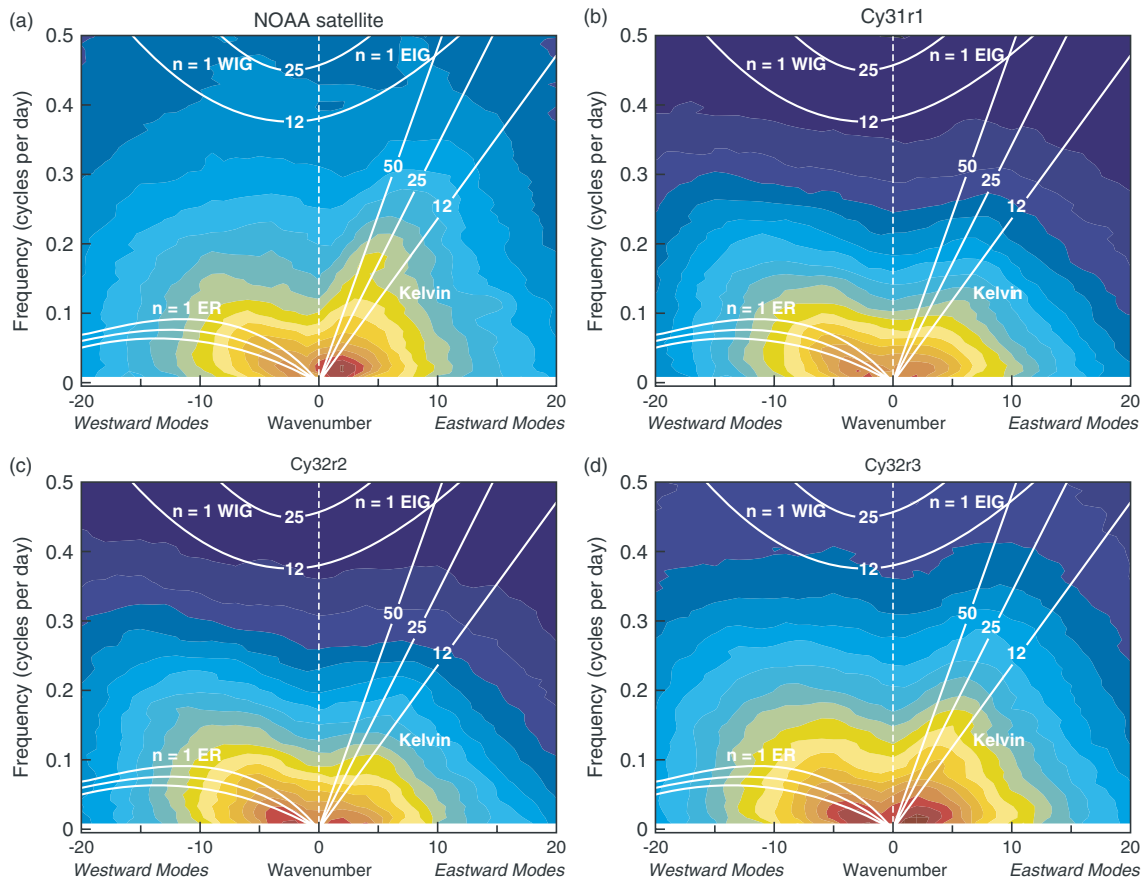
Figure 3.6 *Wavenumber-frequency diagram of equatorially averaged (10°N-10°S) OLR for 15 winters (December-March) from 1990-2005 for (a) NOAA satellite observations, (b) Cy31r1, (c) Cy32r2 and (d) Cy32r3. Contour intervals increase quadratically from 0.4 to 400. Theoretical dispersion curves at different equivalent depths are superimposed (white lines). Reproduced from* Bechtold *et al. (2008).*

provements occurred. The aim of the experiments performed in this thesis is to investigate which physical mechanisms are responsible for the improvements in MJO simulation that resulted from the physics changes in Cy32r3, with particular focus on the effects of the modifications to the convection scheme.

A series of hindcast experiments, initialised in May 2008, were performed. The time period covered in this study has significance in the wider academic and operational forecasting communities. As recognition of the international collaboration effort to address the challenge of modelling and understanding organised convection in the tropics, the World Climate Research Program (WCRP) and World Weather Research Program (WWRP) set up a joint project starting in May 2008 known as the Year of Tropical Convection (YOTC)[1] . YOTC was proposed as a year of coordinated observing, modelling and forecasting activities. At the end of the year, the observing period was extended

---

[1]Year of Tropical Convection; http://www.ucar.edu/yotc
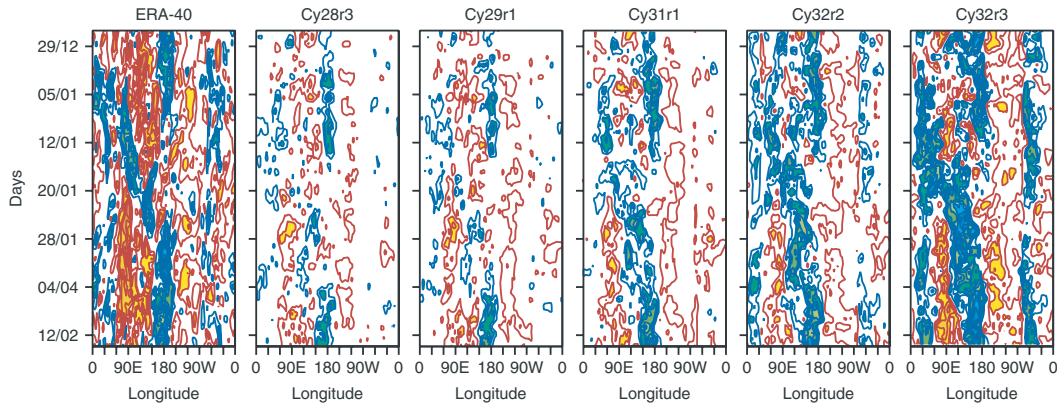
Figure 3.7 *Hovmöller diagrams of equatorially averaged (10°N-10°S) OLR from 29th December 1992 to 15th February 1993 from ERA-40 reanalysis (left panel) and 15-day forecasts for IFS cycles Cy28r3 to Cy32r3. Red shading indicates enhanced OLR anomalies associated with the suppressed phase of the MJO and blue shading indicates suppressed OLR anomalies associated with the active phase of the MJO. Reproduced from Bechtold* et al. *(2008).*

to January 2010. The aim of the project was for members of the academic community and operational forecasting centres to combine computational resources, modelling capabilities and new and existing observational data in an effort to improve our understanding of organised convection in the tropics. ECMWF was one of the contributing operational forecasting centres, therefore particular interest was given to the YOTC period and it is this period which is the focus of the hindcast experiments. The details of the hindcast sets (CONV, ENTRN and CAPE) and control IFS versions (Cy31r1 and OPER) to which they are compared are described below and represented schematically in Fig. 3.8.

3.5.1 Control IFS versions

(a) Cycle 31r1: Cy31r1

Cy31r1 is a pre-Cy32r3 cycle of the IFS. Cycle 31r1 became operational on 12th September 2006 and is the IFS cycle used to produce the ERA-Interim reanalysis dataset. The atmospheric component of the model is run at T$_L$255 resolution (0.721° × 0.721°, ~80 km) with 60 levels in the vertical and a model top at 0.1 hPa. The model time step is 30 minutes. The integrations are initialised using ERA-Interim reanalysis and forced daily by persisted SSTs from the NCEP high-resolution, real-time, global (RTG) SST reanalysis until January 2009. After January 2009, the integrations are forced daily by persisted SSTs from the National Centre for Ocean Forecasting (NCOF) Operational Sea Surface Temperature and Sea Ice Analysis (OSTIA). Cy31r1 uses the 'old' radiation scheme, before the introduction of the McRad scheme (Morcrette *et al.*, 2007). The convection scheme in Cy31r1 (prior to the modifications of Bechtold *et al.* (2008)) uses the mois-
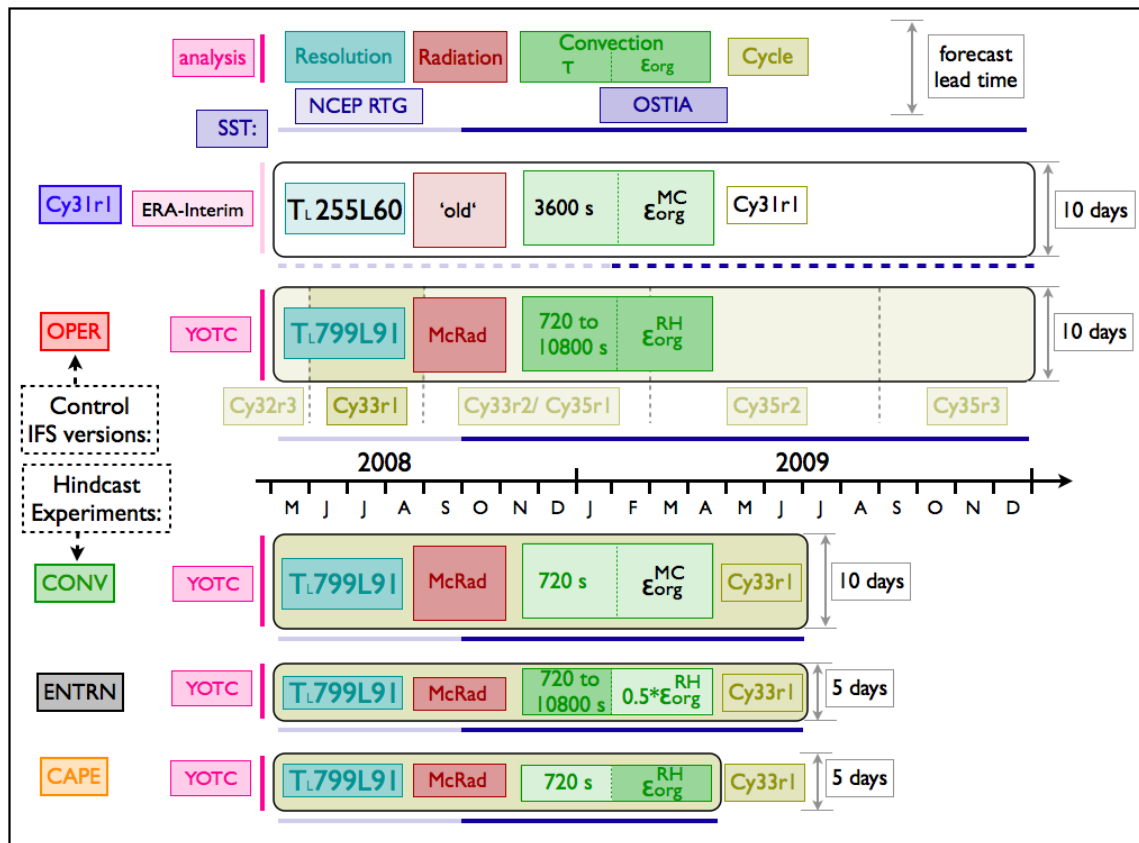
Figure 3.8 *Schematic representation of the hindcast experiments performed (CONV, ENTRN and CAPE) and the control IFS versions to which they are compared (Cy31r1 and OPER). The length of each hindcast set is represented along the x-axis, starting in May 2008. The width of the box encapsulating each hindcast set represents the maximum forecast lead time for which the hindcasts are integrated. The details of the analysis used for initialisation (pink), the atmospheric resolution (blue), the radiation scheme (dark red), the convection scheme (green), the IFS cycle number (light brown) and the SSTs used to force the atmospheric model (dark blue; dashed lines represent persisted SSTs, solid lines represent persisted SST anomalies) are displayed for each model version.*

ture convergence-dependent formulation for organised entrainment (equation 3.15), and a constant, resolution-dependent CAPE adjustment timescale (at T_L255, $\tau = 3600s$).

(b) Operational IFS cycle during YOTC: OPER

OPER refers to the evolving operational IFS cycle during the YOTC period, from Cy32r3 in May 2008 to Cy35r3 in September 2009. All of these cycles include the modifications of Bechtold *et al.* (2008)) and have the same atmospheric resolution: T_L799 (0.225° × 0.225°, ~25 km) with 91 levels in the vertical and a model top at 0.01 hPa. The model time step is 12 minutes. The integrations are initialised using the YOTC operational analysis and forced by persisted SST anomalies from NCEP RTG prior to October 2008 and persisted SST anomalies from OSTIA from October 2008 onwards. The persisted SST anomalies are calculated by persisting the initial SST anomalies

from the climatological seasonal cycle through the forecast, with the seasonal cycle continuing to evolve throughout the integration. The new McRad radiation scheme is used throughout OPER. The convection scheme in OPER (which includes the modifications of Bechtold *et al.* (2008)) uses a relative-humidity-dependent formulation for organised entrainment (ϵ_{org}^{RH}; equation 3.16), and a variable CAPE adjustment timescale (equation 3.11). In the formulation for τ the lower limit is defined by the model time step and the upper limit is 3 hours (at T_L799, $720s < \tau < 10800s$). However, the PDF of the new variable adjustment timescale reveals that at T_L799, τ varies between 720 s and 3600 s (Fig. 3.5).

3.5.2 Hindcast Experiments

All the experiments were performed using Cycle 33r1 (Cy33r1), the post-Cy32r3 cycle of the IFS described in §3.2 and §3.3. The horizontal resolution and initialisation of the experiments was identical to OPER (§3.5.1). Each experiment contained the new radiation package McRad. The experiments were designed to test the sensitivity of MJO simulation to different aspects of the Cy32r3 convection scheme, therefore each experiment had a slightly different formulation of convection. The aims of the individual experiments and how they differed from one another is described below.

(c) Convection experiment: CONV

There are many differences between Cy31r1 and OPER besides the new configuration of convection. For example, they are initialised from different analyses, run at different resolutions, forced by different SSTs and use different formulations for radiation. Therefore, differences detected from a Cy31r1-OPER comparison alone cannot be attributed solely to the new configuration of convection. The aim of the first experiment (CONV) is to isolate the effects of the Cy32r3 convection scheme on the simulation of the MJO. The YOTC period is re-forecast using a post-Cy32r3 Cycle (Cy33r1) with the pre-Cy32r3 formulation of convection. More specifically, the organised entrainment rate is proportional to the moisture convergence (ϵ_{org}^{MC}; equation 3.15) and the CAPE adjustment timescale is a resolution-dependent constant (at T_L799, $\tau = 720s$). The CONV experiment was run from May 2008 to September 2009 (inclusive) out to 10 days forecast lead time. Differences detected between OPER and CONV can be directly attributed to the modified convective parameterization.

(d) Entrainment experiment: ENTRN

The ENTRN experiment is designed to test the sensitivity of MJO simulation to the relative-humidity-dependent formulation for organised entrainment in the Cy32r3 convection scheme. Part of the YOTC period is re-forecast using Cy33r1 with the Cy32r3 formulation for convection (i.e.

a relative-humidity-dependent formulation for organised entrainment and a variable CAPE adjustment timescale (equation 3.11)). However, the contribution of organised entrainment in the formulation for deep convection is halved:

$$\epsilon_{org}^{ENTRN} = 0.5 * \epsilon_{org}^{RH} = \underbrace{0.5 * c_1(1.3 - RH)F^3}_{\text{deep, buoy} > 0}; \quad F = \left(\frac{\bar{q}_s}{\bar{q}_{s,base}}\right); \quad c_1 = 0.8 \times 10^{-3} m^{-1} \qquad (3.17)$$

Before the new relative-humidity-dependent formulation for organised entrainment was implemented in the operational IFS, many tests were carried out to find the optimal value of the tuneable parameter c_1. Therefore, the smaller value $(0.5 * c_1)$ in the ENTRN experiment is likely to degrade the forecast skill of the model. It is not clear, *a priori*, how this change will impact the simulation of the MJO. A smaller value $(0.5 * c_1)$ was chosen in preference to a larger one (e.g. $2 * c_1$) to avoid meaningless results outside the realistic range of values for the organised entrainment rate. The ENTRN experiment was run from May 2008 to June 2009 (inclusive) out to 5 days forecast lead time. For an identified MJO case study in April 2009, the forecast lead time was extended to 10 days.

(e) CAPE experiment: CAPE

The CAPE experiment is designed to test the sensitivity of MJO simulation to the use of a variable CAPE adjustment timescale. Part of the YOTC period is re-forecast using Cy33r1 with the Cy32r3 relative-humidity-dependent formulation for organised entrainment (equation 3.16), but a constant, resolution-dependent, CAPE adjustment timescale (at T_L799, $\tau = 720s$). The CAPE experiment was run from May 2008 to April 2009 (inclusive) out to 5 days forecast lead time. As with the EN-TRN experiment, for the identified MJO case study in April 2009 the forecast lead time is extended to 10 days. This experiment will indicate which of the Cy32r3 modifications to the convection scheme is most influential in improving the predictive skill of the MJO. If, compared with OPER, the CAPE experiment shows no significant differences in MJO simulation, then it can be deduced that the entrainment rate change was the most influential factor. However, if the CAPE experiment is significantly different to OPER, then it suggests that the change from a constant to a variable CAPE adjustment timescale had the most pronounced impact on the representation of the MJO.

3.5.3 Summary

The modifications to the convection scheme in Cy32r3 of the IFS had a significant impact on the simulation of tropical variability. There were two changes to the formulation of deep convection in the Cy32r3 scheme: (1) the introduction of a variable CAPE adjustment timescale τ and (2) a relative-humidity-dependent organised entrainment rate ϵ_{org}^{RH}. By performing hindcast experiments over the YOTC period with different combinations of these physics changes, it was possible to test the sensitivity of MJO simulation to the Cy32r3 configuration of convection. Other than Cy31r1, which differs from the other runs in resolution, radiation package, initialisation analysis and SSTs (Fig. 3.8), the significant differences between the experiments (CONV, ENTRN and CAPE) and OPER are in the formulation of convection. Those differences are summarised in Table 3.1.

Table 3.1 *Summary of the formulation of the CAPE adjustment timescale τ and organised entrainment rate ϵ_{org} in the convective parameterizations in the hindcast experiments and control IFS versions.*

		Convection scheme			
		τ		ϵ_{org}	
		seconds	equation	dependence	equation
Control IFS versions	(a) Cy31r1	3600	-	ϵ_{org}^{MC}	(3.15)
	(b) OPER	720 to 10800	(3.11)	ϵ_{org}^{RH}	(3.16)
Experiments	(c) CONV	720	-	ϵ_{org}^{MC}	(3.15)
	(d) ENTRN	720 to 10800	(3.11)	$0.5*\epsilon_{org}^{RH}$	(3.17)
	(e) CAPE	720	-	ϵ_{org}^{RH}	(3.16)

Fig. 3.9 highlights what the comparisons between experiments reveal about the individual changes to the formulation of ϵ_{org} and τ. Comparing CAPE and CONV isolates the impact of the new relative-humidity-dependent ϵ_{org}^{RH}. Neglecting minor cycle differences, comparing OPER and CAPE isolates the impact of the variable τ; comparing OPER and CONV shows the impact of the entire new convection package (ϵ_{org}^{RH} and τ); and comparing OPER and ENTRN reveals the impact of changing the rate of ϵ_{org}^{RH} rather than its formulation. Comparing Cy31r1 and OPER, between which there are many non-negligible differences including the formulation of convection (Fig. 3.8), gives an indication of the overall progress made in the representation of the MJO in the IFS between 2006 (Cy31r1) and 2008 (post Cy32r3 cycles). This comparison forms the start of the
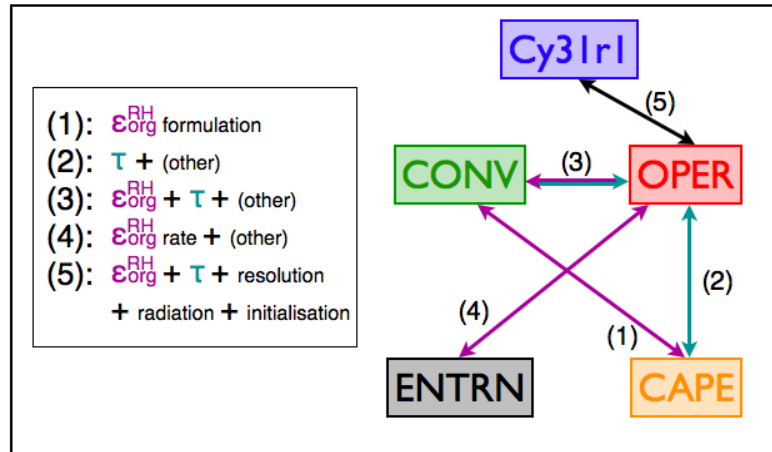
Figure 3.9 *Schematic representation showing what different experiment comparisons reveal about the changes to ϵ_{org}^{RH} and τ. (other) is defined as minor changes between Cy33r1 used for all the experiments and the non-stationary operational cycle used for OPER (Cy32r2 to Cy35r3).*

analysis in Chapter 4.

3.6 Conclusions

This study provides a unique opportunity to perform a detailed analysis of the representation of the MJO in an operational numerical weather prediction system. As discussed in §2.4.6, this approach is distinct from the many previous studies of the MJO which have focused on evaluating statistics from long climate integrations. Although many observed characteristics of the MJO remain poorly predicted by NWP models, the MJO is recognised as an important source of tropical and extra-tropical predictability on sub-seasonal timescales. Due to the interactions of the MJO with other aspects of the climate system, and the teleconnection patterns associated with it, operational centres such as ECMWF place significant emphasis on improving the representation of the MJO in their models and hence improving their medium-range forecasts.

Studying the MJO in an NWP context allows different questions to be asked and answered. While climate integrations reveal how well a model can reproduce MJO activity in general, NWP models are still strongly constrained by the initial conditions. This allows the characteristics of individual case studies in a near-observed state to be compared with observations. However, studying the MJO in an NWP context carries different complications. NWP models are complex and non-stationary with model developments continually being researched, verified and implemented. Changes are often not implemented individually, but as part of a package. For example, at ECMWF a new IFS cycle, with a combination of model developments, is implemented approximately every four to eight months. Comparing model cycles makes it impossible to attribute advances in

the simulation of a particular phenomenon to individual physics changes. By performing hindcast experiments with the same cycle of the model with only a single change to the formulation of convection, impacts on the simulation of the MJO in this study can be directly attributed to particular model developments in the IFS. This enables the study to go further and to investigate what physical mechanisms are responsible for those impacts.

As discussed in §2.4, the representation of the MJO in a model is highly sensitive to that model's physical parameterizations. Over the last decade, the IFS has made significant progress in predicting the onset and evolution of MJO events through changes in resolution, model physics and air-sea coupling. The most marked improvements came after revisions to the convection scheme implemented in Cy32r3 in 2007, which included for deep convection, the introduction of a variable CAPE adjustment timescale and a new relative-humidity-dependent entrainment rate.

The experiments carried out in this study have been designed to separate the effects of the modified formulation of deep convection from other model developments and to go further and separate the individual parts of the new formulation of convection and assess their individual impact on the simulation of the MJO. This study will answer the following research questions:

- To what extent can the advances in the simulation of the MJO in Cy32r3 be attributed to the modified parameterization of convection?

- What effect did the individual components of the modified parameterization of convection have on the simulation of the MJO?

- What are the physical mechanisms responsible for the improvements in MJO simulation resulting from the modified parameterization of convection in Cy32r3?

CHAPTER 4

The Representation of the MJO

4.1 Introduction

According to the recent modelling studies presented in Chapter 2, despite the MJO playing a vital role in our weather and climate system, it is poorly predicted by current numerical models. Model intercomparison studies, such as that of Lin *et al.* (2006), have highlighted discrepancies between models in their representations of the MJO, but have been unable to explain variations in performance among models. To remedy this problem, Waliser *et al.* (2009) proposed a set of MJO diagnostics to act as a validation framework and provide a consistent way to evaluate a model's representation of the MJO. In line with this framework, analysis techniques from Waliser *et al.* (2009), such as band-pass filtering, multivariate EOF analysis and wavenumber-frequency spectral decomposition, have been applied in this study.

This chapter addresses the first two objectives proposed in §3.6: (a) to quantify to what extent the advances in the simulation of the MJO in Cy32r3 can be attributed to the modified parameterization of convection, and (b) to identify the effects of the individual components of the modified parameterization of convection on the simulation of the MJO. Initially, the simulated MJO activity in the two control IFS versions, Cy31r1 and OPER, is compared during the YOTC period from May 2008 to April 2009 (§4.3). This indicates the progress since 2006 in the performance of the IFS in simulating MJO activity. While this "old-model, new-model" comparison highlights the improvements in the representation of MJO activity in the IFS, those differences can be attributed to specific model changes only by using the hindcast experiments in which single changes have been applied (§4.4). Finally, two MJO case studies during the YOTC period are used to make a more detailed comparison of the simulated MJO in the IFS control versions and hindcast experiments (§4.5.1 and §4.5.2).

4.2 Observational datasets

Throughout this chapter comparisons will be made between the IFS simulations and observations. The satellite observations, reanalysis and analysis data used to make these comparisons are described below.

(a) Satellite OLR data

Daily OLR data is obtained from the National Oceanic and Atmospheric Administration (NOAA) Earth System Research Laboratory (ESRL)[1]. Readings from the Advanced Very High Resolution Radiometer (AVHRR) satellite have been interpolated onto a global 2.5°× 2.5° grid. The temporal and spatial interpolation technique used to fill in missing data values is described by Liebmann and Smith (1996).

(b) Reanalysis data

Zonal wind data is obtained from ERA-Interim, the latest global atmospheric reanalysis product from ECMWF (Dee *et al.*, 2011). ERA-Interim is constructed using Cy31r1 of the IFS, which is described in §3.5.1.

(c) Analysis data

ECMWF also produces an operational analysis (OPER analysis) which is constructed using the operational cycle of the IFS at that time. For example, from 3rd June 2008 to 30th September 2008 when Cy33r1 was operational, OPER analysis was produced by Cy33r1.

4.3   Control IFS versions - Cy31r1 and OPER

Before making the comparison between Cy31r1 and OPER, it is worth recalling Fig. 3.9 in §3.5.3, which highlights the main differences between these IFS versions. OPER is run at a higher horizontal and vertical resolution than Cy31r1: $T_L799L91$ compared to $T_L255L60$. OPER is initialised from a different analysis: YOTC operational analysis compared with ERA-Interim. The radiation and convection schemes in OPER and Cy31r1 differ: OPER uses McRAD and a post-Cy32r3 convection scheme, while Cy31r1 uses the old radiation scheme and a pre-Cy32r3 convection scheme.

4.3.1   Filtered Hövmuller diagrams

To extract variability on the intraseasonal timescales of the MJO, a 20-100 day band-pass filter with 181 weights is applied to the IFS control versions, Cy31r1 and OPER. The resulting filtered timeseries of OLR, 200 and 850 hPa zonal wind are averaged between 10° N and 10° S and plotted as Hövmuller (time-longitude) diagrams, which show the eastward propagation of the MJO (Figs. 4.1, 4.2 and 4.3). OLR is used as an indicator of convective activity, while upper- and lower-tropospheric zonal wind show the overturning circulation anomalies associated with the MJO.

---

[1]The data is available online at http://www.esrl.noaa.gov.
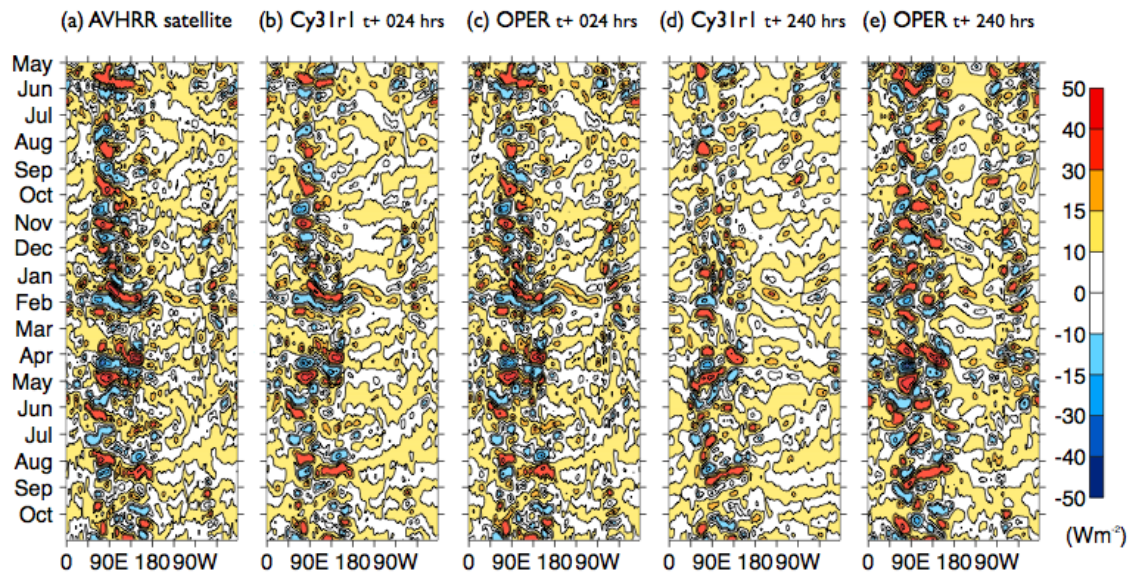
Figure 4.1 *Hövmuller (time-longitude) diagrams of 20-100 day band-pass filtered OLR averaged between 10° N and 10° S. May 2008 to October 2009. (a) NOAA AVHRR satellite data. (b) and (d) Cy31r1 verified at 1- and 10-day forecast lead time, respectively. (c) and (e) OPER verified at 1- and 10-day forecast lead time, respectively.*

In Fig. 4.1, higher (lower) OLR corresponds to suppressed (enhanced) convective activity on intraseasonal timescales. There is evidence of eastward-propagating signals of OLR in the NOAA AVHRR satellite data (§4.2) initiating in the equatorial Indian Ocean near 50°E and propagating through Indonesia to the dateline (Fig. 4.1 (a)). For example, in January - February 2009 and April - May 2009 an eastward-propagating signal of suppressed convection is followed by an eastward-propagating envelope of enhanced convective activity. There is very little convective activity on intraseasonal timescales in the Western Hemisphere; generally the convective anomalies associated with the MJO dissipate in the East Pacific as they encounter cooler SSTs. Comparing satellite data with the IFS at a 1-day forecast lead time, Figs. 4.1 (b)-(c) show that both Cy31r1 and OPER exhibit coherent eastward-propagating signals on intraseasonal timescales, which agree well with observations. At a 10-day forecast lead time the amplitude of convective activity in Cy31r1 has weakened considerably; the convective anomalies which do develop do not exhibit coherent eastward propagation. Increasing forecast lead time has the opposite effect on convective anomalies in OPER, which have strengthened by day 10. At this lead time, OPER is particularly overactive in the Western Hemisphere; the convective anomalies which form between 60° W and 30° W are stronger than those observed by satellite.

The eastward-propagating envelope of enhanced convection associated with the MJO is accompanied by a strong overturning circulation anomaly: lower-tropospheric convergence into the
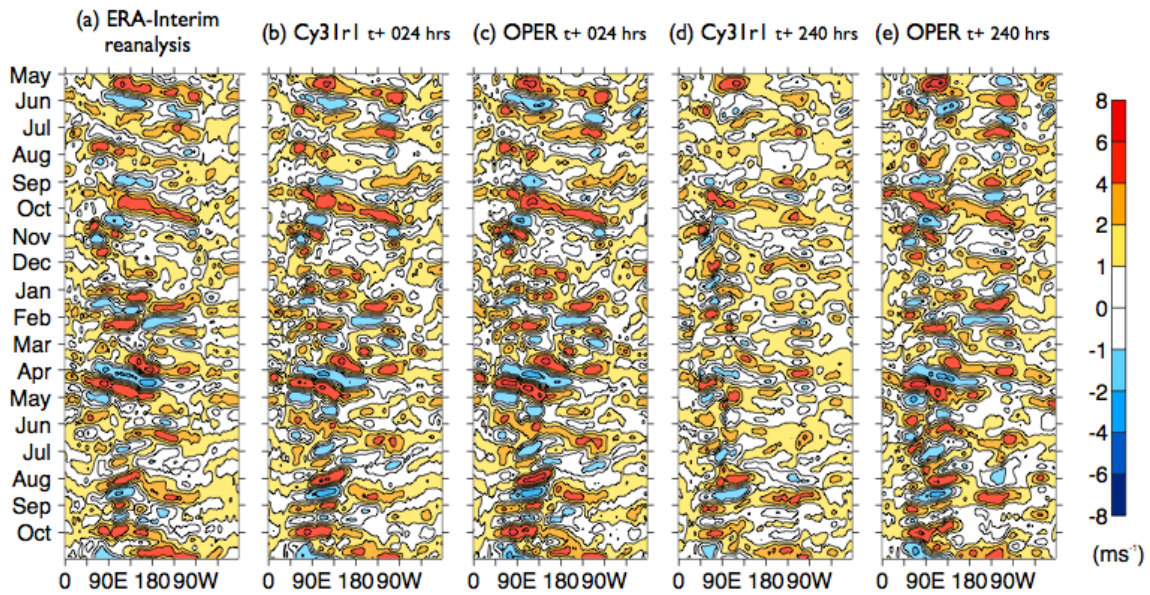
Figure 4.2 *As Fig. 4.1, but for 850 hPa zonal wind compared with, (a) ERA-Interim reanalysis.*

convective centre and upper-tropospheric divergence out of it. Figs. 4.2 and 4.3 show the intrasea-sonal zonal wind anomalies at 850 and 200 hPa, respectively, for ERA-Interim reanalysis compared with the IFS control versions, Cy31r1 and OPER, at increasing forecast lead time. Strong bands of eastward-propagating easterly and westerly anomalies are apparent in the ERA-Interim 850 hPa zonal wind during April - May 2009. This circulation pattern does not extend east of the date-line, but dissipates with the convective anomaly identified in Fig. 4.1. Another prominent feature in the 850 hPa zonal wind is the strong band of eastward-propagating westerlies in October 2008 which extended past the dateline into the East Pacific. At a 1-day forecast lead time both Cy31r1 and OPER capture these features and agree well with ERA-Interim. However, as forecast lead time increases, the amplitude of the lower-tropospheric zonal wind anomalies in Cy31r1 weakens considerably: the eastward-propagating features in October 2008 and April 2009 are evident, but exhibit less coherent eastward propagation. In OPER, the amplitude of the April 2009 feature at a 10-day forecast lead time is equivalent to that at a 1-day forecast lead time. The feature in October 2008 weakens as it crosses the Maritime Continent, but strengthens again in the East Pacific.

The large-scale dynamical signal of the MJO is stronger in the upper troposphere, evident in the intraseasonal anomalies in Fig. 4.3. The eastward-propagating anomalous 200 hPa winds are not confined to the warmer SSTs of the Eastern Hemisphere, but become uncoupled from the re-gion of enhanced convection at the surface and extend into the Western Hemisphere. ERA-Interim exhibits eastward-propagating anomalies through much of the YOTC period. In April 2009 the upper-tropospheric anomalies completed an entire circuit of the equator. Similar to the OLR and
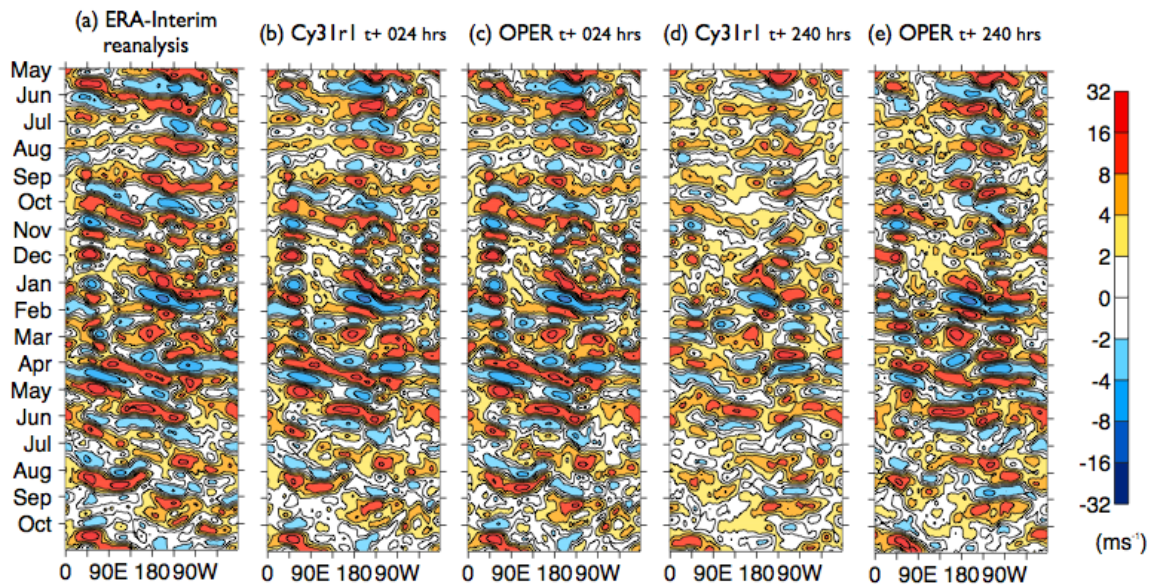
Figure 4.3 *As Fig. 4.1, but for 200 hPa zonal wind compared with, (a) ERA-Interim reanalysis.*

850 hPa zonal wind, at short forecast lead times both Cy31r1 and OPER agree well with ERA-Interim, successfully capturing the eastward propagation into the western Hemisphere. At a 10-day forecast lead time the large-scale dynamical circulation pattern in Cy31r1 has reduced in magnitude, while OPER maintains the observed strength.

The Hövmuller diagrams in Figs. 4.1, 4.2 and 4.3 reveal that at short forecast lead times, when the model is well-constrained by its initial conditions, both Cy31r1 and OPER conserve coherent eastward-propagating anomalies of OLR (zonal wind) on intraseasonal timescales which agree well with satellite observations (ERA-Interim). At longer forecast lead times, OPER significantly outperforms Cy31r1, maintaining the magnitude and eastward propagation of the intraseasonal anomalies, and exhibiting closer agreement with observations throughout the YOTC period.

A consequence of the 181 weights in the 20-100 day band-pass filtering technique is that 90 days are lost from the beginning and end of the timeseries. When the band-pass filter was applied to the hindcast experiments, insufficient filtered data remained to compare with Cy31r1 and OPER for the period shown in Figs. 4.1, 4.2 and 4.3. Therefore, the equivalent 20-100 day band-pass filtered Hövmuller diagrams for the hindcast experiments are not shown.

4.3.2   Variance of convective activity

When considering the ability of a numerical weather model to simulate convective activity in the tropics, it is not sufficient to examine only the mean climate, but necessary also to examine the capability of the model to reproduce the correct variability about that mean. The mean climate is a composite of weather systems on a wide range of spatial and temporal scales, but the variability of convective activity is crucial for modulating the magnitude and location of convection, especially over the islands of the Maritime Continent and West Pacific Warm Pool. Accurately simulating the variability of convective activity, of which the MJO is an important component, is also crucial for a model to successfully reproduce the global teleconnection patterns from that convective activity.

Fig. 4.4 compares 20-100 day band-pass filtered variance of daily OLR from the NOAA AVHRR satellite from February 2008 to October 2009 with OPER and Cy31r1. The largest variance in the satellite-derived OLR during this period is in the eastern Indian Ocean. There are also areas of large variance in OLR north of the equator in the Bay of Bengal, South China Sea, Philippine Sea and south of the equator where the South Pacific Convergence Zone (SPCZ) meets the West Pacific Warm Pool. The satellite data exhibit very little variance in OLR over the eastern Pacific and continent of Africa. There are local minima in variance of OLR over the Indonesian islands themselves; variability over the islands is dominated by the diurnal cycle of convection, which occurs on timescales too short to be selected by the 20-100 day band-pass filter (Fig. 4.4 (a)).

At a 1-day forecast lead time, Cy31r1 and OPER successfully capture the spatial pattern of convective variability: maxima over the Indian Ocean, Bay of Bengal, South China Sea, Philippine Sea and SPCZ and minima over the Indonesian islands. However, Cy31r1 underestimates the magnitude of the maxima in variance of convective activity and overestimates the local minima over the Indonesian islands (Fig. 4.4 (b)). OPER reproduces the observed magnitude of convective activity in most regions, although it does overestimate the variance, most notably in the Bay of Bengal and South China Sea (Fig. 4.4 (c)). The overestimation of intraseasonal convective activity is a feature that the IFS has in common with many GCMs (Kim *et al.*, 2009). For example, Inness and Slingo (2003) showed that HadCM3 overestimated the observed variance of convective activity north of the equator in the Bay of Bengal.

At a 10-day forecast lead time, Cy31r1 continues to underestimate intraseasonal variance in OLR, although it does still reproduce the observed spatial structure (Fig. 4.4 (d)). OPER produces excessive intraseasonal variance in OLR in the Bay of Bengal and South China Sea at a 10-day forecast lead time. Additionally, the spatial area of the maximum in variance over the Indian Ocean
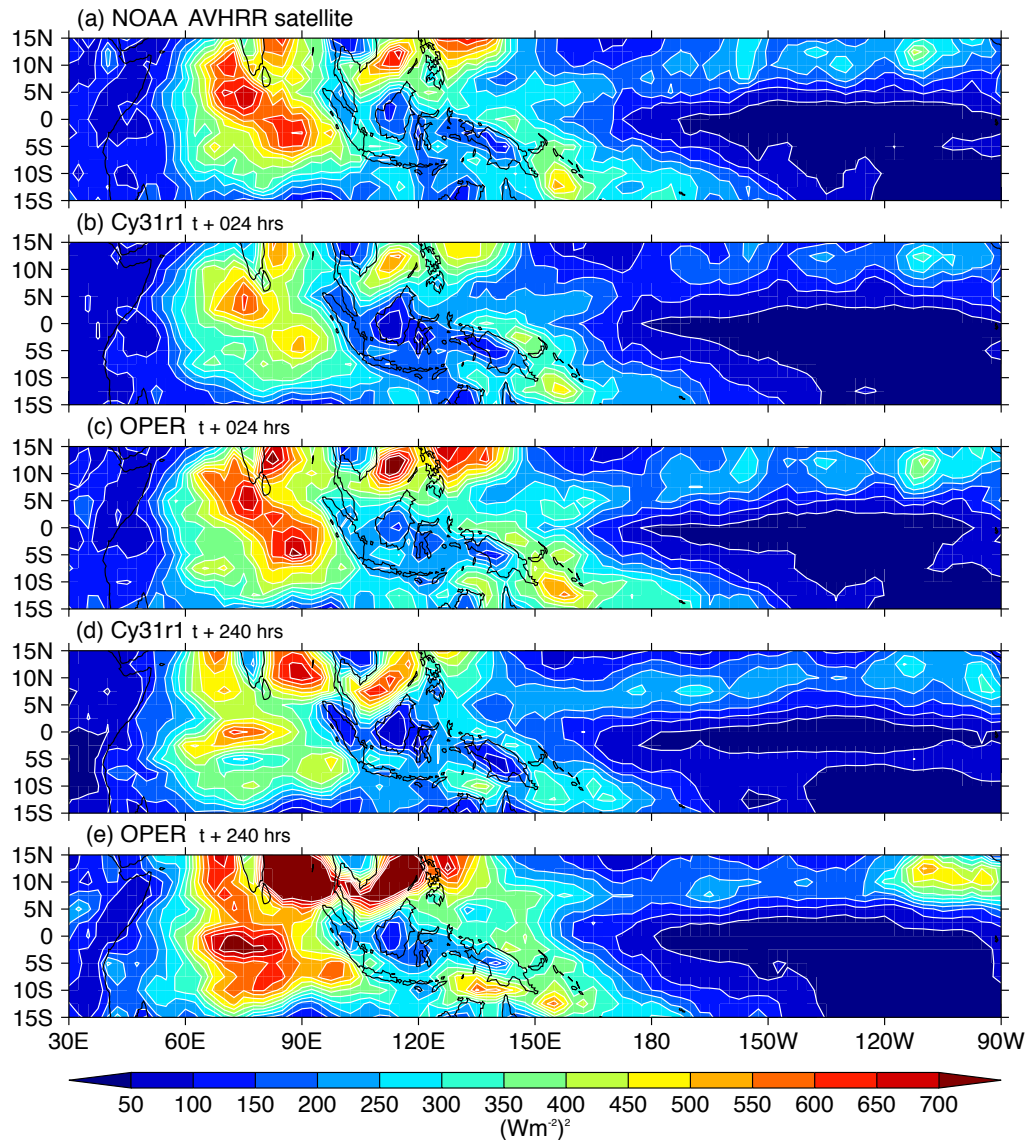
Figure 4.4 *Variance of 20-100 day band-pass filtered OLR for February 2008 to October 2009 from (a) NOAA AVHRR satellite data. (b) and (d) Cy31r1 at 1- and 10-day forecast lead time, respectively. (c) and (e) OPER at 1- and 10-day forecast lead time, respectively. The contour interval is 50 $(Wm^{-2})^2$.*

has increased. At the longer lead time, OPER exhibits a considerable increase in intraseasonal variance in convective activity in the eastern Pacific north of the equator, a feature which is not present in the observations (Fig. 4.4 (e)).

Fig. 4.4 has revealed significant differences in the representations of convective activity in Cy31r1 and OPER as forecast lead time increases. At short forecast lead times, when the model is well constrained by its initial conditions, both Cy31r1 and OPER accurately reproduce the spatial pattern of variability on MJO timescales. However, as forecast lead time increases, Cy31r1

generally underestimates and OPER generally overestimates the variance of convective activity on intraseasonal timescales.

4.4 Hindcast Experiments

The comparison between Cy31r1 and OPER in §4.3 revealed significant differences in the representation of convective variability on timescales of the MJO, especially at longer forecast lead times. While this confirms that advances have been made in the simulation of convective activity on intraseasonal timescales in the IFS, this analysis alone cannot reveal which parts of the OPER model configuration are responsible. The comparison between Cy32r2 and Cy32r3 in the study by Bechtold *et al.* (2008) suggested that the improved representation of the MJO could be attributed to modifications to the convection and vertical diffusion schemes. However, a comparison between two cycles of the IFS inevitably includes other modifications to the model. This thesis is unique in that it is able to isolate individual changes to the model formulation, which consequently allows the resulting differences in the simulation of phenomena such as the MJO to be attributed to those single model changes. Here the aim is to ascertain to what extent the improvements in MJO simulation in Cy32r3 can be directly attributed to the modified convection scheme.

Comparisons are made between the control IFS versions presented in §4.3 and the hindcast experiments described in §3.5.2. Before making those comparisons, it is worth recalling Fig. 3.9 in §3.5.3, which highlights what the comparisons between the hindcast experiments and OPER reveal about different aspects of the Cy32r3 convection scheme. CONV is run using a post-Cy32r3 model configuration with the pre-Cy32r3 convection scheme. Therefore, comparing CONV and OPER isolates the effects of the Cy32r3 convection scheme only and addresses the first research question posed at the end of Chapter 3: To what extent can the advances in the simulation of the MJO in Cy32r3 be attributed to the modified parameterization of convection? A comparison between CONV and Cy31r1, indicates the contribution to the improved simulation of the MJO from other non-convection related changes to the model, such as increased vertical and horizontal resolution and the introduction of McRad, the new radiation scheme.

The hindcast experiments CAPE and ENTRN are designed to address the second research question posed in §3.6: What effect did the individual components of the modified parameterization of convection have on the simulation of the MJO? The modifications to the Cy32r3 convection parameterization included, (a) a relative-humidity-dependent organised entrainment rate (ϵ_{org}^{RH}), and (b) a variable CAPE adjustment timescale, (τ). CAPE uses a post-Cy32r3 model with the post-Cy32r3 convection scheme, but reverts back to a constant CAPE adjustment timescale. Therefore, com-

paring CAPE and OPER isolates the effect of the new formulation of τ on the simulation of the MJO, while a comparison between CAPE and CONV isolates the effect of the ϵ_{org}^{RH} formulation. ENTRN uses a post-Cy3r3 model with a post-Cy32r3 convection scheme, but the rate of ϵ_{org}^{RH} is halved. Therefore, a comparison between ENTRN and OPER reveals how important the rate of entrainment is to the simulation of the MJO. These comparisons are summarised in Table 4.1.

Table 4.1 *Summary of IFS comparisons which isolate the effects of certain model modifications.*

Model Modification	IFS Comparison
Cy32r3 (ϵ_{org}^{RH} & τ)	OPER - CONV
ϵ_{org}^{RH} formulation	CAPE - CONV
τ	OPER - CAPE
ϵ_{org}^{RH} rate	OPER - ENTRN
non-convection modifications	CONV - Cy31r1

4.4.1   Variance of convective activity

The importance of simulating the variability of convective activity in numerical forecasts of the tropics was discussed in §4.3.2; a similar diagnostic is now applied to all versions of the IFS. Due to computational limitations, the hindcast integrations are not long enough to apply the 20-100 day band-pass filtering technique used in §4.3.2. Figs. 4.5, 4.6 and 4.7 show the unfiltered variance of convective activity in the tropics from satellite data, the IFS control versions Cy31r1 and OPER, and the hindcast experiments CONV, ENTRN and CAPE, at increasing forecast lead time. Fig. 4.5 (a) shows the variance of daily OLR from the NOAA AVHRR satellite from May 2008 to April 2009. The satellite data exhibits a similar spatial pattern in the variance of unfiltered OLR compared with the intraseasonally filtered equivalent (Fig. 4.4 (a)). The largest variance of OLR is located over the equatorial Indian Ocean, Bay of Bengal, and West Pacific Warm Pool, extending south of the equator through the Australian monsoon region into the SPCZ. As with the intraseasonally filtered variance of OLR, the larger Indonesian islands exhibit a local minimum in variance. There is little variance in daily OLR along the equatorial eastern Pacific.

At a 1-day forecast lead time, all versions of the IFS reproduce the spatial pattern of variance in daily OLR with reasonable accuracy. However, discrepancies are evident in the magnitude of
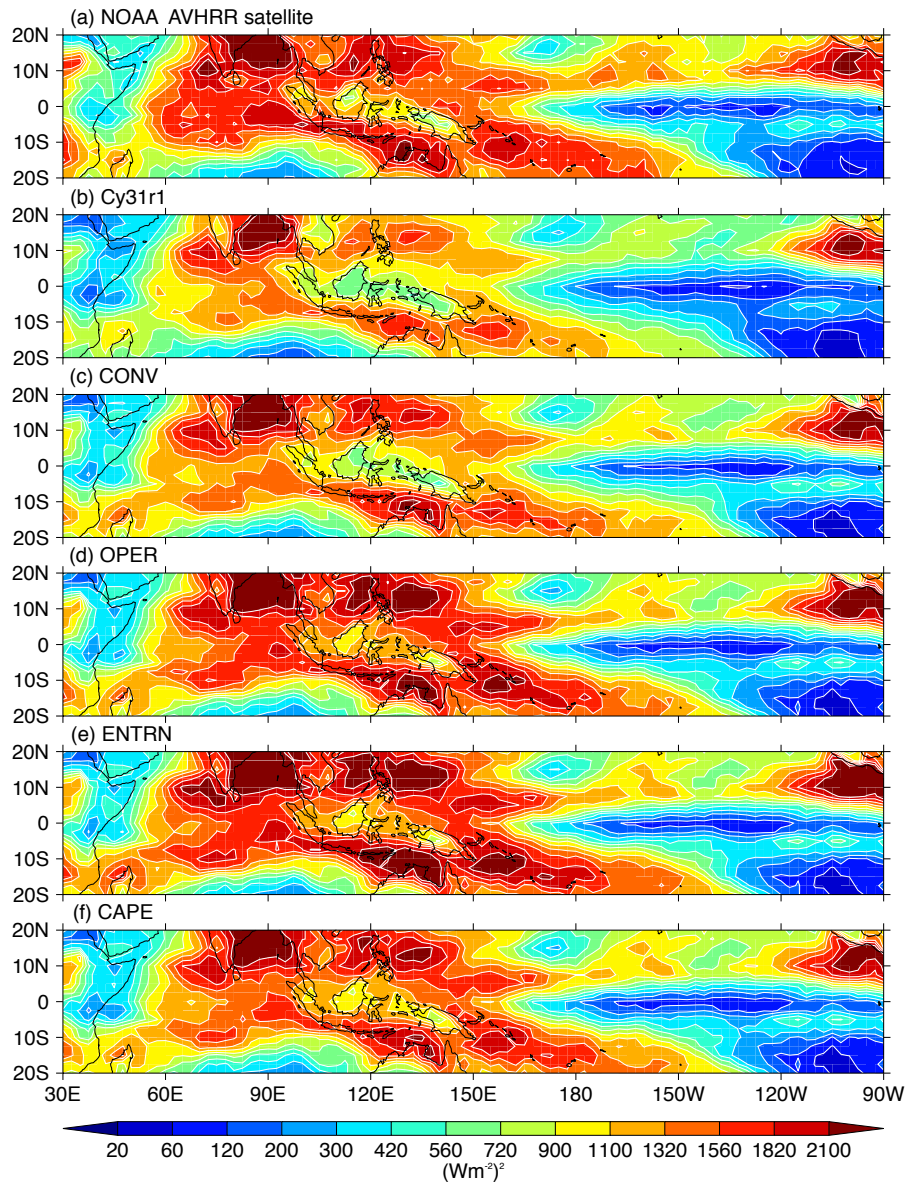
Figure 4.5 *Variance of unfiltered OLR for May 2008 to April 2009 from (a) NOAA AVHRR satellite data and Cy31r1, CONV, OPER, ENTRN and CAPE (b)-(f) at 1-day forecast lead time.*

convective variability. Comparing OPER and CONV with the satellite data indicates that the introduction of the Cy32r3 convection scheme increased the magnitude of convective variability in the entire Indo-Pacific region (Figs. 4.5 (a),(b) and (d)). However, OPER overestimates the magnitude of convective variability in the South China and Philippine Seas, Australian monsoon region and SPCZ. CONV (Fig. 4.5 (c)) shows slightly stronger variance than Cy31r1 (Fig. 4.5 (b)), although both underestimate the magnitude of convective variability in the entire Indo-Pacific region. This suggests that the other, non-convection scheme changes between Cy31r1 and OPER, such as increased horizontal and vertical resolution, and the introduction of McRad, the new radiation scheme, had little effect on the simulation of convective activity in the tropics (Figs. 4.5 (a)-(c)).
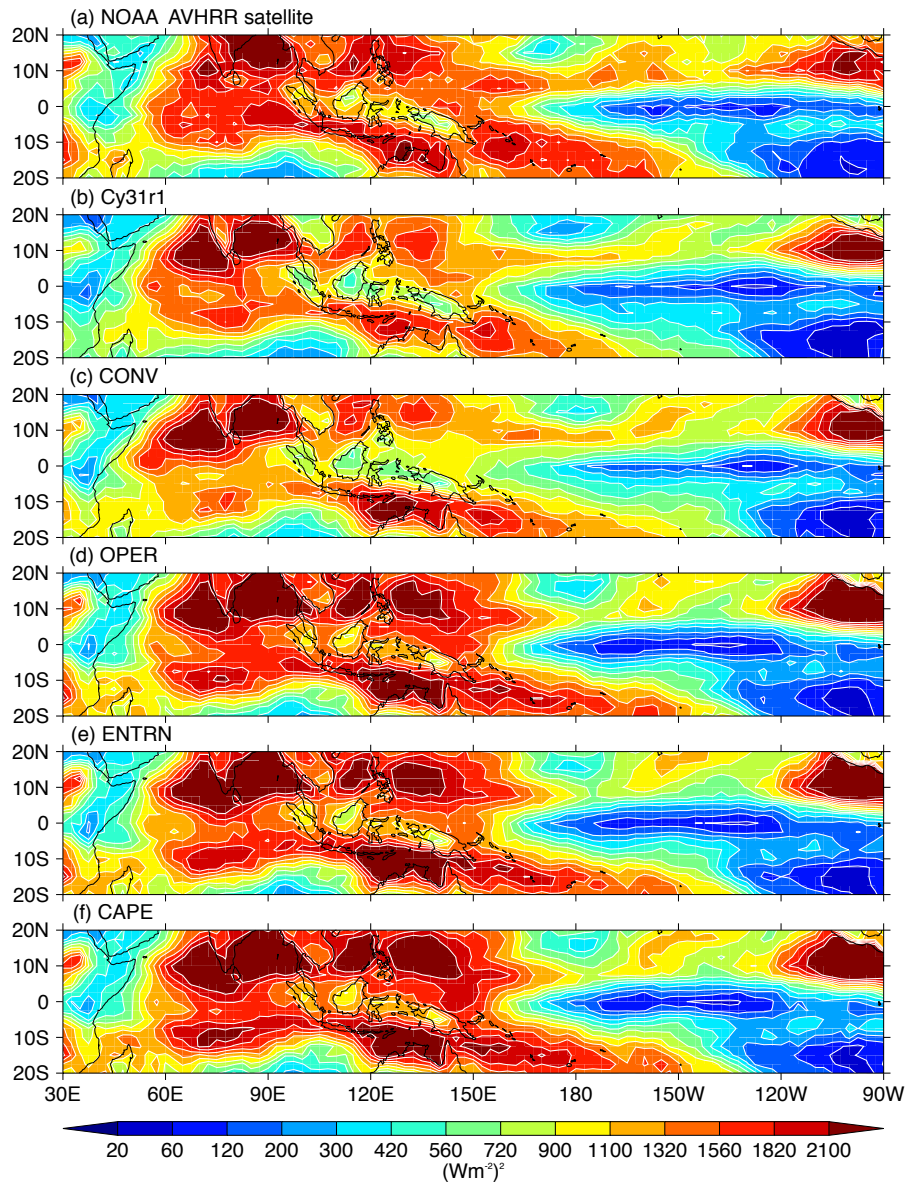
Figure 4.6 *As Fig. 4.5, but at 5-day forecast lead time.*

Comparing CAPE and OPER suggests that the overestimation by OPER north of the equator in the South China and Philippine Seas, and south of the equator in the Australian monsoon region and SPCZ, are consequences of the introduction of the new variable formulation for the CAPE adjustment timescale (τ). A further effect of reverting to a constant τ is that the representation of the minimum in convective activity over the Indonesian islands is slightly improved, although compared with observations, there is still too much variability over the islands (Figs. 4.5 (a),(d) and (f)). Halving the organised entrainment rate has little impact on the variability of convective activity- the overestimations in OPER are slightly amplified in ENTRN (Figs. 4.5 (a),(d) and (e)).

At a 5-day forecast lead time, the longest lead time at which the comparisons between the
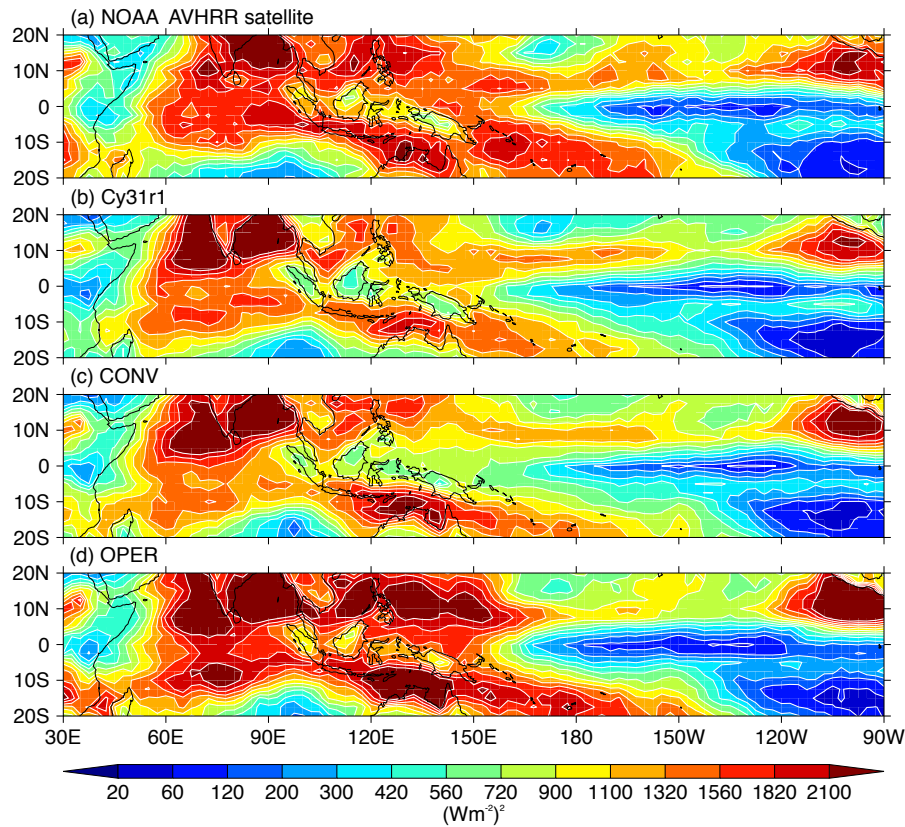
Figure 4.7 *As Fig. 4.5, but at 10-day forecast lead time for (a) NOAA AVHRR satellite data and Cy31r1, CONV, OPER (b)-(d).*

hindcast experiments can be made, all IFS versions exhibit an increase in convective variability compared with a 1-day forecast lead time. An overestimation of OLR variability in the northern Indian Ocean and Australian monsoon region is evident in all IFS versions (Fig. 4.6). Comparing OPER and CONV, it is evident that at longer forecast lead times the effect of the Cy32r3 convection scheme is to further increase convective variability north of the equator in the South China and Philippine Seas as well as in the eastern Pacific, while south of the equator the most prominent increases are in the Indian Ocean and Australian monsoon region. This results in a significant overestimation of convective activity in those regions. The local reduction in convective variability over the Indonesian islands is less well defined with the introduction of the Cy32r3 convection scheme (Figs. 4.6 (a),(c) and (d)). The spatial distributions and magnitudes of convective variability in CAPE, ENTRN and OPER are similar to each other and distinct from Cy31r1 and CONV. This suggests that the relative-humidity-dependent entrainment formulation, used in CAPE, ENTRN and OPER, and not used in Cy31r1 or CONV, is the more dominant of the two modifications to the convective parameterization scheme. Changing the rate of the organised entrainment, derived from a comparison between OPER and ENTRN, has little effect on the variance of convective activity.

At the longer forecast lead times the new formulation for τ does not have a significant impact on the simulation of convective activity in the tropics- CAPE and OPER exhibit similar behaviour.

After 10 days of the forecast, CONV, with the pre-Cy32r3 convection scheme, overestimates the amount of convective variability in the Arabian Sea and Bay of Bengal, and underestimates the variability in the equatorial Indian Ocean, South China and Philippine Seas, Australian monsoon region and SPCZ (Figs. 4.7 (a) and (c)). OPER, with the post-Cy32r3 convection scheme, overestimates the convective variability throughout the Indian Ocean (Figs. 4.7 (a) and (d)). Therefore, Figs. 4.5, 4.6 and 4.7 show that the dominant impact of the modified Cy32r3 convection scheme is to increase the variability of convective activity in the Indo-Pacific region.

4.4.2 Space-time power spectrum

A further diagnostic proposed by Waliser *et al.* (2009), to assess the ability of an NWP model to simulate MJO activity is wavenumber-frequency spectra. Single-field wavenumber-frequency spectra for equatorially averaged (10°N - 10°S) OLR and 850 hPa zonal wind are shown in Figs. 4.8 and 4.9, respectively. The spectra are calculated by applying a Fourier transformation to a 365-day timeseries (from May 2008 to April 2009) and forming power, resulting in a bandwidth of (365 days)$^{-1}$. By construction, positive wavenumbers and frequencies represent eastward propagation. For westward propagation to be identified, either the wavenumber or frequency must be negative. Horizontal dashed lines have been added to the diagrams at 20 and 80 days to highlight the typical period of the MJO. If there is equal power in the eastward and westward directions, then a standing oscillation is present.

The satellite-derived AVHRR OLR and 850 hPa ERA-Interim reanalysis show that there is a concentration of power at 20-80 day periods and eastward-propagating zonal wavenumber 1-3, consistent with the intraseasonal frequency and propagation characteristics of the MJO. At 20-80 day periods the eastward power in OLR and 850 hPa zonal wind are approximately 5 and 3 times the westward power, respectively. Both eastward and westward power are evident at higher frequencies in the OLR (850 hPa zonal wind), although the eastward (westward) power is slightly stronger (Figs. 4.8 (a), 4.9 (a)). This indicates the existence of standing oscillations and lower-frequency propagating features.

The equivalent wavenumber-frequency spectra of equatorially averaged OLR from the control IFS versions and the hindcast experiments are shown in Figs. 4.8 (b)-(n). At a 1-day forecast lead time, all versions of the IFS exhibit a concentration of power at 20-80 day periods and zonal wavenumber 1, the intraseasonal frequency and spatial scales of the MJO. However, at these fre-
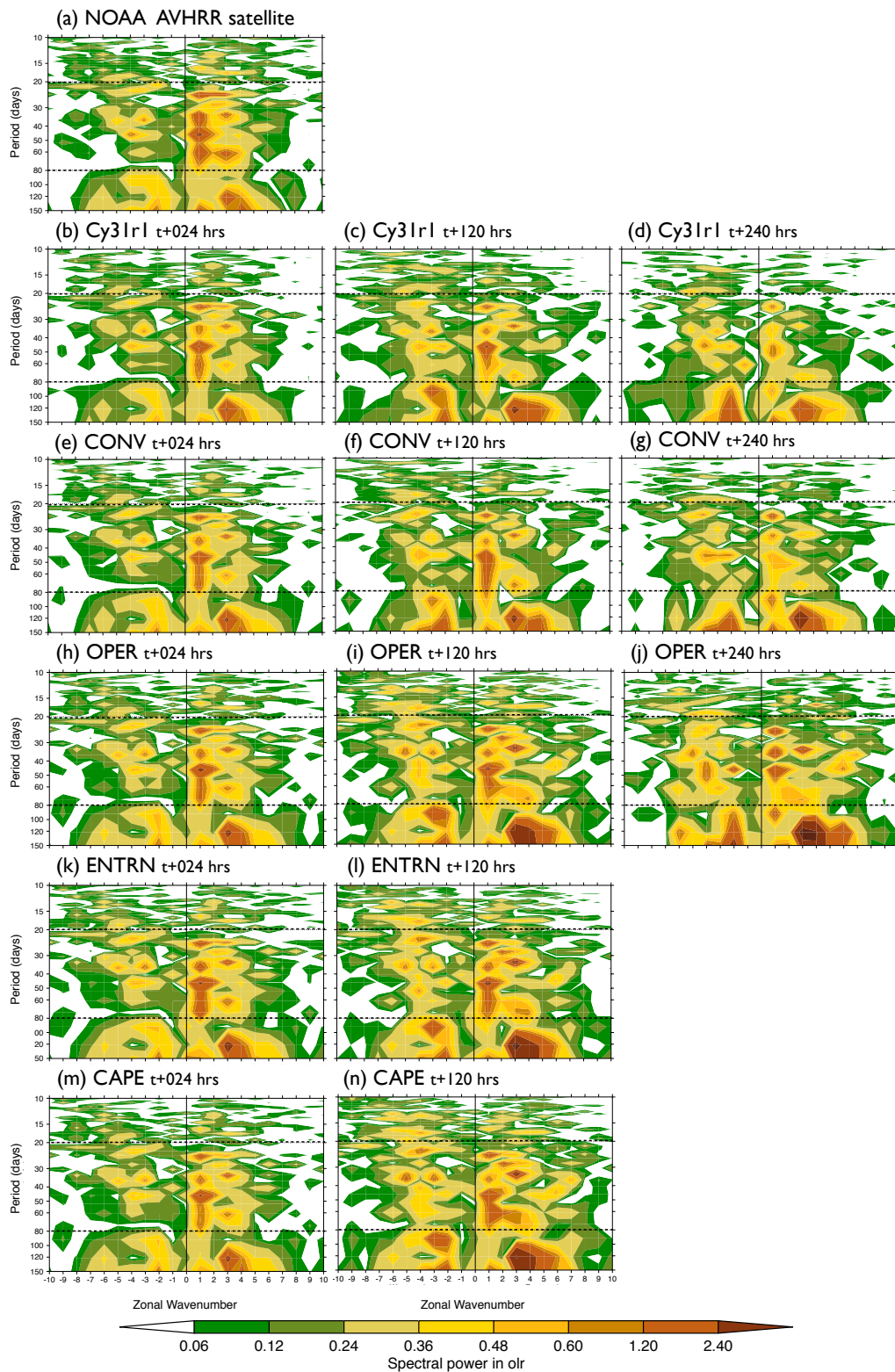
Figure 4.8   *Space-time power spectra in equatorially averaged (10°N - 10°S) OLR for (a) NOAA AVHRR satellite data, (b)-(j) Cy31r1, CONV and OPER at 1-, 5- and 10-day forecast lead time, (k)-(n) ENTRN and CAPE at 1- and 5-day forecast lead time. Eastward and westward propagation are represented by the right and left hand side of the diagrams, respectively.*

quencies the modelled power is weaker than the observed power (Figs. 4.8 (b),(e),(h),(k) and (m)). At a 5-day forecast lead time there is a consistent overestimation, compared with observations, of power in low-frequency westward- and eastward-propagating wavenumbers. The impact of the Cy32r3 convection scheme at a 5-day forecast lead time (comparing Figs. 4.8 (f) and (j)) is to increase the power in low-frequency eastward-propagating wavenumbers, and slightly increase the power in the MJO signal and intraseasonal westward-propagating wavenumbers. Since Figs. 4.8 (i) and (n) are very similar, it can be deduced that the impacts of the Cy32r3 convection scheme described above are almost exclusively due to the new relative-humidity-dependent formulation for organised entrainment, with the variable τ having little effect. Figs. 4.8 (i) and (l) are also similar, suggesting that the simulated MJO is not sensitive to halving the organised entrainment rate. At a 10-day forecast lead time, those models with the pre-Cy32r3 convection scheme (Cy31r1 and CONV) exhibit a distinct weakening of the power in the intraseasonal frequencies associated with the MJO. The Cy32r3 convection scheme (OPER) is able to maintain the power of the eastward-propagating intraseasonal frequencies at a 10-day forecast lead time, although the power of the westward-propagating intraseasonal frequencies also increases, and is stronger than observed (Figs. 4.8 (d),(g) and (j)).

In Fig. 4.9, the power in the 850 hPa zonal wind across the whole spectrum of frequencies is much weaker than that of OLR. At a 1-day forecast lead time all versions of the IFS reproduce the power in the eastward-propagating intraseasonal frequencies associated with the MJO (Figs. 4.9 (b),(e),(h),(k) and (m)), although they all slightly underestimate its magnitude compared with the ERA-Interim reanalysis (Fig. 4.9 (a)). At a 5-day forecast lead time, in models without the new relative-humidity-dependent formulation for organised entrainment (Cy31r1 and CONV), the magnitude of the MJO-related power is reduced. Halving the rate of the organised entrainment (ENTRN), and reverting back to a constant CAPE adjustment timescale (CAPE) have little effect on the MJO-related power in 850 hPa zonal wind (comparing Fig. 4.9 (i) with Figs. 4.9 (l) and (n)). This suggests that, in terms of MJO-related power in 850 hPa wind, the change to the entrainment dominates the change to the CAPE timescale. Furthermore, the comparison with ENTRN suggests that the underlying formulation of entrainment is more important than the rate of entrainment for reproducing the correct MJO-related power. At a 10-day forecast lead time in models with a pre-Cy32r3 convection scheme (Cy31r1 and CONV), the MJO-related power in 850 hPa zonal wind has decreased in magnitude (Figs. 4.9 (d) and (g)), similar to the power of OLR. With the Cy32r3 convection scheme (OPER), the eastward-propagating intraseasonal power signal in the lower-tropospheric zonal wind is maintained throughout the 10-day forecast (Fig. 4.9 (j)).
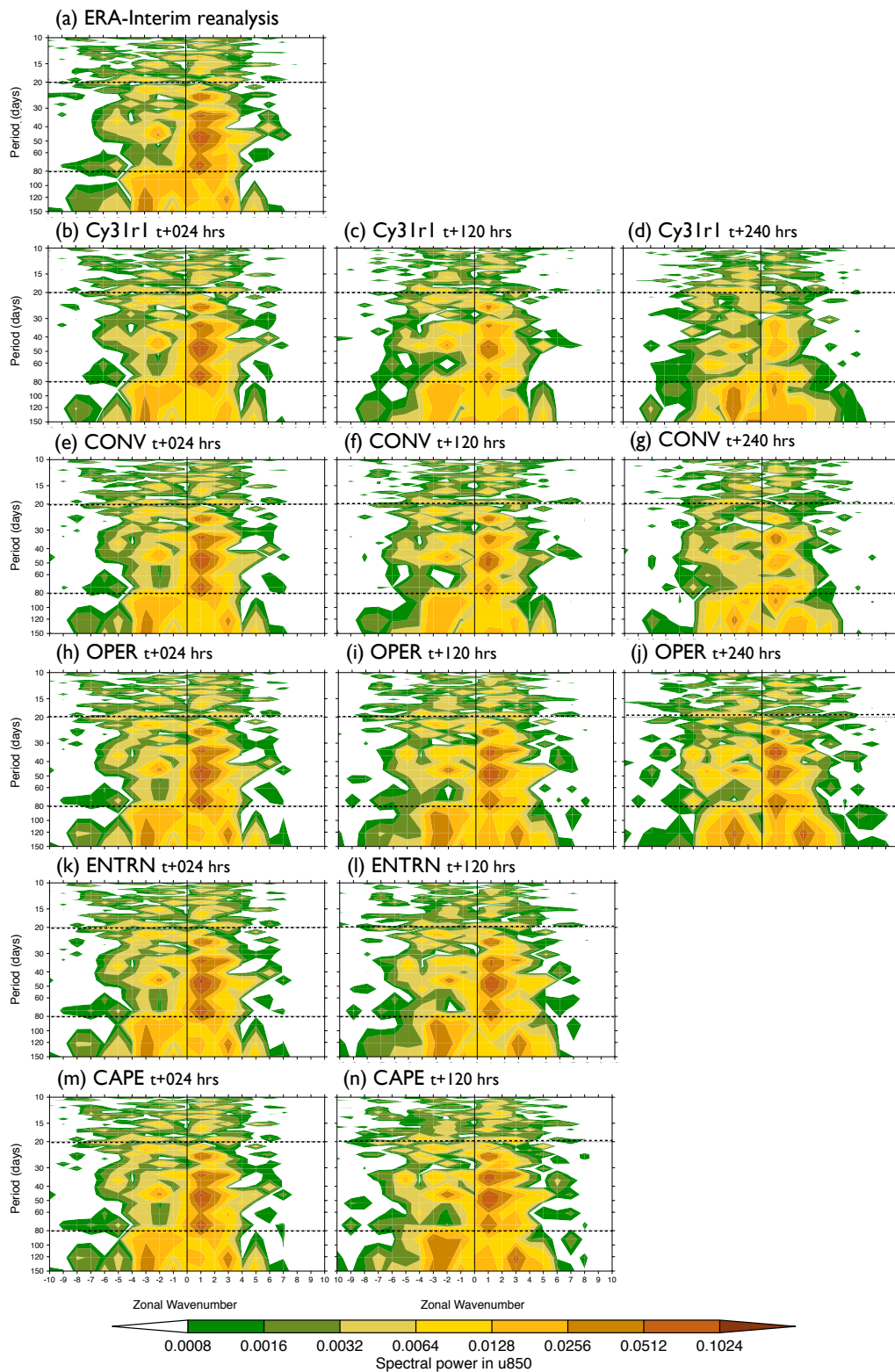
Figure 4.9 *As Fig. 4.8, but for 850 hPa zonal wind compared with (a) ERA-Interim reanalysis.*

Figs. 4.8 and 4.9 show that, with the Cy32r3 convection scheme, the eastward-propagating intraseasonal power signal in OLR and 850 hPa wind associated with the MJO is maintained at longer forecast lead times. It is clear that the relative-humidity-dependent organised entrainment

rate is responsible for nearly all of this improvement; the new variable CAPE timescale has little effect. It is also clear, from comparison with ENTRN, that this result is not sensitive to the rate of organised entrainment, but the dependence of the entrainment rate on relative humidity rather than moisture convergence.

4.4.3   Multivariate MJO Index

Wheeler and Hendon (2004) defined a seasonally independent, real-time multivariate index for the MJO. As a widely used measure of MJO activity, which featured in the diagnostic study by Waliser *et al.* (2009), this index forms an important tool for model evaluation and inter-comparison. The index is based on the first two combined EOFs of near-equatorially averaged OLR, and zonal winds at 850 hPa and 200 hPa.
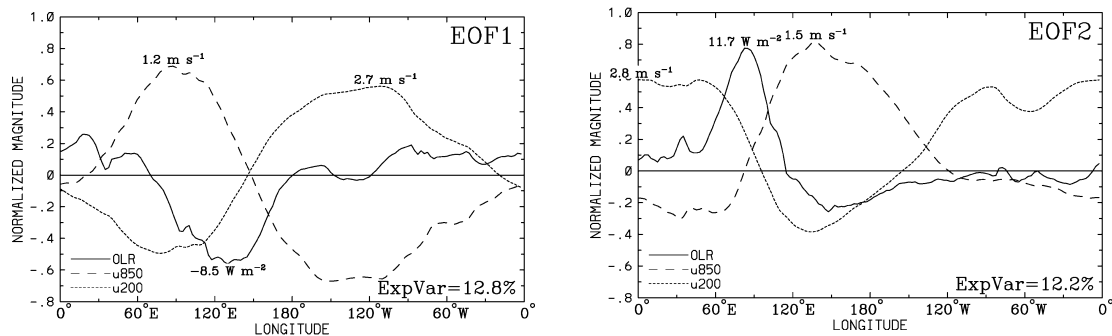
Figure 4.10   *The spatial structure of the Wheeler and Hendon (2004) combined EOFs of OLR and zonal winds at 850 hPa and 200 hPa. Fields are equatorially averaged between 15°N and 15°S. The variance explained by EOF1 and EOF2 is 12.8 % and 12.2 %, respectively. Reproduced from Wheeler and Hendon (2004).*

Fig. 4.10 shows the spatial structures of the first two EOFs of the combined fields, which together account for 25 % of the total variance. It is important to construct a physical interpretation of the EOFs. The positive (negative) phase of EOF1 describes enhanced (suppressed) convection over the Maritime Continent with low-level westerlies behind the convective centre and low-level easterlies ahead of it; winds in the upper-troposphere are in the opposite direction to the low-level winds. The positive (negative) phase of EOF2 describes enhanced (suppressed) convection over the West Pacific and suppressed (enhanced) convection over the Indian Ocean.

The projection of daily model or observed data, with components of seasonal and interannual variability removed, onto the two combined EOFs produces two principal component timeseries, referred to by Wheeler and Hendon (2004) as the Real-time Multivariate MJO series 1 (RMM1) and 2 (RMM2), which vary on intraseasonal timescales. The RMM indices locate the region of enhanced convection associated with the MJO, and, plotted in RMM phase space, the propagation

of individual events. Fig. 4.11 shows the evolution of the April 2009 MJO event highlighted in the filtered Hövmuller diagrams in Figs. 4.1- 4.3. The amplitude increases with distance from the origin; eastward propagation is represented as anti-clockwise rotation around the diagram. Weak MJO activity is defined as when the RMM amplitude is inside the unit circle. This case study is analysed in more detail in §4.5.
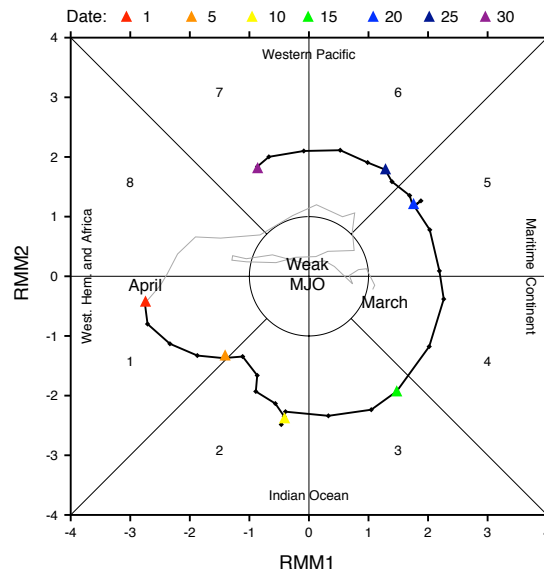
Figure 4.11 *RMM1 and RMM2 of satellite-derived OLR and NCEP reanalysis zonal winds at 850 hPa and 200 hPa for a strong MJO event in April 2009, taken from Wheeler (2009). The black (grey) line indicates the evolution of MJO activity during April (March). Coloured triangles represent the date in April. Text labels indicate the approximate location of the enhanced convective signal of the MJO.*

The multivariate MJO index described above is used to evaluate the skill of the control IFS versions and hindcast experiments to simulate MJO activity through the YOTC period. The procedure followed by Wheeler and Hendon (2004) prior to calculating their EOFs is replicated here. Before projecting the model data onto the observed EOFs, the fields are equatorially averaged (15°S - 15°N) and the seasonal cycle is removed by calculating daily anomalies of OLR and zonal winds at 850 hPa and 200 hPa relative to the 1990-2007 climatology. Interannual variability associated with the ENSO cycle is removed by applying a 120-day running mean to the daily anomalies. The observational multivariate MJO index is taken from data made available by Wheeler (2009). It is constructed using AVHRR satellite-derived OLR and 850 hPa and 200 hPa zonal wind from the National Center for Environmental Prediction (NCEP) reanalysis. The RMM amplitude[2] of the MJO from May 2008 to April 2009 is plotted at 1- , 5- and 10-day forecast lead times in Figs. 4.12, 4.13 and 4.14, respectively.

---

   [2] $\sqrt{(RMM1^2) + (RMM2^2)}$

t + 024 hrs

	Mean		
– – – Obs	1.31123		
······· ERA Interim	1.30669		
······· OPER analysis	1.29099		

	Mean	r (Obs)	r (ERA Interim)
—— Cy 31r1	1.24791	0.874009	0.989069
—— CONV	1.25901	0.826229	0.977440
—— OPER	1.30030	0.872362	0.992711
—— ENTRN	1.29343	0.838872	0.972929
—— CAPE	1.28387	0.822136	0.969757
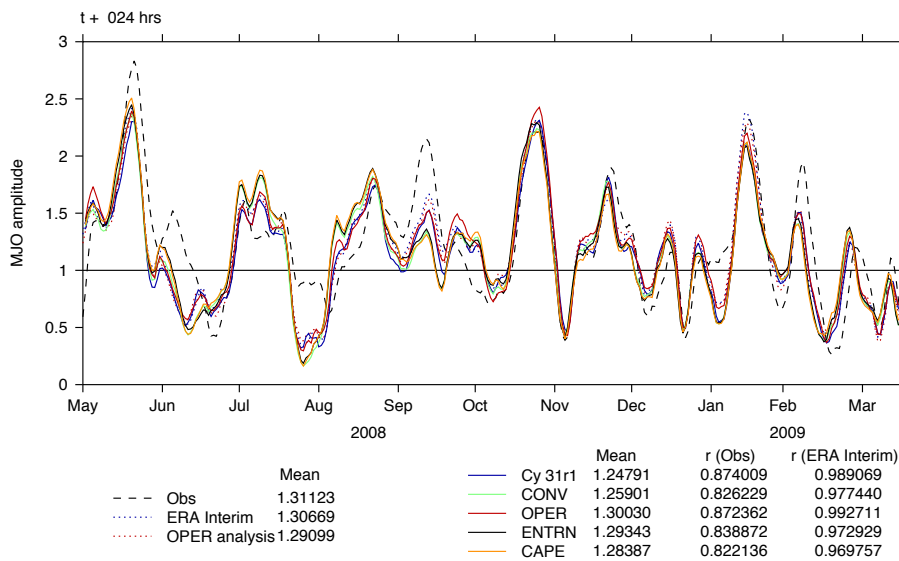
Figure 4.12 *5-day running means of MJO amplitude from May 2008 to April 2009 at a 1-day forecast lead time, plotted on the validation date of the forecast. The mean and correlations with Observations and ERA-Interim are also shown. "Obs" refers to RMM1 and RMM2 calculated using satellite observed OLR and NCEP reanalysis zonal winds.*

The amplitude of the MJO exhibits considerable variability through the YOTC period, with months such as May and October 2008 and January and April 2009 showing very strong MJO activity, and months such as June, August and December 2008 and February and March 2009 showing very little MJO activity (Fig. 4.12). At a 1-day forecast lead time, all the versions of the IFS reproduce the observed peaks in MJO activity, exhibiting correlations above 0.8 (0.95) with respect to observations (ERA-Interim). At such short forecast lead times one would expect the IFS to correlate well with ERA-Interim, since the IFS produces the ERA-Interim reanalysis and the ERA-Interim (or OPER analysis) is used to initialise the model.

At a 5-day forecast lead time, discrepancies between IFS versions become more apparent (Fig. 4.13). The mean MJO activity in all the versions of the IFS has reduced, although some periods of strong activity, such as that in October 2008, remain reasonably accurately simulated. However, during April 2009 there is a distinct loss of amplitude in Cy31r1 and CONV, the pre-Cy32r3 convection scheme versions of the IFS. Those versions with the Cy32r3 relative-humidity-dependent organised entrainment rate (OPER, ENTRN and CAPE) maintain higher mean MJO activity and higher correlations with observations at the longer forecast lead time. With respect to the observations, OPER, ENTRN and CAPE all exhibit linear correlations greater than 0.75 after five days of the forecast. The effect of the relative-humidity-dependent ϵ_{org}^{RH} (variable τ), calculated by subtracting CONV from CAPE (CAPE from OPER), was to increase the correlation of MJO amplitude with respect to the observations by approximately 0.12 (0.06). This measure suggests that both

t + 120 hrs

	Mean			Mean	r (Obs)	r (ERA Interim)
– – – Obs	1.31123		— Cy 31r1	1.08511	0.709564	0.843115
⋯ ERA Interim	1.30669		— CONV	1.13271	0.661997	0.802465
⋯ OPER analysis	1.29099		— OPER	1.22122	0.834905	0.920415
			— ENTRN	1.24895	0.751047	0.781501
			— CAPE	1.27122	0.777176	0.807452
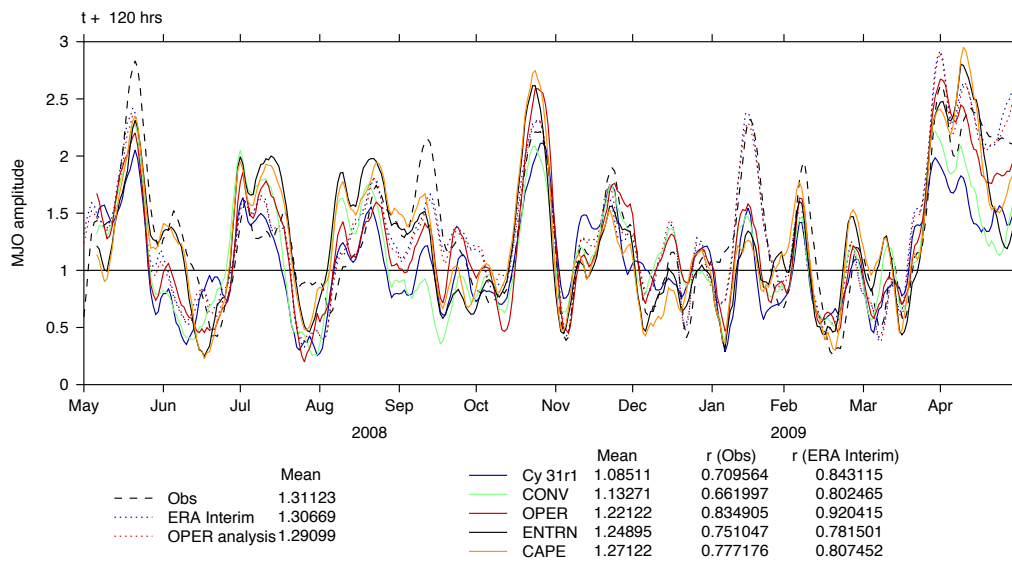
Figure 4.13   *As in Figure 4.12, but at 5-day forecast lead time.*

modifications to the Cy32r3 convection scheme had a positive impact on the simulation of MJO activity, but that the effect of ϵ_{org}^{RH} formulation was stronger than that of τ. However, considering the same calculations for the correlation of the modelled MJO with respect to ERA-Interim reanalysis yields different results; both modifications have a positive impact on the simulation of the MJO, but the τ change dominates the ϵ_{org}^{RH} formulation change.

t + 240 hrs

	Mean			Mean	r (Obs)	r (ERA Interim)
– – – Obs	1.31123		— Cy 31r1	0.984362	0.372088	0.452151
⋯ ERA Interim	1.30669		— CONV	1.05920	0.450247	0.503113
⋯ OPER analysis	1.29099		— OPER	1.18390	0.690831	0.699378
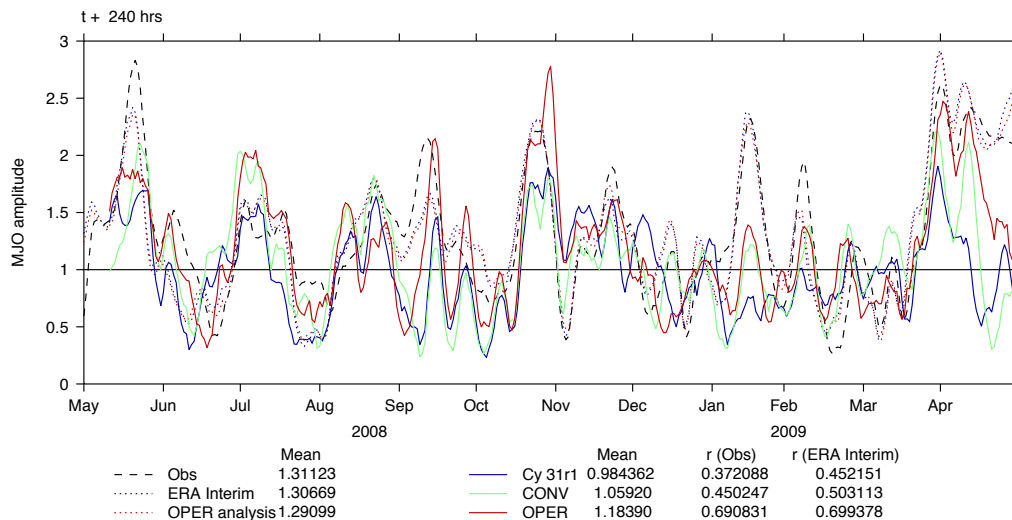
Figure 4.14   *As in Figure 4.12, but at 10-day forecast lead time. The CAPE and ENTRN hindcast experiments do not extend to 10-day forecast lead time.*

Fig. 4.14 shows an equivalent plot to Figs. 4.12 and 4.13 but at a 10-day forecast lead time, where only a comparison of the control IFS versions with the CONV hindcast experiment is possi-

ble. At the longer forecast lead time, Cy31r1 and CONV consistently underestimate the magnitude of MJO amplitude. OPER, with the Cy32r3 convection scheme, is able to maintain the highest mean and correlation scores during the YOTC period. During May 2008 and January and April 2009, OPER underestimates the peak in MJO amplitude, whereas during July and October 2008 it overestimates the magnitude of the peak. This diagnostic indicates the ability of a model to simulate both the active and suppressed phases of MJO activity. It is clear from Figs. 4.12, 4.13 and 4.14 that the introduction of the Cy32r3 convection scheme significantly improved the simulation of MJO amplitude in the IFS.

To evaluate the overall skill of the IFS in predicting the onset and evolution of the MJO, linear correlations are performed between the timeseries of observed EOF1, EOF2 and MJO amplitude and those produced from the IFS at each forecast lead time. In addition, the MJO amplitude timeseries were restricted to days when there was a "strong" MJO in observations (MJO amplitude $\geq$ 1) and the linear correlations repeated (Fig. 4.15) (d)). A forecast is typically considered as skilful if the correlation exceeds 0.6 (e.g. Vitart and Molteni, 2009b), therefore, this threshold has been included in the diagrams.
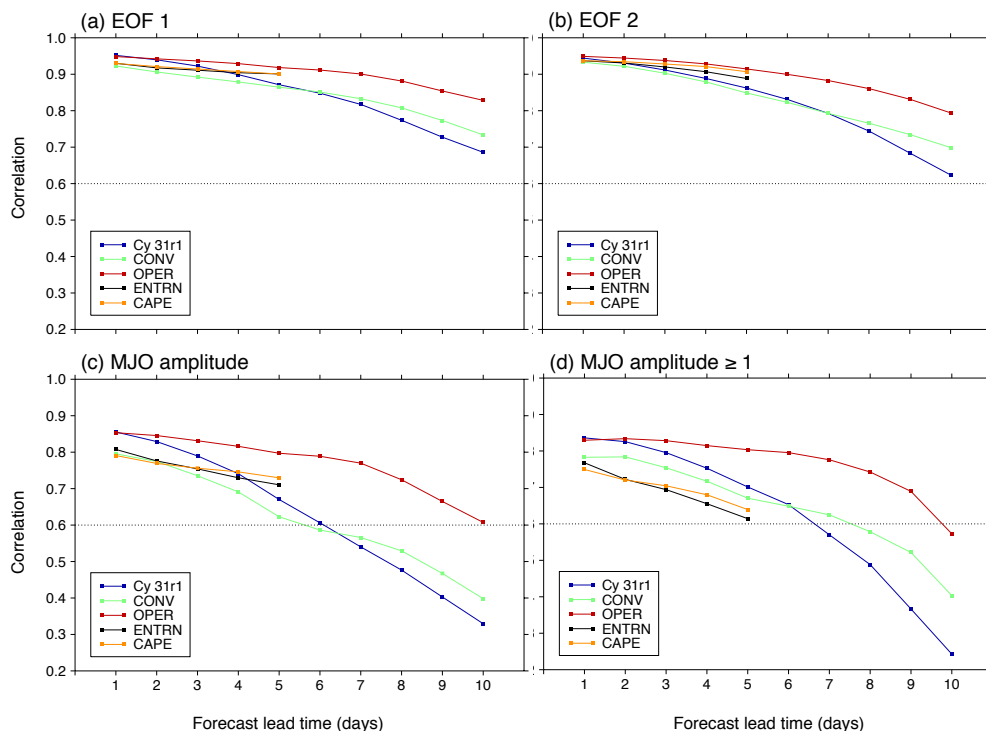
Figure 4.15 *Linear correlations between observed and forecast (a) EOF1, (b) EOF2, (c) MJO amplitude and (d) MJO amplitude $\geq$ 1 as a function of forecast lead time for the period from May 2008 to April 2009. The CAPE and ENTRN hindcast experiments do not extent to a 10-day forecast lead time.*

According to Figs. 4.15 (a) and (b), at a 5-day forecast lead time, ENTRN and CAPE exhibit

similar levels of skill as OPER in predicting EOF1 and EOF2. Cy31r1, CONV and OPER all have skill (correlation > 0.6) in predicting EOF1 and EOF2 at a 10-day forecast lead time. At the longer lead times, the IFS exhibits more skill in predicting EOF1, the positive phase of which describes enhanced convection over the Maritime Continent, than EOF2, the positive phase of which describes enhanced and suppressed convection over the West Pacific and Indian Ocean respectively. This is consistent with previous studies which have shown that the IFS has difficulty propagating the enhanced convection associated with the MJO through the Maritime Continent (e.g. Vitart and Molteni, 2009b). Although slight improvements in skill are apparent between Cy31r1 and CONV at longer forecast lead times, comparing CONV and OPER shows that large improvements in skill can be directly attributed to the Cy32r3 convection scheme. Skilful prediction of the MJO amplitude (MJO amplitude $\geq$ 1) is increased by four (two) days with the introduction of the Cy32r3 convection scheme (Fig. 4.15).
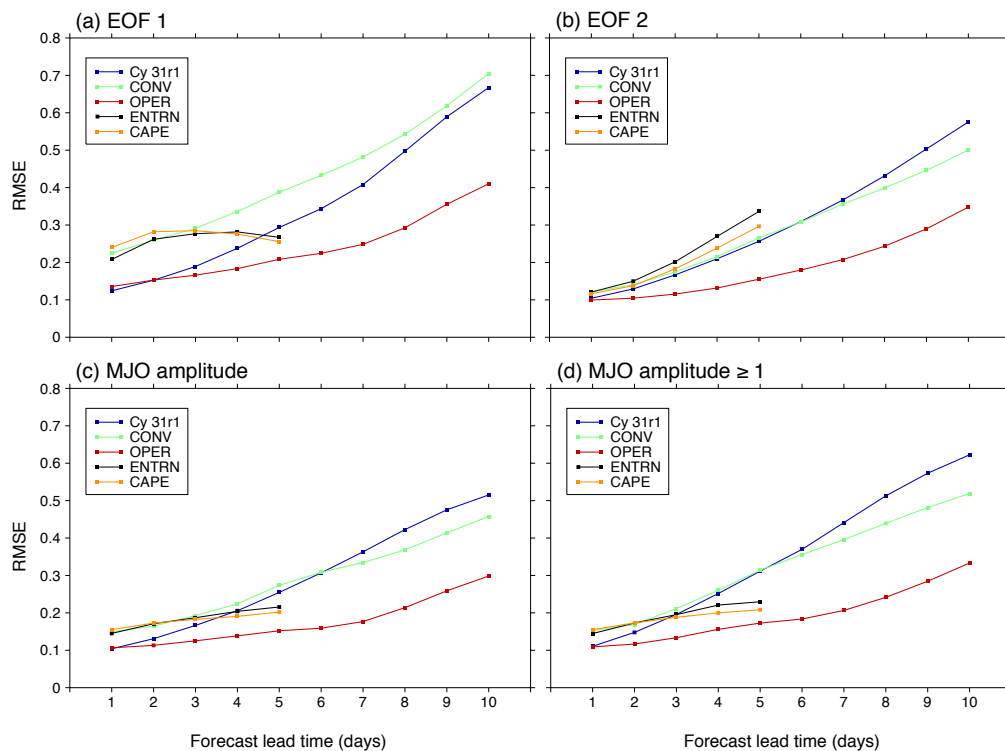
Figure 4.16 *As Fig. 4.15, but for root mean square error (RMSE).*

A further measure of skill used to analyse the performance of the IFS at predicting MJO activity at increasing forecast lead time is the root mean square error (RMSE) which is computed against the same timeseries as in Fig. 4.15 and shown in Fig. 4.16. The RMSE increases with forecast lead time in all versions of the IFS with the exception of the prediction of EOF1 by ENTRN and CAPE, which increases until day 2 then exhibits a slight reduction in RMSE from day 2 to day 5

(Fig. 4.16 (a)). The impact of the Cy32r3 convection scheme is to reduce the RMSE of the MJO metrics by 30-40 %; the RMSE obtained by Cy31r1 and CONV at a 5-day forecast lead time is approximately equivalent to the RMSE obtained by OPER after ten days. Discrepancies between the different versions of the IFS early in the forecast are likely to be spin-up related errors to which the OLR is the major contributor.

4.5 MJO case study analysis

The MJO does not oscillate regularly; it is highly episodic. Although the lifecycle of a canonical MJO event was described in Chapter 2, the location of initiation and propagation characteristics of individual MJO events vary significantly. The NWP approach employed in this thesis allows individual MJO events to be studied in detail and direct comparisons to be made with model simulations. Two case studies have been chosen from the YOTC period: October 2008 and April 2009. Both were identified as periods with strong eastward-propagating anomalies on intraseasonal timescales (e.g. Fig. 4.2) and both exhibit a strong amplitude of the MJO (Fig. 4.12). A further reason for choosing these particular MJO events is that they have been identified as case studies for the Cascade[3] project, which has allowed for interesting comparisons and discussions with colleagues at the University of Reading.

4.5.1 October 2008

Fig. 4.17 shows the observed characteristics of the October 2008 MJO case study. At the end of September 2008, suppressed convective conditions dominated over the eastern Indian Ocean and Maritime Continent.

As the suppressed phase of the MJO propagated eastwards, active convective conditions developed in the eastern Indian Ocean and grew in magnitude (Fig. 4.17 (a)). The intraseasonal zonal wind anomalies from ERA-Interim reanalysis show low-level divergence into the convective anomaly and strong upper-level convergence out of it (Figs. 4.17 (b) and (c)). Strong eastward propagation of the intraseasonal signal of the MJO is evident in the Eastern Hemisphere but only the upper-level signal remains strong in the Western Hemisphere.

The multivariate MJO index described in §4.4.3, which combines all the fields shown in Fig. 4.17, is plotted in RMM phase space for October 2008 in Fig. 4.18. By first considering the observations (Fig. 4.18, black line), made up of the combined EOFs of AVHRR satellite-derived OLR and NCEP reanalysis zonal winds, the growth of the MJO signal in early October in the

---

[3]Cascade is a NERC-funded consortium project focused on studying organised convection in the tropical atmosphere. http://climate.ncas.ac.uk/Cascade
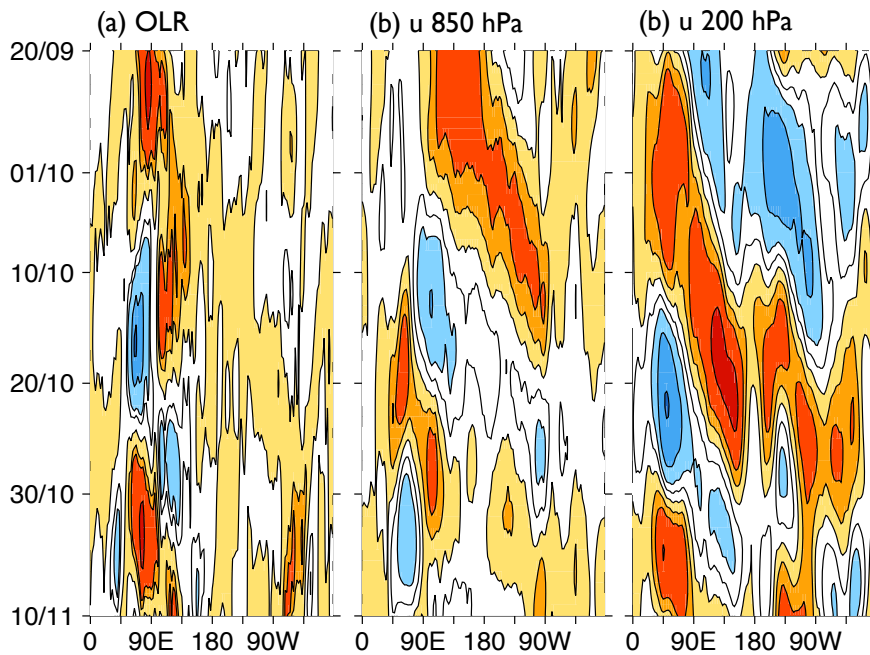
Figure 4.17 *Hövmuller (time-longitude) diagrams of 20-100 day band-pass filtered (a) OLR from the NOAA AVHRR satellite, (b) 850 hPa and (c) 200 hPa zonal wind from ERA-Interim reanalysis for the October 2008 case study. Fields are averaged between 10° N and 10° S. Contour intervals for OLR, 850 hPa and 200 hPa zonal wind are identical to Figs. 4.1, 4.2 and 4.3 respectively.*

eastern Indian Ocean (phase 3 on the diagram) is consistent with the picture described in Fig. 4.17. The magnitude continues to increase as the MJO signal propagates through the Maritime Continent (phases 4 and 5 on the diagram). Then, as in the Hövmuller diagrams of Fig. 4.17, the active phase of the MJO weakens in late October in the West Pacific (phase 6 in the diagram).

All versions of the IFS capture the growth in amplitude and propagation of the enhanced convection through the Maritime Continent. However, the pre-Cy32r3 IFS consistently underestimates the amplitude of the MJO as the convective signal enters the Maritime Continent (phase 3 to 4) and overestimates the amplitude as it enters the West Pacific (phase 5 to 6). The effect of the Cy32r3 convection scheme, which can be identified by comparing CONV and OPER (Figs. 4.18 (b) and (c)), for the October 2008 case study is an increase in the amplitude of the MJO. Therefore, at a 5-day forecast lead time, this results in OPER being able to maintain the amplitude of the MJO in phases 3 and 4, but exacerbates the overestimation of MJO amplitude in phase 5. To extract the contribution from the ϵ_{org}^{RH} and τ modifications in the Cy32r3 convection scheme, comparisons must be made between CONV and CAPE and CAPE and OPER, respectively. The effect of ϵ_{org}^{RH} at longer forecast lead times is to increase (decrease) the amplitude of the MJO in phases 3 and 4 (phase 5), resulting in an overestimation (underestimation) (Figs. 4.18 (b) and (e)). Conversely, the effect of the variable τ at longer lead times is to increase (decrease) the amplitude of the MJO in phase 5
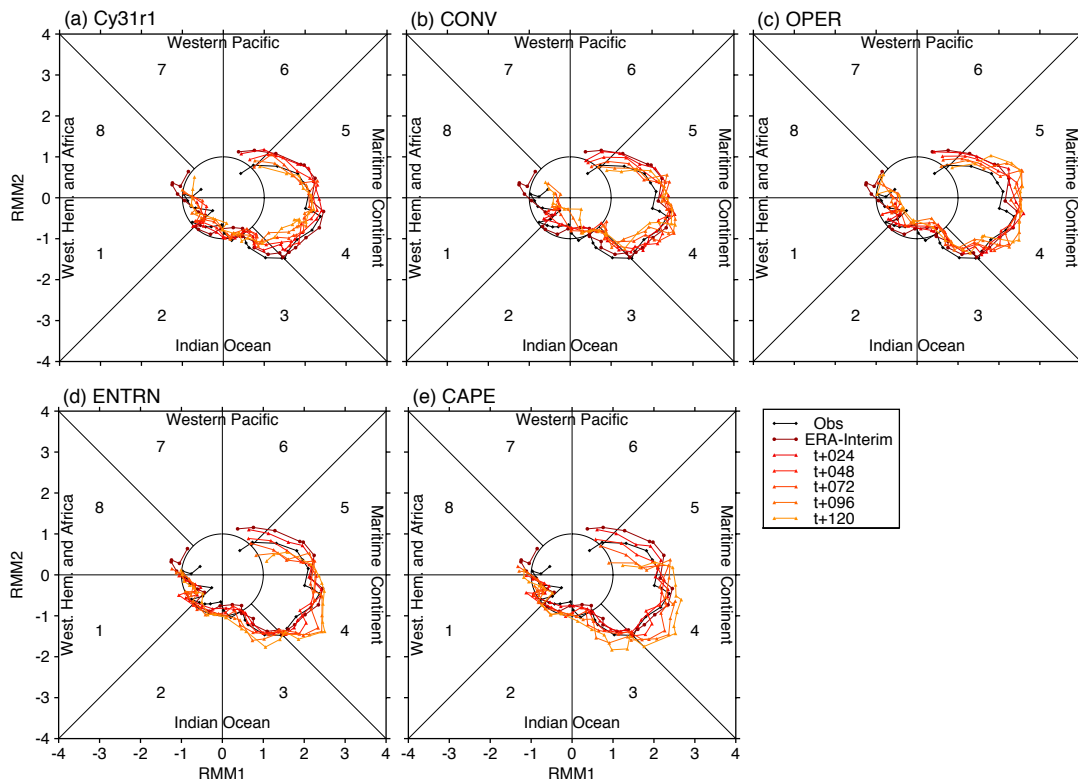
Figure 4.18 *Multivariate MJO index (§4.4.3) for the October 2008 case study from observations (black line), ERA-Interim reanalysis (dark red line) and versions of the IFS plotted on forecast validation date at increasing forecast lead time from 1-day (red line) to 5-days (light orange line). Observations refer to RMM1 and RMM2 calculated using satellite-derived OLR and NCEP reanalysis zonal winds at 850 hPa and 200 hPa.*

(phases 3 and 4) (Figs. 4.18 (c) and (e)).

4.5.2 April 2009

The observed characteristics of the MJO case study in April 2009 are shown in Fig. 4.19. A region of enhanced convection developed in early April in the Indian Ocean; the envelope of convection is preceded and succeeded by suppressed convective conditions.

Compared with the October 2008 case study, the convective signal associated with the MJO in April 2009 developed further west, grew to a stronger magnitude and showed more coherent eastward propagation. Therefore, this event is in better agreement with the canonical MJO described in Chapter 2. Low-level westerlies (easterlies) are evident in the ERA-Interim reanalysis behind (ahead of) the convective envelope, with anomalies of the opposite sign in the upper-troposphere. Compared with the October 2008 case study, the intraseasonal circulation anomalies associated with the April 2009 case study were not only stronger but extended further into the Western Hemisphere with more coherent eastward propagation.
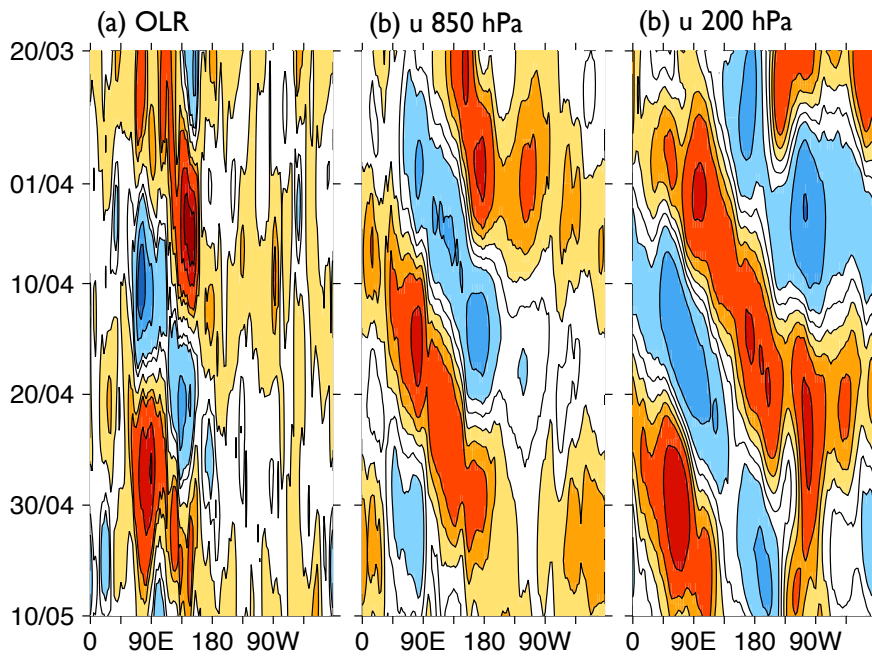
Figure 4.19   *As Fig. 4.17, but for the April 2009 case study.*
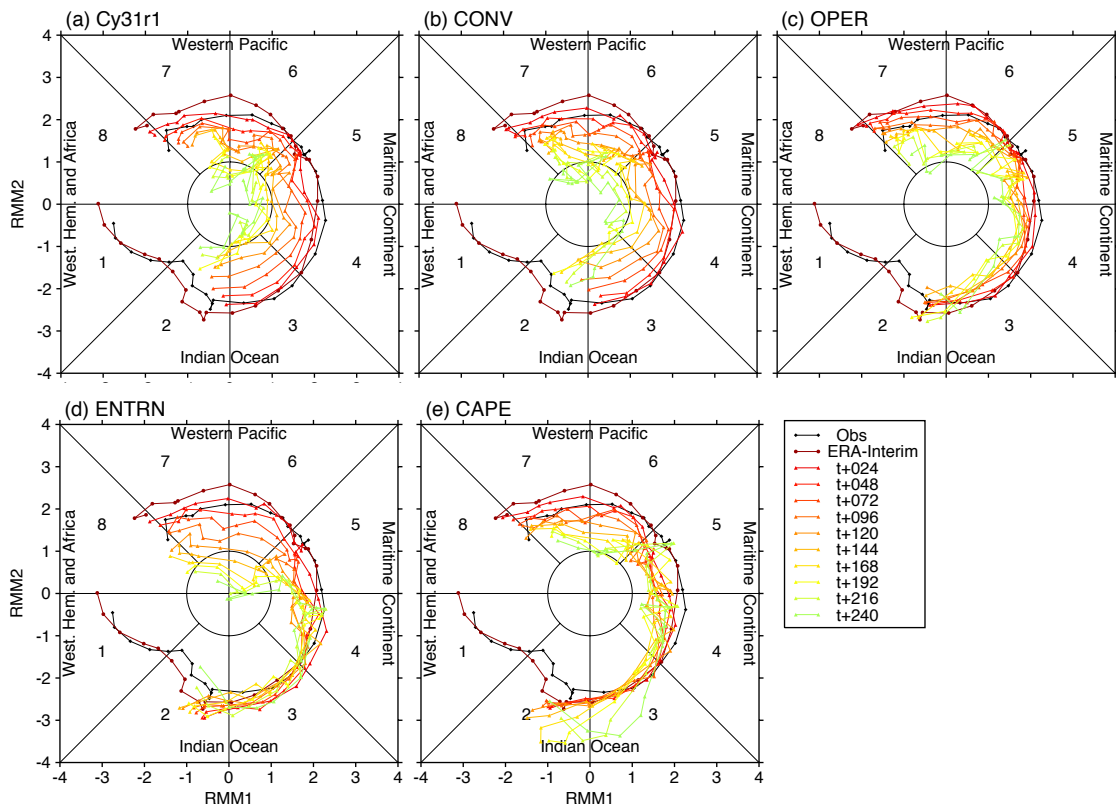
Figure 4.20   *As Fig. 4.18 but for the April 2009 case study and with all versions of the IFS plotted on forecast validation date from 1-day (red line) to 10-day (green line) forecast lead time.*

Since the April 2009 case study was identified as the strongest MJO event during the YOTC period, the hindcast experiments were extended to a 10-day forecast lead time for that month only. The April 2009 case study is plotted in RMM phase space in Fig. 4.20. The strong amplitude and eastward propagation are clear in both the observations (black line) and ERA-Interim reanalysis (dark red line). At the start of April, as the enhanced convection associated with the MJO entered the Indian Ocean, it already had a large amplitude. The amplitude remained large as, during April, the MJO signal propagated across the Indian Ocean, through the Maritime Continent and into the West Pacific. As forecast lead time increases, there is a distinct loss of MJO amplitude in the pre-Cy32r3 convection scheme cycles of the IFS (Cy31r1, CONV; Figs. 4.20 (a) and (b)). At longer forecast lead times, the effect of the new relative-humidity-dependent formulation (ϵ_{org}^{RH}; comparing CONV with CAPE) is to increase the amplitude of the MJO. The most prominent increase in MJO amplitude is in the Indian Ocean, resulting in a large overestimation compared with observations. In the Maritime Continent and West Pacific the increase in MJO amplitude results in a small and large underestimation of MJO activity respectively. The main effect of the variable τ (comparing CAPE with OPER) is to reduce the amplitude of the MJO in the Indian Ocean; there is little impact in other regions. The compensating effects of ϵ_{org}^{RH} and τ which increase and decrease the amplitude of the MJO in the Indian Ocean respectively, mean that at longer forecast lead times, the Cy32r3 convection scheme (comparing CONV and OPER) maintains the observed magnitude of MJO amplitude in that region. However, at longer forecast lead times, in the Maritime Continent, and especially in the West Pacific, the Cy32r3 convection scheme exhibits less skill than in the Indian Ocean in predicting the evolution of the April 2009 MJO.

4.6   Discussion of results

This chapter has described advances in MJO simulation with the introduction of the Cy32r3 convective parameterization. Unique to this thesis is the attribution of those advances to the modified formulation of organised entrainment, which is dependent on relative humidity (ϵ_{org}^{RH}) as opposed to the previous moisture-convergent-dependent formulation (ϵ_{org}^{MC}). Particular results are chosen for discussion and presented below.

4.6.1   Convective versus dynamical signal of the MJO

The comparison between the control versions of the IFS (§4.3) suggests that, at short forecast lead times, both Cy31r1 and OPER are able to reproduce anomalous, eastward-propagating signals in the OLR and zonal wind associated with the MJO (Figs. 4.1, 4.2 and 4.3). At a 10-day forecast lead time, however, OPER consistently maintains the intraseasonal MJO signal better than

Cy31r1. The large-scale dynamical signal of the MJO (Figs. 4.2 and 4.3) is better preserved at a 10-day forecast lead time in OPER than the associated convective signal (Fig. 4.1). The convective and large-scale circulation signals associated with the MJO are widely considered to be strongly coupled; however, this result implies that there is a lack of coherence between the convection and dynamical overturning in the IFS as forecast lead time increases. This characteristic of the IFS prompts the question of whether the model is producing an MJO-like signal for the wrong reasons. The diagnostics applied in this chapter are not capable of answering this question; further analysis is required (§4.6.3). Interestingly, this is not a feature exclusive to the IFS, but is consistent with other studies. Comparing four pairs of coupled and uncoupled global simulations, Zhang *et al.* (2006) showed that the precipitation signal associated with the MJO was much weaker than observed, while the dynamical signal in the zonal winds was stronger than observed, a characteristic common among many global circulation models (Kim *et al.*, 2009).

4.6.2 Reduction of eastward-propagating spectral power
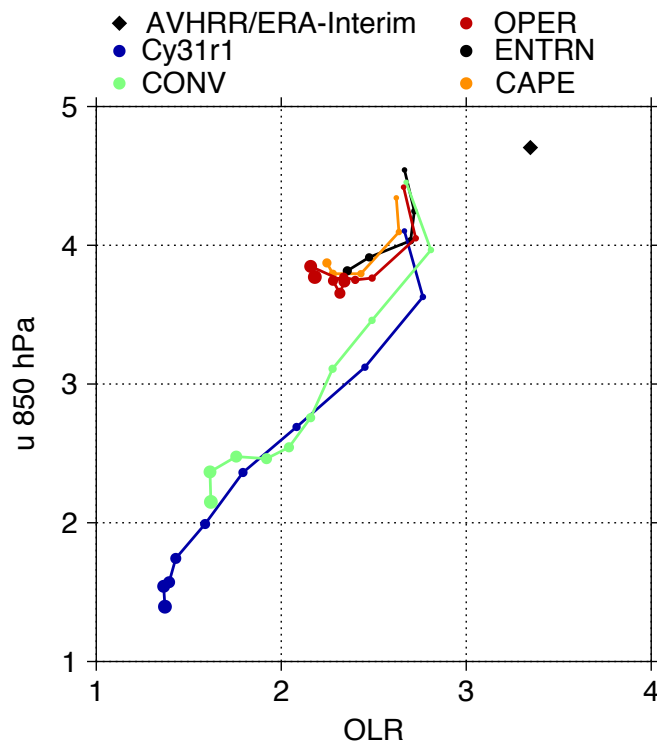
Figure 4.21 *East-west ratio of MJO (20-80 day mode, within wavenumbers 1-3 for OLR and 1-2 for zonal wind) spectral power calculated by dividing the sum of eastward-propagating power by the westward-propagating equivalent. The ratio from AVHRR OLR and ERA-Interim 850 hPa zonal wind (black diamond) is referred to as observations and is compared to all of the versions of the IFS described in §3.5.2. Lines (and increasing dot size) refer to increasing forecast lead time up to 5 days for CAPE and ENTRN (orange and black lines) and 10 days for Cy31r1, CONV and CAPE (blue, green and red lines).*

The advances in MJO simulation described in this chapter can be summarised using a metric derived from the wavenumber-frequency spectra discussed in §4.4.2. Fig. 4.21 shows the east-west ratio of MJO spectral power, defined as the 20-80 day mode within wavenumbers 1-3 for OLR and 1-2 for 850 hPa zonal wind. In observations (AVHRR OLR and ERA-Interim 850 hPa zonal wind), the east-west power is 3-4 for OLR and 4-5 for zonal wind. Since the forecasts are initiated from ERA reanalysis, unsurprisingly all versions of the IFS exhibit equivalent east-west ratios of zonal wind to ERA-Interim (4-5). The forecast east-west ratios of OLR, however, are significantly reduced (2-3) compared with observations (3-4). As forecast lead time increases, versions of the IFS with ϵ_{org}^{RH} (OPER, CAPE and ENTRN; red, orange and black lines) maintain a higher east-west ratio than those with ϵ_{org}^{MC} (Cy31r1 and CONV; blue and green lines), which are reduced significantly by a 10-day forecast lead time. Therefore, Fig. 4.21 shows that, with the modified formulation of organised entrainment, the IFS is able to maintain the eastward-propagating spectral power of the MJO at longer forecast lead times. Using a similar metric, studies have shown that a smaller-than-observed east-west ratio of MJO spectral power is a common feature among most of the CMIP3 models (Lin *et al.*, 2006) and state-of-the-art climate models (Kim *et al.*, 2009).

4.6.3 Motivation for a new generation of diagnostics

While the diagnostics applied in this chapter, and metrics such as that in Fig. 4.21, can highlight deficiencies in the ability of numerical models to simulate the MJO, they cannot alone provide insight into the physical mechanisms responsible. This has led to the recognition that more process-based diagnostics should be applied to simulations of the MJO (e.g. Zhu *et al.*, 2009, Kim *et al.*, 2009). The discussion and application of such diagnostics will be the subject of Chapter 6.

4.7 Conclusions

This chapter has focused on the representation of the MJO in the control versions of the IFS (Cy31r1 and OPER) and the hindcast experiments (CONV, ENTRN and CAPE) both during the YOTC period as a whole and for individual MJO case studies during this period. The hindcast sets performed in this study present a unique opportunity to attribute changes in the simulation of the MJO to individual model modifications. Previously, Bechtold *et al.* (2008) has shown significant advances in the simulation of MJO-related variability in Cy32r3 of the IFS compared with its predecessor Cy32r2. However, the analysis carried out here has quantified to what extent those advances in the simulation of the MJO in Cy32r3 can be directly attributed to the modified parameterization of convection. Furthermore, the hindcast experiments have been designed to identify the effects of individual components of the modified convective parameterization on the representation of the

MJO.

Established MJO diagnostics have been applied to the model simulations to assess the ability of all the versions of the IFS to predict the onset and evolution of the MJO. The diagnostics used in this study form part of the MJO Simulation Diagnostics (MSD) set presented by CLIVAR (Waliser *et al.*, 2009). When evaluating the ability of a model to represent MJO-related variability, it is important to be consistent in the diagnostics applied. That consistency enables a thorough characterisation of the representation of the MJO, meaningful model intercomparisons, and an understanding of where the IFS fits into the wider MJO modelling efforts. A band-pass filtering technique has been applied to the control versions of the IFS to extract variability on the intraseasonal timescales of the MJO (§4.3). More complex techniques, such as wavenumber-frequency spectrum decomposition (§4.4.2) and multivariate EOF analysis (§4.4.3), have been applied to the hindcast sets. Comparisons have been continually made with observations and reanalysis data (§4.2).

Although both Cy31r1 and OPER are able to reproduce the eastward-propagating, intraseasonal signal of the MJO at a 1-day forecast lead time (Figs. 4.1, 4.2 and 4.3), Cy31r1 underestimates the variance in convective activity across the equatorial Indo-Pacific region. OPER is able to reproduce the observed variance of convective activity on the intraseasonal timescales of the MJO after a 1-day forecast lead time but, because variance increases with increasing lead time, OPER significantly overestimates the convective variance later in the forecast (Fig. 4.4). Although these results give an indication of the evolution of MJO simulation in the IFS, it is only through comparisons with the hindcast sets that specific conclusions can be made about the effect of the Cy32r3 convective parameterization.

The Cy32r3 convective parameterization alone increased the predictive skill of the MJO amplitude during the YOTC period by 4 days (Fig. 4.15 (c)). Additionally, the Cy32r3 formulation of convection increased the variability of convective activity across the entire equatorial Indian Ocean and West Pacific Warm Pool. The variance of convective activity continues to increase with increasing forecast lead time, leading to an overestimation compared with satellite observations (Fig. 4.6). The new relative-humidity-dependent formulation for organised entrainment is responsible for the increase in convective activity associated with the MJO (Figs. 4.6 (c) and (f), and Figs. 4.9 (f) and (l)). The simulation of convective variability is more sensitive to the formulation of entrainment than the rate of entrainment (Figs. 4.6 (c),(d) and (e), and Figs. 4.9 (f),(i) and (l)). Changing to a variable CAPE timescale in the closure for deep convection had little effect on the simulation of the variance of convective activity (Figs. 4.6 (d) and (f), and Figs. 4.9 (i) and (n)). The introduction of the Cy32r3 convective parameterization has led to an overactive MJO in the IFS; cycle 35r3

implemented in October 2009 has been shown to partially solve this problem (Vitart and Molteni, 2009b).

As was highlighted in §2.4.6, an advantage of the NWP approach to studying the MJO is that the specific characteristics of individual events can be examined in model simulations and direct comparisons can be made with observational data. Two MJO case studies during the YOTC period were identified, each displaying very different propagation characteristics. Consistent with the increased convective activity, the relative-humidity-dependent formulation for organised entrainment increased the amplitude of the MJO in all regions. The new variable CAPE adjustment timescale reduced the amplitude of the MJO in the Indian Ocean. Therefore, the impact of the Cy32r3 convective parameterization, a combination of the two effects, was to maintain the amplitude of the MJO at longer forecast lead times. Again, the simulation of the MJO was shown to be more sensitive to the formulation of entrainment than the entrainment rate (Fig. 4.20).

In this chapter, improvements in the simulation of the MJO have been directly attributed to the formulation of convection in Cy32r3, specifically, the relative-humidity-dependent formulation for organised entrainment. The decision to move to a formulation for entrainment that was dependent on relative humidity was motivated by the recognition that environmental moisture is crucial in modulating the location and strength of convective activity on MJO timescales (Redelsperger *et al.*, 2002; Grabowski, 2003; Grabowski and Moncrieff, 2004). While the motivation behind the modified entrainment rate may be clear, the mechanisms through which it led to a better simulation of the MJO are as yet unclear. Therefore, further questions are raised which will be addressed in later chapters:

- What effect does the Cy32r3 convective parameterization have on the mean state of the IFS?

- What are the physical mechanisms in the IFS through which an entrainment rate dependent on relative humidity leads to a better representation of intraseasonal variability?

- How do the improvements in MJO performance, and their attribution to particular elements of the convection scheme, map onto existing theories for the existence and propagation of the MJO?

CHAPTER 5

The Role of the Mean State

5.1 Introduction

The mean state of a model is thought to be important to the dynamics of the MJO (e.g. Ray *et al.*, 2011). Modelling studies have shown that improving the quality of the background state, through flux-adjustment techniques, can lead to a better representation of the MJO (e.g. Inness *et al.*, 2003; Sperber *et al.*, 2005). For example, Inness *et al.* (2003) showed that mean low-level and surface westerlies favour MJO development, a hypothesis confirmed in observations by Zhang *et al.* (2006). Furthermore, the background state of a model is crucial to instability theories of the MJO, such as wave-CISK, where the distribution of low-level environmental moisture defines the growth rate and propagation speed of the MJO.

To understand why the introduction of the modified parameterization of convection in Cy32r3 so dramatically improved the simulation of the MJO, it is important to quantify the impact of the new scheme on the basic state of the model. In an NWP model like the IFS, the basic state is not constant, but evolves with increasing forecast lead-time. The aim of this analysis is to understand whether the new convection scheme has resulted in a favourable background state for the initiation and evolution of the MJO. More specifically, results from the previous chapter show that the relative-humidity-dependent formulation for entrainment is largely responsible for increasing variability on intraseasonal timescales. Therefore, it is important to understand how this new formulation of organised entrainment has changed the mean state of the IFS.

5.2 Mean state

5.2.1 The zonal-mean vertical structure of T, U and q

The initial analysis in this chapter will focus on the zonal-mean structures of temperature, zonal wind and specific humidity. Fig. 5.1 (a) shows the vertical structure of the zonal-mean temperature at a 5-day forecast lead time from OPER. Figs. 5.1 (b)-(e) show the differences between (b) OPER and CONV, (c) CAPE and CONV, (d) OPER and CAPE, and (e) OPER and ENTRN which, re-calling Table 4.1, highlight the effect of the (b) Cy32r3 convective parameterization (ϵ_{org}^{RH} & τ), (c)
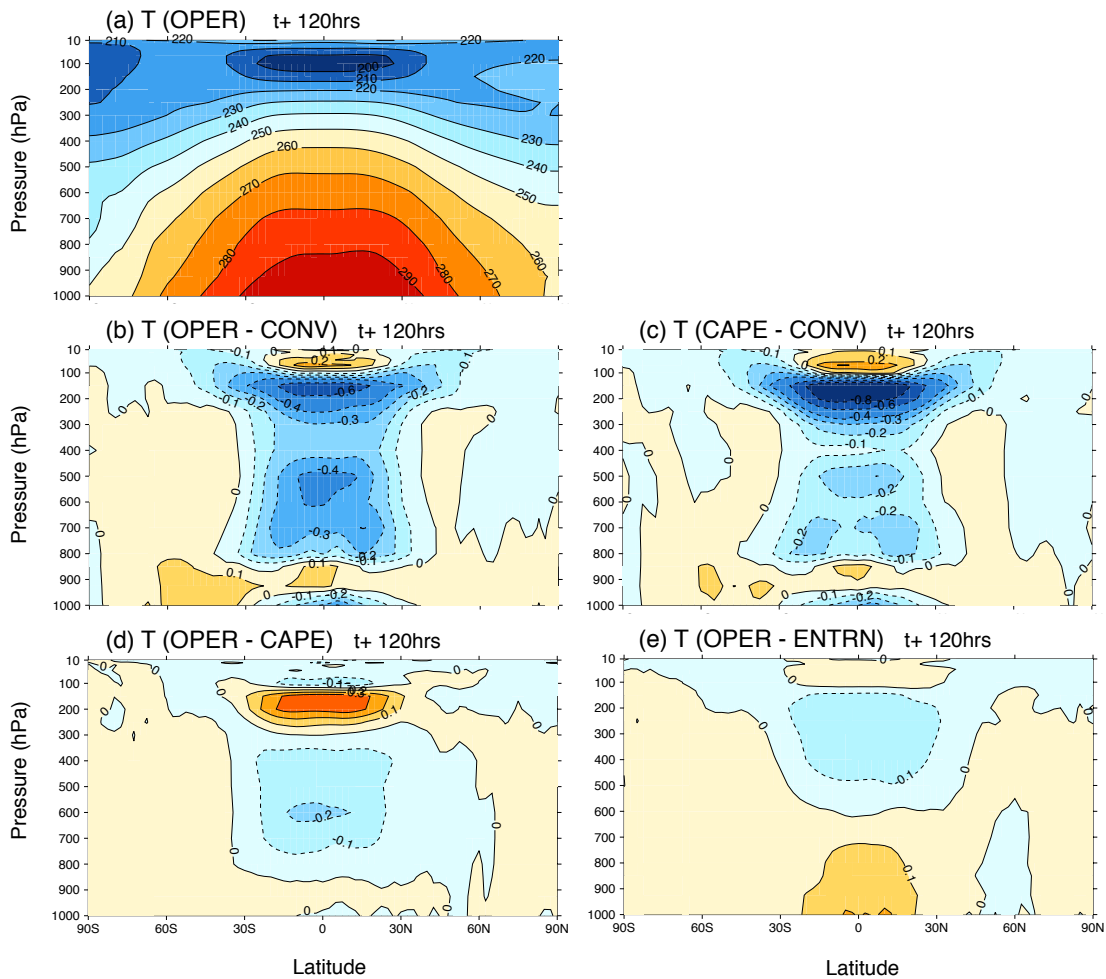
Figure 5.1 *(a) Zonal-mean temperature from OPER at a 5-day forecast lead time. (b) Zonal-mean temperature difference between OPER and CONV (effect of Cy32r3) at a 5-day forecast lead time. (c)-(e) as in (b) but difference between (c) CAPE and CONV (effect of ϵ_{org}^{RH} formulation), (d) OPER and CAPE (effect of τ), and (e) OPER and ENTRN (effect of ϵ_{org}^{RH} rate). The zonal mean is calculated for the period from May 2008 to April 2009 using all longitudes.*

ϵ_{org}^{RH} formulation, (d) τ and (e) ϵ_{org}^{RH} rate respectively. Fig. 5.1 (b) shows that the effect of the modified convective parameterization in Cy32r3 is to cool the depth of the troposphere between 30°S and 30°N, with the exception of a thin layer between 950 hPa and 850 hPa. The largest cooling, of about 0.6K, occurs in the tropical upper-troposphere between 100 hPa and 200 hPa. The Cy32r3 convective parameterization warms the tropical stratosphere between 20°S and 20°N by up to 0.2K. The cooling suggests that there is, on average, less convection penetrating into the upper-troposphere in the post-Cy32r3 IFS. The magnitude of the temperature anomalies is relatively small, indicative of the homogeneous distribution of temperature in the tropics. The spatial structure of the difference in zonal-mean temperature in Fig. 5.1 (c) is similar to that in Fig. 5.1 (b), suggesting that the cooling throughout the tropical troposphere is a consequence of the ϵ_{org}^{RH} formulation. In the mid- and
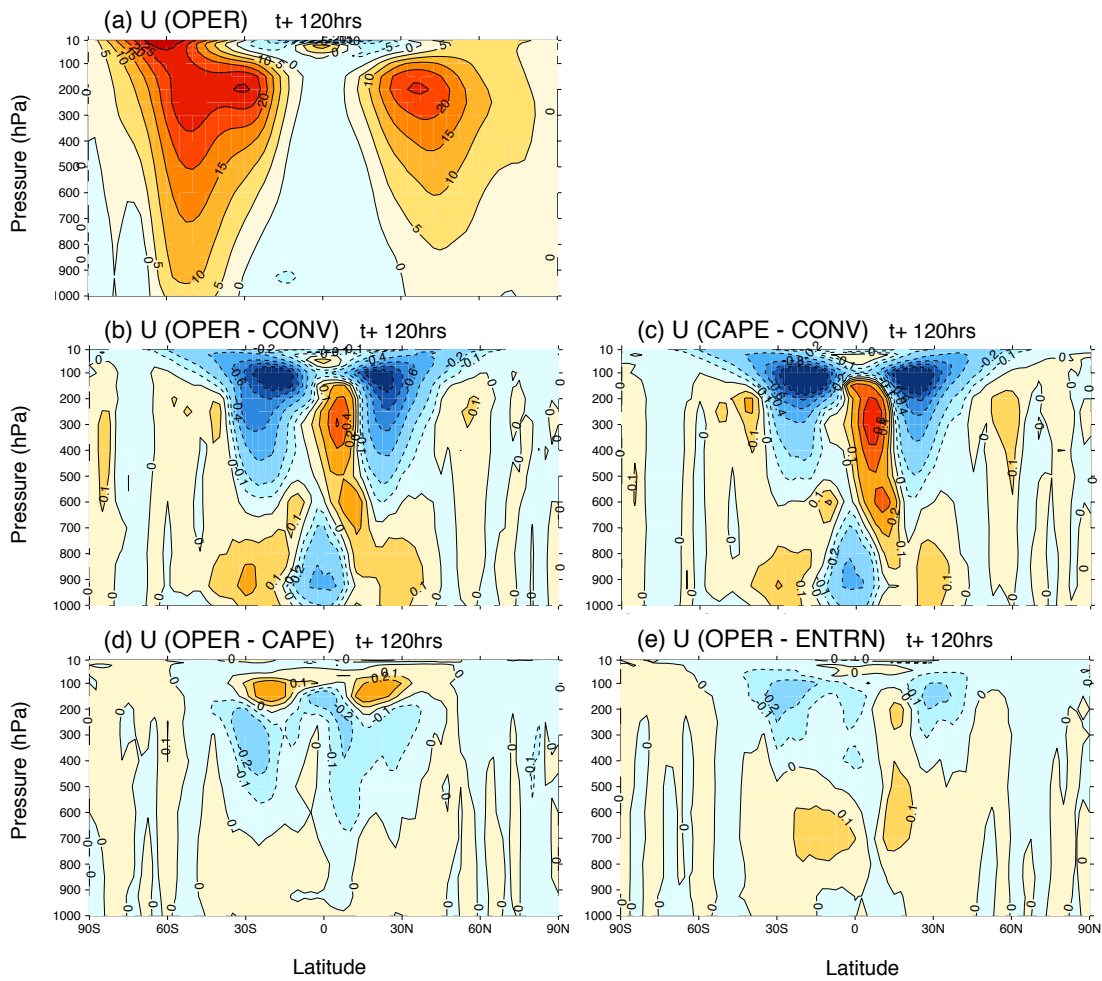
Figure 5.2 *As Fig. 5.1, but for zonal-mean zonal wind.*

lower-troposphere (upper-troposphere), with only the effect of ϵ_{org}^{RH}, the cooling signal is reduced (increased) by approximately 0.2K, compared to the combined effects of ϵ_{org}^{RH} and τ. The mean reduction in active convection shown by the cooling here, combined with the better representation of the MJO (Chapter 4) suggest that an effect of ϵ_{org}^{RH} is to prevent the triggering of spurious deep convection. The introduction of the variable τ in the closure for deep convection had a warming effect in the upper-troposphere with a maximum magnitude above 0.3K at 200 hPa (Fig. 5.1 (d)). Halving the rate of ϵ_{org}^{RH} had little effect on the vertical structure of zonal-mean temperature at a 5-day forecast lead time: Fig. 5.1 (e) shows a slight warming (cooling) in the lower-troposphere (mid- and upper-troposphere) of about 0.1K.

The vertical structure of the zonal-mean zonal wind from OPER at a 5-day forecast lead time is shown in Fig. 5.2 (a). The upper-level subtropical jets, which form in both hemispheres at the poleward boundary of the tropical Hadley Cell, exhibit a maximum intensity greater than 25 m s^{-1}

at 200 hPa approximately 30° north and south of the equator. The effect of the Cy32r3 convective parameterization is to weaken the subtropical jets by up to 1 m s^{-1} at approximately 100 hPa between 20°N and 20°S, above and equatorward of their maxima (Fig. 5.2 (b)). This dampening of the large-scale circulation pattern is consistent with the mean reduction of active convection penetrating into the tropical upper troposphere shown in Fig. 5.1. A further effect of the scheme is that the equatorial upper- and mid-tropospheric (lower-tropospheric) flow is more westerly (easterly) with the Cy32r3 convective parameterization by magnitudes up to 0.6 (0.4) ms^{-1} at 300 (900) hPa. Hsu *et al.* (1990) proposed that the MJO was maintained by extra-tropical Rossby wave trains propagating into the tropics through regions of upper-tropospheric westerly winds. Therefore, Slingo *et al.* (1996) suggested that the enhancement of equatorial upper-tropospheric westerly flow, exhibited in the models in their study, led to a better representation of MJO activity. According to the Hsu *et al.* (1990) mechanism, the modified Cy32r3 mean state in Fig. 5.2 (b) is more conducive to the propagation of wave energy into the tropics from the extra-tropics, which may lead to better maintenance of the MJO. However, the more easterly flow in the tropical lower troposphere contrasts with the hypothesis discussed in §5.1: that the MJO favours low-level and surface westerlies (Inness *et al.*, 2003; Zhang *et al.*, 2006). In §5.2.2 this zonal-mean analysis is extended to investigate the spatial distribution across an equatorial domain.

In Fig. 5.2 (c), extracting the effect of the ϵ_{org}^{RH} formulation yields the same spatial structure of changes to the zonal-mean zonal wind: a reduction in the intensity of the subtropical jets upward and equatorward of their maximum and enhanced upper- and mid-tropospheric westerly (lower-tropospheric easterly) flow in equatorial regions. However, as with the vertical structure of zonal-mean temperature, the magnitude of the effect of the ϵ_{org}^{RH} formulation alone differs from that of the Cy32r3 convective parameterization. The upper-tropospheric signals in the subtropical jets and equatorial westerlies are stronger by up to 0.2 m s^{-1}. The corollary of Fig. 5.2 (c) is that the effect of τ is to slightly increase the strength of the subtropical jets between 100 and 200 hPa, and decrease the equatorial westerly signal, by approximately 0.2 m s^{-1} (Fig. 5.2 (d)). As with temperature, halving the rate of ϵ_{org}^{RH} has little effect on the vertical structure of zonal-mean zonal wind.

The vertical structures of zonal wind and temperature are intimately linked through thermal-wind balance; the subtropical jets form in response to large horizontal temperature gradients. Therefore, the cooling in the tropical upper-troposphere in Fig. 5.1 is consistent with the reduction in the strength of the subtropical jets in Fig. 5.2. In the tropics, the vertical structure of the zonal-mean specific humidity (Fig. 5.3) is linked to the vertical structures of temperature and zonal wind through convection. Fig. 5.3 (a) shows the zonal mean specific humidity from OPER at a 5-day forecast lead
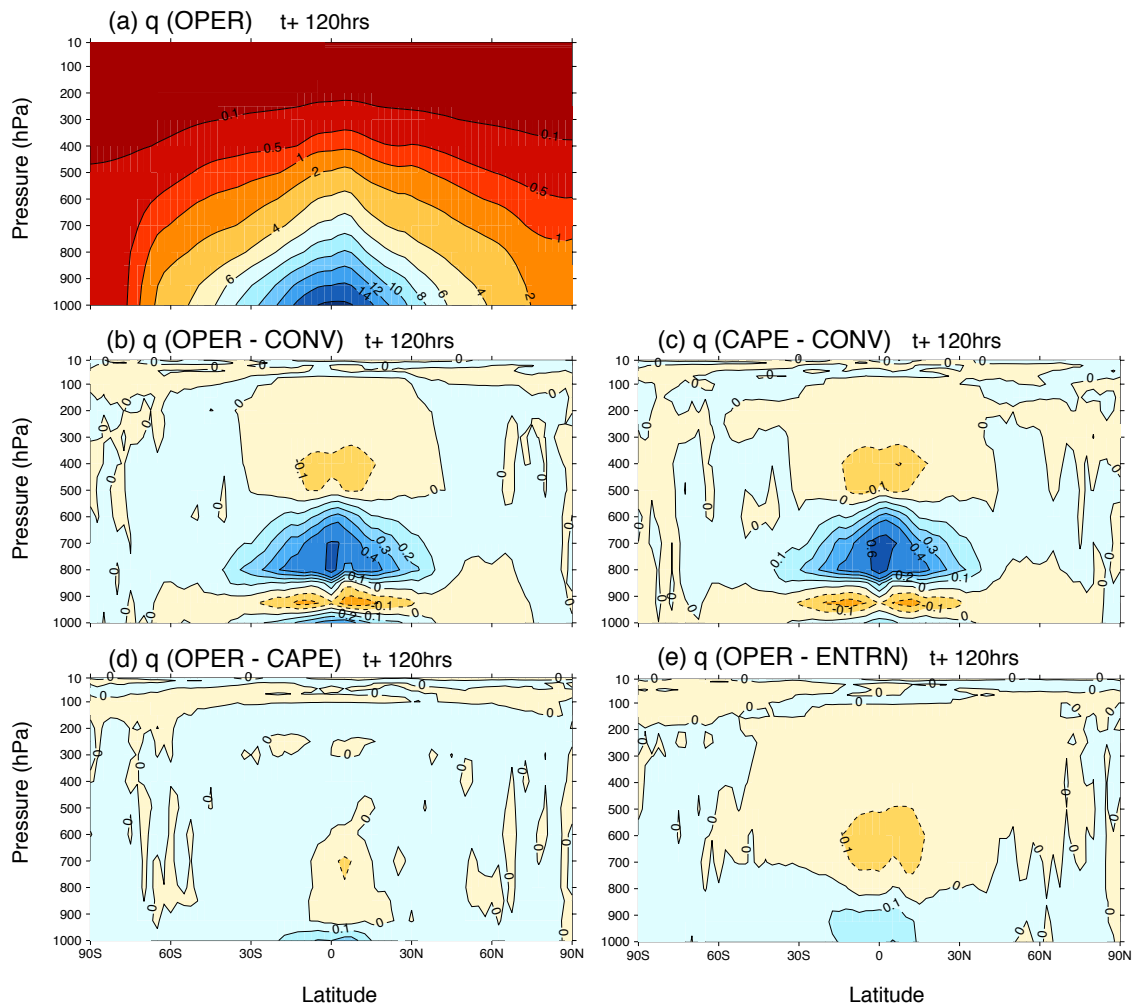
Figure 5.3   *As Fig. 5.1, but for zonal-mean specific humidity.*

time. Values of specific humidity decrease with height and distance from the equator. The largest difference in zonal-mean specific humidity from the Cy32r3 convective parameterization is a tropical mid-tropospheic moistening, with an equatorial maximum of approximately 0.6 g kg^{-1} between 800 and 700 hPa. The cooling in Fig. 5.1 suggested that less active convection was penetrating into the upper-troposphere; the moistening at mid-levels in Figs. 5.3 (b)-(c) suggests that clouds are detraining (and hence moistening their environment) in the mid-troposphere. Environmental moisture is crucial in modulating convective activity on the intraseasonal timescales of the MJO (e.g. Redelsperger *et al.* 2002; Grabowski 2003). The aim of the Cy32r3 convective parameterization was to increase the sensitivity of convection in the IFS to environmental moisture (Bechtold *et al.*, 2008), which was suggested by Derbyshire *et al.* (2004) to be too low. While the Cy32r3 convection scheme clearly moistens the mid-troposphere, it is yet unclear whether that is the result or the cause of a more active MJO. The increments from individual physical parameterizations will

be compared with the contribution from the dynamics in §5.5 to assess the role of the model physics in producing the modified basic state observed here.

Additionally, Fig. 5.3 (b) shows that at a 5-day forecast lead time, the Cy32r3 scheme exhibits an equatorial surface (boundary-layer) moistening (drying) of about 0.2 (0.2) g kg^{-1}. Fig. 5.3 (c) shows that ϵ_{org}^{RH} is almost entirely responsible for the vertical structure of zonal-mean moisture observed with the introduction of the Cy32r3 convective parameterization. With the ϵ_{org}^{RH} formulation alone, the mid-tropospheric (surface) moistening is slightly stronger (weaker), while the drying signal in the boundary layer between 950 and 900 hPa is unchanged. The new variable τ and the change to rate of ϵ_{org}^{RH} have little impact on the vertical structure of zonal-mean specific humidity (Figs. 5.3 (d) and (e)).

Figs. 5.1, 5.2 and 5.3 show that the introduction of the Cy32r3 convective parameterization, more specifically the new relative-humidity-dependent formulation for organised entrainment (ϵ_{org}^{RH}), has had a significant impact on the mean state of temperature, zonal wind and specific humidity across the tropics in the IFS. At a 5-day forecast lead time, the ϵ_{org}^{RH} formulation cools the tropical upper-troposphere (Fig. 5.1), indicative of clouds not penetrating as far into the free troposphere; the detrainment of these clouds at mid-levels moistens the mid-troposphere (Fig. 5.3). The dynamical response to less deep, penetrative convection is a reduction in the magnitude of the subtropical jets upward and equatorward of their maxima (Fig. 5.2).

5.2.2 Equatorial domain

Results from §5.2.1 showed that the main differences with the introduction of the Cy32r3 convective parameterization in the vertical structure of zonal-mean temperature, zonal wind and specific humidity are located in the tropics. Fig. 5.4 shows the spatial distribution across the equatorial domain of the difference in 850 and 200 hPa zonal wind, OLR and precipitation at a 5-day forecast lead time between (a) OPER and CONV, (b) CAPE and CONV, (c) OPER and CAPE and (d) OPER and ENTRN, which extract the effect of the Cy32r3 convective parameterization, ϵ_{org}^{RH} formulation, τ and ϵ_{org}^{RH} rate, respectively.

The introduction of the Cy32r3 convective parameterization increases convective activity and precipitation in the West Pacific, characterised by a decrease (increase) of OLR (precipitation) by approximately 12 W m^{-2} (4 mm day^{-1}), on the equator between 130° and 150° E (Fig. 5.4 (a)). East of this region of enhanced convective activity, there is an increase (decrease) in OLR (precipitation) in the equatorial central Pacific along the ITCZ by approximately 20 Wm^{-2} (5 mm day^{-1}). In Chapter 4 it was shown that, with the introduction of the Cy32r3 convection scheme, the IFS

(a) Cy32r3: (OPER - CONV)

(b) ϵ_{org}^{RH} formulation: (CAPE - CONV)

(c) τ: (OPER - CAPE)

(d) ϵ_{org}^{RH} rate: (OPER - ENTRN)
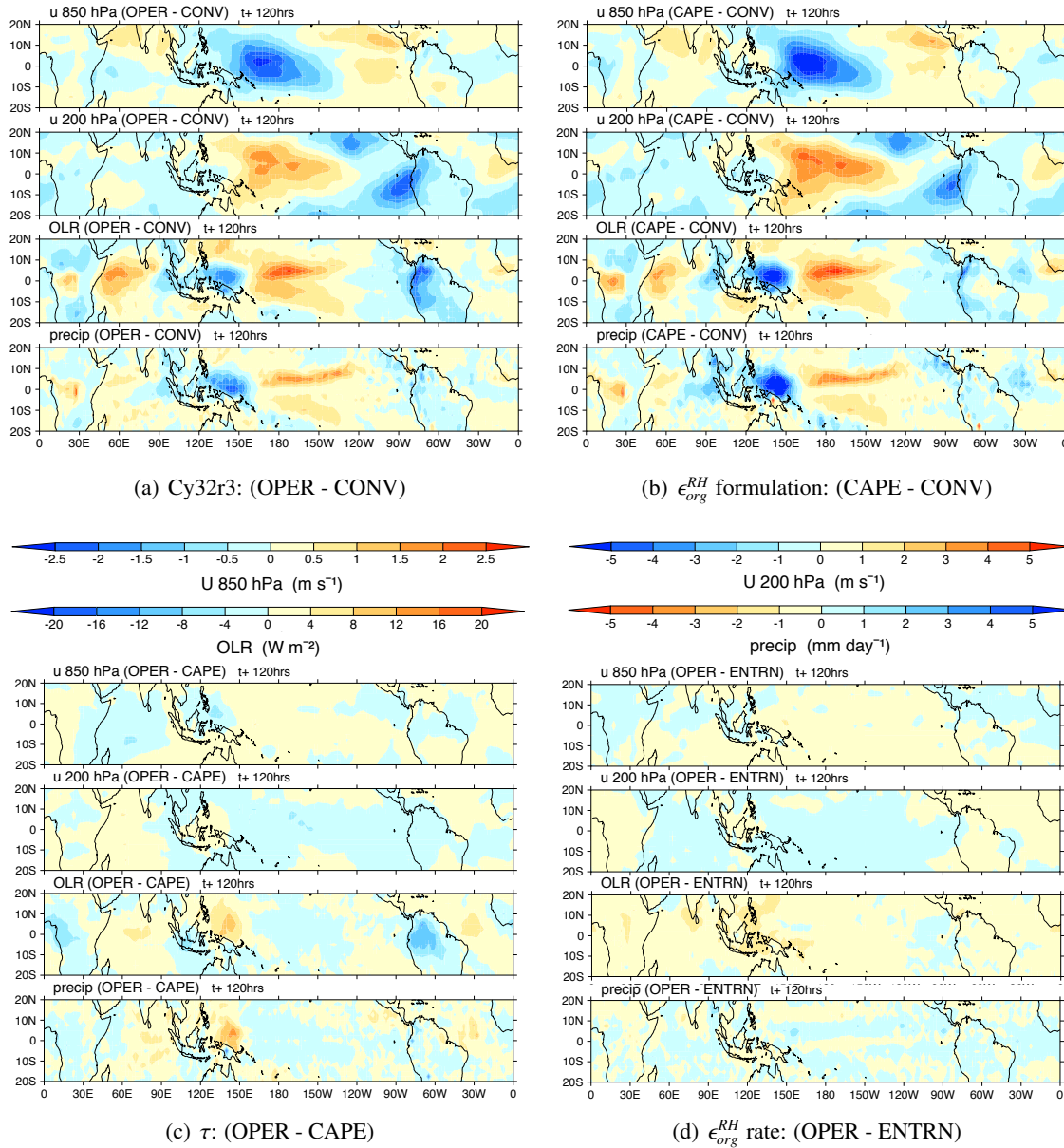
Figure 5.4   *5-day forecast of 850 hPa and 200 hPa zonal wind, OLR and precipitation. Difference between (a) OPER and CONV (effect of Cy32r3), (b) CAPE and CONV (effect of ϵ_{org}^{RH}), (c) OPER and CAPE (effect of τ) and (d) OPER and ENTRN (effect of ϵ_{org}^{RH} rate). In zonal wind, precipitation and OLR panels, orange shading indicates more westerly flow, less rain and enhanced OLR, respectively.*

more accurately simulated the MJO. Therefore, the increase in convective activity in the Maritime Continent and West Pacific in Fig. 5.4 (a) may be a consequence of more events propagating into that region. However, Bechtold *et al.* (2008) suggested that there was an overestimation of convective precipitation in the Maritime Continent in Cy32r3, which was responsible for the slower-than-observed propagation speed of the MJO. The associated dynamical signal in the upper- and lower-tropospheric zonal wind is consistent with the increased convective activity in the equatorial

West Pacific. This is also consistent with the equatorial structure of zonal-mean zonal wind shown in §5.2.1 (Figs. 5.2 (b)-(c)). With the modified formulation of convection, flow into (out of) the region of enhanced convection in the lower- (upper-) troposphere over the West Pacific Warm Pool is more easterly (westerly) by up to 2.5 (3) ms^{-1}. At upper-levels, the flow in the eastern Pacific, south of the equator, is more easterly with the Cy32r3 convective parameterization by approximately 4 ms^{-1}.

Consistent with results from §5.2.1, isolating the effect of the new formulation of organised entrainment (Fig. 5.4 (b)) reveals the same spatial structure, but an increased magnitude of the changes in the convective and dynamical signal across the equatorial domain. In the West Pacific, the difference in OLR and precipitation is almost doubled. There are associated increases in the strength of the easterly and westerly differences in the lower- and upper-troposphere, respectively. The enhanced convection and upper-level easterlies over the eastern Pacific are the only differences that are reduced in magnitude when the ϵ_{org}^{RH} formulation is isolated. In Figs. 5.4 (a) and (b) there is very little precipitation associated with this convective signal. The corollary of Figs. 5.4 (a) and (b) is that the effect of τ is to decrease convective activity in the equatorial West Pacific and reduce OLR over South America (Fig. 5.4 (c)). Changing the rate of ϵ_{org}^{RH} has little effect on the mean state over the equatorial domain (Fig. 5.4 (d)).

Figs. 5.1 - 5.4 have shown that the largest changes to the mean state of the IFS in the hindcast experiments are located in the tropics, and are a result of ϵ_{org}^{RH}. Most notably, Fig. 5.4 (b) showed that ϵ_{org}^{RH} increased precipitation in the equatorial Maritime Continent and West Pacific region. The remainder of the chapter will investigate what effect ϵ_{org}^{RH} had on the overall distribution of precipitation and the vertical structure of clouds. Through analysis of the tendencies from the physics packages in the IFS, §5.5 will investigate the contributions to the changes in the basic state from the dynamics and the convective parameterization.

5.3 Distribution of precipitation and CAPE

The ϵ_{org}^{RH} formulation increased in precipitation in the Maritime Continent and West Pacific (Fig. 5.4). However, Bechtold *et al.* (2008) suggested that the Cy32r3 convective parameterization overestimated precipitation in this region. Here, the distributions of equatorial, 1-mm day^{-1}-wide binned precipitation from the IFS are compared with those from the Tropical Rainfall Measuring Mission (TRMM) satellite. The distribution of non-zero precipitation values at a 1-day forecast lead time for the control versions of the IFS and the hindcast experiments are compared to TRMM in Fig. 5.5 (a). The contribution of each rain rate bin to the total precipitation is shown in Fig. 5.5

(b). Versions of the IFS with a pre-Cy32r3 convection scheme (Cy31r1 and CONV) agree well with TRMM observations at low precipitation rates, but produce too much (not enough) rain at medium (high) precipitation rates of between 3 and 23 mm day^{-1} (above 23 mm day^{-1}). Additionally, Cy31r1 and CONV exhibit a preferred, but unrealistic, precipitation rate of approximately 10 mm day^{-1} (Fig. 5.5 (b)). This behaviour has also been seen in the UKMO UM[1] (Holloway, 2011) and NCAR CAM3.0[2] (Thayer-Calder and Randall, 2009).

(a) PDF of precipitation   (b) Contribution to total precipitation per rain rate bin
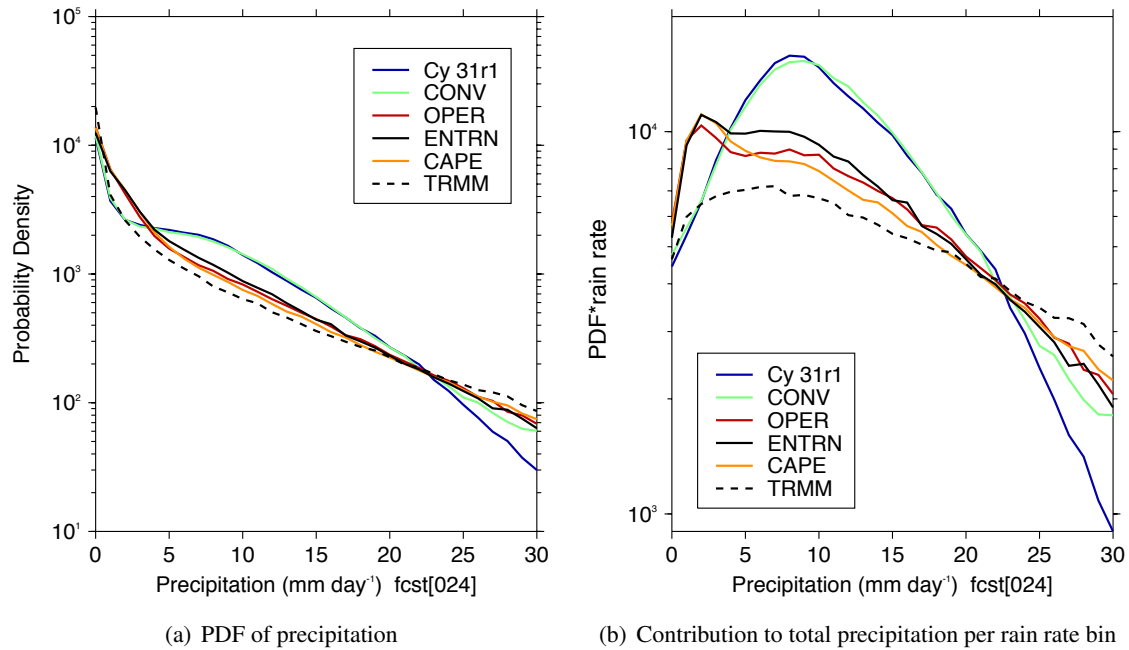
Figure 5.5 *(a) Probability density function (PDF) for non-zero values of precipitation at a 1-day forecast lead time in mm day^{-1} from TRMM observations (dashed line), Cy31r1 (blue line), CONV (green line), OPER (red line), ENTRN (black line) and CAPE (orange line). The PDF is calculated from 1-mm day^{-1}-wide bins of precipitation in the equatorial belt (all longitudes) between 10°N and 10°S. (b) As (a), but the contribution to the total precipitation by each rain rate.*

Comparing OPER and CONV shows that the introduction of the Cy32r3 convection scheme increased the amount of precipitation at low and high rain rates and decreased precipitation at medium rain rates. The modified formulation of convection results in a distribution of precipitation that no longer exhibits a preferred precipitation rate of 10 mm day^{-1} and, therefore, shows closer agreement with TRMM observations at medium and high rain rates. Since OPER, CAPE and ENTRN all contain the ϵ_{org}^{RH} formulation and all exhibit similar distributions of precipitation, the differences attributed to the Cy32r3 convective parameterization can be more directly attributed to the relative-humidity-dependent formulation of organised entrainment (ϵ_{org}^{RH}). However, in OPER, CAPE and ENTRN there is still not enough heavy rain and too much light rain, with an unrealistic

---

[1]the Unified Model from the Met Office, UK

[2]Community Atmosphere Model version 3.0 from the National Center of Atmospheric Research, USA

peak at approximately 2 mm day^{-1} (Fig. 5.5 (b)), a feature in common with simulations from the NCAR SP-CAM[3] (Thayer-Calder and Randall, 2009). All versions of the IFS underestimate the number of dry days compared with TRMM, which, using data from CAM3.0 and SP-CAM, Thayer-Calder and Randall (2009) suggest could contribute to the unrealistic peaks in rainfall at 10 and 2 mm day^{-1}, respectively.

(a) PDF of CAPE   (b) Contribution to total CAPE per CAPE rate bin
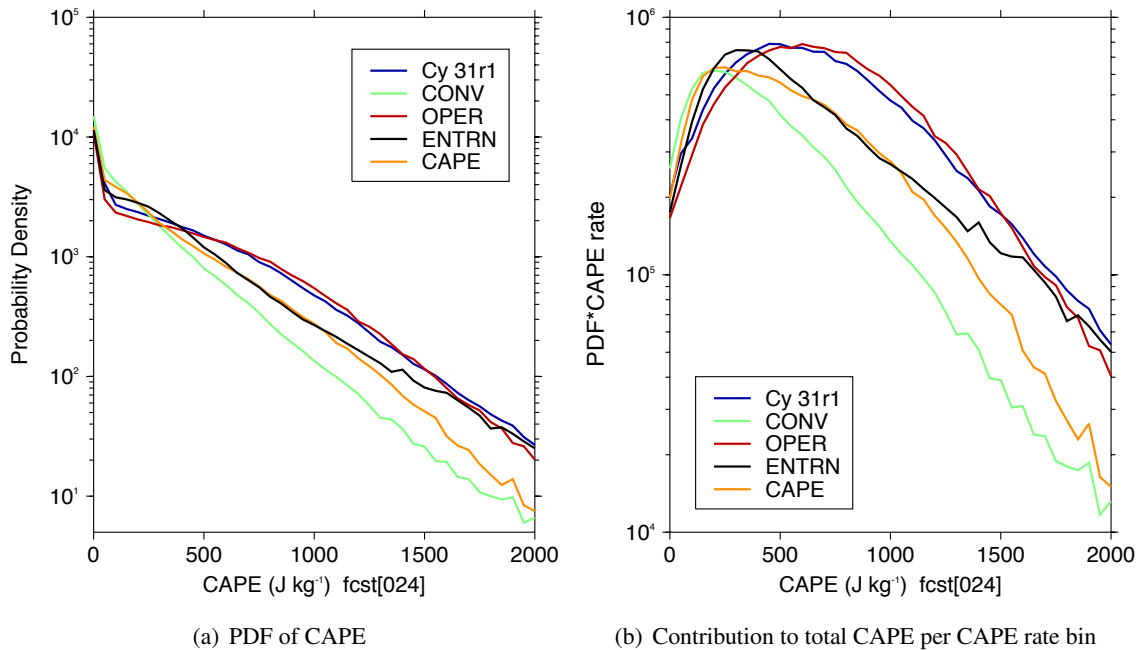
Figure 5.6   *As Fig. 5.5, but for 50-J kg^{-1}-wide bins of CAPE.*

CAPE is an important parameter for the strength of convection; generally larger values of CAPE imply more vigorous convection. However, in recent idealised cloud-resolving simulations, environmental moisture was shown to be more important than CAPE in modulating cloud depth (Waite and Khouider, 2010). Fig. 5.6 (a) shows the distribution of 50-J kg^{-1}-wide binned CAPE; Fig. 5.6 (b) displays the contribution to the total CAPE by each CAPE rate bin. Distinctions between IFS versions are only apparent as CAPE increases. Comparing OPER and CONV shows that the effect of the Cy32r3 convective parameterization is to significantly increase the occurrence of days with CAPE values above 500 J kg^{-1}. This is an effect of both the variable τ (in T$_L$799L91 simulations, comparing CAPE and CONV) and the ϵ_{org}^{RH} formulation (comparing OPER and CAPE), which both increase CAPE. These results suggest that the IFS is able to build up more CAPE with the Cy32r3 convection scheme, which will enable more vigorous deep convection and is consistent with the increase in heavy precipitation days seen in Fig. 5.5. The process-based diagnostics applied in the next chapter will explore this further.

---

[3]"superparameterized" version of CAM from NCAR

Although Cy31r1 is included in Figs. 5.5 and 5.6, comparisons with it are somewhat misleading because it differs from the other versions of the IFS in horizontal and vertical resolution, SST forcing, initialisation analysis and radiation scheme as well as aspects of the convection scheme (Fig. 3.8). The effect of increasing the horizontal and vertical resolution (comparing Cy31r1 and CONV), including the change in the resolution-dependent constant τ which differs between 3600 seconds in $T_L255L60$ and 720 seconds in $T_L799L91$), is to reduce CAPE.

5.4 The vertical structure of cloud variables

To investigate the effect of the modified mean state on clouds, the vertical structure of equatorially averaged cloud cover is examined. There are three prominent modes of convection in the tropics: shallow convection, cumulus congestus and deep precipitating convection (e.g. Johnson *et al.*, 1999; Fig. 2.5 in §2.2).
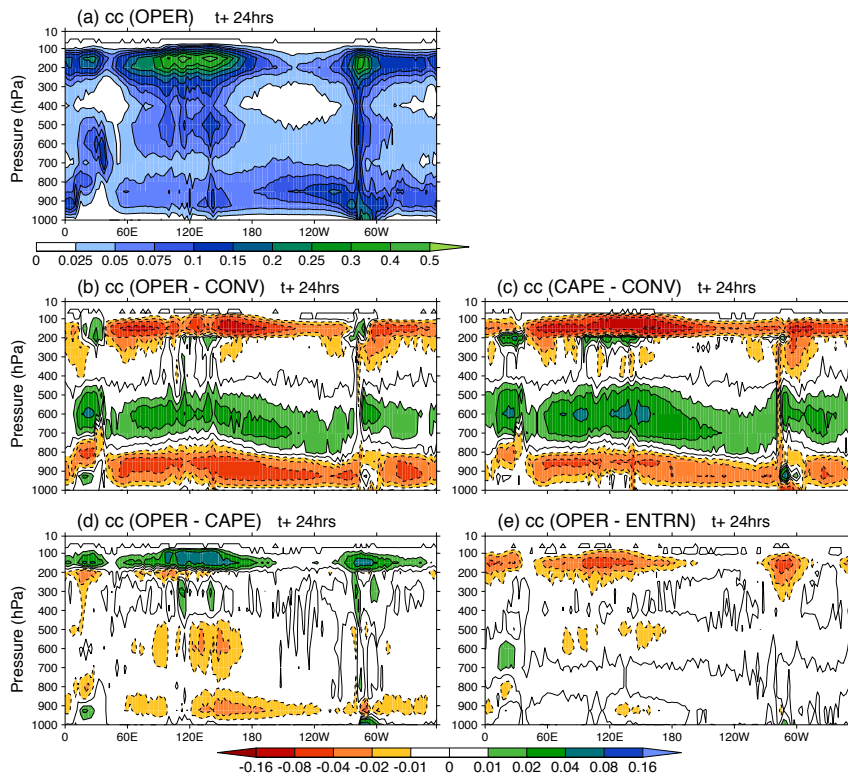
Figure 5.7 *(a) Vertical structure of equatorially averaged ($10°N$ - $10°S$) cloud fraction from OPER at a 1-day forecast lead time, the scale goes from 0 to 1. (b) Difference in equatorially averaged cloud cover between OPER and CONV (effect of Cy32r3) at a 1-day forecast lead time. (c),(d) and (e), as (b) but difference between CAPE and CONV (effect of ϵ_{org}^{RH}), OPER and CAPE (effect of τ), and OPER and ENTRN (effect of ϵ_{org}^{RH} rate) respectively.*

Shallow convection detrains at the height of the boundary-layer inversion; deep convection penetrates into the upper troposphere, usually detraining at the tropopause. Cumulus congestus

penetrates to a thin stable layer at the zero-degree isotherm, which, in the tropics, is at approximately 500 hPa. The layer is maintained by the heat absorbed by the melting of precipitation from ice to liquid phase. Fig. 5.7 (a) shows the vertical structure of equatorially averaged cloud cover from OPER at a 1-day forecast lead time. The trimodal distribution of tropical cloud described above is apparent, with maxima above the boundary layer, at the melting layer (approximately 500 hPa), and at the tropopause (approximately 100 hPa). The equatorially averaged cloud cover is largest for deep convection over the Indo-Pacific between 60°E and the dateline, the region where convection associated with the MJO occurs.
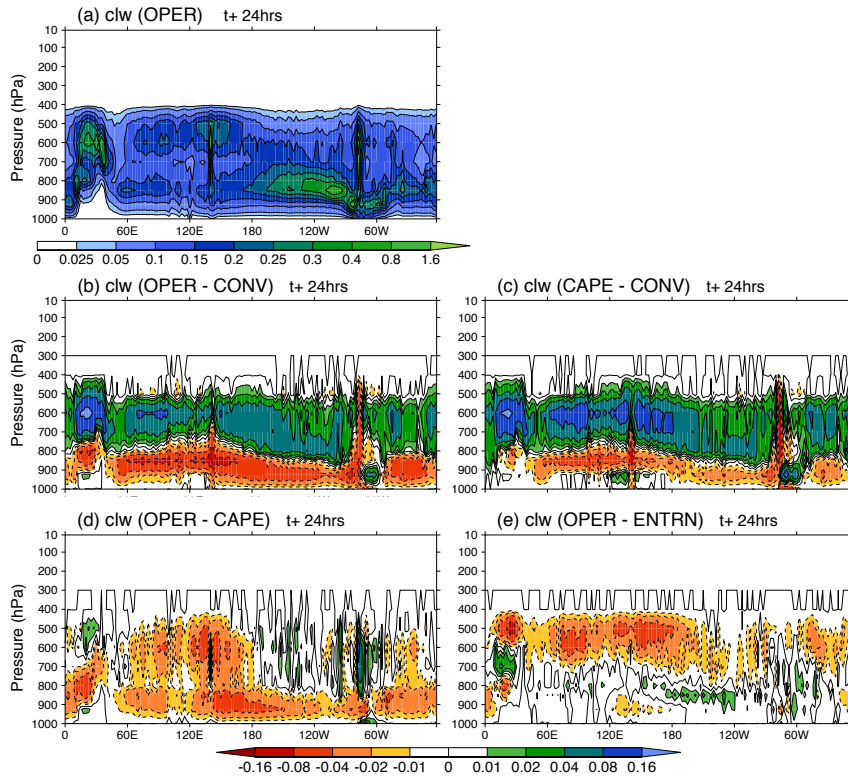
Figure 5.8   *As Fig. 5.7, but for cloud liquid water content. Units are $\times 10^3$ kg kg^{-1}.*

Figs. 5.7 (b)-(e) show the difference in equatorially averaged cloud cover between OPER and CONV, CAPE and CONV, OPER and CAPE and OPER and ENRTN, which highlight the effects of the Cy32r3 convection scheme (ϵ_{org}^{RH} and τ), ϵ_{org}^{RH} formulation, τ and ϵ_{org}^{RH} rate, respectively. The introduction of the Cy32r3 convective parameterization (Fig. 5.7 (b)), and more specifically the modified ϵ_{org}^{RH} formulation (Fig. 5.7 (c)), increase the amount of cumulus congestus cloud in the mid-troposphere and decrease the amount of shallow and deep convection in the lower- and upper-troposphere at a 1-day forecast lead time. Although the differences are small in magnitude, they are consistent across the equatorial belt. Figs. 5.8 (c) and 5.9 (c) show that the increase in cumulus congestus with the ϵ_{org}^{RH} formulation is a result of an increase in both cloud liquid- and ice-water
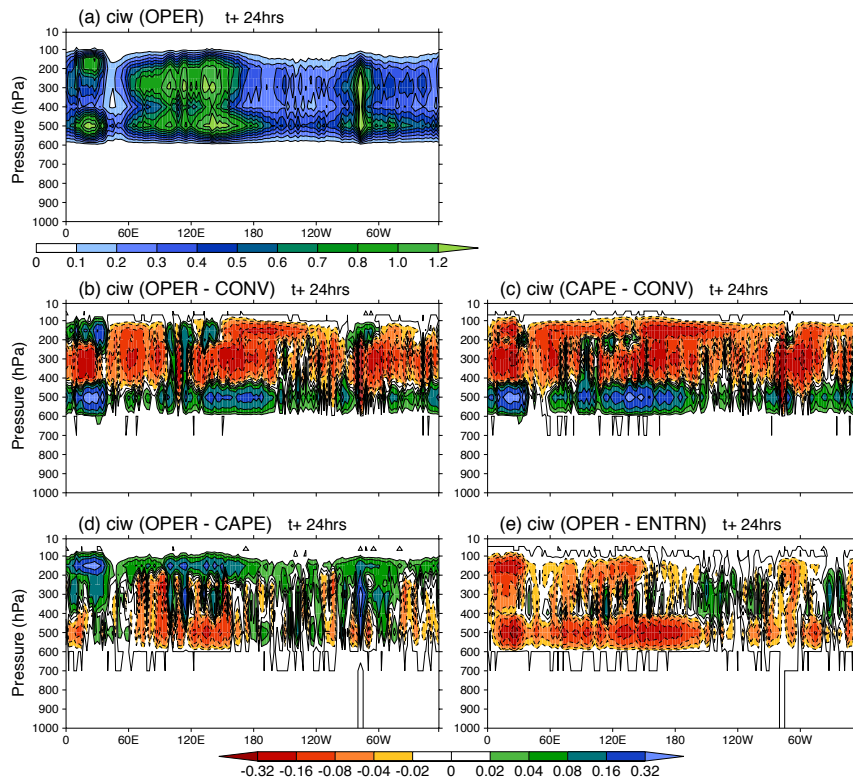
Figure 5.9 *As Fig. 5.7, but for cloud ice water content. Units are $\times 10^1$ kg kg^{-1}.*

content between 500 and 800 hPa and 400 and 600 hPa, respectively. An increase in cumulus congestus detraining at mid levels is consistent with the moistening of the mid-troposphere (Fig. 5.3) and less deep, penetrative convection reaching as far into the free troposphere, resulting in an upper-tropospheric cooling (Fig. 5.1).

At a 5-day forecast lead time, the effect of the ϵ_{org}^{RH} formulation in the mid-troposphere is consistent with that of the the start of the forecast: there is a distinct increase in cumulus congestus, and both cloud liquid- and ice-water content, across the equatorial belt (Fig. 5.10). At upper-levels, however, there is no longer a uniform decrease in tropical cloud; over the islands of the Maritime Continent and equatorial South America there are increases in cloud cover, and cloud ice water content, consistent with the changes in convection and precipitation seen in Fig. 5.4.

The role of deep and shallow convection has long been established, but, the importance of cumulus congestus in the transition from shallow to deep convection has been recognised only more recently (e.g. Johnson *et al.*, 1999; Waite and Khouider, 2010). In a dry environment, the entrainment of dry air into a convective plume will dilute the plume, reducing the cloud buoyancy and inhibiting the development of deep convection, resulting in a lower cloud-top level (CTL). The ϵ_{org}^{RH} formulation is designed to entrain more in a dry column, which will enhance the process
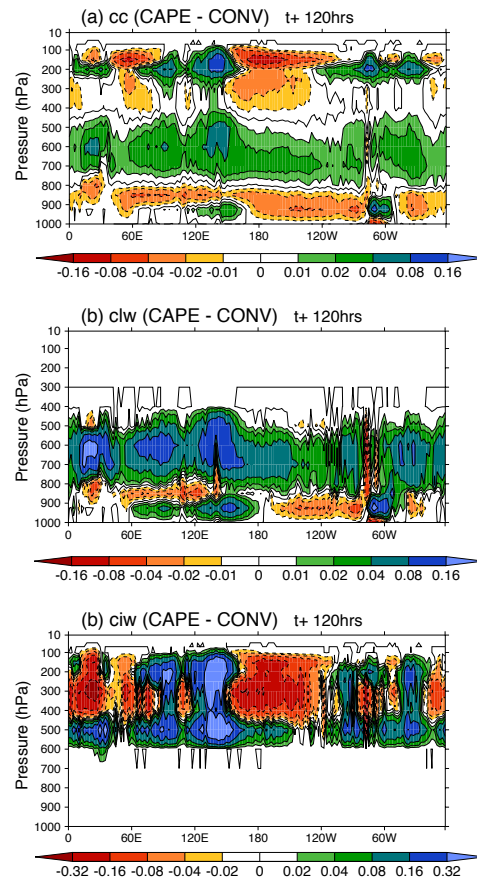
Figure 5.10 *Difference in equatorially averaged (10°N - 10°S) (a) cloud cover, (b) cloud liquid water content and (c) cloud ice content between CAPE and CONV (effect of ϵ_{org}^{RH} formulation) at a 5-day forecast lead time.*
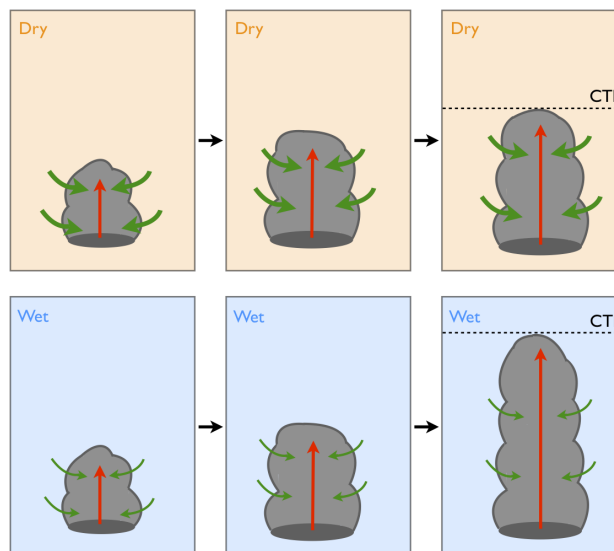
Figure 5.11 *Schematic representation of the entrainment process (green arrows) in a dry (top panels) and wet (bottom panels) environment. The dotted line represents the cloud-top level (CTL).*

described above. This explains why more clouds are detraining in the mid-troposphere, and increasing the cloud cover and liquid- and ice-water content there (Fig. 5.10). This process is represented schematically in Fig. 5.11. The mid-tropospheric moistening from the detrainment of congestus clouds results in conditions which are more favourable for deep convection. When a convective plume encounters high humidity in the mid-troposphere, moister air is entrained which limits the decreasing of the cloud buoyancy and results in the development of deeper convection (Fig. 5.11). The importance of the transition from shallow to deep convection in the tropics is discussed further in §5.6.1.

5.5   Contribution from physics tendencies

The ϵ_{org}^{RH} formulation modified the vertical structure of temperature, zonal wind and specific humidity in the IFS (Figs. 5.1 (c), 5.2 (c) and 5.3 (c), respectively). Here, through analysis of the heating, moisture and wind tendencies, the contribution from individual components of the IFS to the modified vertical structures shown in §5.2.1 can be identified. Figs. 5.12, 5.13 and 5.14 show the vertical structure of the zonal-mean increments in temperature, zonal wind and specific humidity from the dynamics, convective parameterization, and - by removing the effect of the shallow convection scheme - the contribution from deep convection only. The zonal-mean is calculated over all longitudes. The domain has been limited to tropical latitudes (30°N - 30°S) where the effect of the modified ϵ_{org}^{RH} formulation on the mean state of the IFS was largest.

Fig. 5.1 (c) showed that the main effect of ϵ_{org}^{RH} on the zonal-mean temperature was to cool the tropical troposphere, especially at upper levels. Fig. 5.12 (a) shows that the dynamics are not responsible for any of that cooling; in fact, there is a slight warming at upper levels. Over the first 5 days of the forecast, the convective parameterization has cooled the tropical upper- and lower-troposphere and boundary layer by up to 2, 2.5 and 8 K, respectively (Fig. 5.12 (b)). In addition, there is a distinct warming of the mid-troposphere by up to 3 K after 5 days. Fig. 5.12 (c) reveals that the deep convective parameterization is largely responsible for the vertical structure of increments in temperature, exhibiting a strong cooling at the surface and in the lower and upper troposphere. The deep convective parameterization is only responsible for a weaker, thinner layer of warming in the mid-troposphere; the shallow convection scheme is responsible for the remaining warming. Fig. 5.12 suggests some aspects of the modified vertical structure of the zonal-mean temperature with the modified ϵ_{org}^{RH} formulation are a direct result of the convective parameterization, or more specifically the deep convection scheme. However, the convective parameterization cannot explain the observed cooling through the entire depth of the tropical troposphere (Fig. 5.1 (c)) because it
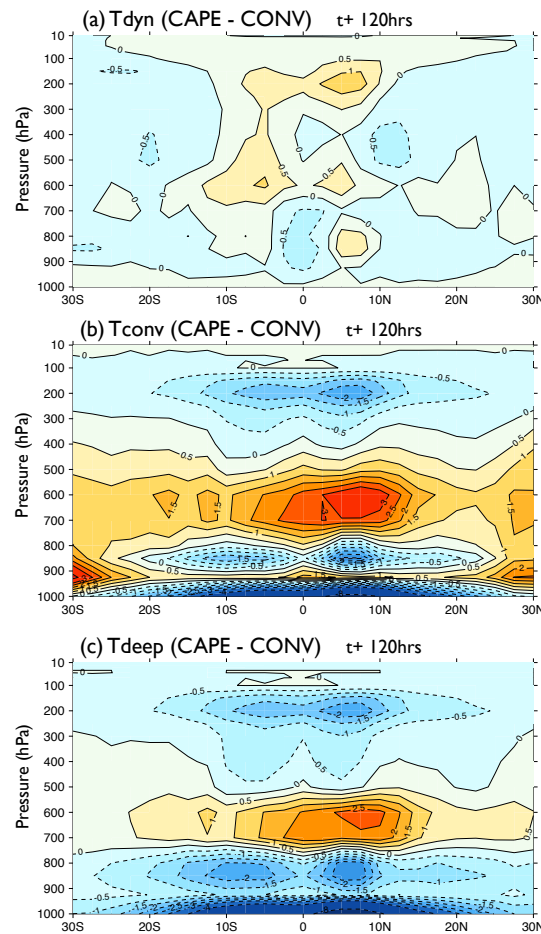
Figure 5.12 *Zonal mean temperature increment (K) from (a) dynamics, (b) convection scheme and (c) the contribution from deep convection accumulated after 5 days of the forecast. The zonal mean is calculated for the period from May 2008 to April 2009 at all longitudes. Negative values are shown by dashed contours.*

exhibits a distinct warming in the mid-troposphere.

In contrast, Fig. 5.13 (b) and (c) show that the convective parameterization, or indeed the deep convection scheme, had little direct effect on the increments in zonal wind over the first 5 days of the forecast. Therefore, at least at upper levels, the modified zonal-mean zonal wind structure observed in Fig. 5.2 (c) is a secondary effect of the modified vertical structure of temperature caused by the convective parameterization. The reduction in the strength of the subtropical jets, by over 1.5 m s^{-1}, is the dynamical response (Fig. 5.13 (a)) to the cooling at upper levels caused by the deep convection scheme (Fig. 5.12 (c)).

Fig. 5.3 (c) showed that the effect of the modified ϵ_{org}^{RH} formulation was to moisten the mid-troposphere between 600 and 800 hPa. Fig. 5.14 (a) shows that while the effect of the moisture increments from the dynamics is to moisten the boundary layer and lower troposphere by up to 2 g
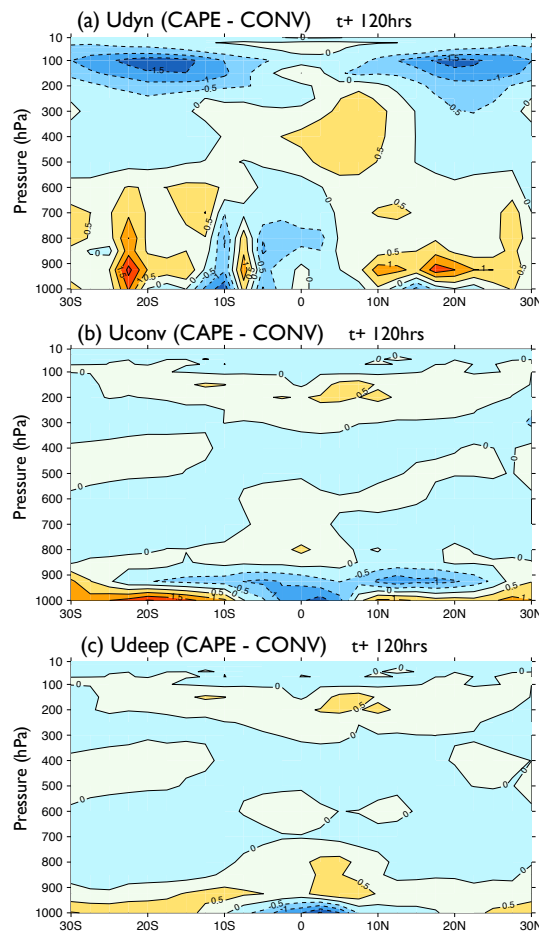
Figure 5.13 *As Fig. 5.12, but for zonal mean zonal wind increments (m s^{-1}).*

kg^{-1}, in the mid-troposphere their effect is a drying of up to 1.5 g kg^{-1} after 5 days of the forecast. The contribution of the convection scheme to the increment in humidity is of the opposite sign to the dynamics: in the lower-troposphere there is a consistent drying across the entire equatorial belt of up to 2 g kg^{-1}, with a maximum around 900 hPa (Fig. 5.14 (b)). Comparison with Fig. 5.14 (c) shows that the shallow convection scheme is responsible for all the convective drying near the surface. Above the dry layer, Fig. 5.14 (b) exhibits convective moistening of over 1 g kg^{-1} near the equator. The deep convection scheme moistens the lower troposphere from the surface up to 750 hPa, with a maximum of approximately 2.5 g kg^{-1} north of the equator between 800 and 950 hPa. Therefore, it can be concluded that convective moistening contributes to the mid-tropospheric moistening in the tropics which is observed in the zonal-mean specific humidity. Fig. 5.14 (a) confirms that the mid-tropospheric moistening is not a result of the dynamics.
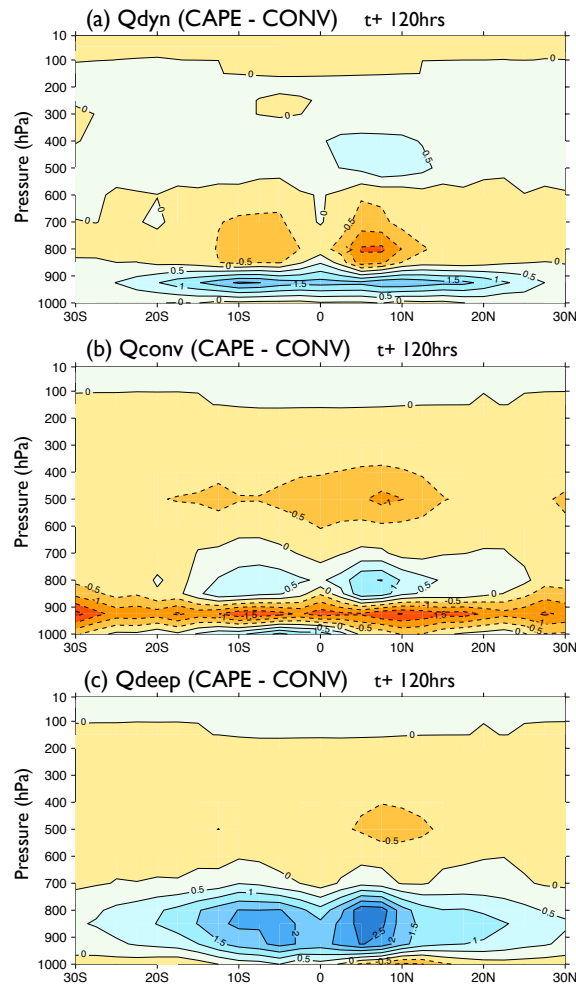
Figure 5.14 *As Fig. 5.12, but for zonal mean specific humidity increments (g kg^{-1}).*

5.6 Discussion and conclusions

5.6.1 Discussion of results

To understand why the ϵ_{org}^{RH} formulation resulted in the modified background state of the IFS described here, it is worth recalling the physical interpretation of ϵ_{org}^{RH} (equation 3.16), discussed in §3.4. The motivation for the change from a moisture-convergent-dependent to a relative-humidity-dependent formulation for organised entrainment was to increase the sensitivity of the formulation to environmental moisture. Physically, equation 3.16 results in larger and smaller entrainment in regions of low and high humidity, respectively (Fig. 5.11). Therefore, with the ϵ_{org}^{RH} formulation, if convection is triggered in a dry environment, more dry air will be entrained into the cloud and the convective plume will not penetrate as far into the free troposphere. This will prevent spurious deep convection being triggered in a dry environment, a problem that the modified formulation for organised entrainment was designed to 'fix' in the IFS (Bechtold *et al.*, 2008), but which was shown

previously to be a source of errors in the simulation of the MJO (Lin *et al.*, 2006). The resulting distribution of cloud exhibits a more realistic trimodal structure (Johnson *et al.*, 1999), with more cumulus congestus detraining in the mid troposphere (Fig. 5.7). An effect of the detrainment of cumulus congestus at the melting level is to moisten the mid troposphere (Fig. 5.3), preconditioning the atmosphere for deep convection. The ability of a model to moisten its mid-levels has been shown to be crucial to its success at reproducing the observed magnitude of convective heating and drying associated with the MJO (Thayer-Calder and Randall, 2009). Conversely, without mid-tropospheric moistening, the evaporation of precipitation from strong convective events increases, reducing the strength and depth of convection. These results are discussed further in the context of the process-based diagnostics applied in Chapter 6.

5.6.2 Conclusions

Results from Chapter 4 showed that the introduction of the Cy32r3 convective parameterization significantly improved the simulation of the MJO. It was shown that the relative-humidity-dependent formulation for organised entrainment (ϵ_{org}^{RH}) was responsible for the advances in simulating intraseasonal variability. In light of this, the focus here has been to identify how the ϵ_{org}^{RH} formulation has modified the mean state of the IFS, and to understand how that modified mean state may lead to, or indeed result from, a better representation of the MJO.

The main changes to the mean state of the IFS with the introduction of the relative-humidity-dependent formulation for organised entrainment are:

(a) a cooling through the depth of the tropical troposphere, largest in the upper troposphere (Fig. 5.1), likely to be as a result of less active convection that does not penetrate as deep into the upper troposphere.

(b) an associated increase in the occurrence of cumulus congestus clouds detraining in the mid-troposphere (Fig. 5.7).

(c) a moistening of the tropical mid-troposphere (Fig. 5.3), likely to be due to (b).

(d) a reduction in the magnitude of the subtropical jets above and equatorward of their maxima (Fig. 5.2), a dynamical "response" to (a)-(c) (Fig. 5.13 (a)).

(e) a large increase in convective activity and rainfall in the Maritime Continent and West Pacific (Fig. 5.4).

(f) enhanced westerly and easterly flow in the equatorial upper- and lower-troposphere respectively (Fig. 5.2), likely to be due to (e).

(g) a more realistic distribution of precipitation rates, compared with TRMM observations (Fig. 5.5).

Analysis of the physical tendencies from the IFS revealed that the convective parameterization, more specifically the deep convection scheme, contributed to the change in the vertical structure of the zonal-mean temperature in the tropics (Fig. 5.12). Since the convective parameterization showed little increment in the zonal-mean zonal wind structure (Fig. 5.13), the modified mean state in zonal wind can not be directly attributed to the convection scheme, but is likely a consequence of the modified vertical structure in temperature. The increments in moisture from the dynamics and from convective parameterization are opposite in sign (Fig. 5.14): the dynamics (convection scheme) increments moisten (dry) at the surface across the entire tropics and dry (moisten) the mid-troposphere, with maxima near the equator.

The modified mean state of the IFS reported here, with the introduction of ϵ_{org}^{RH}, results in an IFS that is better able to represent the transition from shallow to deep convection through more effective preconditioning of the mid levels. These processes could contribute to the improved representation of the MJO in the IFS with the modified ϵ_{org}^{RH} formulation. The application of process-based diagnostics in Chapter 6 explores this hypothesis and examines the role of convective moistening in the simulation of the MJO.

CHAPTER 6

Application of process-based diagnostics

6.1   Introduction

It is well known that there are large discrepancies between numerical models in their ability to simulate intraseasonal variability associated with the MJO (e.g. Lin *et al.* 2006, Kim *et al.* 2009). While diagnostics, such as those applied in Chapter 4, can determine to what extent a model is able to reproduce the MJO, they cannot indicate why a particular model is better than another. This has led to recognition, both at academic workshops (Sperber and Waliser, 2008) and in the literature (e.g. Kim *et al.*, 2009; Zhu *et al.*, 2009), that there is a need for process-based diagnostics of the MJO. Such diagnostics are designed to reveal which physical processes are responsible for differences in MJO simulation, and consequently, reveal why some models are able to reproduce the MJO while others are not. Process-based diagnostics aim not only to deepen our understanding of the origins of advances in MJO simulation, but also, to inform improvements in other models.

The MJO diagnostics applied in Chapter 4 showed that modifications to the convective parameterization in Cy32r3 led to advances in the simulation of the MJO (summarised in Fig. 4.21). Unique to this thesis is the attribution of those improvements in MJO simulation to the modified relative-humidity-dependent formulation for organised entrainment. Despite this attribution, the MJO diagnostics applied so far have not shown why changing from a moisture-convergence- to a relative-humidity-dependent formulation for organised entrainment resulted in such pronounced advances. Investigation of the modified mean state of the IFS (Chapter 5) suggests that with ϵ_{org}^{RH}, the IFS is better able to simulate the transition from shallow to deep convection. A set of process-based diagnostics are applied to the IFS output too understand the physical mechanisms underlying the advances shown in Chapter 4, and the improved preconditioning hypothesis proposed in Chapter 5:

(a) TCW - precipitation statistics: Through analysis of four years of tropical rainfall and column water vapour satellite measurements, Bretherton *et al.* (2004) showed that there was a direct, non-linear relationship between precipitation and the total amount of water in the atmospheric column (TCW). According to their study, the relationship between humidity and rainfall could be an efficient test of a model's ability to simulate deep convection in the tropics. A similar diagnostic is applied to the different versions of the IFS in §6.2.

(b) Parameters binned based on precipitation: Previous studies have investigated the efficiency of convective moistening in the tropics by compositing or binning parameters, such as relative humidity and temperature, based on precipitation (Thayer-Calder and Randall, 2009; Zhu *et al.*, 2009). Here, §6.3 tests the sensitivity of the relationship between precipitation and various parameters to the formulation of ϵ_{org}^{RH}, the variable adjustment timescale τ and the rate of ϵ_{org}^{RH}.

(c) Vertical structure of moisture: Since it was shown in Chapter 4 that, with the modified convective parameterization, the IFS is able to reproduce a realistic MJO, the April 2009 case study is used to analyse the role of moisture throughout the passage of an MJO (§6.4). This analysis investigates the hypothesis proposed in Chapter 5 that the post-Cy32r3 IFS is better able to simulate the transition from shallow to deep convection.

(d) Temperature and moisture tendencies: Investigation of the model physics tendencies through the passage of the April 2009 MJO case study are shown in §6.5.

6.1.1 Definition of regions and MJO metric
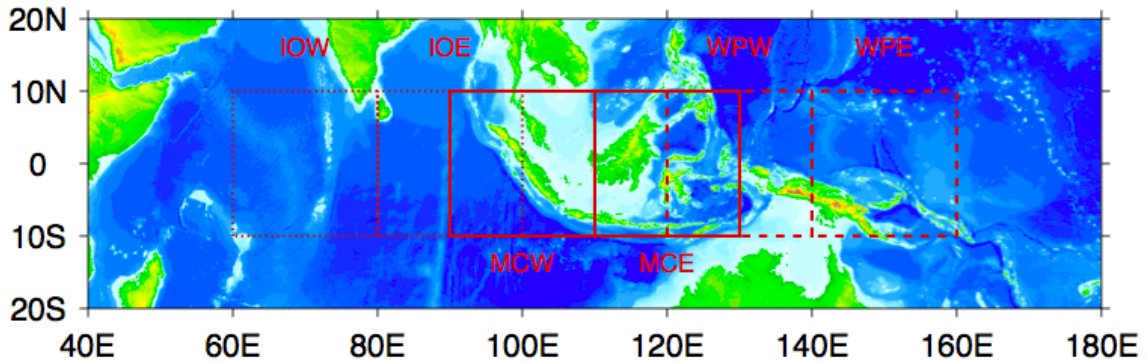
Figure 6.1 *Map to show the six equatorial regions of study: western and eastern Indian Ocean (IOW, IOE; dotted line), Maritime Continent (MCW, MCE; solid line) and West Pacific (WPW,WPE; dashed line). The text refers to the equatorial regions by their abbreviations.*

The process-based diagnostics described above have been applied to six equatorial areas in the Indo-Pacific region (Fig. 6.1). Throughout the text the regions will be referred to by the abbreviations in Fig. 6.1: western and eastern Indian Ocean (IOW and IOE), Maritime Continent (MCW and MCE) and West Pacific (WPW and WPE). To define a metric of MJO activity, 20-100 day band-pass filtered OLR from the AVHRR satellite has been averaged over each of the six equatorial regions. Active, suppressed and weak MJO days are defined as days below, above and within one standard deviation of the mean filtered OLR, respectively (Fig. 6.2). Throughout this chapter, reference will continually be made to both the equatorial regions and MJO metric. For brevity the notation ϵ_{org}^{RH} and ϵ_{org}^{MC} will be used for the modified relative-humidity- and previous moisture-convergent-dependent

formulation for organised entrainment respectively.
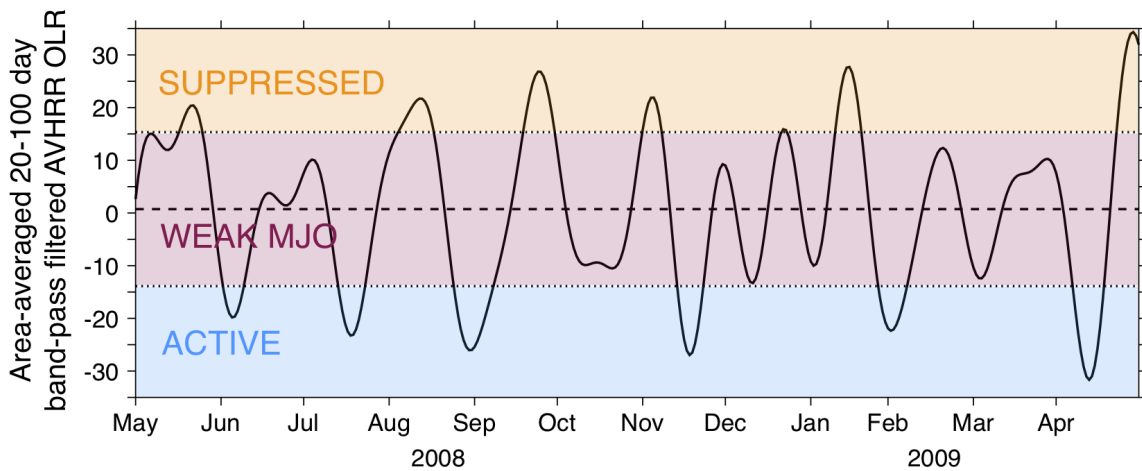
Figure 6.2 *Metric of MJO activity using area-averaged (Fig. 6.1) 20-100 day band-pass filtered OLR from the AVHRR satellite (W m^2). Active, suppressed and weak MJO days are defined as below, above and within one standard deviation of the mean, respectively. The example here is for IOE.*

6.2 TCW and precipitation statistics

In the tropics, sustained deep convection has long been associated with a humid environment (e.g. Raymond, 2000; Derbyshire *et al.*, 2004). However, the relationship between the total column precipitable water (TCW) and precipitation has only emerged more recently as being important to the simulation of intraseasonal phenomena such as the MJO (Bretherton *et al.*, 2004). To investigate this relationship in each of the equatorial regions in Fig. 6.1, the daily accumulated precipitation is binned into 1-$kg\,m^{-2}$-wide bins of TCW and divided into weak, active and suppressed MJO days according to the MJO metric described in Fig. 6.2. In all versions of the IFS, across all regions, precipitation values increase rapidly with increasing TCW; results for IOW (Fig. 6.3), MCE (Fig. 6.4) and WPE (Fig. 6.5) are shown as a representative sample of the Indo-Pacific region. The observed relationship between precipitation and TCW, plotted as the dash dot line, is defined using TRMM satellite precipitation and ECMWF operational analysis TCW.

In Fig. 6.3, for quantities of TCW above 40 kg m^{-2}, there is a clear distinction between the behaviour of precipitation at different values of TCW in the versions of the IFS with ϵ_{org}^{RH} (OPER, ENTRN and CAPE) and those with ϵ_{org}^{MC} (Cy31r1 and CONV). This distinction is consistent at longer forecast lead times (Figs. 6.3 (b), (d) and (f)) and for all types of days defined by the MJO metric in Fig. 6.2; active and suppressed days exhibit a noisier distribution, but this is due to fewer days in the TCW bins compared with weak MJO days (dashed lines). For TCW amounts between
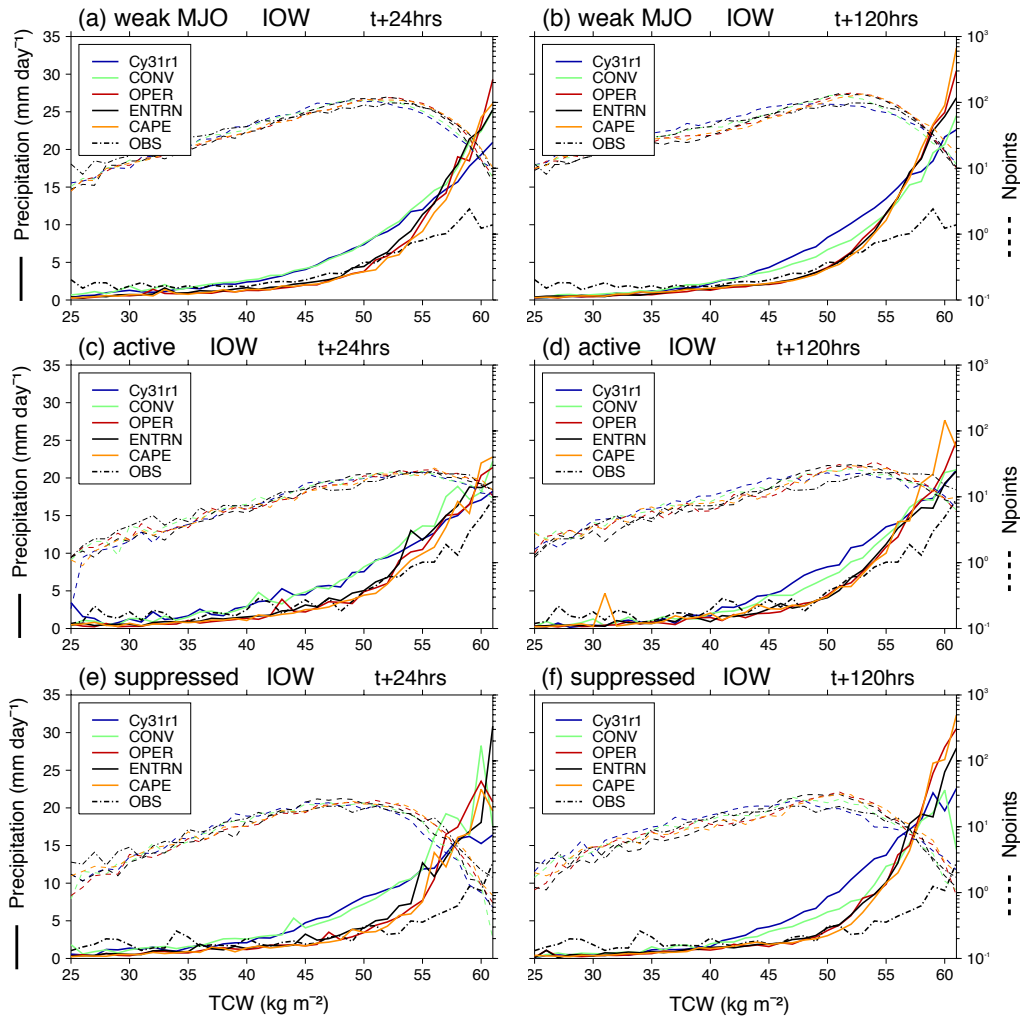
Figure 6.3 *Solid lines represent daily averaged precipitation in 1-kg m^{-2}- wide bins of total column water (TCW) for grid points in IOW at a 1-day (left) and 5-day (right) forecast lead time for weak MJO (a,b), active (c,d) and suppressed days (e,f). Distribution of data points in each bin is represented by the dashed lines. Observations (dash dot) refers to precipitation from TRMM satellite data and TCW from ECMWF operational analysis.*

40 and 55 kg m^{-2}, versions of the IFS with ϵ_{org}^{RH} agree well with observations, exhibiting a lower precipitation rate at the same quantities of TCW than versions of the IFS with ϵ_{org}^{MC}. At higher values of TCW, above 55 kg m^{-2}, precipitation rates in OPER, ENTRN and CAPE all increase sharply. At these values, versions of the IFS with ϵ_{org}^{RH} precipitate more than those with ϵ_{org}^{MC}; all versions of the IFS produce more precipitation than that observed by satellite. The rapid increase in precipitation at higher TCW contents in the IFS is more apparent during suppressed days than active MJO days, especially at longer forecast lead times (Fig. 6.3 (f)). The relationship described above between TCW and precipitation in IOW is also true of IOE and MCW (not shown).

The relationship does not hold, however, in MCE (Fig. 6.4). In MCE, the main differences
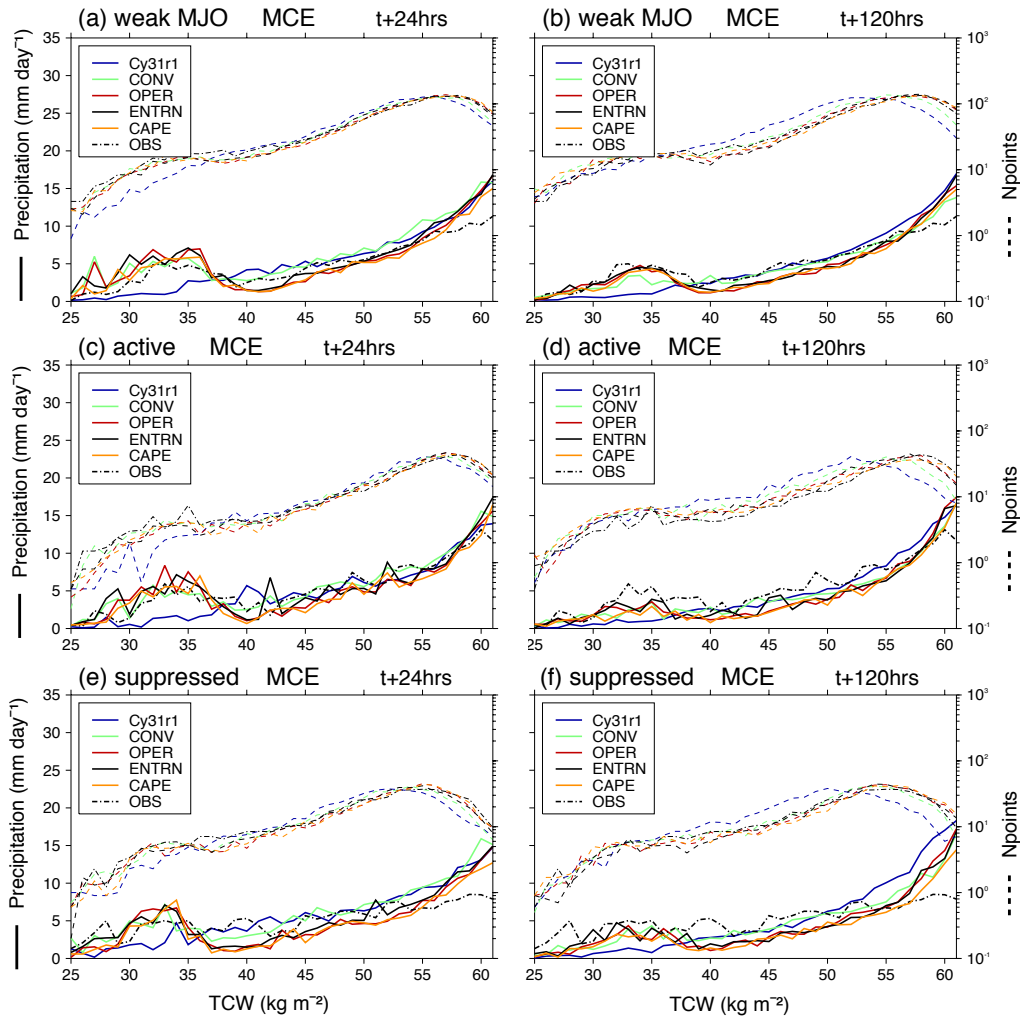
Figure 6.4 *As Fig. 6.3, but for MCE.*

between the versions of the IFS are at low values of TCW. At a 1-day forecast lead time all versions of the IFS, with the exception of Cy31r1, display a small peak in precipitation rates between 25 and 37 kg m^{-2}, followed by a rapid decrease between 37 and 40 kg m^{-2} (Fig. 6.4 (a),(c) and (e)). The same feature is reproduced in the observations (dash dot line). Therefore, at a 1-day forecast lead time in MCE, TCW values between 30 and 35 kg m^{-2} produce the same amount of precipitation, approximately 5 mm day^{-1}, as TCW values between 50 and 55 kg m^{-2}. At longer forecast lead times, this peak is reduced significantly; at a 5-day forecast lead time TCW values between 30 and 35 kg m^{-2} produce equivalent precipitation rates with TCW values between 40 and 45 kg m^{-2} (Figs. 6.4 (b), (d) and (f)). This feature is present, but to a lesser extent, in WPW (not shown). The formulation of ϵ_{org}^{RH} is not responsible for this peak; both OPER and CONV display the same behaviour despite having different entrainment formulations: ϵ_{org}^{RH} and ϵ_{org}^{MC} respectively. Since Cy31r1 is the only version of the IFS run at a lower horizontal resolution, T$_L$255 ($\sim$80 km)

compared with T_L799 (~25 km), capturing this observed feature could be a consequence of the islands of the Maritime Continent being represented more accurately. This could also be related to orographic enhancement of precipitation or the strength of the land-sea breeze around the islands. Above $40\,\mathrm{kg\,m^{-2}}$, similar to Fig. 6.3, versions of the IFS with ϵ_{org}^{RH} produce slightly less precipitation for a given amount of water in the atmospheric column than versions with ϵ_{org}^{MC}. MCE does not exhibit the rapid increase in precipitation rates at large TCW values with ϵ_{org}^{RH} which is observed in all the equatorial regions to the west of it (Fig. 6.3). In MCE, the overesitmation, compared with observations, of precipitation at high TCW values is reduced.
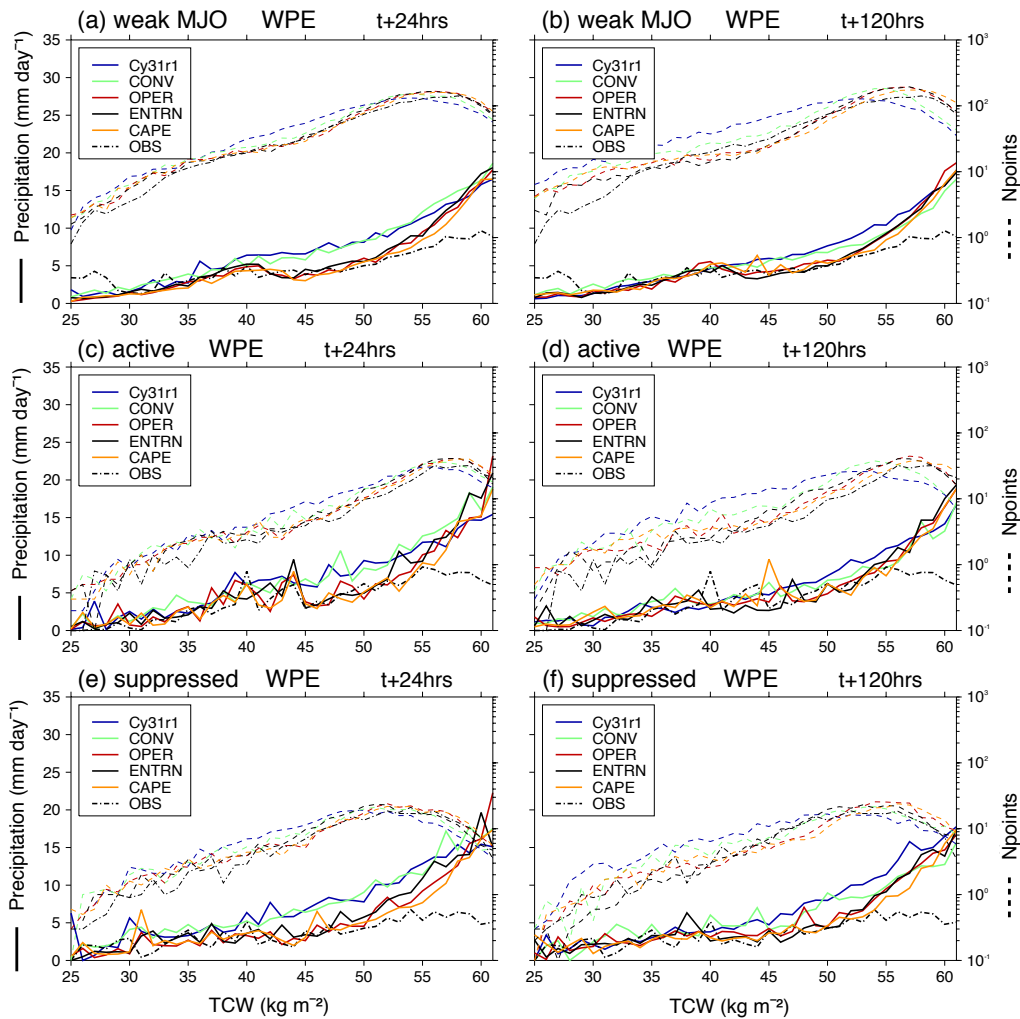
Figure 6.5   *As Fig. 6.3, but for WPE.*

In WPE, all versions of the IFS exhibit similar behaviour between precipitation and TCW at low water contents and rain rates, and all agree well with the observed relationship at these values (Fig. 6.5). Above $40\,\mathrm{kg\,m^{-2}}$ ($45\,\mathrm{kg\,m^{-2}}$), versions of the IFS with ϵ_{org}^{RH} produce less precipitation on weak and suppressed (active) MJO days for a given TCW than those with ϵ_{org}^{MC}. The distinction

between versions of the IFS with ϵ_{org}^{RH} and ϵ_{org}^{MC} can not only be made at lower values of TCW on suppressed days, but, especially at a 5-day forecast lead time, is more prominent compared with days when the MJO is active (Fig. 6.5 (d)). For TCW values between 40 and 55 kg m^{-2}, versions of the IFS with ϵ_{org}^{RH} agree better with observations than IFS versions with ϵ_{org}^{MC}. For values of TCW above 55 kg m^{-2}, all versions of the IFS overestimate the amount of precipitation compared with observations. Since OPER and CAPE behave similarly in Figs. 6.3, 6.4 and 6.5, it can be concluded that the modified variable adjustment timescale τ had little effect on the relationship between TCW and precipitation.
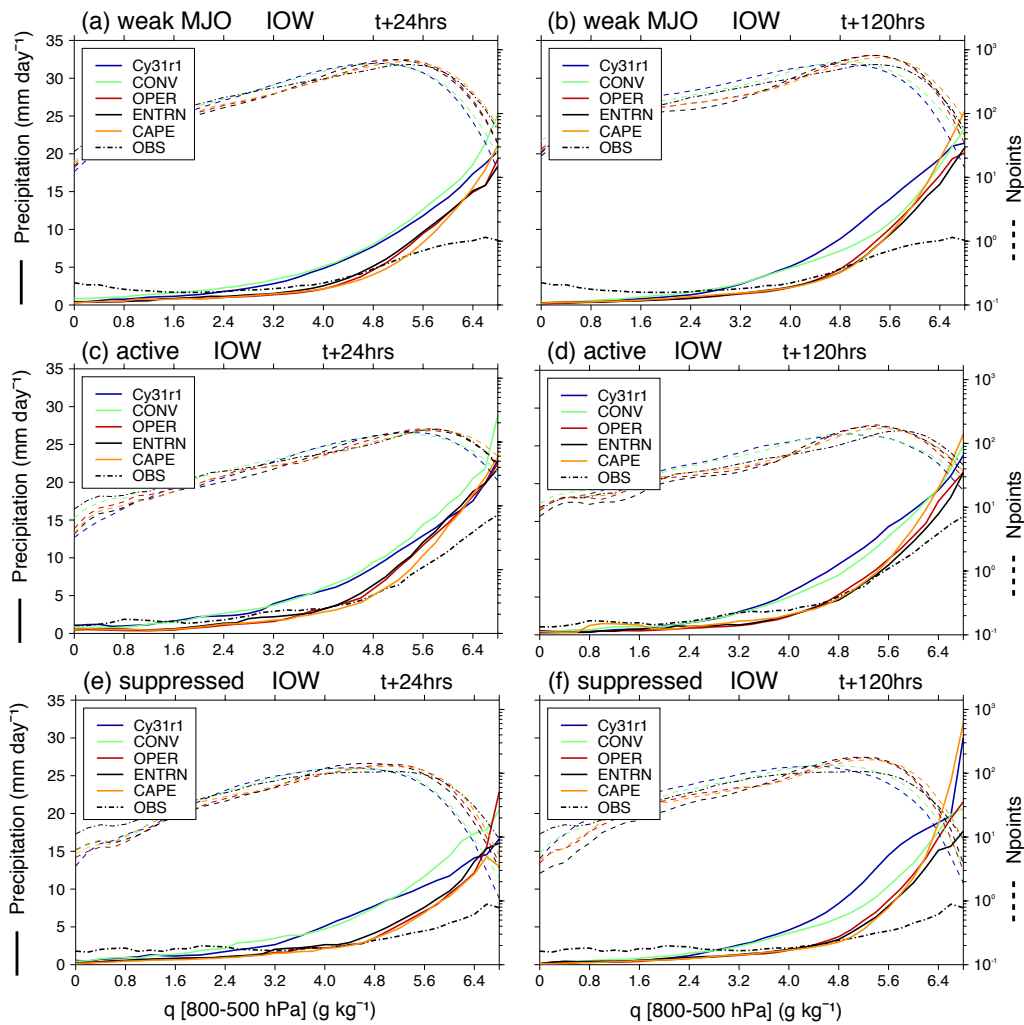
Figure 6.6 *As Fig. 6.3, but for daily averaged precipitation in 0.2-g kg^{-1}- wide bins of 800 to 500 hPa averaged specific humidity.*

The 'best' MJO was produced with ϵ_{org}^{RH} (Chapter 4), and an effect of ϵ_{org}^{RH} was to moisten the tropical mid-troposphere between 800 and 500 hPa (Chapter 5). Therefore, the TCW-precipitation diagnostic has been repeated for mid-level specific humidity - averaged between 800 and 500 hPa

- to identify whether the relationship between precipitation and environmental humidity at those levels has changed with the introduction of ϵ_{org}^{RH}. For consistency, the same equatorial regions, IOW, MCE and WPE, are shown in Figs. 6.6, 6.7 and 6.8 respectively. As with the TCW-precipitation diagnostic, comparisons are made with observations (dash dot line), using TRMM precipitation and ECMWF operational analysis specific humidity.

In all versions of the IFS, across all equatorial regions, precipitation rates increase with increasing mid-level humidity. As with TCW and precipitation, there is a distinction between versions of the IFS with ϵ_{org}^{RH} and versions with ϵ_{org}^{MC}, but only above approximately 2.4 g kg^{-1}. At low precipitation rates and dry mid-tropospheric humidity values, all versions of the IFS exhibit similar behaviour: in IOW and WPE, the model underestimates the amount of precipitation compared with observations, especially during weak MJO days (Figs. 6.6 (a) and (b), and 6.8 (a) and (b), respectively). This is not a characteristic observed in other equatorial regions (e.g. MCE; Fig. 6.7).
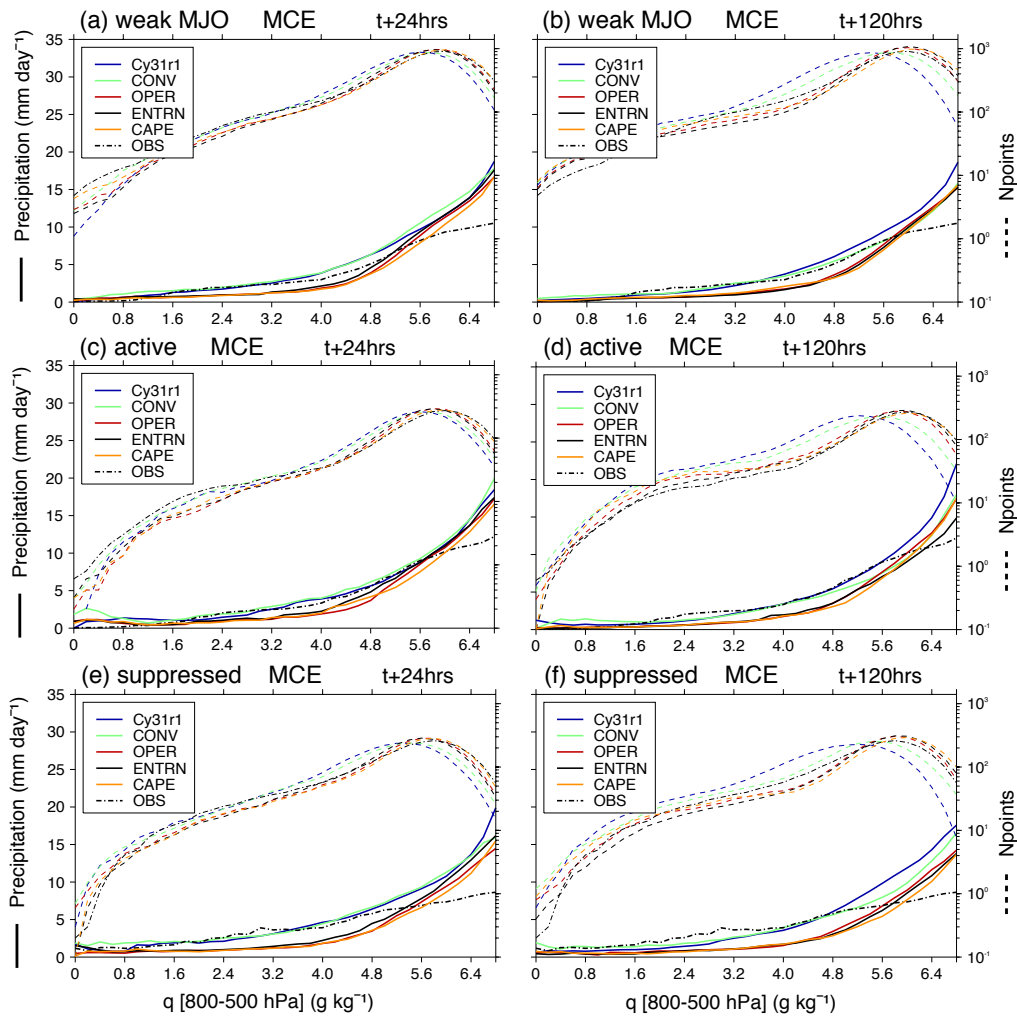
Figure 6.7 *As Fig. 6.6, but for MCE.*

Between 2.4 and 4.8 g kg^{-1}, where precipitation rates increase gradually with increasing humidity, for a given amount of humidity at mid-levels, versions of the IFS with ϵ_{org}^{RH} are able to maintain a lower precipitation rate than those with ϵ_{org}^{MC}. In the equatorial regions which are predominantly made up of ocean, IOW (Fig. 6.6), IOE (not shown) and WPE (Fig. 6.8), this results in a closer agreement with observations between 2.4 and 4.8 g kg^{-1}. Conversely, in the equatorial regions containing the Indonesian islands, MCW (not shown), MCE (Fig. 6.7) and WPW (not shown), maintaining a lower precipitation rate for a given mid-tropospheric humidity leads to a less realistic relationship compared with observations. These results suggest that, with ϵ_{org}^{RH}, the IFS is able to build up more moisture in the atmospheric column before it is removed by convective precipitation. The increase of entrainment in dry columns could be the mechanism through which convection is suppressed and the build up of humidity is achieved.
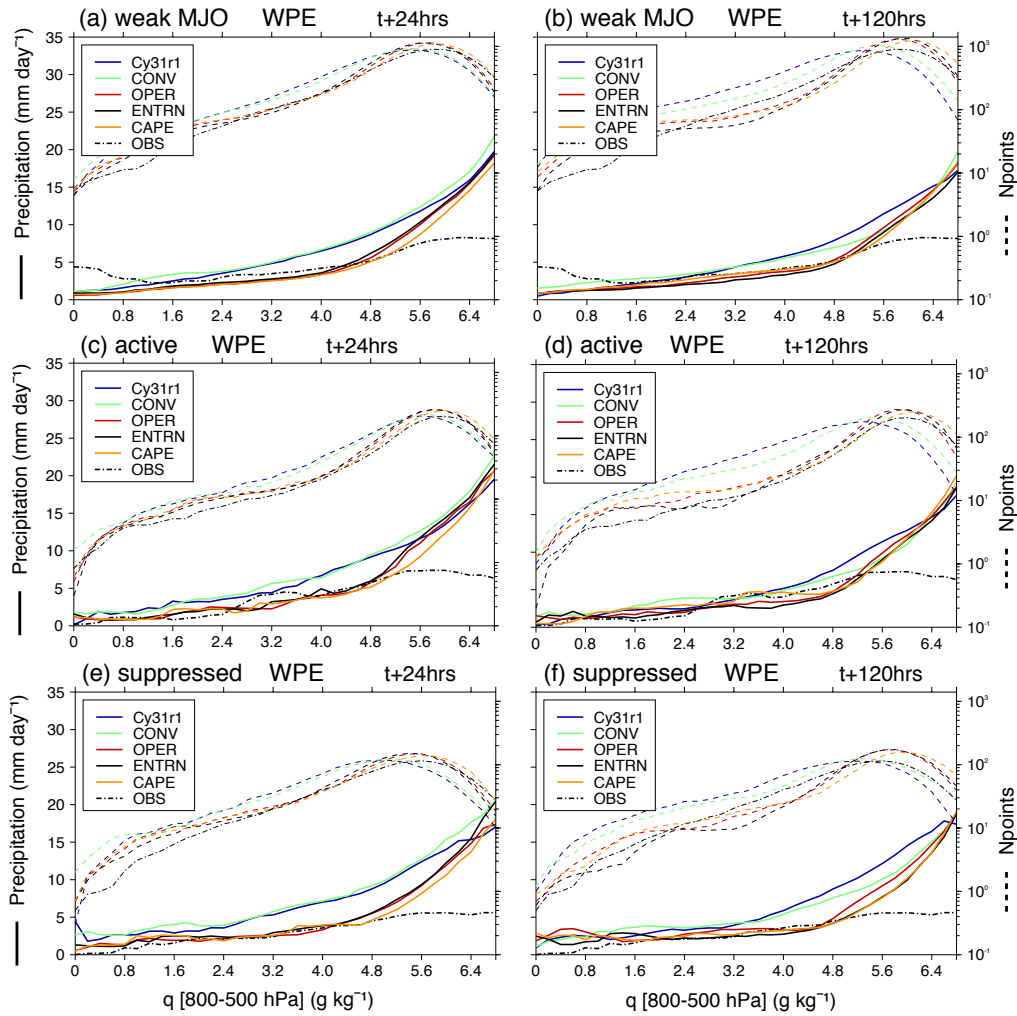
Figure 6.8 *As Fig. 6.6, but for WPE.*

Above 4.8 g kg^{-1}, precipitation rates in ϵ_{org}^{RH} versions of the IFS increase more rapidly than

those versions with ϵ_{org}^{MC}, resulting in all versions of the IFS behaving similarly when the mid-troposphere is very moist. However, compared with observations, all versions of the IFS overestimate the amount of precipitation, a characteristic true of all equatorial regions for all types of days. Comparing OPER and CAPE in Figs. 6.6, 6.7 and 6.8 shows that, as with the TCW-precipitation statistics, the variable adjustment timescale τ does not substantially affect the relationship between moisture in the mid-troposphere and precipitation rates.

Figs. 6.3 - 6.5 (Figs. 6.6 - 6.8) show that the introduction of ϵ_{org}^{RH} in the IFS has changed the behaviour between precipitation and TCW (mid-level humidity) for moderate values between 40 and 55 kg m^{-2} (2.4 and 4.8 g kg^{-1}). At these values, with ϵ_{org}^{RH}, the IFS is able to maintain lower precipitation rates for a given amount of TCW or mid-tropospheric moisture, which, for the equatorial oceanic regions of IOW, IOE and WPE, result in a closer agreement with observations. This change in relationship means that moderately moist columns remain moist for longer due to the suppression of convection, allowing instability to build. All versions of the IFS, across all equatorial regions, overestimate precipitation rates in the humid tail of the distribution. Moving to a variable adjustment timescale τ in the closure for deep convection, however, had little effect on the TCW- and humidity-precipitation relationships.

Therefore, it seems that a requirement of a model that reproduces a strong MJO signal, as OPER, CAPE and ENTRN with ϵ_{org}^{RH} do (Chapter 4), is to (a) refrain from producing precipitation in dry columns, and (b) exhibit an exponential increase in precipitation with TCW when the environment is very humid, although this results in an overestimation of precipitation compared with observations. These findings are consistent with work that compared simulations from the Community Atmosphere Model (CAM) with its "superparameterized" counterpart (SP-CAM; Zhu *et al.*, 2009).

6.3   2-dimensional histograms based on precipitation

Fig. 5.5 revealed that IFS versions with ϵ_{org}^{MC} exhibited an unrealistic preferred rainfall rate of approximately 10 mm day^{-1}, while versions with ϵ_{org}^{RH} had a distribution that, although overestimating precipitation at low rainfall rates, agreed more closely with TRMM. The aim of the analysis carried out here is to further investigate the relationship between rainfall rate and (a) OLR, (b) TCW, (c) 800 to 500 hPa averaged specific humidity and (d) CAPE, shown in Figs. 6.9, 6.10, 6.11 and 6.12 respectively. The 2-dimensional histograms of the convection-related parameters versus daily precipitation rate are calculated for all days between May 2008 and April 2009, and averaged over the IOW region. Only IOW at a 1-day forecast lead time is shown; consistent behaviour was found

for the remaining five equatorial regions and for longer forecast lead times.
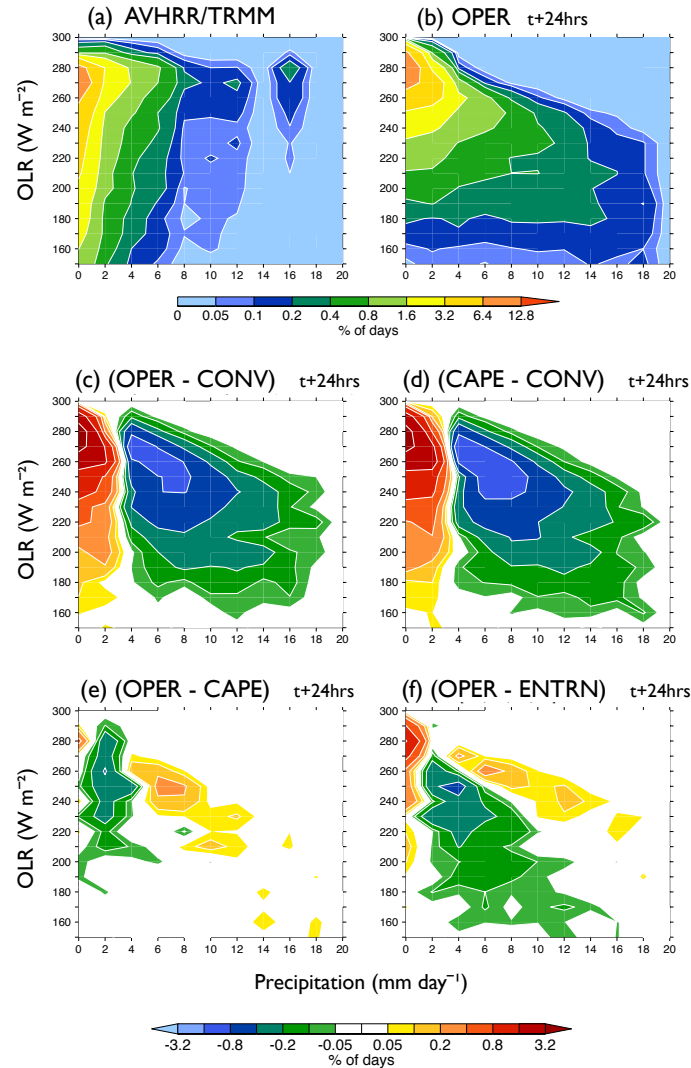
Figure 6.9 *2-dimensional histogram of OLR ($W\,m^{-2}$) versus precipitation ($mm\,day^{-1}$) averaged over IOW from (a) AVHRR OLR and TRMM precipitation satellite data and (b) OPER at a 1-day forecast lead time, (c) difference between OPER and CONV (effect of Cy32r3), (d) CAPE and CONV (effect of ϵ_{org}^{RH} formulation), (e) OPER and CAPE (effect of τ), (f) OPER and ENTRN (effect of ϵ_{org}^{RH} rate). The histograms are calculated for all days between May 2008 and April 2009.*

Fig. 6.9 (a) shows the observed 2-dimensional histogram of OLR versus precipitation from AVHRR and TRMM satellite data respectively; Fig. 6.9 (b) shows the equivalent from OPER at a 1-day forecast lead time. In both model and observations, the maximum in the percentage of days occurs at low values of precipitation (up to 1 mm day^{-1}) and high values of OLR (260 - 280 W m^{-2} in observations and 270 - 290 W m^{-2} in OPER). However, as precipitation increases OPER displays a different distribution of OLR compared with observations. Consistent with §6.2, OPER produces more heavy rainfall than observed, especially during convectively active conditions. Figs. 6.9 (c)-

(f) compare (c) OPER and CONV, (d) CAPE and CONV, (e) OPER and CAPE and (f) OPER and ENTRN, revealing the effect of the Cy32r3 convective parameterization, ϵ_{org}^{RH} formulation, τ and ϵ_{org}^{RH} rate, respectively. Consistent with previous findings in this thesis, Figs. 6.9 (c) and (d) result in the same change in behaviour, confirming that the introduction of ϵ_{org}^{RH} is responsible; changing τ and the rate of ϵ_{org}^{RH} show little change in the distribution of OLR versus precipitation (Figs. 6.9 (e) and (f)). Similarly, ϵ_{org}^{RH} is responsible for the change in behaviour of TCW (Fig. 6.10) and mid-level humidity (Fig. 6.11) versus precipitation. The same cannot be said, however, of the behaviour of CAPE versus precipitation (Fig. 6.12), which is discussed in further detail below.
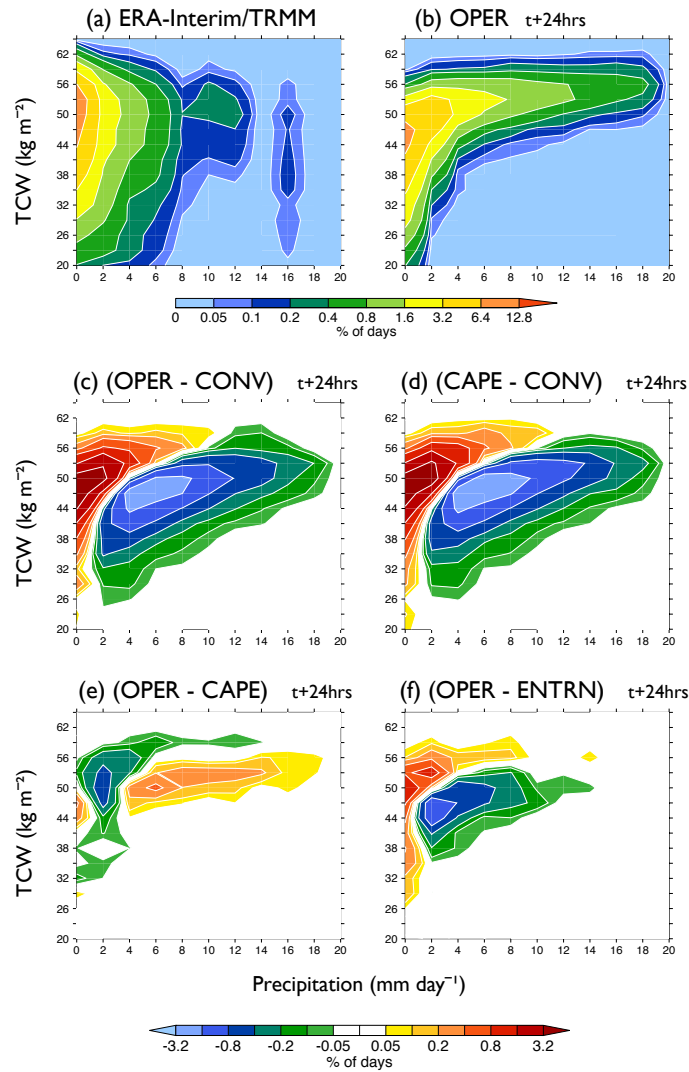
Figure 6.10 *As Fig. 6.9, but for Total Column Water (TCW; kg m^{-2}) versus precipitation (mm day^{-1}). (a) ERA-Interim reanalysis and TRMM satellite data.*

In Fig. 6.9 (d), for a given value of OLR, with ϵ_{org}^{RH}, the IFS produces less rain than with ϵ_{org}^{MC}, especially at high OLR values. For example, in suppressed convective conditions when OLR is

high, approximately 280 W m^{-2}, the effect of ϵ_{org}^{RH} is to produce more days with rain rates between 0 and 3 mm day^{-1} and fewer days with rain rates between 4 and 8 mm day^{-1}. This result suggests that with ϵ_{org}^{RH}, the suppressed phase of the MJO would be 'more' suppressed, which would allow more instability to accumulate.

Consistent with the analysis in §6.2, Fig. 6.10 (d) shows that in a moist column with ϵ_{org}^{RH} the IFS produces less rain than with ϵ_{org}^{MC}. For example, for a value of TCW of approximately 50 kg m^{-2} with ϵ_{org}^{RH} the IFS produces more days with precipitation of up to 3 mm day^{-1} and fewer days with precipitation at values above 4 mm day^{-1}. Reducing the rate of ϵ_{org}^{RH} has the equivalent change in behaviour but it is somewhat weakened (Fig. 6.10 (f)). The effect of the variable τ is weak and has the opposite sign; in a moist column with the variable τ the IFS produces more days with more rain and fewer days with less rain.

The behaviour of mid-level humidity versus precipitation in OPER differs from observations. In OPER the maximum percentage of days is found at low humidity and precipitation values, and precipitation rates increase steadily as humidity increases (Fig. 6.11 (b)). However, in observations, defined here as ERA-Interim humidity and TRMM precipitation, there are no days with high area-averaged rain rates and the maximum percentage of days is found at high humidity, low precipitation values (Fig. 6.11 (a)). Fig. 6.11 (d) shows that the effect of ϵ_{org}^{RH} is, for all values of mid-tropospheric humidity, to produce more days with low precipitation up to 3 mm day^{-1} and fewer days with more than 4 mm day^{-1}. Therefore, results from Figs. 6.10 and 6.11 show that with ϵ_{org}^{RH} the IFS is able to accumulate more moisture in the tropical atmosphere, with the convection scheme removing less moisture from dry or moderately moist columns. As with TCW, halving the rate of ϵ_{org}^{RH} weakens the signal of the ϵ_{org}^{RH} formulation (Fig. 6.11 (e)), and τ has a weak signal of the opposite sign (Fig. 6.11 (f)).

Changes in the CAPE versus precipitation behaviour cannot be attributed to ϵ_{org}^{RH} alone; introducing a variable τ (Fig. 6.12 (d)) and reducing the rate of ϵ_{org}^{RH} (Fig. 6.12 (e)) also affect the relationship. With ϵ_{org}^{RH} there are, for all rain rates, fewer days with very low values of CAPE. Therefore, there is more CAPE overall in the ϵ_{org}^{RH} IFS, a finding consistent with Fig. 5.6. For moderate and high values of CAPE, larger than 100 J kg^{-1}, with ϵ_{org}^{RH} the IFS produces more days with less rain, up to 4 mm day^{-1}, and fewer days with rain rates larger than 4 mm day^{-1} (Fig. 6.12 (c)). Therefore, with ϵ_{org}^{RH}, the IFS is able to further destabilise the atmospheric column by building up more CAPE, with less being removed by convection when CAPE is low. For CAPE versus precipitation, both τ and the halved ϵ_{org}^{RH} have the same effect, consistent across all rain rates- fewer days with CAPE values below 400 J kg^{-1}, and more days with high CAPE values, above 500 J kg^{-1}.
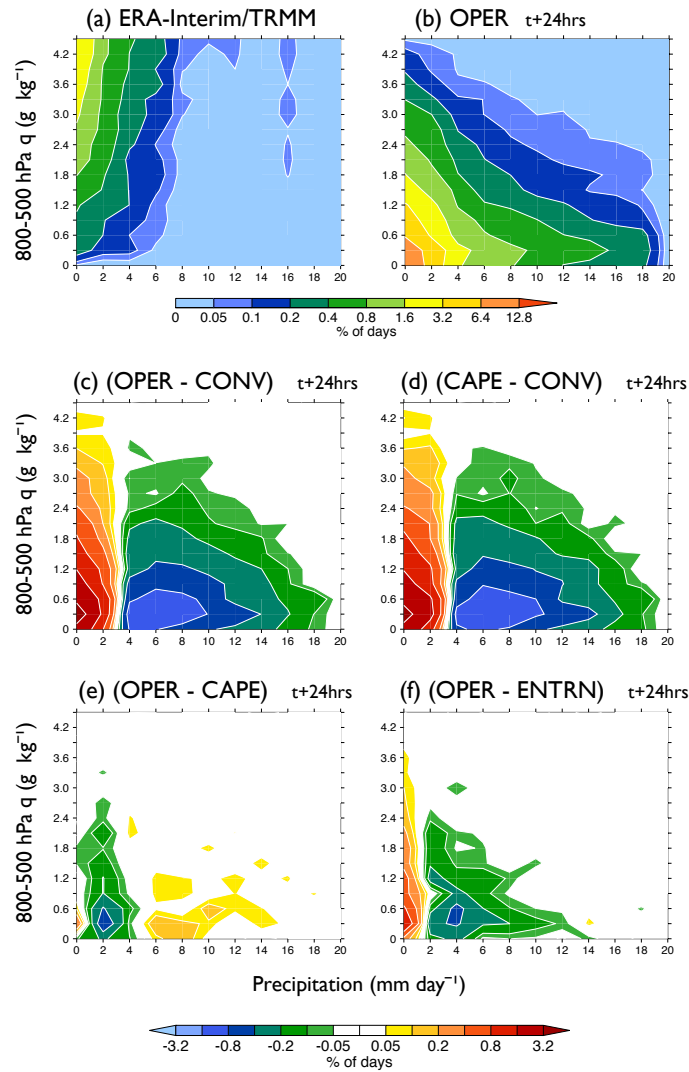
Figure 6.11 *As Fig. 6.9, but for 800 - 500 hPa averaged specific humidity (g kg^{-1}) versus precipitation (mm day^{-1}). (a) ERA-Interim reanalysis and TRMM satellite data.*

The analysis here of convection-related parameters versus precipitation rates builds up a consistent picture of the effect of changing the formulation of organised entrainment from ϵ_{org}^{MC} to ϵ_{org}^{RH}. It is worth recalling the discussion in Chapter 2 on the "recharge-discharge" theory of the MJO proposed by Bladé and Hartmann (1993). They suggest that the period of an MJO is set by the time it takes for the atmosphere to build up instability, or "recharge", after stabilisation through convection, or "discharge", has occurred. Results here suggest that the modified IFS, with ϵ_{org}^{RH}, is able to more effectively "recharge" the atmosphere. More CAPE (Fig. 6.12) and moisture (Figs. 6.10 and 6.11) are able to build up in the tropical atmosphere without being released through convective precipitation; this results in suppressed convective conditions becoming more suppressed (Fig. 6.9). The mechanisms described here lead to a better representation of the suppressed phase of the MJO
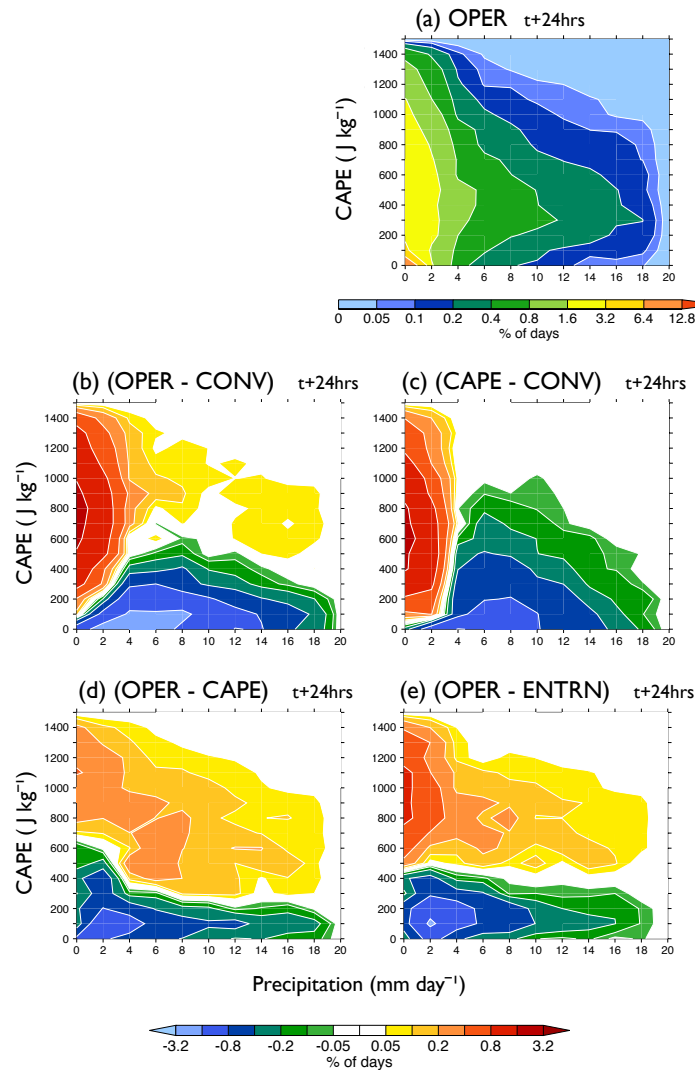
Figure 6.12 *As Fig. 6.9, but for CAPE (J kg^{-1}) versus precipitation (mm day^{-1}). No observational data is available for comparison.*

and, since more instability is built up, lead to more vigorous deep convection when that instability is released, hence also a better representation of the active phase of the MJO.

6.4 Tropical convective moistening

The April 2009 case study discussed in Chapter 4, is used to test the hypothesis that the modified IFS, with ϵ_{org}^{RH}, is better able to simulate the destabilisation of the tropical atmosphere before a deep convective event. Figs. 6.13, 6.14 and 6.15 show how the vertical structure of moisture changes during a 50 day period in March and April 2009 in IOW, MCE and WPE respectively. These regions are shown for consistency with §6.2. The 20-100 day band-pass filtered OLR from the AVHRR satellite is also plotted (thick black line); the minimum in filtered OLR indicates the maximum

strength of the convective event in that region.
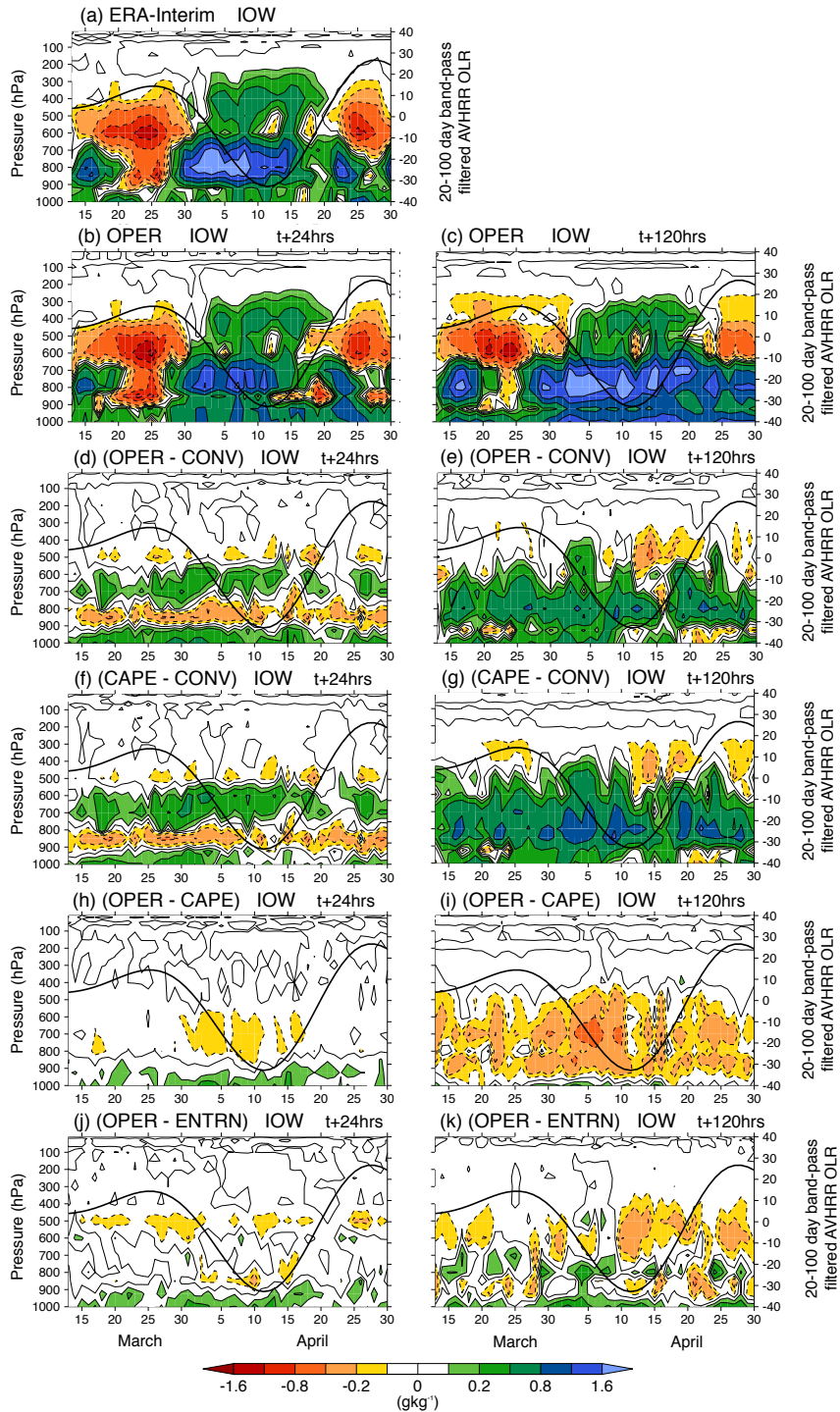
Figure 6.13 *Change from the initial state in the vertical structure of specific humidity averaged over IOW for a 50-day period in March and April 2009. (a) ERA-Interim, (b) and (c) OPER at a 1- and 5-day forecast lead time. Difference at a 1- and 5-day forecast lead time between OPER and CONV (effect of Cy32r3; (d),(e)), CAPE and CONV (effect of ϵ_{org}^{RH} formulation; (f),(g)), OPER and CAPE (effect of τ; (h),(i)) and OPER and ENTRN (effect of ϵ_{org}^{RH} rate; (j),(k)). Area-averaged 20-100 day band-pass filtered OLR from the AVHRR satellite (thick black line).*

Fig. 6.13 (a) shows, over IOW, the 'observed' change from the initial state in the vertical structure of moisture with data from ERA-Interim reanalysis. In mid-March, approximately 25 days prior to the strong minimum in filtered OLR which occurred on 12th April, ERA-Interim displays a drying of more than 1.2 g kg^{-1} at mid-levels, with a maximum at 600 hPa. This drying coincides with the maximum in filtered OLR, or the suppressed phase of the MJO. Approximately 10 days prior to the convective maximum, there is a distinct moistening of more than 1.6 g kg^{-1} in the lower-troposphere, which, with the passage of the wave, extends into the mid- and upper-troposphere reaching 300 hPa during mid-April. In late April, there was a further mid-troposphere drying with a maximum at 600 hPa, associated with the return to suppressed conditions over IOW. Fig. 6.13 (b) shows that compared with ERA-Interim, OPER successfully captures the mid-tropospheric drying before and after the convective maximum, but underestimates the lower-tropospheric moistening prior to the minimum in filtered OLR at a 1-day forecast lead time. The moist layer in OPER between 900 and 600 hPa has strengthened considerably at a 5-day forecast lead time (Fig. 6.13 (c)).

At a 1-day forecast lead time, the effect of the modified Cy32r3 convective parameterization (Fig. 6.13 (d)) is, irrespective of the phase of the wave, to (a) moisten the surface, and a layer in the mid troposphere between 700 and 600 hPa by more than 0.4 g kg^{-1}, and (b) dry a layer in the lower troposphere between 900 and 800 hPa by more than 0.4 g kg^{-1}. This effect can be directly attributed to ϵ_{org}^{RH} (Fig. 6.13 (f)). At longer forecast lead times, however, the effect of ϵ_{org}^{RH} is to moisten the tropical troposphere up to 400 hPa, with a maximum of more than 0.8 g kg^{-1} at approximately 800 hPa. Therefore, with ϵ_{org}^{RH}, the IFS is able to build up considerably more moisture prior to the convective maximum associated with the MJO; Thayer-Calder and Randall (2009) showed this was a feature which is also apparent in SP-CAM. However, as forecast lead time increases, an effect of ϵ_{org}^{RH} is to moisten throughout the entire passage of the wave, resulting in an overestimation of mid-tropospheric moisture compared with ERA-Interim, especially in late April after the convective maximum has occurred. Halving the rate of ϵ_{org}^{RH} and changing to a variable τ had little effect on the change in moisture during the MJO event after 1 day of the forecast (Figs. 6.13 (h) and (j)). At a 5-day forecast lead time, τ exhibits a drying in the middle and lower troposphere throughout the passage of the MJO, which compensates for the moistening effect of ϵ_{org}^{RH} and reduces the overestimation of humidity in Cy32r3.

In MCE and WPE, the convective maximum is weaker and occurred later, on 19th and 21st April respectively. As with IOW, ERA-Interim exhibits mid-tropospheric drying in March before the convective maximum, lower- and mid-tropospheric moistening immediately prior to and during
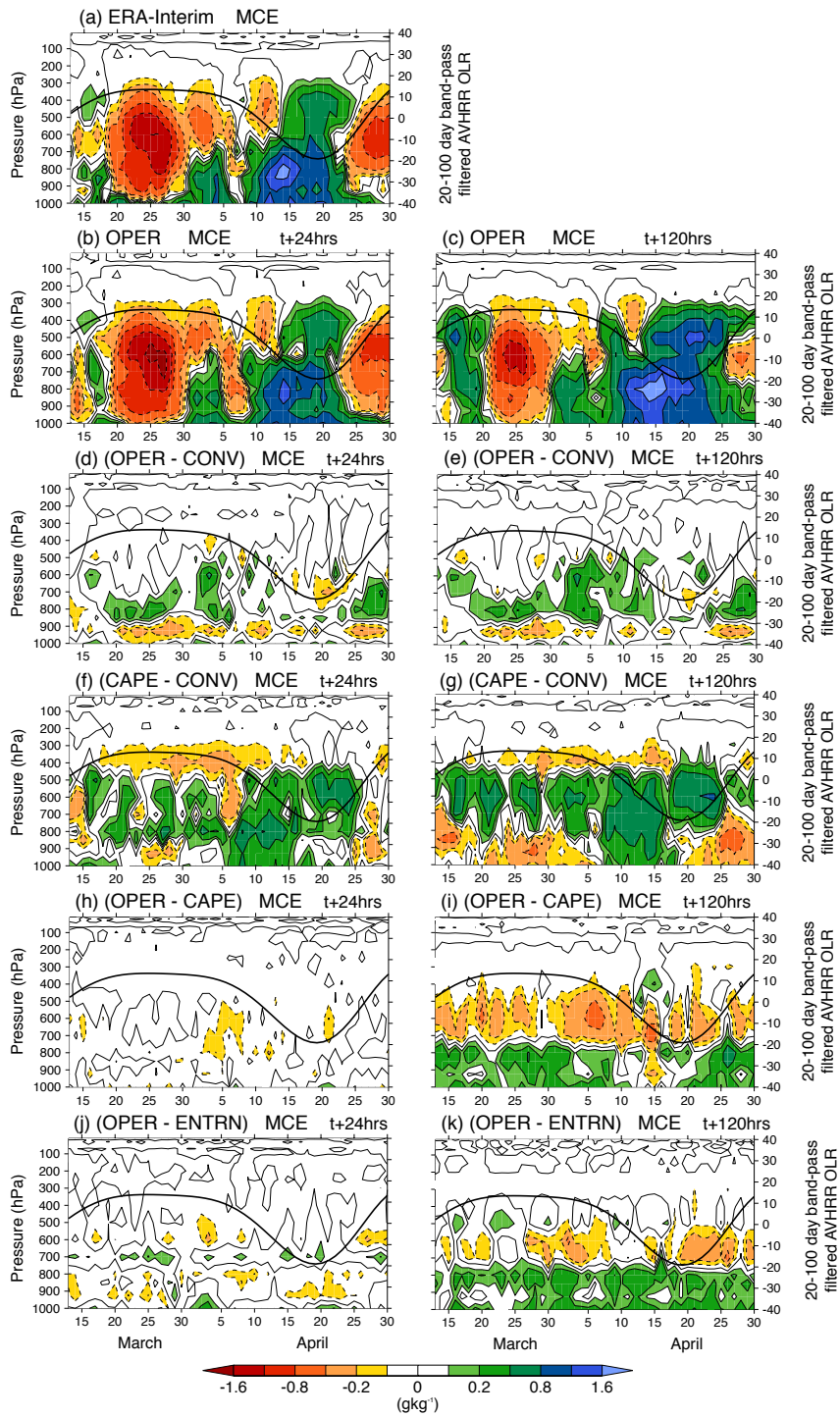
Figure 6.14 *As Fig. 6.13, but for MCE.*

the convective maximum, and in MCE, drying in late April after the passage of the wave (Figs. 6.14 (a), 6.15 (a)). OPER successfully captures these features at both a 1-day and 5-day forecast lead time (Figs. 6.14 and 6.15 (b) and (c)), although, the lower- and mid-tropospheric moistening prior to the convective maximum are underestimated (overestimated) at a 1-day (5-day) forecast

lead time in MCE.
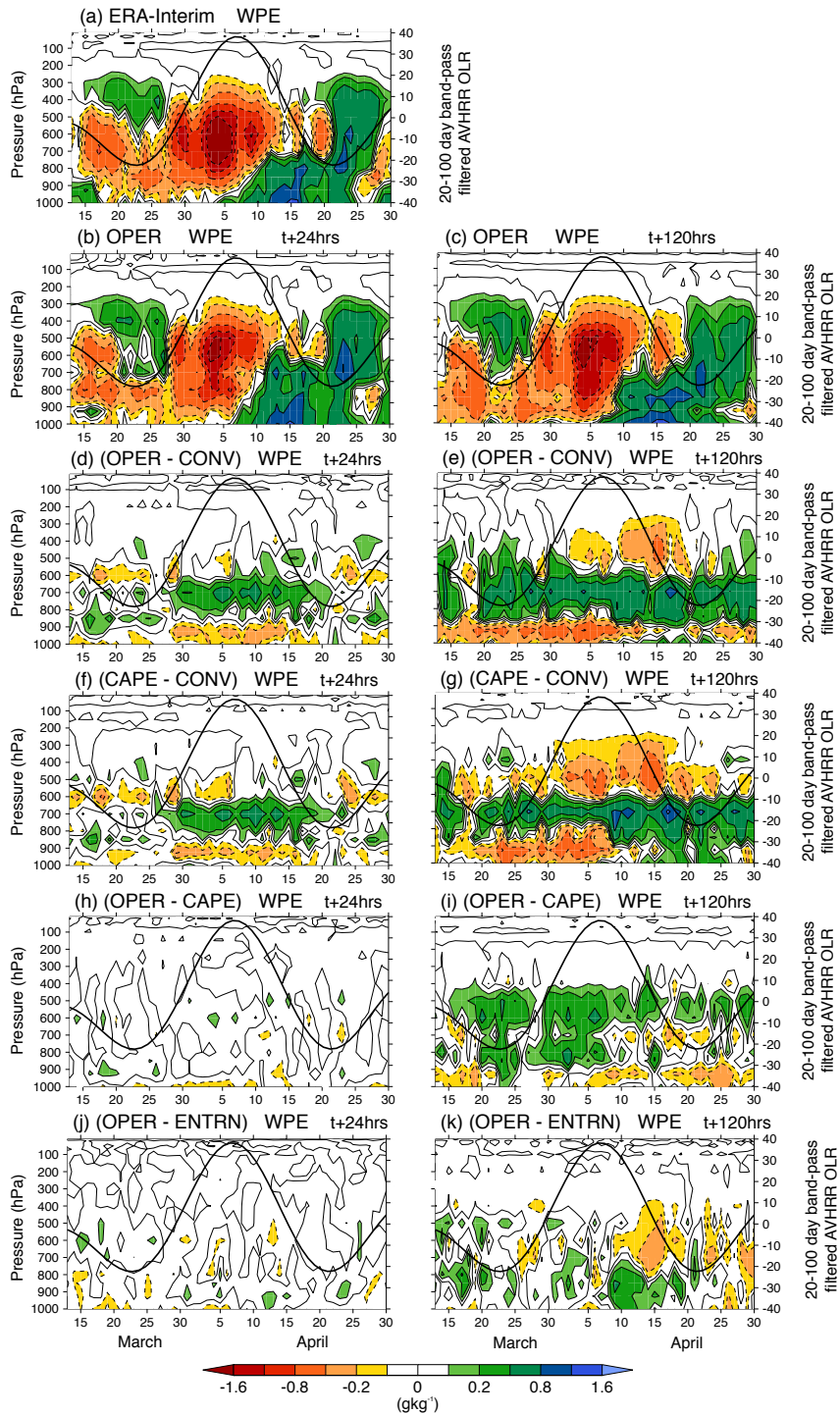
Figure 6.15 *As Fig. 6.13, but for WPE.*

Consistent with IOW, in MCE and WPE, ϵ_{org}^{RH} has the largest impact on the simulation of mois-
ture during the passage of an MJO event, especially at the longer lead time (Figs. 6.14 and 6.15
(g)). However, in MCE and WPE the effect is not to moisten the entire lower- and mid-troposphere

as it was in IOW (Fig. 6.13 (g)), but to dry a layer at the surface before the convective maximum, moisten the entire mid-troposphere and dry a layer above. Convective moistening prior to the convective maximum is stronger at longer lead times in the IFS with ϵ_{org}^{RH}; both MCE and WPE exhibit moistening from the surface up to the mid-troposphere in the days leading up to the late April minimum in filtered OLR (Figs. 6.14 and 6.15 (g)), a feature consistent across all regions.

Changing to a variable τ has little effect on the convective moistening in any region at a 1-day forecast lead time (Figs. 6.14 and 6.15 (h)). At the longer lead time, however, the sign of the effect of τ varies between regions: across the Indian Ocean (IOW; Fig. 6.13 (i), IOE; not shown) τ dries the mid- and lower-troposphere, in MCW, the lower-troposphere dries and mid-troposphere moistens, a signal only observed during the convective maximum (not shown). In MCE and WPW there is a consistent moistening of the lower-troposphere and drying of the mid-troposphere throughout the entire 50 day period (Fig. 6.14 (i); not shown). Finally, in WPE τ exhibits a slight drying at the surface, but otherwise moistens the lower- and mid-troposphere. It is not clear what causes the effect of τ on the convective moistening to differ so much across the equatorial regions of the Indo-Pacific.

Figs. 6.13, 6.14 and 6.15 have shown, by comparison to ERA-Interim, that OPER is able to capture the features of convective moistening during the passage of the MJO. Across each equatorial region in the Indo-Pacific, OPER, like ERA-Interim, exhibits mid-tropospheric drying during periods of maximum filtered OLR and mid-tropospheric moistening during periods of minimum filtered OLR. With ϵ_{org}^{RH}, the IFS is able to better simulate the transition between the two phases. Approximately 10 days prior to the convective maximum, across all regions, the IFS with ϵ_{org}^{RH}, starts to moisten the surface and lower-troposphere. Increasing the entrainment in HadGEM3 integrations ($1.5*\epsilon$) had a similar effect to introducing ϵ_{org}^{RH} in the IFS (Klingaman, 2011). This preconditions the atmosphere for the deep convection associated with the MJO; in a moister environment, convective plumes can penetrate further into the free troposphere without the dilution, by entrainment, of too much dry air. At longer lead times, the IFS with ϵ_{org}^{RH} is often too moist, a problem that the modified IFS shares with SP-CAM (Thayer-Calder and Randall, 2009). If more data were available, it would be worth compositing over a number of MJO events to assess the consistency of these findings.

6.5   Convective moistening by sub-grid scale processes

Continuing with the case study analysis, temperature (T_{phys}; equation 6.1), and humidity, (q_{phys}; equation 6.2) increments for IOW (Fig. 6.16), MCE (Fig. 6.17) and WPE (Fig. 6.18) from the IFS model physics are analysed. Since ϵ_{org}^{RH} is responsible for the advances in MJO simulation (Chapter 4), the analysis here focuses on the effect of ϵ_{org}^{RH} (CAPE-CONV), by examining the role

of convective moistening by the sub-grid scale processes in the IFS during the same 50 day period as in §6.4. The tendencies are calculated by summing contributions from shallow and deep convection ($_{shal}$; $_{deep}$), the cloud and turbulent diffusion schemes ($_{cld}$; $_{turb}$), and, for heating only, the radiation scheme ($_{rad}$). Although all the sub-grid scale processes are included in the analysis presented here, the largest contribution comes from the convection scheme (§6.5.1).

$$T_{phys} \quad = \quad T_{shal} + T_{deep} + T_{cld} + T_{turb} + T_{rad} \tag{6.1}$$

$$q_{phys} \quad = \quad q_{shal} + q_{deep} + q_{cld} + q_{turb} \tag{6.2}$$

A deep convective plume will moisten its immediate environment through the detrainment of moist air into the free troposphere. However, observational studies have shown that vigorous, precipitating convection is associated with a heat source and moisture sink in the mid-troposphere (e.g. Lin and Johnson, 1996a). The moisture sink is due to the removal of moisture from the atmosphere in the form of precipitation, and further drying of the atmosphere through compensating subsidence-the balance of the ascending, moist air with descending, dry air between convective plumes. These features are reproduced in the CAPE experiment; Fig. 6.16 shows that in mid-April, in IOW, during the period of maximum convection (minimum filtered OLR), there is a clear mid-tropospheric heating of more than 4 K day^{-1}, and drying of more than 1.6 g kg^{-1} day^{-1}. The heating and drying associated with the passage of the MJO are stronger at longer forecast lead times (Figs. 6.16 (b) and (f)).

Shallow convection does not penetrate as far into the free troposphere. It detrains more moist air out of the ascending plume, has weaker compensating descent and produces less precipitation than deep convection; therefore, the overall effect of shallow convection is to moisten the lower troposphere. Based on this, Figs. 6.16 (e) and (f) show the moistening of the lower troposphere, and hence the occurrence of shallow convection, in mid-March, during the days of maximum filtered OLR prior to the convective maximum. However, the strongest lower-tropospheric moistening, by more than 1.6 g kg^{-1} day^{-1}, occurs during and in the days immediately after the convective maximum associated with the MJO, a feature which is slightly weakened at longer lead times (Fig. 6.16 (f)).

Apart from a few days with slight cooling and moistening, the sub-grid scale processes are acting to heat and dry the depth of the atmosphere for the entire 50-day period in MCE (Figs. 6.17 (a),(b),(e) and (f)); the same can be said of MCW and WPW (not shown). Although the MJO
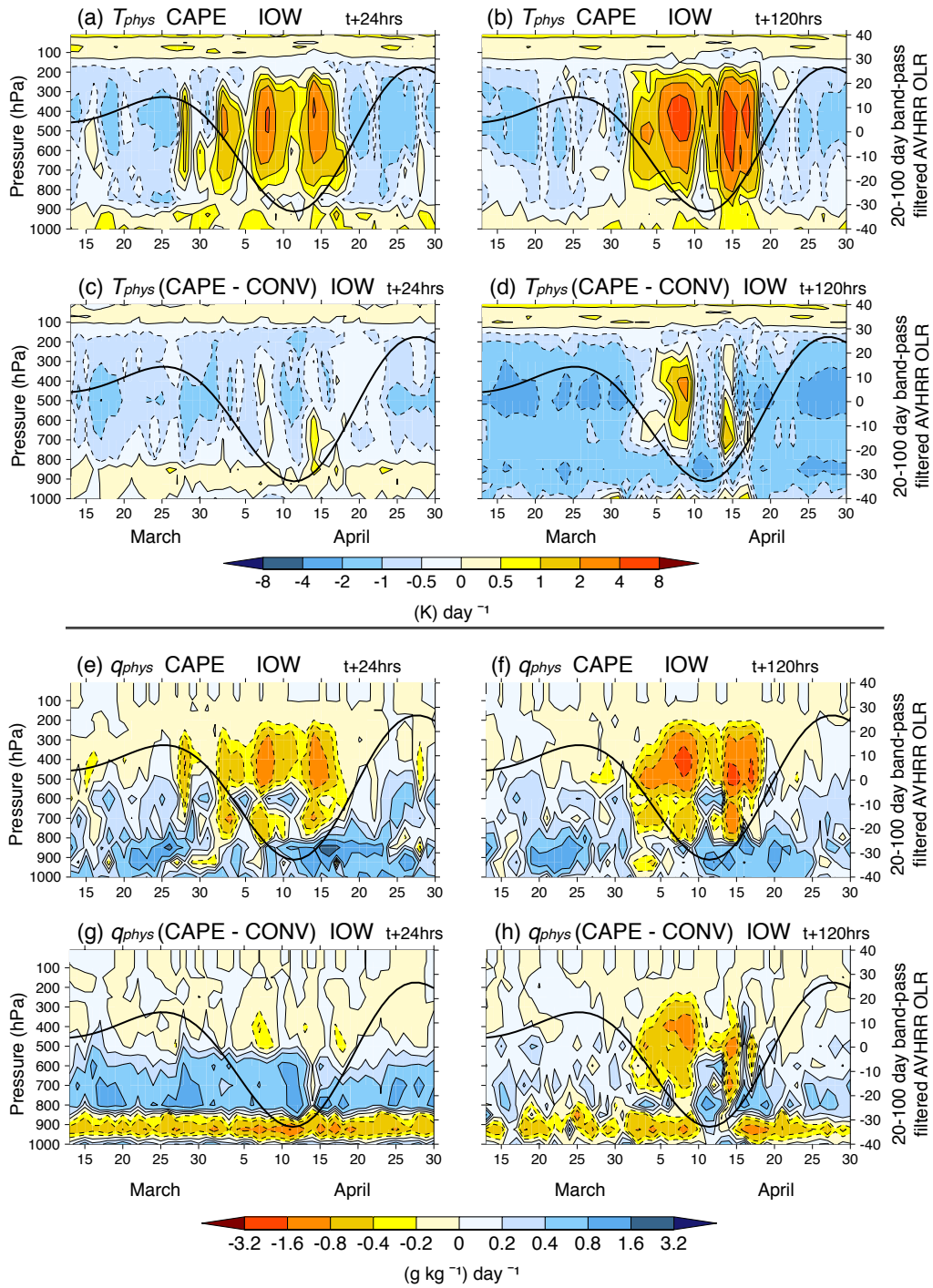
Figure 6.16 *Heating (T_{phys}, equation 6.1; top) and moistening (q_{phys}, equation 6.2; bottom) tendencies from the IFS model physics, accumulated over a day and averaged over IOW. (a),(b),(e) and (f) show CAPE at a 1- and 5-day forecast lead time. (c),(d),(g) and (h) show the difference between CAPE and CONV (effect of ϵ_{org}^{RH} formulation) at a 1- and 5-day forecast lead time. Area-averaged 20-100 day band-pass filtered OLR from the AVHRR satellite (W m^{-2}; thick black line). Negative values are shown by dashed contours.*
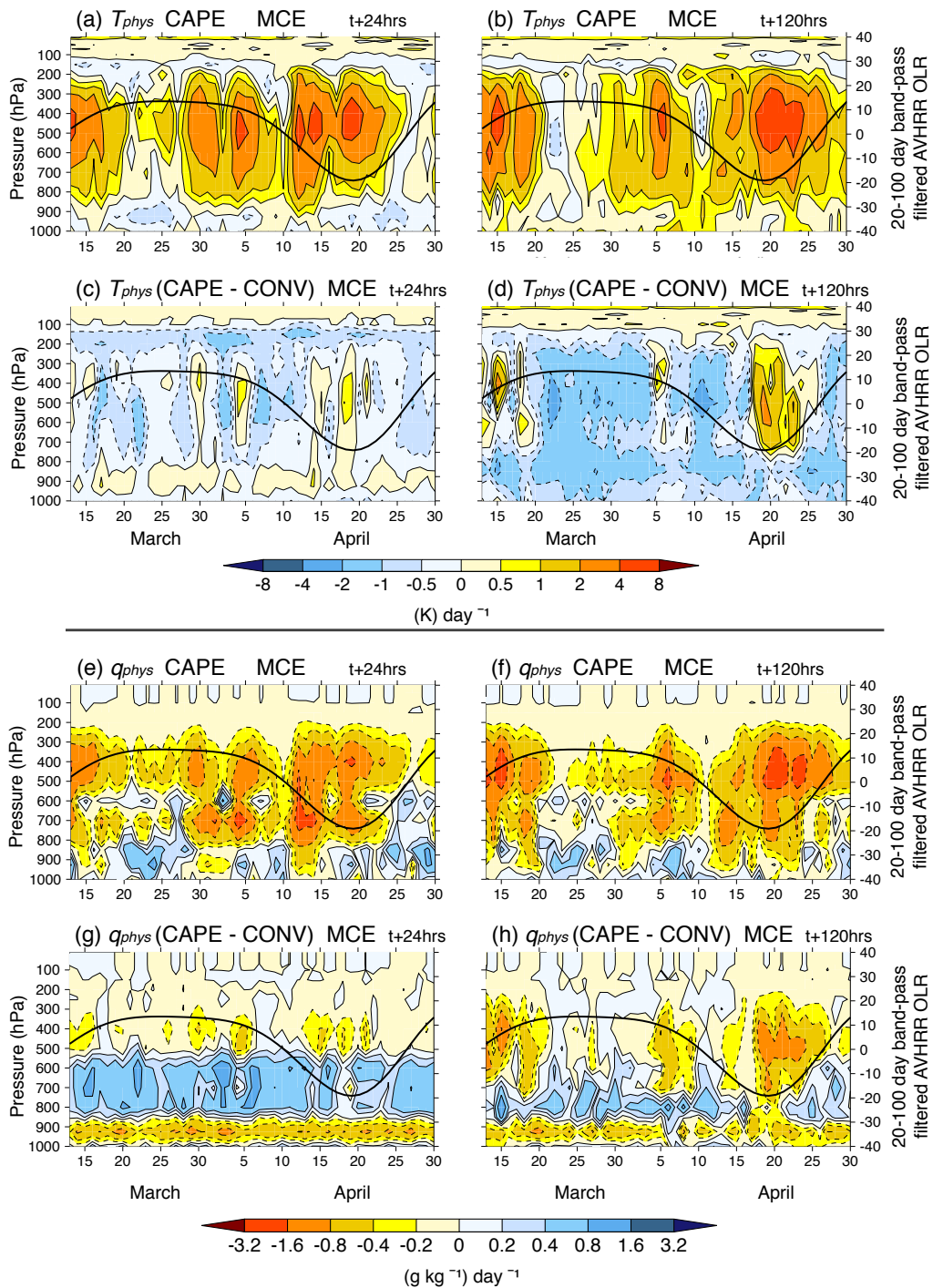
Figure 6.17 *As Fig. 6.16, but for MCE.*

propagated through the Maritime Continent during March and April, deep convection, penetrating above the melting layer, occurred almost all the time in these regions containing the Indonesian islands. Only the equatorial regions which are mostly ocean (IOW; Fig. 6.16, IOE; not shown and WPE; Fig. 6.18) show convective cooling and moistening during the suppressed phase of the MJO.

By comparing the difference between CAPE and CONV across all the equatorial regions, a con-
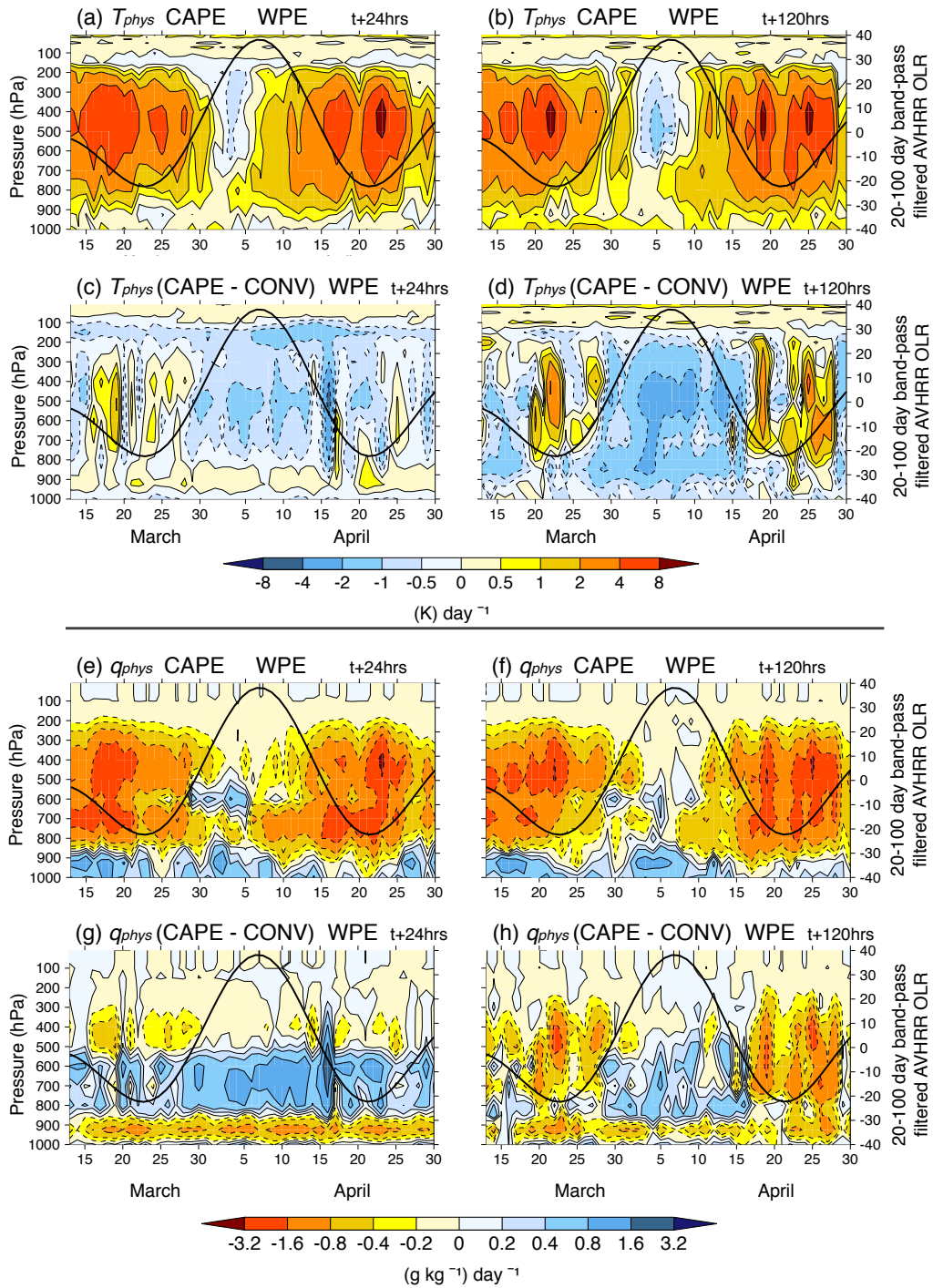
Figure 6.18 *As Fig. 6.16, but for WPE.*

sistent picture emerges of the effect of ϵ_{org}^{RH} on convective moistening by sub-grid scale processes. At a 1-day forecast lead time, ϵ_{org}^{RH} dries (moistens) the lower troposphere (mid-troposphere) between 1000 and 850 (850 and 500) hPa; there is a further, weaker dry layer at 400 hPa (Figs. 6.16, 6.17 and 6.18 (g)). Additionally, at the 1-day forecast lead time, ϵ_{org}^{RH} cools the tropical troposphere through the entire period, apart from a small warming of the mid-troposphere at or near the time

of minimum filtered OLR (Figs. 6.16, 6.17 and 6.18 (c)). At a 5-day forecast lead time, the near-surface drying between 1000 and 850 hPa is still apparent throughout the 50 day period; when the filtered OLR is at a minimum, the entire troposphere dries, with a maximum at approximately 400 hPa. The moist layer, seen after the first day of the forecast, weakened and became confined to days when the filtered OLR was at a maximum (Figs. 6.16, 6.17 and 6.18 (h)). The signal in the heating, observed after a 1-day forecast lead time is consistent, but strengthened, at a 5-day lead time: when filtered OLR is at a maximum (minimum), there is cooling (heating) throughout the troposphere (in the mid-troposphere), strongest between 400 and 500 hPa (Figs. 6.16, 6.17 and 6.18 (d)).

The dry and moist layers in the lower- and mid-troposphere at a 1-day forecast lead time show that the IFS, with ϵ_{org}^{RH}, is producing less shallow, weak-precipitating convection and more convection detraining at mid-levels during the entire 50 day period, a finding consistent with Fig. 5.7 in §5.4. The fact that the IFS, with ϵ_{org}^{RH}, is capable of moistening the mid-levels will result in (a) a weaker trade inversion at the melting level during weak convective events, and (b) a reduction in evaporation at those levels during strong convective events. Therefore, the heating and drying associated with the deep, penetrative convection of the MJO is strengthened. As the IFS moves through the forecast, with ϵ_{org}^{RH}, the periods of strong convective activity are strengthened (more heating and drying), and the periods of weak convective activity become more suppressed (more cooling and moistening). This could explain how the IFS is able to maintain the amplitude of the MJO at longer forecast lead times with ϵ_{org}^{RH}.

6.5.1   Contribution from the convective parameterization

In §6.5 the total heating and moistening from the IFS sub-grid physics was shown. Since the ϵ_{org}^{RH} modification was applied to the convective parameterization, more specifically the formulation for deep convection, the heating and moistening from the entire convection and deep convection scheme alone are isolated for IOW (Fig. 6.19), MCE (Fig. 6.20) and WPE (Fig. 6.21).

In IOW, the convection scheme cools and heats the troposphere during periods of maximum and minimum filtered OLR, respectively (Figs. 6.19 (a) and (b)). This is consistent with the other oceanic equatorial regions (IOE; not shown, WPE; Fig. 6.21). The maximum heating (cooling) occurs at a 5-day (1-day) forecast lead time in the mid troposphere, at approximately 600 hPa (400 hPa). Figs. 6.19 (c) and (d) show that the deep convection scheme is responsible for the signal of heating described above. In the equatorial regions which cover the islands of the Maritime Continent, where convection is occurring most of the time, the deep convection scheme exhibits heating throughout the 50-day period (Fig. 6.20 (c)), which strengthens considerably at a 5-day
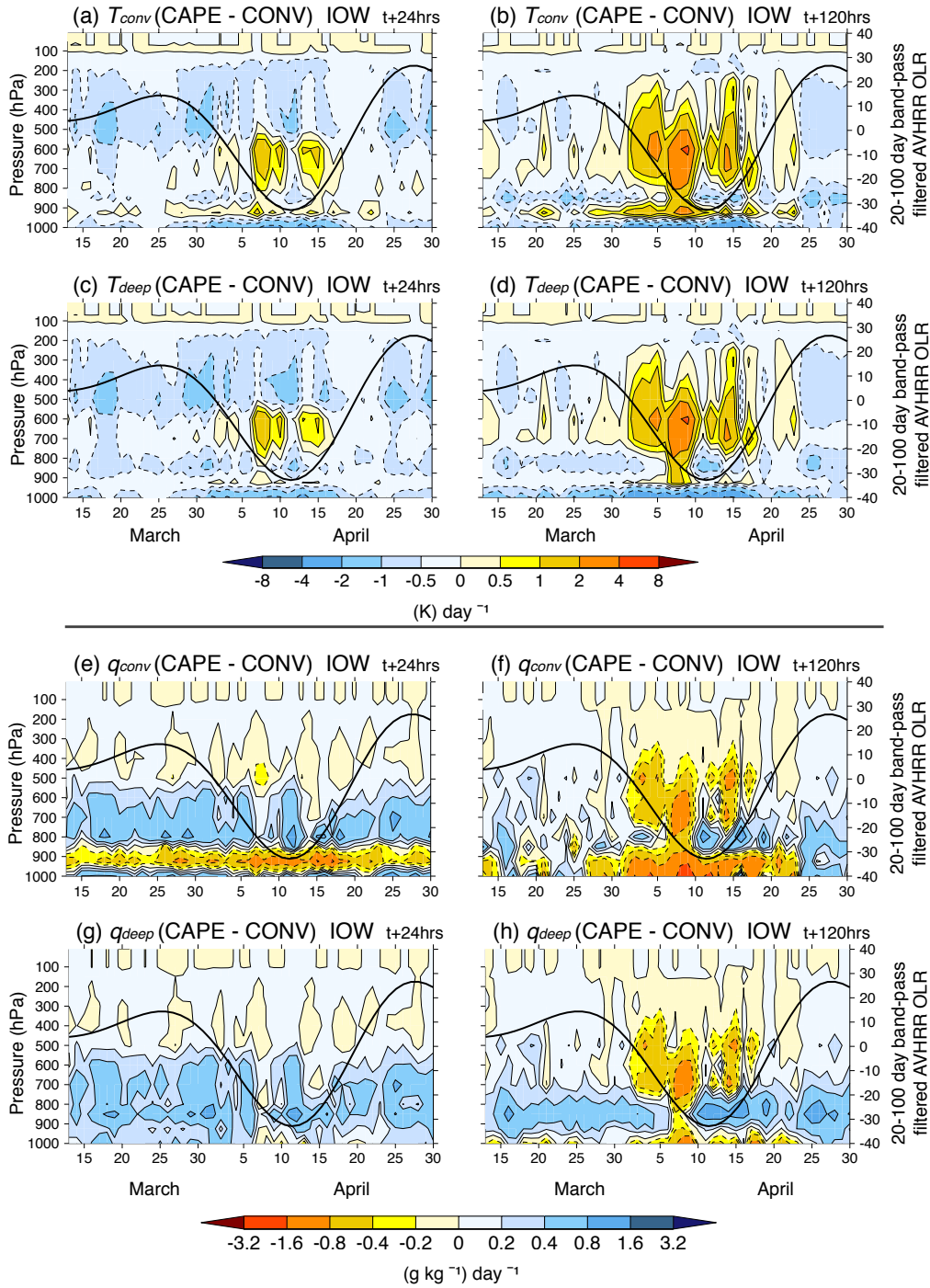
Figure 6.19 *Heating (top) and moistening (bottom) tendencies from the IFS convection scheme ($_{conv} = _{shal} + _{deep}$), accumulated over a day and averaged over IOW. The difference between CAPE and CONV (effect of ϵ_{org}^{RH} formulation) at a 1- and 5-day forecast lead time is shown from the deep and shallow convection schemes combined ($_{conv}$; (a),(b),(e) and (f)) and from only the deep convection scheme ($_{deep}$; (c),(d),(g) and (h)). Area-averaged 20-100 day band-pass filtered OLR from the AVHRR satellite ($W\,m^{-2}$; thick black line). Negative values are shown by dashed contours.*
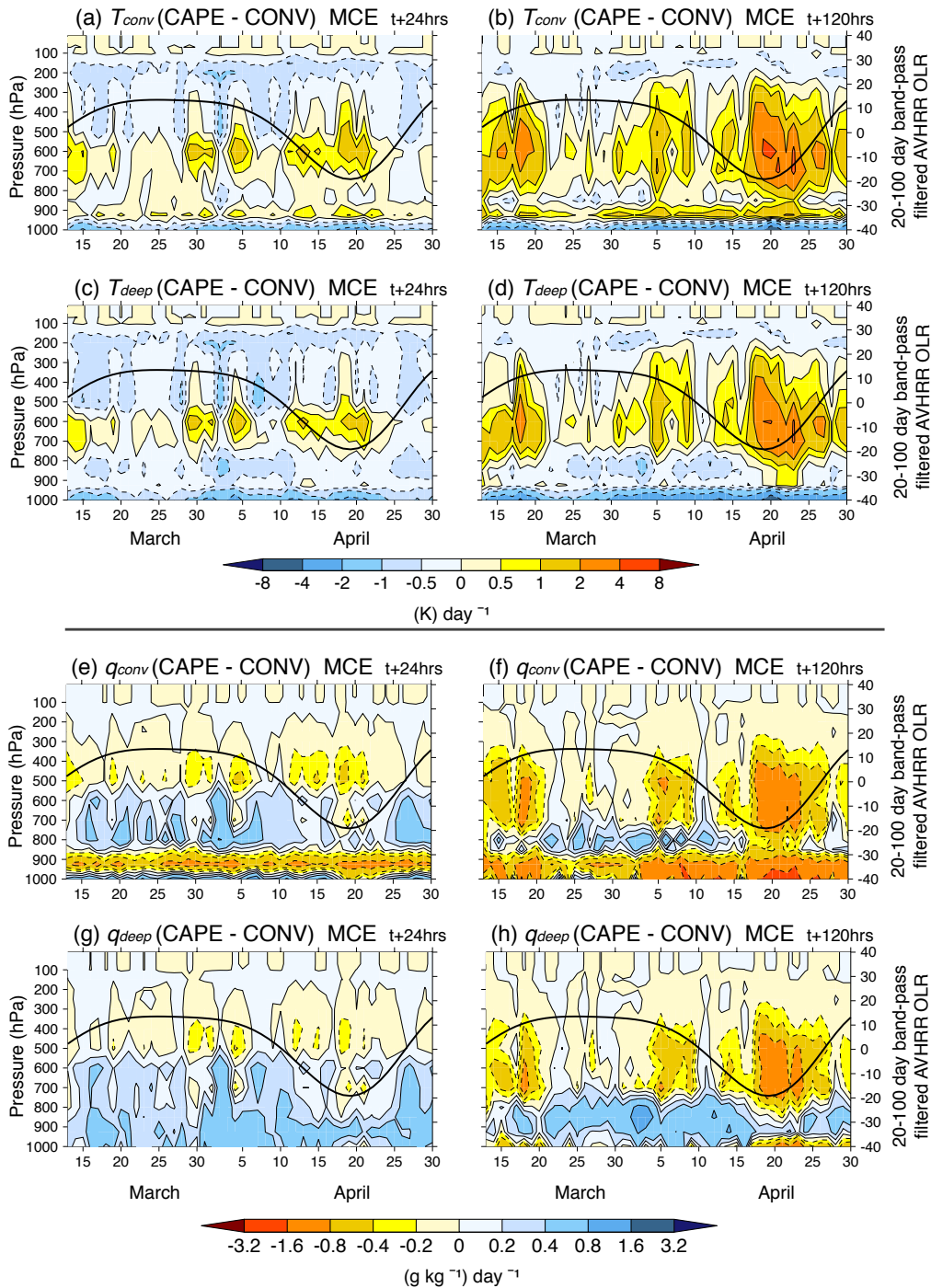
Figure 6.20 *As Fig. 6.19, but for MCE.*

forecast lead time (Fig. 6.20 (d)).

Unlike the vertical structure of heating through the passage of the MJO, a distinction can be made between the contributions to the moistening from the shallow and deep convection schemes. Fig. 6.19 (g) shows that, at a 1-day forecast lead time, the deep convection scheme moistens the middle and lower troposphere through the passage of the wave. At a 5-day forecast lead time,
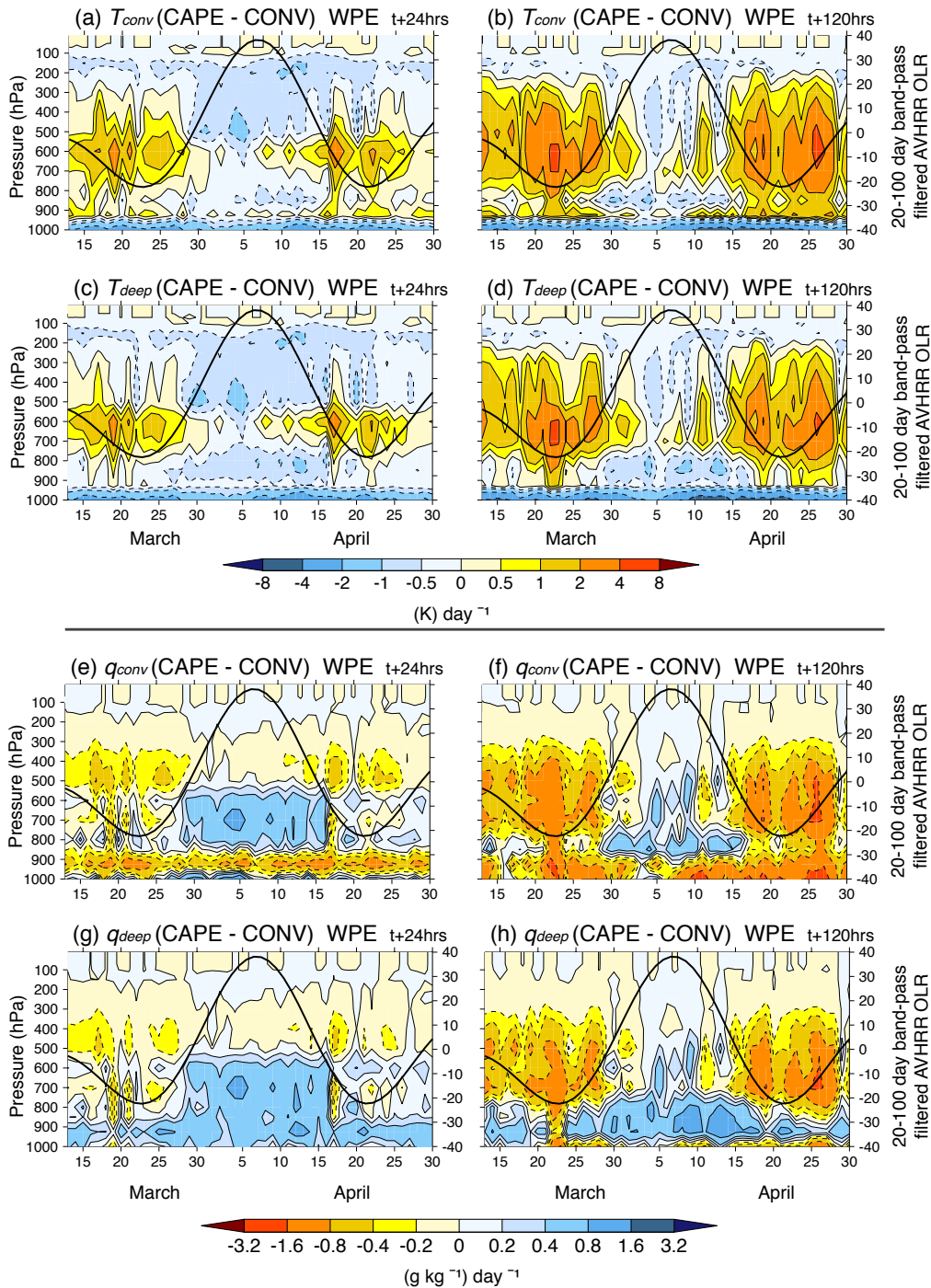
Figure 6.21 *As Fig. 6.19, but for WPE.*

however, the deep convection scheme exhibits a layer of moistening between 950 and 750 hPa during periods of maximum filtered OLR and a distinct mid-tropospheric drying, exceeding 0.8 g kg^{-1}, at around 600 hPa during the minimum in filtered OLR (Fig. 6.19 (h)). Broadly speaking, this signal is consistent throughout the equatorial region (e.g. Figs. 6.20, 6.21 (g) and (h)). Figs. 6.19, 6.20 and 6.21 (e) show that the shallow convection scheme is responsible for the dry layer between

1000 and 850 hPa that was observed at a 1-day forecast lead time in Figs. 6.16, 6.17 and 6.18 (g). At a 5-day forecast lead time, this layer is strengthened during periods of minimum filtered OLR (Figs. 6.19, 6.20 and 6.21 (f)).

Figs. 6.19, 6.20 and 6.21 show that, with ϵ_{org}^{RH}, the occurrence of shallow convection is reduced, especially at longer forecast lead times and during the active phase of MJO convection. This further analysis of the convection scheme tendencies has revealed that the deep convection scheme is directly responsible for (a) the increased drying and heating during phases of active MJO convection (minimum filtered OLR); and (b) the moistening of the mid troposphere during the suppressed phase of the MJO.

6.6 Discussion of results

Through the application of process-based diagnostics, this chapter has focused on the physical mechanisms responsible for the advances in MJO simulation, with ϵ_{org}^{RH}, in the post-Cy32r3 IFS. It is worth recalling the motivation (§3.4) and the physical interpretation (Fig. 5.11) of the modified formulation for organised entrainment. Changing from a moisture-convergent-dependent formulation for organised entrainment (ϵ_{org}^{MC}) to one dependent on relative humidity (ϵ_{org}^{RH}) modified the control on convection and addressed two problems in the IFS. Firstly, it removed the nonlinear feedback between the convection and large-scale dynamics which was responsible for discrepancies in the simulated precipitation and cloud-top height (Bechtold *et al.*, 2008). Secondly, it addressed the emerging consensus that convective parameterizations in NWP models, such as the IFS, do not exhibit sufficient sensitivity to environmental moisture (Derbyshire *et al.*, 2004). By increasing the entrainment in dry columns and decreasing it in humid conditions, ϵ_{org}^{RH} has increased the sensitivity of individual convective plumes to the surrounding moisture field; the intensity of convection is now controlled by the amount of water vapour in a column. The discussion below focuses on the physical mechanisms, presented in this chapter, through which this increased sensitivity to environmental moisture has led to a more accurate simulation of the MJO.

6.6.1 Precipitation-moisture relationship

The introduction of ϵ_{org}^{RH} changed the relationship between precipitation and moisture in the IFS (§6.2), a relationship shown to be highly nonlinear in observations (Bretherton *et al.*, 2004), but very important to the simulation of the MJO (Kim *et al.*, 2009; Zhu *et al.*, 2009; Thayer-Calder and Randall, 2009). In general, the modified relationship between tropical rainfall and column humidity is more realistic compared with observations (Figs. 6.3 - 6.8). With ϵ_{org}^{RH}, the IFS is able to accumu-

late more moisture in the atmospheric column before it starts producing precipitation. This results in (a) fewer occurrences of low-humidity environments producing moderate precipitation rates, i.e. too frequent weak convection; and (b) heavy precipitation occurring only when the atmospheric column is sufficiently moist. The former is likely be the physical mechanism through which the modified IFS, with ϵ_{org}^{RH}, no longer exhibits an unrealistic preferred rainfall peak of approximately 10 mm day^{-1} (Fig. 5.5); and the latter is likely to be a physical mechanism through which the IFS is better able to simulate the transition from shallow to deep convection through the build up of mid-tropospheric moisture (see §6.6.2 for further discussion).

The modified precipitation-moisture relationship in the post-Cy32r3 IFS is by no means perfect. In versions of the IFS with ϵ_{org}^{RH}, at the humid end of the distribution precipitation increases exponentially with column water vapour. This is a feature that the IFS shares with SP-CAM, and which is suggested to be crucial to the successful simulation of the MJO (Zhu *et al.*, 2009). However, in both the IFS and SP-CAM, this results in an overestimation of precipitation in a humid environment compared with observations. Over the islands of the Maritime Continent, versions of the IFS with ϵ_{org}^{RH} exhibit too little precipitation when the atmosphere is dry, and too much precipitation when the atmosphere is moist (Fig. 6.7). This result suggests that the improved mean state over the Indonesian islands, characterised by an increase in convective activity there (Fig. 5.4), is being achieved for the wrong reasons. Bechtold *et al.* (2008) suggested there was an overestimation in precipitation over the Maritime Continent islands in Cy32r3 that was responsible for the IFS producing an MJO that propagated slower than observed. This is not a characteristic that is observed in the case studies shown in this thesis (Figs. 4.18 and 4.20). However, the characteristics of individual MJO events differ so considerably, that with only two case studies the analysis presented here cannot robustly test this hypothesis.

The results from this thesis suggest that tropospheric moisture control on precipitation is a necessary process to for a model to capture if it is to be successful at simulating intraseasonal variability (Figs. 6.3 - 6.8). This adds weight to the existing evidence in the literature that the relationship between precipitation and humidity is important to the representation of the MJO in numerical simulations. Kim *et al.* (2009) applied "process-based" diagnostics to output from eight climate models and showed that the dependence of precipitation on the vertical structure of tropospheric humidity was a feature common among models that produced the most accurate simulations of the MJO. Similar findings have emerged from comparisons between CAM and SP-CAM (Zhu *et al.*, 2009; Thayer-Calder and Randall, 2009). CAM, like versions of the IFS with ϵ_{org}^{MC}, allows strong convection to occur in a dry column. Thayer-Calder and Randall (2009) suggest the dependence on

CAPE in the closure for deep convection in CAM is partly responsible for a missing link between convective mass transport and environmental moisture. This thesis has shown that the IFS is able to increase the sensitivity of convection to column moisture through changing the formulation of organised entrainment, without replacing its CAPE trigger for deep convection.

6.6.2   Preconditioning of the tropical atmosphere

A hypothesis of this thesis is that the modified formulation for organised entrainment, through a modified tropospheric moisture control on precipitation, produces an IFS that is better able to simulate the transition from shallow to deep convection, resulting in a better representation of the MJO. The processes through which this is achieved are the focus of the discussion here.

By relating the convective mass-flux of deep, entraining plumes to the environmental moisture field, the introduction of ϵ_{org}^{RH} changed the control on convection in the IFS; the sensitivity of deep convection to the amount of water vapour in the atmospheric column was increased. Recalling Fig. 5.11, this led to an increase in dry-air entrainment in low-humidity environments. The dilution of a convective plume by dry air will reduce net condensation and buoyancy, inhibit the development of deep cumulonimbus and result in lower cloud-top heights. Therefore, with ϵ_{org}^{RH}, convective plumes ascending in a dry environment will not penetrate as high into the upper-troposphere; fewer deep convective plumes penetrating into the upper-troposphere results in a cooling there (Fig. 5.1). The overestimation of the depth and intensity of convection in dry conditions has been reported as a possible cause for poor simulations of the MJO (e.g. Lin *et al.*, 2006), and proved a tough test for a model's moist physics to represent. However, dry-air entrainment has previously been shown to be an effective mechanism through which tropospheric moisture modulates cloud depth in observational studies (Holloway and Neelin, 2009) and cloud-resolving numerical simulations (Waite and Khouider, 2010).

An effect of the lower cloud-top heights, produced through increased dry-air entrainment, is that more convective plumes will terminate near the melting layer. Recalling Fig. 2.5, the melting layer is a thin stable layer at the zero-degree isotherm (approximately 500 hPa in the tropics) that is maintained by heat absorbed by the melting of precipitation from ice to liquid phase (Johnson *et al.*, 1999). The occurrence of more clouds which terminate near this stable layer and the melting of the associated frozen precipitation results in a loss of heat and an increase in stability at this level. This is suggested as the process through which ϵ_{org}^{RH} increases cumulus congestus in the IFS (Figs. 5.7 - 5.10). A strong stable layer in the middle troposphere will result in more convective plumes detraining there. A similar effect, albeit by a different mechanism, has been seen in GCM

simulations; Inness *et al.* (2001) showed that improving the representation of the freezing level, through a finer vertical resolution, led to a more realistic trimodal distribution of cloud compared with observation.

The increase in cumulus congestus detraining at the melting layer acts to moisten the mid troposphere (Fig. 5.3), slowly eroding the stable layer. As the cumulus congestus deepens, the moistening penetrates further into the free troposphere (Figs. 6.6 - 6.8). Due to the modified tropospheric moisture control on precipitation described above, deep cumulonimbus is only triggered when the environment is sufficiently humid (Figs. 6.3 - 6.8). Therefore, during this transition phase more moisture (Fig. 6.10 and 6.11) and CAPE (Fig. 6.12) can build up, with the convection scheme removing less moisture from dry or moderately moist columns. Waite and Khouider (2010) suggest that, for the transition from shallow to deep convection, the build up of free-tropospheric moisture is more important than the build up of CAPE. In their cloud-resolving simulations, if there is sufficient moisture in the mid troposphere then deep convection can be triggered with relatively low CAPE.

A corollary of the tropospheric moisture control on convection is that once deep cumulonimbus does develop, it does so in a moist environment. When convection occurs in a moist environment, the entrainment of air into the convective plume does not result in significant dilution or loss of buoyancy, but rather strengthens the convective heating. The compensating subsidence between ascending convective plumes results in the formation of a large-scale circulation, which is maintained by a mechanism referred to by Grabowski and Moncrieff (2004) as the moisture-convection feedback. The large-scale circulation deepens the moist layer in the free troposphere and increases the compensating subsidence, which in turn strengthens the large-scale circulation. The findings of this thesis are consistent with the moisture-convection feedback being a physical mechanism which contributes to better maintaining the intraseasonal variability associated with the MJO in the modified IFS.

Recognising the role that thermodynamic feedback processes play in the initiation and evolution of the MJO, Bladé and Hartmann (1993) proposed a "discharge-recharge" theory for the MJO (recall the discussion in §2.3.6). According to their theory, the period of the MJO is set by the time it takes the atmosphere over the tropical Indian Ocean to destabilise or "recharge". The build up of moisture through low- and mid-level cloud increases instability until finally deep convection is triggered and the atmosphere stabilises again. This stabilisation, or "discharge", removes the moisture from the tropical atmosphere and returns it to a dry, suppressed regime. Consistent with this theory, the build up of moisture in the lower and middle troposphere prior to the convective maximum associated with the MJO (Figs. 6.6 - 6.8), suggests that the modified IFS is better able to "recharge"

the tropical atmosphere. Through increasing the stability of the atmosphere, dry-air entrainment is a crucial mechanism through which the modified IFS inhibits the premature development of deep convection, resulting in an improved representation of the suppressed phase of the MJO (Fig. 6.9). Therefore, with ϵ_{org}^{RH}, there is a clearer distinction between active and suppressed conditions associated with the MJO (Figs. 6.9, 6.16, 6.17 and 6.18), as well as a smoother transition between the regimes.

6.7 Conclusions

Despite being able to directly attribute advances in MJO simulation to the introduction of ϵ_{org}^{RH} (Chapter 4), the physical mechanisms responsible were not clear. To address this, a set of process-based diagnostics have been applied to the IFS. By comparing the characteristics of a 'bad MJO' version of the IFS (CONV) with 'good MJO' versions of the IFS (OPER, CAPE and ENTRN), from the analysis presented here, some observations can be made about the physical processes required to be able to successfully simulate the characteristics of the MJO.

Making the organised entrainment rate in the IFS parameterization for deep convection more sensitive to the environmental humidity surrounding the convective plume has confirmed the hypothesis proposed in Chapter 5: that the modified IFS is better able to simulate the transition from shallow to deep convection. With ϵ_{org}^{RH}, the IFS starts to produce precipitation with more water in the atmospheric column (Figs 6.3, 6.4 and 6.5) and a mid-troposphere that is more moist (Figs. 6.6, 6.7 and 6.8). This allows the build up of more CAPE (Fig. 6.12) and moisture (Figs. 6.10 and 6.11) without much release or removal from the atmospheric column through convective precipitation. The modified relationship between precipitation and moisture allows for better preconditioning of the lower- and mid-troposphere prior to a large convective event. During the passage of an MJO event in April 2009, with ϵ_{org}^{RH} the IFS was able to moisten the lower troposphere in the days prior to the convective maximum associated with the MJO (Figs. 6.13, 6.14 and 6.15). The moistening of mid-levels (Figs. 6.16, 6.17 and 6.18) decreases the stability of the mid-troposphere at the melting level, which enables the following convective plumes to overcome the stable layer and penetrate into the upper-troposphere. As well as simulating the transition from shallow to deep convection through convective preconditioning by cumulus congestus at mid-levels, with ϵ_{org}^{RH} the distinction between suppressed and active conditions is larger. Suppressed conditions become more suppressed and active conditions more active (Figs. 6.9, 6.16, 6.17 and 6.18). However, in the case of the active phase of the MJO, this has resulted in an overestimation of precipitation compared with observations.

CHAPTER 7

Conclusions

The main findings of the work described in this thesis are summarised in this chapter (§7.1). The extent to which the results described in this thesis have been able to answer the questions raised in §3.6 are discussed, along with potential avenues for future work (§7.2).

7.1 Summary of key findings

This thesis has investigated the representation of the Madden-Julian Oscillation (MJO) in the Integrated Forecasting System (IFS) at the European Centre for Medium-Range Weather Forecasting (ECMWF), a state-of-the-art Numerical Weather Prediction (NWP) model. In particular, the sensitivity of MJO simulation to recent modifications to the convective parameterization in Cycle 32r3 (Cy32r3) of the IFS has been examined.

Bechtold *et al.* (2008) showed that modifications to the model physics, introduced in Cy32r3 of the IFS, led to a more realistic representation of convectively coupled equatorial Kelvin and Rossby waves, as well as improving the simulation of tropical intraseasonal variability associated with the MJO. The Cy32r3 modifications included changes to the convection and vertical diffusion schemes. The work reported in this thesis has isolated and investigated the effect of the modifications to the convective parameterization in Cy32r3 on the simulation of the MJO in the IFS. The revisions to the convection scheme in Cy32r3 included (a) replacing the constant, resolution-dependent CAPE adjustment timescale (τ) in the closure for deep convection with a variable τ, dependent on the updraught vertical velocity averaged over the cloud depth; and (b) changing the dependence of organised entrainment in the formulation for deep convection from a moisture-convergent-dependent formulation (ϵ_{org}^{MC}) to one dependent on the relative humidity of the surrounding environment (ϵ_{org}^{RH}).

The motivation for changing the formulation of entrainment in the deep convection scheme was twofold. Firstly, changing the control on convection was aimed at removing known model errors. The previous moisture-convergent-dependent formulation created a nonlinear feedback between convection and large-scale dynamics that resulted in errors in precipitation and cloud-top height (Bechtold *et al.*, 2008). Secondly, changing to a relative humidity control addressed the emerging recognition in the literature that convective parameterizations in NWP models do not exhibit

sufficient sensitivity to environmental humidity (e.g. Derbyshire *et al.*, 2004).

When multiple changes are implemented in an NWP model, as with those in Cy32r3 of the IFS, it is only possible to speculate about the effect of individual components. The experiments reported in this thesis present a unique opportunity to isolate individual components of the IFS convective parameterization. Recalling Fig. 3.8 and Table 3.1, comparing (a) OPER and CONV, (b) CAPE and CONV and (c) OPER and CAPE isolates the effect of (a) the Cy32r3 convective parameterization (ϵ_{org}^{RH} formulation and τ), (b) the ϵ_{org}^{RH} formulation and (c) the variable τ. The inclusion of the ENTRN experiment addresses the relative importance of the entrainment rate versus formulation of organised entrainment. Following the discussion of the experiments, a number of questions were raised in §3.6. Addressing these questions will provide the structure for the conclusions of this thesis.

To what extent can the advances in the simulation of the MJO in Cy32r3 be attributed to the modified parameterization of convection?

Although it had previously been hypothesised that the convection scheme played a crucial role in the simulation of a more realistic MJO in Cy32r3 of the IFS, the work presented here has provided confirmation. The impact of the Cy32r3 convective parameterization on the representation of the MJO was isolated by comparing hindcast integrations that differed only in their formulation of convection (Fig. 3.8). A set of recognised MJO diagnostics (Waliser *et al.*, 2009) were applied to the YOTC-period integrations to provide a consistent framework for assessing the representation of the MJO. Results have shown that the Cy32r3 convective parameterization is responsible for increasing the variance of convective activity across the Indo-Pacific region (§4.4), and better maintaining the eastward-propagating spectral power (§4.4.2, §4.6.2) and amplitude (§4.5) of the MJO. More specifically, it has been shown that the introduction of the Cy32r3 convection scheme accounts for all of the 4-day extension in predictive skill of the MJO amplitude during the YOTC period (§4.4.3).

Despite the advances in MJO simulation with the Cy32r3 convective parameterization, problems still remain. Cy32r3 exhibits an overestimation of tropical convective activity at longer forecast lead times (§4.4), a slower-than-observed phase speed and, in some cases, still has difficulty propagating the convective signal associated with the MJO through the Maritime Continent (Vitart and Molteni, 2009b). These deficiencies are discussed in more detail in §7.2.

What effect did the individual components of the modified parameterization of convection have on the simulation of the MJO?

Having established that the Cy32r3 convective parameterization was responsible for the improvements in MJO simulation, the hindcast experiments were analysed to determine which part of the modified scheme, the variable τ or the entrainment formulation (ϵ_{org}^{RH}), was responsible. Results have conclusively shown that changing the control on convection, by modifying the formulation of entrainment from ϵ_{org}^{MC} to ϵ_{org}^{RH}, was the key to the advances in MJO simulation described above. Contrastingly, analysis of the ENTRN hindcast experiment showed that, within the ϵ_{org}^{RH} formulation, the simulation of the MJO was not sensitive to changing the rate of entrainment.

A relative-humidity-dependent formulation for organised entrainment led to an IFS that produced a more realistic distribution of precipitation (§5.3) and a trimodal structure of tropical cloud (§5.4), with more cumulus congestus moistening the mid-troposphere (§5.2.1). This resulted in an IFS that was able to increase convective activity in the Maritime Continent and West Pacific (§5.2.2) without producing deep, penetrative convection too often (§5.2.1, §5.3). These results suggest that, with ϵ_{org}^{RH}, the IFS has improved its simulation of the MJO through a better representation of the transition from shallow to deep convection. The physical mechanisms through which this was achieved were the focus of chapter 6 and will be addressed in more detail below.

Moving to a variable CAPE adjustment timescale had a small compensating effect on the mean state of the IFS (chapter 5) but little overall impact on the simulation of the MJO (chapter 4). Recalling Fig. 3.5, the value of the primary peak in the PDF of the variable τ was close to the previous, resolution-dependent constant. This may account for the lack of impact on the simulation of the MJO.

What are the physical mechanisms responsible for the improvements in MJO simulation resulting from the modified parameterization of convection in Cy32r3?

Being able to attribute the advances in MJO simulation to the relative-humidity-dependent formulation for organised entrainment has been a key result of this thesis. However, in order to move away from model specific conclusions and provide information that is relevant to the wider modelling community, the question of how the ϵ_{org}^{RH} formulation was able to achieve a more realistic representation of the MJO must be addressed. This was done in chapter 6 through the application of process based diagnostics which were designed to understand the physical mechanisms at work. This thesis has shown that the introduction of ϵ_{org}^{RH} led to a better representation of the MJO through the mechanisms listed here and described in detail below:

(a) the introduction of a tropospheric moisture control on deep convection.

(b) a more realistic, precipitation-moisture relationship, due to (a).

(c) a better simulation of the transition from shallow to deep convection by the moistening, or preconditioning, of the mid-troposphere, due to (b).

(a) Tropospheric moisture control on convection

Through the commonly used CAPE closure for deep convection, the simulation of penetrative convective plumes in NWP models is often closely linked to the amount of CAPE in an atmospheric column. The build up of tropospheric moisture, however, has been shown to be more important than the build up of CAPE for the accurate simulation of the transition to deep convection (e.g. Redelsperger *et al.*, 2002; Derbyshire *et al.*, 2004; Waite and Khouider, 2010). CAPE is only sensitive to moisture in the boundary layer; a CAPE closure for deep convection was held responsible for the missing link between environmental moisture and convective mass transport which led to a poor simulation of the MJO in CAM (Thayer-Calder and Randall, 2009). The work presented in this thesis supports the shift from CAPE-sensitive to moisture-sensitive formulations for convection. The post-Cy32r3 IFS still has a CAPE closure for deep convection, but in recognition of the importance of environmental humidity the ϵ_{org}^{RH} formulation increases the sensitivity of convection to free-tropospheric moisture. By implementing a formulation that increases entrainment in dry environmental conditions and decreases it in a moist environment (Fig. 5.11), the intensity of convection is controlled by the amount of water in the atmospheric column, not just the moisture in the boundary layer.

(b) Modified precipitation-moisture relationship

The introduction of ϵ_{org}^{RH} and resulting tropospheric moisture control on convection has been shown to modify the relationship between precipitation and moisture (§6.2). With ϵ_{org}^{RH}, the IFS is able to build up more moisture in the atmospheric column before it starts being removed by precipitation. This prevents the IFS from producing weak convection too often, and ensures that heavy rainfall can only occur when the column is sufficiently moist. In general, the modified precipitation-moisture relationship is more realistic compared with observations. However, with ϵ_{org}^{RH}, the IFS is shown to overestimate precipitation at the humid end of the distribution, a problem that also occurs in SP-CAM simulations (Zhu *et al.*, 2009).

(c) Improved preconditioning of the tropical atmosphere

The modified precipitation-moisture relationship and tropospheric control on moisture, more specifically the increased dry-air entrainment in low-humidity environments, has led to an IFS that is bet-

ter able to simulate the transition to deep convection. With the ϵ_{org}^{RH} formulation, dry-air entrainment dilutes ascending plumes in a dry environment. This inhibits the premature development of deep, penetrative convection, a problem previously shown to lead to a poor representation of the MJO (Lin *et al.*, 2006). As a result of forcing convection to terminate lower in a dry environment, more convective plumes detrain in the mid-troposphere. This is evident by the increase in the occurrence of cumulus congestus (§5.4), which results in a more realistic trimodal structure of tropical cloud that is apparent in observations (Johnson *et al.*, 1999) and modelling studies (Inness *et al.*, 2001). The detraining congestus at the melting layer moisten the surrounding environment, acting to recharge the tropical atmosphere so that succeeding convective plumes can penetrate further into the free troposphere. Due to the modified precipitation-moisture relationship described above, during this transition phase more moisture can build up without being released, so that when deep convection does occur it is supported by a moist environment. It has been shown that, through this mechanism, the suppressed phase of the MJO is more suppressed and the transition to the deep, active phase is more realistic. The processes described above are consistent with the "discharge-recharge" theory of the MJO (Bladé and Hartmann, 1993), in which instability builds up through moistening by low- and mid-level clouds ("recharge"), before the moisture is removed by deep convection ("discharge"). Furthermore, it has been shown that the ϵ_{org}^{RH} formulation creates a feedback between convection and the large-scale circulation; dry-air entrainment results in more cumulus congestus which moisten the environment, while a moister environment promotes deep convection and strengthens the large-scale circulation. Grabowski and Moncrieff (2004) showed that this mechanism, referred to as the moisture-convection feedback, was responsible for improvements in MJO simulations with a cloud-resolving convective parameterization.

7.2 Future Work

Increasing the hindcast period and length of the integrations performed in this study would be an obvious initial extension of this work. Due to computational limitations, the integrations performed were relatively short in period and length- between 12 and 14 months and 5 to 10 days forecast lead time, respectively. A consequence of this was that only two strong MJO events could be identified for the case study analysis presented in §4.5. Since individual MJO events exhibit such varying characteristics, while these case studies can be compared with observations, drawing general conclusions about all MJO events in the IFS based on these findings alone would be inappropriate. A natural extension of this work would, therefore, be to perform hindcast experiments of other identified MJO events using the CAPE and CONV experimental setup to assess whether

ϵ_{org}^{RH} improves MJO simulation in all cases. It would be interesting to also extend the length of the integrations to assess the effect of ϵ_{org}^{RH} on predictive skill of the MJO at longer forecast lead times.

Despite understanding the physical mechanisms responsible for the advances in MJO simulation in the post-Cy32r3 IFS, simulation of tropical intraseasonal variability with the ϵ_{org}^{RH} formulation for entrainment is by no means perfect. The post-Cy32r3 MJO in the IFS is overactive, exhibits a slow phase speed and still has difficulty propagating the convective signal through the Maritime Continent. As a result, after 20 days the forecasted MJO can be completely out of phase with the verifying observations (Vitart and Molteni, 2009b). The fact that problems remain in representing the phase speed and propagation characteristics of the MJO supports the consensus that there is no unifying theory for the MJO which is able to explain all aspects of its behaviour. This thesis has focused on the "physics" of the MJO and understanding how changing the local control on convection can affect the large-scale circulation in terms of the amplitude of the MJO. There is plenty of scope in the future for further understanding of the interactions between the physics and dynamics of the MJO in terms of its phase speed and propagation through the Maritime Continent.

While the MJO is primarily an atmospheric phenomenon, including a better representation of air-sea interactions by coupling to the ocean has been shown to improve the simulation of the MJO. For example, Woolnough *et al.* (2007) coupled the monthly forecasting system at ECMWF to a 1D mixed layer ocean model and showed that it improved skilful predictability of the MJO by up to a week. Since this thesis has shown that the introduction of ϵ_{org}^{RH} in Cy32r3 of the IFS has significantly improved the simulation of the MJO through a more realistic moisture control on convection, repeating the integrations of Woolnough *et al.* (2007) with the modified convective parameterization would be an informative experiment. Would coupling to a mixed layer ocean model further improve the simulation of the MJO in the post-Cy32r3 IFS?

As computational capacity increases, the way in which convection is formulated in global simulations is changing dramatically. The emerging generation of superparameterizations, in which conventional convective schemes are replaced by a cloud-resolving model (CRM) embedded in each GCM column, have been shown to realistically simulate tropical variability (e.g. Khairoutdinov *et al.*, 2005). Although, with increasing resolution and in this multi-scale modelling framework (MMF) deep convection can be explicitly resolved, it does not negate the need for convective parameterizations. Shallow convection schemes are, and will in the foreseeable future be, necessary to represent convection on the smallest scales. These methods indicate an exciting future for the simulation of convection and merit further study. However, the results presented in this thesis have shown that it is possible to represent atmospheric variability in the tropics with comparable accu-

racy to the MMF using a conventional parameterization which does not explicitly resolve convection. This is important for operational centres, such as ECMWF, where the computational cost of their global forecasts is a key consideration; increased resolution must be balanced against forecast length, ensemble size and model complexity.

References

Arakawa, A. (2004). The Cumulus Parameterization Problem: Past, Present and Future. *J. Climate.*, **17**, 2493–2525.

Arakawa, A. and Schubert, W. H. (1974). Interaction of a Cumulus Cloud Ensemble with the Large-Scale Environment, Part I. *J. Atmos. Sci.*, **31**, 674–701.

Bechtold, P., Chaboureau, J.-P., Beljaars, A., Betts, A. K., Köhler, M., Miller, M., and Redelsperger, J.-L. (2004). The simulation of the diurnal cycle of convective precipitation over land in a global model. *Q. J. R. Meteorol. Soc.*, **130**, 3119–3137.

Bechtold, P., Köhler, M., Jung, T., Doblas-Reyes, F., Leutbecher, M., Rodwell, M. J., Vitart, F., and Balsamo, G. (2008). Advances in simulating atmospheric variability with the ECMWF model: From synoptic to decadal time-scales. *Q. J. R. Meteorol. Soc.*, **134**, 1337–1351.

Beljaars, A. C. M. and Betts, A. K. (1992). Validation of the Boundary Layer Representation in the ECMWF Model. In *Seminar on Validation of Models over Europe*, volume II, pages 159–195. ECMWF, Reading, UK.

Benedict, J. J. and Randall, D. A. (2009). Structure of the Madden-Julian Oscillation in the Super-parameterized CAM. *J. Atmos. Sci.*, **66**, 3277–3296.

Bessafi, M. and Wheeler, M. C. (2006). Modulation of South Indian Ocean Tropical Cyclones by the Madden-Julian Oscillation and Convectively Coupled Equatorial Waves. *Mon. Wea. Rev.*, **134**, 638–656.

Betts, A. K. (1986). A new convective adjustment scheme. Part I: Observational and theoretical basis. *Q. J. R. Meteorol. Soc.*, **112**, 677–691.

Betts, A. K. and Miller, M. J. (1986). A new convective adjustment scheme. Part II: Single column test using GATE wave, BOMEX, ATEX and arctic air-mass data sets. *Q. J. R. Meteorol. Soc.*, **112**, 693–709.

Bladé, I. and Hartmann, D. L. (1993). Tropical Intraseasonal Oscillations in a Simple Nonlinear Model. *J. Atmos. Sci.*, **50**(17), 2922–2939.

Bond, N. A. and Vecchi, G. A. (2003). The Influence of the Madden-Julian Oscillation on Precipitaion in Oregon and Washington. *Weather Forecasting*, **18**, 600–613.

Bretherton, C. S., Peters, M. E., and Back, L. E. (2004). Relationships between Water Vapor Path and Precipitation over the Tropical Oceans. *J. Climate.*, **17**, 1517–1528.

Brown, R. G. and Bretherton, C. S. (1995). Tropical Wave Instabilities: Convective Interaction with Dynamics Using the Emanuel Convective Parameterization. *J. Atmos. Sci.*, **52**(1), 67–82.

Camargo, S. J., Robertson, A. W., Barnston, A. G., and Ghil, M. (2008). Clustering of eastern North Pacific tropical cyclone tracks: ENSO and MJO effetcs. *Geochem. Geophys. Geosyst.*, **9**(Q06V05 doi:10.1029/2007GC001861).

Cassou, C. (2008). Intraseasonal interaction between the Madden-Julian Oscillation and the North Atlantic Oscillation. *Nature*, **455**, 523–527.

Chang, C.-P. (1977). Viscous Internal Gravity Waves and Low-Frequency Oscillations in the Tropics. *J. Atmos. Sci.*, **34**, 901–910.

Chao, W. C. (1987). On the Origin of the Tropical Intraseasonal Oscillation. *J. Atmos. Sci.*, **44**(15), 1940–1949.

Charney, J. G. and Eliassen, A. (1964). On the Growth of the Hurricane Depression. *J. Atmos. Sci.*, **21**, 68–75.

Clayson, C. A., Strahl, B., and Schrage, J. (2002). 2-3-Day Convective Variability in the Tropics Western Pacific. *Mon. Wea. Rev.*, **130**, 529–548.

Crum, F. X. and Stevens, D. E. (1983). A Comparison of Two Cumulus Parameterization Sschemes in a Linear Model of Wave-CISK. *J. Atmos. Sci.*, **40**, 2671–2688.

Dee, D. P., Uppala, S. M., Simmons, A. J., Berrisford, P., Poli, P., Kobayashi, S., Andrae, U., Balmaseda, M. A., Balsamo, G., Bauer, P., Bechtold, P., Beljaars, A. C. M., van de Berg, L., Bidlot, J., Bormann, N., Delsol, C., Dragani, R., Fuentes, M., Geer, A. J., Haimberger, L., Healy, S. B., Hersbach, H., Holm, E. V., Isaksen, L., Kallberg, P., Kohler, M., Matricardi, M., McNally, A. P., Monge-Sanz, B. M., Morcrette, J.-J., Park, B.-K., Peuby, C., de Rosnay, P., Tavolato, C., Thepaut, J.-N., and Vitart, F. (2011). The ERA-Interim reanalysis: configuration and performance of the data assimilation system. *Q. J. R. Meteorol. Soc.*, **137**, 553–597.

Deng, L. and Wu, X. (2010). Effect of Convective Processes on GCM Simulations of the Madden-Julian Oscillation. *J. Climate.*, **23**, 352–377.

Derbyshire, S. H., Beau, I., Bechtold, P., Grandpeix, J.-Y., Piriou, J.-M., Redelsperger, J.-L., and Soares, P. M. M. (2004). Sensitivity of moist convection to environmental humidity. *Q. J. R. Meteorol. Soc.*, **130**, 3055–3079.

Dunkerton, T. J. and Crum, F. X. (1991). Scale Selection and Propagation of Wave-CISK with Conditional Heating. *J. Met. Soc. Japan*, **69**(4), 449–458.

Dunkerton, T. J. and Crum, F. X. (1995). Eastward propagating 2- to 15-day equatorial convection and its relation to the tropical intraseasonal oscillation- to 15-day equatorial convection and its relation to the tropical intraseasonal oscillation. *J. Geophys. Res*, **100**, 25,781–25,790.

ECMWF (2007a). IFS documentation. Cy33r1. http://www.ecmwf.int/research/ifsdocs/CY33r1/.

ECMWF (2007b). IFS documentation. Cy33r1 Part IV: Physical processes. http://www.ecmwf.int/research/ifsdocs/CY33r1/PHYSICS/IFSPart4.pdf.

ECMWF (2010). IFS documentation. Cy36r1 Part IV: Physical processes. http://www.ecmwf.int/research/ifsdocs/CY36r1/PHYSICS/IFSPart4.pdf.

Emanuel, K. A. (1987). An Air-Sea Interaction Model of Intraseasonal Oscillations in the Tropics. *J. Atmos. Sci.*, **44**(16), 2324–2340.

Emanuel, K. A. (1993). The Effect of Convective Response Time on WISHE Modes. *J. Atmos. Sci.*, **50**(12), 1763–1775.

Emanuel, K. A., Neelin, J. D., and Bretherton, C. S. (1994). On large-scale circulations in convecting atmospheres. *Q. J. R. Meteorol. Soc.*, **120**(519), 1111–1143.

Flatau, M., Flatau, P. J., Phoebus, P., and Niler, P. P. (1997). The Feedback between Equatorial Convection and Local Radiative and Evaporative Processes: The Implications for Intraseasonal Oscillations. *J. Atmos. Sci.*, **54**, 2373–2386.

Fritsch, J. M. and Chappell, C. F. (1980). Numerical Prediction of Convectively Driven Mesoscale Pressure Systems. Part I: Convective Parameterization. *J. Atmos. Sci.*, **37**, 1722–1733.

Fuchs, Z. and Raymond, D. J. (2002). Large-Scale Modes of a Nonrotating Atmosphere with Water Vapor and Cloud-Radiation Feedbacks. *J. Atmos. Sci.*, **59**, 1669–1679.

Fuchs, Z. and Raymond, D. J. (2005). Large-Scale Modes in a Rotating Atmosphere with Radiative-Convective Instability and WISHE. *J. Atmos. Sci.*, **62**, 4084–4094.

Gill, A. E. (1980). Some simple solutions for heat-induced tropical circulation. *Q. J. R. Meteorol. Soc.*, **106**, 447–462.

Goswami, B. N. (2005). South asian monsoon. In W. K. M. Lau and D. E. Waliser, editors, *Intraseasonal Variability of the Atmosphere-Ocean Climate System*, pages 19–62. Springer, Heidelberg, Germany.

Gottschalck, J., Wheeler, M. C., Weickmann, K. M., Vitart, F., Savage, N., Lin, H., Hendon, H. H., Waliser, D., Sperber, K., Nakagawa, M., Prestrelo, C., Flatau, M., and Higgins, W. (2010). A framework for assessing operational Madden-Julian Oscillation Forecasts: A CLIVAR MJO Working Group Project. *Bull. Amer. Meteor. Soc*, **91**, 1247–1258.

Grabowski, W. W. (2001). Coupling Cloud Processes with the Large-Scale Dynamics using the Cloud-Resolving Convection Parameterization (CRCP). *J. Atmos. Sci.*, **58**, 978–997.

Grabowski, W. W. (2003). MJO-like Coherent Structures: Sensitivity Simulations using the Cloud-Resolving Convection Parameterization (CRCP). *J. Atmos. Sci.*, **60**, 847–864.

Grabowski, W. W. and Moncrieff, M. W. (2004). Moisture-convection feedback in the tropics. *Q. J. R. Meteorol. Soc.*, **130**, 3081–3104.

Gregory, D. and Rowntree, P. R. (1990). A Mass Flux Convection Scheme with Representation of Cloud Ensemble Characteristics and Stability-Dependent Closure. *Mon. Wea. Rev.*, **118**, 1483–1506.

Gregory, D., Morcrette, J.-J., Jakob, C., Beljaara, A. C. M., and Stockdale, T. (2000). Revision of convection, radiation and cloud schemes in the ECMWF Integrated Forecasting System. *Q. J. R. Meteorol. Soc.*, **126**, 1685–1710.

Hall, J. D., Matthews, A. J., and Karoly, D. J. (2001). The Modulation of Tropical Cyclone Activity in the Australian Region by the Madden-Julian Oscillation. *Mon. Wea. Rev.*, **129**, 2970–2982.

Hayashi, Y. (1970). A Theory of Large-Scale Equatorial Waves Generated by Condensation Heat and Accelerating the Zonal Wind. *J. Met. Soc. Japan*, **48**(2), 140–160.

Hayashi, Y. and Golder, D. G. (1986). Tropical Intraseasonal Oscillations Appearing in a GFDL General Circulation Model and FGGE Data. Part I: Phase Propagation. *J. Atmos. Sci.*, **43**(24), 3058–3067.

Hayashi, Y. and Golder, D. G. (1997). United Mechanisms for the Generation of Low- and High-Frequency Tropical Waves. Part I: Control Experiments with Moist Convective Adjustment. *J. Atmos. Sci.*, **54**, 1262–1276.

Hendon, H. H. (2000). Impact of Air-Sea Coupling on the Madden-Julian Oscillation in a General Circulation Model. *J. Atmos. Sci.*, **57**, 3939–3952.

Hendon, H. H. and Glick, J. (1997). Intraseasonal Air-Sea Interaction in the Tropical Indian and Pacific Oceans. *J. Climate.*, **10**, 647–661.

Hendon, H. H. and Liebmann, B. (1990). The Intraseasonal (30-50 day) Oscillation of the Australian Summer Monsoon. *J. Atmos. Sci.*, **47**, 2909–2923.

Hendon, H. H. and Liebmann, B. (1994). Organization of convection within the Madden-Julian oscillation. *J. Geophys. Res*, **99**, 8073–8083.

Hendon, H. H. and Salby, M. L. (1994). The Life Cycle of the Madden-Julian Oscillation. *J. Atmos. Sci.*, **51**(15), 2225–2237.

Holloway, C. (2011). Cascade: High-resolution large-domain simulations of tropical convection. In *YOTC International Science Symposium & 8th AMY Worshop*, Beijing, China.

Holloway, C. E. and Neelin, J. D. (2009). Moisture Vertical Structure, Column Water Vapour, and Tropical Deep Convection. *J. Atmos. Sci.*, **66**, 1665–1683.

Hsu, H.-H., Hoskins, B. J., and Jin, F.-F. (1990). The 1985/86 Intraseasonal Oscillation and the Role of the Extratropics. *J. Atmos. Sci.*, **47**(7), 823–839.

Hu, Q. and Randall, D. A. (1994). Low-Frequency Oscillations in Radiative-Convective Systems. *J. Atmos. Sci.*, **51**(8), 1089–1099.

Hu, Q. and Randall, D. A. (1995). Low-Frequency Oscillations in Radiative-Convective Systems. Part II: An Idealized Model. *J. Atmos. Sci.*, **52**(4), 478–490.

Hu, X.-M., Nielsen-Gammon, J. W., and Zhang, F. (2010). Evaluation of Three Planetary Boundary Layer Schemes in the WRF Model. *J. Appl. Meteor. Climatol*, **49**, 1831–1844.

Inness, P. M. and Slingo, J. M. (2003). Simulation of the Madden-Julian Oscillation in a Coupled General Circulation Model: Part I: Comparison with Observations and an Atmosphere-Only GCM. *J. Climate.*, **16**, 345–364.

Inness, P. M., Slingo, J. M., Woolnough, S. J., Neale, R. B., and Pope, V. D. (2001). Organization of tropical convection in a GCM with varying vertical resolution; implications for the simulation of the Madden-Julian Oscillation. *Climate Dynamics*, **17**, 777–793.

Inness, P. M., Slingo, J. M., Guilyardi, E., and Cole, J. (2003). Simulation of the Madden-Julian Oscillation in a Coupled General Circulation Model: Part II: The Role of the Basic State. *J. Climate.*, **16**, 365–382.

Jakob, C. and Siebesma, A. P. (2003). A New Subcloud Model for Mass-Flux Convection Schemes: Influence on Triggering, Updraft Properties, and Model Climate. *Mon. Wea. Rev.*, **131**, 2765–2778.

Jiang, X., Waliser, D. E., Wheeler, M. C., Jones, C., Lee, M.-I., and Schubert, S. D. (2008). Assessing the Skill of an All-Season Statistical Forecast Model for the Madden-Julian Oscillation. *Mon. Wea. Rev.*, **136**, 1940–1956.

Johnson, R. H., Rickenbach, T. M., Rutledge, S. A., Ciesielski, P. E., and Schubert, W. H. (1999). Trimodal Characteristics of Tropical Convection. *J. Climate.*, **12**, 2397–2418.

Jones, C., Waliser, D. E., Schemm, J.-K. E., and Lau, W. K. M. (2000). Prediction skill of the Madden and Julian Oscillation in dynamical extended range forecasts. *Climate Dynamics*, **16**, 273–289.

Jones, C., Carvalho, L. M. V., Higgins, R. W., and Waliser, D. E. (2004). A Statistical Forecast Model of Tropical Intraseasonal Convection Anomalies. *J. Climate.*, **17**, 2078–2095.

Kemball-Cook, S., Wang, B., and Fu, X. (2002). Simulation of the Intraseasonal Oscillation in the ECHAM-4 Model: The Impact of Coupling with an Ocean Model. *J. Atmos. Sci.*, **59**(9), 1433–1453.

Kessler, W. S. and McPhaden, M. J. (1995). Forcing of intraseasonal Kelvin waves in the equatorial Pacific. *J. Geophys. Res*, **100**, 10,613–10,631.

Khairoutdinov, M., Randall, D. A., and DeMott, C. (2005). Simulations of the Atmospheric General Circulation Using a Cloud-Resolving Model as a Superparameterization of Physical Processes. *J. Atmos. Sci.*, **62**, 2136–2154.

Khairoutdinov, M. F. and Randall, D. A. (2001). A Cloud Resolving Model as a Cloud Parameterization in the NCAR Community Climate System Model: Preliminary Results. *Geophys. Res. Lett*, **28**, 3617–3620.

Kiladis, G. N., Straub, K. H., and Haertel, P. T. (2005). Zonal and Vertical Structure of the Madden-Julian Oscillation. *J. Atmos. Sci.*, **62**, 2790–2809.

Kiladis, G. N., Wheeler, M. C., Haertel, P. T., and Straub, K. H. (2009). Convectively Coupled Equatorial Waves. *Rev. Geophys.*, **47**(RG2003), doi:10.1029/2008RG000266.

Kim, D., K., Stern, W., Waliser, D., Kang, I.-S., Maloney, E. D., Wang, W., Weickmann, K., J. Benedict, M. K., Lee, M.-I., Neale, R., Suarez, M., Thayer-Calder, K., and Zhang, G. (2009). Application of MJO Simulation Diagnostics to Climate Models. *J. Climate.*, **22**, 6413–6436.

Klingaman, N. (2011). Using a case-study approach to improve the MJO in the Hadley Centre climate model (HadGEM). In *YOTC International Science Symposium & 8th AMY Worshop*, Beijing, China.

Klingaman, N. P., Woolnough, S. J., Weller, H., and Slingo, J. M. (2011). The Impact of Finer-Resolution Air-Sea Coupling on the Intraseasonal Oscillation of the Indian Monsoon. *J. Climate.*, **24**, 2451–2468.

Klotzbach, P. J. (2010). On the Madden-Julian Oscilation-Atlantic Hurricane Relationship. *J. Climate.*, **23**, 282–293.

Knutson, T. R. and Weickmann, K. M. (1987). 30-60 Day Atmospheric Oscillations: Composite Life Cycles of Convection and Circulation Anomalies. *Mon. Wea. Rev.*, **115**, 1407–1436.

Knutson, T. R., Weickmann, K. M., and Kutzbach, J. E. (1986). Global-Scale Intraseasonal Oscillations of Outgoing Longwave Radiation and 250 mb Zonal Wind during Northern Hemisphere Summer. *Mon. Wea. Rev.*, **114**, 605–623.

Kuang, Z. and Bretherton, C. S. (2006). A Mass-Flux Scheme View of a High-Resolution Simulation of a Transition from Shallow to Deep Convection. *J. Atmos. Sci.*, **63**, 1895–1909.

Kuo, H. L. (1965). On Formation and Intensification of Tropical Cyclones Through Latent Heat Release by Cumulus Convection. *J. Atmos. Sci.*, **22**, 40–63.

Kuo, H. L. (1974). Further Studies of the Parametrization of the Influence of Cumulus Convection on Large-Scale Flow. *J. Atmos. Sci.*, **31**, 1232–1240.

Lau, K. M. and Peng, L. (1987). Origin of Low-Frequency (Intraseasonal) Oscillations in the Tropical Atmosphere. Part I: Basic Theory. *J. Atmos. Sci.*, **44**(6), 950–972.

Lau, N.-C. and Lau, K.-M. (1986). The Structure and Propagation of Intraseasonal Oscillations Appearing in a GFDL General Circulation Model. *J. Atmos. Sci.*, **43**(19), 2023–2047.

Lawrence, D. M. and Webster, P. J. (2002). The Boreal Summer Intraseasonal Oscillation: Relationship between Northward and Eastward Movement of Convection. *J. Atmos. Sci.*, **59**, 1593–1606.

Lee, M.-I., Kang, I.-S., Kim, J.-K., and Mapes, B. E. (2001). Influence of cloud-raidation interaction on simulating tropical intraseasonal oscillation with an atmospheric general circulation model. *J. Geophys. Res*, **106**, 14,219–14,233.

Lee, M.-I., Kang, I.-S., and Mapes, B. E. (2003). Impacts of Cumulus Convection Parameterization on Aqua-planet AGCM Simulations of Tropical Intraseasonal Variability. *J. Met. Soc. Japan*, **81**(5), 963–992.

Liebmann, B. and Hartmann, D. L. (1984). An Observational Study of Tropical-Midlatitude Interaction on Intraseasonal Time Scales during Winter. *J. Atmos. Sci.*, **41**, 3333–3350.

Liebmann, B. and Smith, C. A. (1996). Description of a complete (interpolated) OLR dataset. *Bull. Amer. Meteor. Soc*, **77**, 1275–1277.

Liebmann, B., Kiladis, G. N., Vera, C. S., Saulo, A. C., and Carvalho, L. M. V. (2004). Subseasonal Variations of Rainfall in South America in the Vacinity of the Low-Level Jet East of the Andes and Comparison to Those in the South Atlantic Convergence Zone. *J. Climate.*, **17**, 3829–3842.

Liess, S. and Bengtsson, L. (2004). The intraseasonal oscillation in ECHAM4 Part II: sensitivity studies. *Climate Dynamics*, **22**, 671–688.

Lin, H., Brunet, G., and Derome, J. (2007). Intraseasonal Variability in a Dry Atmospheric Model. *J. Atmos. Sci.*, **64**, 2422–2441.

Lin, H., Brunet, G., and Derome, J. (2008a). Forecast Skill of the Madden-Julian Oscillation in Two Canadian Atmospheric Models. *Mon. Wea. Rev.*, **136**, 4130–4149.

Lin, H., Brunet, G., and Derome, J. (2009). An Observed Connection between the North Atlantic Oscillation and the Madden-Julian Oscillation. *J. Climate.*, **22**, 364–380.

Lin, J.-L., Kiladis, G. N., Mapes, B. E., Weickmann, K. M., Sperber, K. R., Lin, W., Wheeler, M. C., Schubert, S. D., Genio, A. D., Donner, L. J., Emori, S., Gueremy, J.-F., Hourdin, F., Rasch, P. J., Roeckner, E., and Scinocca, J. F. (2006). Tropical Intraseasonal Variability in 14 IPCC AR4 Climate Models. Part I: Convective Signals. *J. Climate.*, **19**, 2665–2690.

Lin, J.-L., Lee, M.-I., Kim, D., Kang, I.-S., and Frierson, D. M. W. (2008b). The Impacts of Convective Parameterization and Moisture Triggering on AGCM-Simulated Convectively Coupled Equatorial Waves. *J. Climate.*, **21**, 883–909.

Lin, J. W., Neelin, J. D., and Zeng, N. (2000). Maintenance of Tropical Intraseasonal Variability: Impact of Evapouration-Wind Feedback and Midlatitude Storms. *J. Atmos. Sci.*, **57**(17), 2793–2823.

Lin, X. and Johnson, R. H. (1996a). Heating, Moistening and Rainfall over the Western Pacific Warm Pool during TOGA COARE. *J. Atmos. Sci.*, **53**, 3367–3383.

Lin, X. and Johnson, R. H. (1996b). Kinematic and Thermodynamic Characteristics of the Flow over the Western Pacific Warm Pool during TOGA COARE. *J. Atmos. Sci.*, **53**(5), 695–715.

Lindzen, R. S. (1974). Wave-CISK in the Tropics. *J. Atmos. Sci.*, **31**, 156–179.

Lindzen, R. S. (1988). Some Remarks on Cumulus Parameterization. *PAGEOPH*, **126**, 123–134.

Liu, P., Wang, B., Sperber, K. R., Li, T., and Meehl, G. A. (2005). MJO in the NCAR CAM2 with the Tiedtke Convection Scheme. *J. Climate.*, **18**, 3007–3020.

Lo, F. and Hendon, H. H. (2000). Empirical Extended-Range Prediction of the Madden-Julian Oscillation. *Mon. Wea. Rev.*, **128**, 2528–2543.

Love, B. S. and Matthews, A. J. (2009). Real-time localised forecasting of the Madden-Julian Oscillation using neural network models. *Q. J. R. Meteorol. Soc.*, **135**, 1471–1483.

Love, B. S., Matthews, A. J., and Janacek, G. J. (2008). Real-Time Extraction of the Madden-Julian Oscillation Using Empirical Mode Decomposition and Statistical Forecasting with a VARMA Model. *J. Climate.*, **21**, 5318–5335.

Madden, R. A. (1986). Seasonal Variations of the 40-50 Day Oscillation in the Tropics. *J. Atmos. Sci.*, **43**(24), 3138–3158.

Madden, R. A. and Julian, P. R. (1971). Detection of a 40-50 Day Oscillation in the Zonal Wind in the Tropical Pacific. *J. Atmos. Sci.*, **28**, 702–708.

Madden, R. A. and Julian, P. R. (1972). Description of Global-Scale Circulation Cells in the Tropics with a 40-50 Day Period. *J. Atmos. Sci.*, **29**, 1109–1123.

Maloney, E. D. (2009). The Moist Static Energy Budget of a Composite Tropical Intraseasonal Oscillation in a Climate Model. *J. Climate.*, **22**, 711–729.

Maloney, E. D. and Hartmann, D. L. (1998). Frictional Moisture Convergence in a Composite Life Cycle of the Madden-Julian Oscillation. *J. Climate.*, **11**, 2387–2403.

Maloney, E. D. and Hartmann, D. L. (2000a). Modulation of Eastern North Pacific Hurricanes by the Madden-Julian Oscillation. *J. Climate.*, **13**, 1451–1460.

Maloney, E. D. and Hartmann, D. L. (2000b). Modulation of Hurricane Activity in the Gulf of Mexico by the Madden-Julian Oscillation. *Science*, **287**, 2002–2004.

Maloney, E. D. and Hartmann, D. L. (2001). The Sensitivty of Intraseasonal Variability in the NCAR CCM3 to Changes in Convective Parameterization. *J. Climate.*, **14**, 2015–2034.

Maloney, E. D. and Sobel, A. H. (2004). Surface Fluxes and Ocean Coupling in the Tropical Intraseasonal Oscillation. *J. Climate.*, **17**, 4368–4386.

Manabe, S. and Stricker, R. F. (1964). Thermal Equilibrium of the Atmosphere with a Convective Adjustment. *J. Atmos. Sci.*, **21**, 361–385.

Mapes, B. E. and Houze, R. A. (1993). Cloud Clusters and Superclusters over the Oceanic Warm Pool. *Mon. Wea. Rev.*, **121**, 1398–1415.

Matsuno, T. (1966). Quasi-Geostrophic Motions in the Equatorial Area. *J. Met. Soc. Japan*, **44**, 25–42.

Matthews, A. J. (2000). Propagation mechanisms for the Madden-Julian Oscillation. *Q. J. R. Meteorol. Soc.*, **126**(569), 2637–2651.

Matthews, A. J. (2004). Intraseasonal Variability over Tropical Africa during Northern Summer. *J. Climate.*, **17**, 2427–2440.

Matthews, A. J. (2008). Primary and successive events in the Madden-Julian Oscilltion. *Q. J. R. Meteorol. Soc.*, **134**, 439–453.

Matthews, A. J. and Kiladis, G. N. (1999). The Tropical-Extratropical Interaction between High-Frequency Transients and the Madden-Julian Oscillation. *Mon. Wea. Rev.*, **127**, 661–677.

McPhaden, M. J. (1999). Genesis and Evolution of the 1997-98 El Niño. *Science*, **283**, 950–954.

Miller, A. J., Zhou, S., and Yang, S.-K. (2003). Relationship of the Arctic and Antarctic Oscillation to outgoing longwave radiation. *J. Climate.*, **16**, 1583–1592.

Miller, M., Buizza, R., Haseler, J., Hortal, M., Janssen, P., and Untch, A. (2010). Increase resolution in the ECMWF determinisitc and ensemble prediction systems. *ECMWF Newsletter*, **124**, 10–16.

Milliff, R. F. and Madden, R. A. (1996). The Existence and Vertical Structure of Fast, Eastward-Moving Disturbances in the Equatorial Troposphere. *J. Atmos. Sci.*, **53**(4), 586–597.

Mo, K. C. (2000). Intraseasonal Modulation of Summer Precipitation over North America. *Mon. Wea. Rev.*, **128**, 1490–1505.

Mo, K. C. (2001). Adaptive Filtering and Prediction of Intraseasonal Oscillations. *Mon. Wea. Rev.*, **129**, 802–817.

Morcrette, J.-J., Barker, H. W., Iacono, M. J., Mozdzynski, G., Pincus, R., Salmond, D., and Serrar, S. (2007). A new radiation package McRAD. *ECMWF Newsletter*, **112**, 22–32.

Morcrette, J.-J., Barker, H. W., Cole, J. N. S., Iacono, M. J., and Pincus, R. (2008). Impact of a New Radiation Package, McRad, in the ECMWF Integrated Forecasting System. *Mon. Wea. Rev.*, **136**, 4773–4798.

Moskowitz, B. M. and Bretherton, C. S. (2000). An Analysis of Frictional Feedback on a Moist Equatorial Kelvin Mode. *J. Atmos. Sci.*, **57**, 2188–2206.

Nakazawa, T. (1988). Tropical Super Clusters within Intraseasonal Variations over the Western Pacific. *J. Met. Soc. Japan*, **66**(6), 823–839.

Neelin, J. D., Held, I. M., and Cook, K. H. (1987). Evaporation-Wind Feedback and Low-Frequency Variability in the Tropical Atmosphere. *J. Atmos. Sci.*, **44**, 2341–2348.

Nordeng, T. E. (1994). Extended versions of the convective paramterization scheme at ECMWF and their impact on the mean and transient activity of the model tropics. Technical Report 206, ECMWF.

Ohuchi, K. and Yamasaki, M. (1997). Kelvin Wave-CISK Controlled by Surface Friction: A Possible Mechanism of Super Cloud Cluster Part I: Linear Theory. *J. Met. Soc. Japan*, **75**(2), 497–511.

Park, C.-K., Straus, D. M., and Lau, K.-M. (1990). An Evaluation of the Structure of Tropical Intraseasonal Oscillations in Three General Circulation Models. *J. Met. Soc. Japan*, **68**(4), 403–417.

Randall, D. A., Arakawa, A., and Grabowski, W. W. (2003). Breaking the Cloud Parameterization Deadlock. *Bull. Amer. Meteor. Soc*, **84**, 1547–1564.

Randall, D. A., Wood, R. A., Bony, S., Colman, R., Fichefet, T., Fyfe, J., Kattsov, V., Pitman, A., Shukla, J., Srinivasan, J., Stouffer, R. J., Sumi, A., and Taylor, K. (2007). Climate Models and Their Evaluation. In *The IPCC Fourth Assessment Report*. Cambridge University Press.

Rao, S. A. and Yamagata, T. (2004). Abrupt termination of Indian Ocean dipole events in repsonse to intraseasonal disturbances. *Geophys. Res. Lett*, **31**(L19306), doi:10,1029/2004GL020842.

Rashid, H. A., Hendon, H. H., Wheeler, M. C., and Alves, O. (2010). Prediction of the Madden-Julian Oscillation with the POAMA dynamical prediction system. *Climate Dynamics*, **36**, 649–661.

Ray, P., Zhang, C., Dudhia, J., and Chen, S. S. (2009). A Numerical Case Study on the Initiation of the Madden-Julian Oscillation. *J. Atmos. Sci.*, **66**, 310–331.

Ray, P., Zhang, C., Moncrieff, M. W., Dudhia, J., Caron, J. M., Leung, L. R., and Bruyere, C. (2011). Role of the atmospheric mean state on the initiation of the Madden-Julian Oscillation in a tropical channel model. *Climate Dynamics*, **36**, 161–184.

Raymond, D. J. (1994). Cumulus convection and the Madden-Julian Oscillation of the tropical troposphere. *Physica D*, **77**, 1–22.

Raymond, D. J. (2000). Thermodynamic control of tropical rainfall. *Q. J. R. Meteorol. Soc.*, **126**, 889–898.

Raymond, D. J. (2001). A New Model of the Madden-Julian Oscillation. *J. Atmos. Sci.*, **58**, 2807–2819.

Redelsperger, J.-L., Parsons, D. B., and Guichard, F. (2002). Recovery processes and factors limiting cloud-top height following the arrival of a dry intrusion observed during TOGA-COARE. *J. Atmos. Sci.*, **59**, 2438–2457.

Reichler, T. and Roads, J. O. (2005). Long-Range Predictability in the Tropics. Part II: 30-60-Day Variability. *J. Climate.*, **18**, 634–650.

Rui, H. and Wang, B. (1990). Development Characteristics and Dynamic Structure of Tropical Intraseasonal Convection Anomalies. *J. Atmos. Sci.*, **47**(3), 357–379.

Salby, M. L., Garcia, R. R., and Hendon, H. H. (1994). Planetary-Scale Circulations in the Presence of Climatological and Wave-Induced Heating. *J. Atmos. Sci.*, **51**(16), 2344–2367.

Seo, K.-H. and Kim, K.-Y. (2003). Propagation and initiaion mechanisms of the Madden-Julian Oscillation. *J. Geophys. Res*, **108**(D13), 4384, doi:10.1029/2002JD002876.

Slingo, J. M., Sperber, K. R., Boyle, J. S., Ceron, J. P., Dix, M., Dugas, B., Ebisuzaki, W., Fyfe, J., Gregory, D., Gueremy, J. F., Hack, J., Harzallah, A., Inness, P., Kitoh, A., Lau, W. K. M., McAvaney, B., Madden, R. A., Matthews, A. J., Palmer, T. N., Park, C. K., Randall, D. A., and Renno, N. (1996). Intraseasonal oscillations in 15 atmospheric general circulation models: results from an AMIP diagnostic subproject. *Climate Dynamics*, **12**, 325–357.

Sperber, K. R. (2003). Propagation and the Vertical Structure of the Madden-Julian Oscillation. *Mon. Wea. Rev.*, **131**, 3018–3037.

Sperber, K. R. (2004). Madden-Julian variability in NCAR CAM2.0 and CCSM2.0. *Climate Dynamics*, **23**, 259–278.

Sperber, K. R. and Waliser, D. E. (2008). New Approaches to Understanding, Simulating, and Forecasting the Madden-Julian Oscillation. *Bull. Amer. Meteor. Soc*, **89**, 1917–1920.

Sperber, K. R., Slingo, J. M., Inness, P. M., and Lau, W. K.-M. (1997). On the maintenance and initiaion of the intraseasonal oscillation in the NCEP/NCAR reanalysis and in the GLA and UKMO AMIP simulations. *Climate Dynamics*, **13**, 769–795.

Sperber, K. R., Gualdi, S., Legutke, S., and Gayler, V. (2005). The Madden-Julian Oscillation in ECHAM4 Coupled and Uncoupled GCMs. *Climate Dynamics*, **25**, 117–140.

Stein, T. (2011). Composite of vertical cloud profiles for the Madden-Julian Oscillation from Cloud-Sat and CALIPSO observations. In *YOTC International Science Symposium & 8th AMY Worshop*.

Swinbank, R., Palmer, T. N., and Davey, M. K. (1988). Numerical Simulations of the Madden and Julian Oscillation. *J. Atmos. Sci.*, **45**(5), 774–788.

Thayer-Calder, K. and Randall, D. A. (2009). The Role of Convective Moistening in the Madden-Julian Oscillation. *J. Atmos. Sci.*, **66**, 3297–3312.

Tiedtke, M. (1989). A Comprehensive Mass Flux Scheme for Cumulus Parameterization in Large-Scale Models. *Mon. Wea. Rev.*, **117**, 1779–1800.

Tompkins, A. M. (2001). Organization of Tropical Convection in Low Vertical Wind Shears: The Role of Water Vapour. *J. Atmos. Sci.*, **58**(6), 529–545.

Tompkins, A. M. and Giuseppe, F. D. (2009). Cloud Radiative Interactions and their uncertainty in climate models. In P. Williams and T. Palmber, editors, *Stochastic Physics and Climate Models*. Cambridge University Press.

Vitart, F. (2003). Monthly forecasting system. Technical Report 424, ECMWF.

Vitart, F. (2009). Impact of the Madden Julian Oscillation on tropical storms and risk of landfall in the ECMWF forecast system. *Geophys. Res. Lett*, **36**(L15802), doi:10.1029/2009GL039089.

Vitart, F. and Molteni, F. (2009a). Dynamical Extended-Range Prediction of Early Monsoon Rainfall over India. *Mon. Wea. Rev.*, **137**, 1480–1492.

Vitart, F. and Molteni, F. (2009b). Simulation of the MJO and its teleconnections in an ensemble of 46-day EPS hindcasts. Technical Report 597, ECMWF.

Vitart, F., Woolnough, S. J., Balmaseda, M. A., and Tompkins, A. M. (2007). Monthly Forecast of the Madden-Julian Oscillation using a Coupled GCM. *Mon. Wea. Rev.*, **135**, 2700–2715.

Waite, M. L. and Khouider, B. (2010). The Deepening of Tropical Convection by Congestus Preconditioning. *J. Atmos. Sci.*, **67**, 2601–2615.

Waliser, D. E., Jones, C., Schemm, J.-K. E., and Graham, N. E. (1999). A Statistical Extended-Range Tropical Forecast Model Based on the Slow Evolution of the Madden-Julian Oscillation. *J. Climate.*, **12**, 1918–1939.

Waliser, D. E., Lau, K. M., Stern, W., and Jones, C. (2003). Potential Predictability of the Madden-Julian Oscillation. *Bull. Amer. Meteor. Soc*, **84**, 33–50.

Waliser, D. E., Sperber, K. R., Hendon, H. H., Kim, D., Maloney, E. D., Wheeler, M. C., Weickmann, K. M., Zhang, C., Donner, L., Gottschalck, J., Higgins, W., Kang, I.-S., Legler, D., Moncrieff, M., Schubert, S., Stern, W., Vitart, F., Wang, B., Wang, W., and Woolnough, S. J. (2009). MJO Simulation Diagnostics. *J. Climate.*, **22**, 3006–3030.

Wang, B. (1988a). Comments on "An Air-Sea Interaction Model of Intraseasonal Oscillation in the Tropics". *J. Atmos. Sci.*, **45**, 3521–3525.

Wang, B. (1988b). Dynamics of Tropical Low-Frequency Waves: An Analysis of the Moist Kelvin Wave. *J. Atmos. Sci.*, **45**(14), 2051–2065.

Wang, B. and Rui, H. (1990). Dynamics of the Coupled Moist Kelvin-Rossby Wave on an Equatorial -Plane. *J. Atmos. Sci.*, **47**(4), 397–413.

Wang, B. and Xie, X. (1998). Coupled Modes of the Warm Pool Climate System. Part I: The Role of Air-Sea Interaction in Maintaining Madden-Julian Oscillation. *J. Climate.*, **11**(8), 2116–2135.

Wang, W. and Schlesinger, M. E. (1999). The Dependence on Convection Parameterization of the Tropical Intraseasonal Oscillation Simulated by the UIUC 11-Layer Atmospheric GCM. *J. Climate.*, **12**, 1423–1457.

Weickmann, K. M. (1983). Intraseasonal Circulation and Outgoing Longwave Radiation Modes During Northern Hemisphere Winter. *Mon. Wea. Rev.*, **111**, 1838–1858.

Weickmann, K. M. and Khalsa, S. J. S. (1990). The Shift of Convection from the Indian Ocean to the Western Pacific Ocean during a 30-60 Day Oscillation. *Mon. Wea. Rev.*, **118**, 964–978.

Weickmann, K. M., Lussky, G. R., and Kutzbach, J. E. (1985). Intraseasonal (30-60 Day) Fluctuations of Outgoing Longwave Radiation and 250 mb Streamfunction during Northern Winter. *Mon. Wea. Rev.*, **113**, 941–961.

Wheeler, M. (2009). An All-Seasonal Real-Time Multivariate MJO Index. http://www.cawcr.gov.au/staff/mwheeler/maproom/RMM/.

Wheeler, M. and McBride, J. L. (2005). Australian-Indonesian monsoon. In W. K. M. Lau and D. E. Waliser, editors, *Intraseasonal Variability of the Atmosphere-Ocean Climate System*, pages 125–174. Springer, Heidelberg, Germany.

Wheeler, M. and Weickmann, K. M. (2001). Real-Time Monitoring and Prediction of Modes of Coherent Synoptic to Intraseasonal Tropical Variability. *Mon. Wea. Rev.*, **129**, 2677–2694.

Wheeler, M. C. and Hendon, H. H. (2004). An All-Seasonal Real-Time Multivariate MJO Index: Development of an Index for Monitoring and Prediction. *Mon. Wea. Rev.*, **132**, 1917–1932.

Wheeler, M. C. and Kiladis, G. N. (1999). Convectively Coupled Equatorial Waves: Analysis of Clouds and Temperature in the Wavenumber-Frequency Diagram. *J. Atmos. Sci.*, **56**, 374–399.

Woolnough, S. J., Slingo, J. M., and Hoskins, B. J. (2000). The Relationship between Convection and Sea Surface Temperature on Intraseasonal Timescales. *J. Climate.*, **13**, 2086–2104.

Woolnough, S. J., Vitart, F., and Balmaseda, M. A. (2007). The role of the ocean in the Madden-Julian Oscillation: Implications for MJO prediction. *Q. J. R. Meteorol. Soc.*, **133**, 117–128.

Yamagata, T. and Hayashi, Y. (1984). A Simple Diagnotstic Model for the 30-50 Day Oscillation in the Tropics. *J. Met. Soc. Japan*, **62**(5), 709–717.

Yamasaki, M. (1969). Large-Scale Disturbances in the Conditionally Unstable Atmosphere in Low Latitudes. *Pap. Meteor. Geophys.*, **20**(4), 289–336.

Yano, J. I. and Emanuel, K. A. (1991). An Improved Model of the Equatorial Troposphere and Its Coupling with the Stratosphere. *J. Atmos. Sci.*, **48**(3), 377–389.

Yasunari, T. (1979). Cloudiness Fluctuations Associated with the Northern Hemipshere Summer Monsoon. *J. Met. Soc. Japan*, **57**, 227–242.

Zhang, C. and Dong, M. (2004). Seasonality in the Madden-Julian Oscillation. *J. Climate.*, **17**, 3169–3180.

Zhang, C. and Hendon, H. H. (1997). Propagating and Standing Components of the Intraseasonal Oscillation in Tropical Convection. *J. Atmos. Sci.*, **54**, 741–752.

Zhang, C. and McPhaden, M. J. (2000). Intraseasonal Surface Cooling in the Equatorial Western Pacific. *J. Climate.*, **13**, 2261–2276.

Zhang, C., Dong, M., Gualdi, S., Hendon, H. H., Maloney, E. D., Marshall, A., Sperber, K. R., and Wang, W. (2006). Simulations of the Madden-Julian Oscillation in four paris of coupled and uncoupled global models. *Climate Dynamics*, **27**, 573–592.

Zhu, H., Hendon, H. H., and Jakob, C. (2009). Convection in a Parameterized and Superparameterized Model and Its Role in the Representation of the MJO. *J. Atmos. Sci.*, **66**, 2796–2811.

APPENDIX:

Acronyms and Abbreviations

Abbreviation or Acronym	Definition
4D-VAR	Four-dimensional multivariate variational assimilation
AGCM	Atmospheric Global Circulation Model
AMIP	Atmospheric Model Intercomparrison Project
AR4	Fourth Assessment Report
AS	Arakawa-Schubert scheme
ASCII	Air-Sea Convective Intraseasonal Interaction
CALIPSO	Cloud-Aerosol Lidar and Infrared Pathfinder Satellite Observations
CAPE	Convective Available Potential Energy
CAPE	*Experiment*: post-Cy32r3 convection scheme with constant τ
CAM2	Community Atmosphere Model, version 2 (NCAR)
CAM3	Community Atmosphere Model, version 3 (NCAR)
CBL	Cloud-base level
CISK	Conditional Instability of the Second Kind
CLAUS	Cloud Archive User Service
CLIVAR	Climate Variability and Predictability
COADS	Comprehensive ocean-atmosphere datasets
CONV	*Experiment*: post-Cy32r3 IFS with pre-Cy32r3 convection scheme
CRCP	Cloud Resolving Convection Parameterization
CRM	Cloud Resolving Model
CTL	Cloud-top level
Cy31r1	*Control IFS version*: Cycle 31r1 of the IFS
Cy32r3	Cycle 32r3 of the IFS
DYNAMO	Dynamics of the MJO
ECHAM-4	Hamburg Atmospheric Model, version 4
ECMWF	European Centre of Medium-Range Weather Forecasting
EMD	Empirical mode decomposition
ENSO	El Niño Southern Oscillation

ENTRN	*Experiment*: post-Cy32r3 convection scheme with 0.5*entrainment
EOF	Empirical Orthogonal Functions
ER	Equatorial Rossby wave
ERA	ECMWF re-analysis
ERSL	Earth System Research Laboratory
GATE	Global Atlantic Tropical Experiment
GCM	Global Circulation Model
GEM	Global Environmental Multi-scale Model
GLA	Goddard Laboratory for the Atmospheres (NASA)
HadCM3	Hadley Centre Coupled Ocean Atmosphere General Circulation Model, version 3 (Met Office, UK)
HOPE	Hamburg Ocean Primitive Equations
IFS	Integrated Forecasting System (at ECMWF, Reading UK)
IOD	Indian Ocean Dipole
IPCC	Intergovernmental Panel on Climate Change
ITCZ	Inter-tropical Convergence Zone
KNUST	Kwame Nkrumah University of Science and Technology, Kumasi Ghana.
KUO	Kuo-type convection scheme
LCL	Lifting condensation level
LFS	Level of free sink
LH	Latent Heat
LNB	Level of neutral buoyancy
MCA	Moist convective adjustment scheme
McICA	Monte Carlo Independent Column Approximation
McRAD	New radiation package in the IFS (implemented in Cy32r2)
MJO	Madden-Julian Oscillation
MFS	Monthly Forecasting System (ECMWF)
MMF	Multi-scale Modelling Framework
MODIS	Moderate Resolution Imaging Spectroradiometer
MRF	Medium-Range Forecast (NCEP)
MRG	Mixed Rossby-Gravity wave
NAO	North Atlantic Oscillation

NASA   National Aeronautics and Space Administration

NCAR   National Centre for Atmospheric Research (U.S.A)

NCOF   National Centre of Ocean Forecasting

NCEP   National Centre for Environmental Prediction (U.S.A)

NOAA   National Oceanic and Atmospheric Administration

NPISO   Northward-propagating Intraseasonal Oscillation

NWP   Numerical Weather Prediction

OLR   Outgoing Longwave Radiation

OPER   *Control IFS version*: Operational cycle of the IFS through the
                        YOTC period

OSTIA   Operational Sea Surface Temperature and Sea Ice Analysis

PC   Principal Component

POAMA   Predictive Ocean Atmosphere Model for Australia

RH   Relative humidity

RMSE   Root mean square error

SFM   Seasonal Forecasting Model (NCEP)

SNU   Seoul National University

SP-CAM   Superparameterized CAM3 (NCAR)

SSA   Singular spectral analysis

SST   Sea Surface Temperature

SVD   Singular vector decomposition

SWEs   Shallow water equations

TOGA-COARE   Tropical Ocean Global Atmosphere
                        Coupled Ocean-Atmosphere Response Experiment

WISHE   Wind-induced surface heat exchange

WWB   Westerly Wind Burst

YOTC   Year of Tropical Convection (May 2008 - January 2010)